Culture of Excellence

ISSCR ANNUAL MEETING GOLD SUPPORTER

Visit BI booth
#1419

Redefining Stem Cell Excellence

and Advancing Clinical Applications

NutriStem® Family of Stem Cell Products

- Defined, serum-free, xeno-free, and feeder-free culture systems for hiPSC, hESC and hMSC
- Specially developed solutions for attachment, dissociation, cryopreservation and differentiation
- Hundreds of publications
- Complete protocols and application data
- FDA Drug Master File (DMF) available

Discover how our innovative, reliable, high performance products facilitate stem cell research and advancing cell-based therapies

Growth curve of hPSC

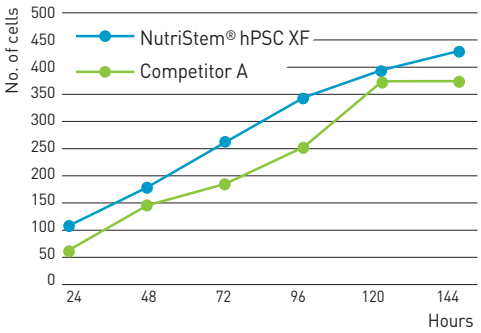

H1 cells (passage 6) were seeded in 96 well plates (Matrigel-coated) in the various media. Media were changed every 24 hours. The number of cells was determined using a CyQuant cell proliferation assay kit.

Growth Curve of hMSC

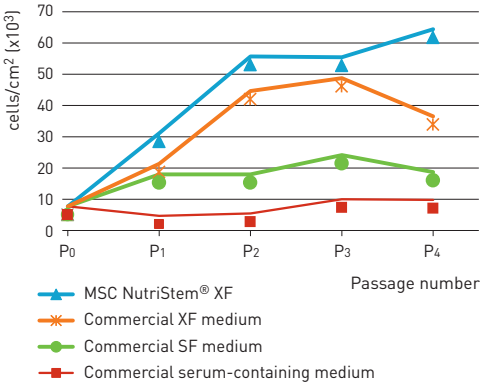

Expansion of hMSC-AT in MSC NutriStem® XF and commercial competitors XF, SF, and serum-containing media. Cells were cultured in plates, pre-coated with MSC Attachment Solution. Initial seeding was 5000 cells/cm² for each of the tested media (Day 0). Cells were counted at day 3 in each passage.

BI Biological Industries
Culture of Excellence

USA - Tel. 860-316-2702 | orders-usa@bioind.com
Global - Tel. 972-4-9960595 | info@bioind.com
www.bioind.com

CERTIFIED QMS ISO 9001 2008
CERTIFIED QMS ISO 13485 2003
CE
cGMP Manufacturing Facility

STEM CELL REPORTS

BEST OF 2015–2016

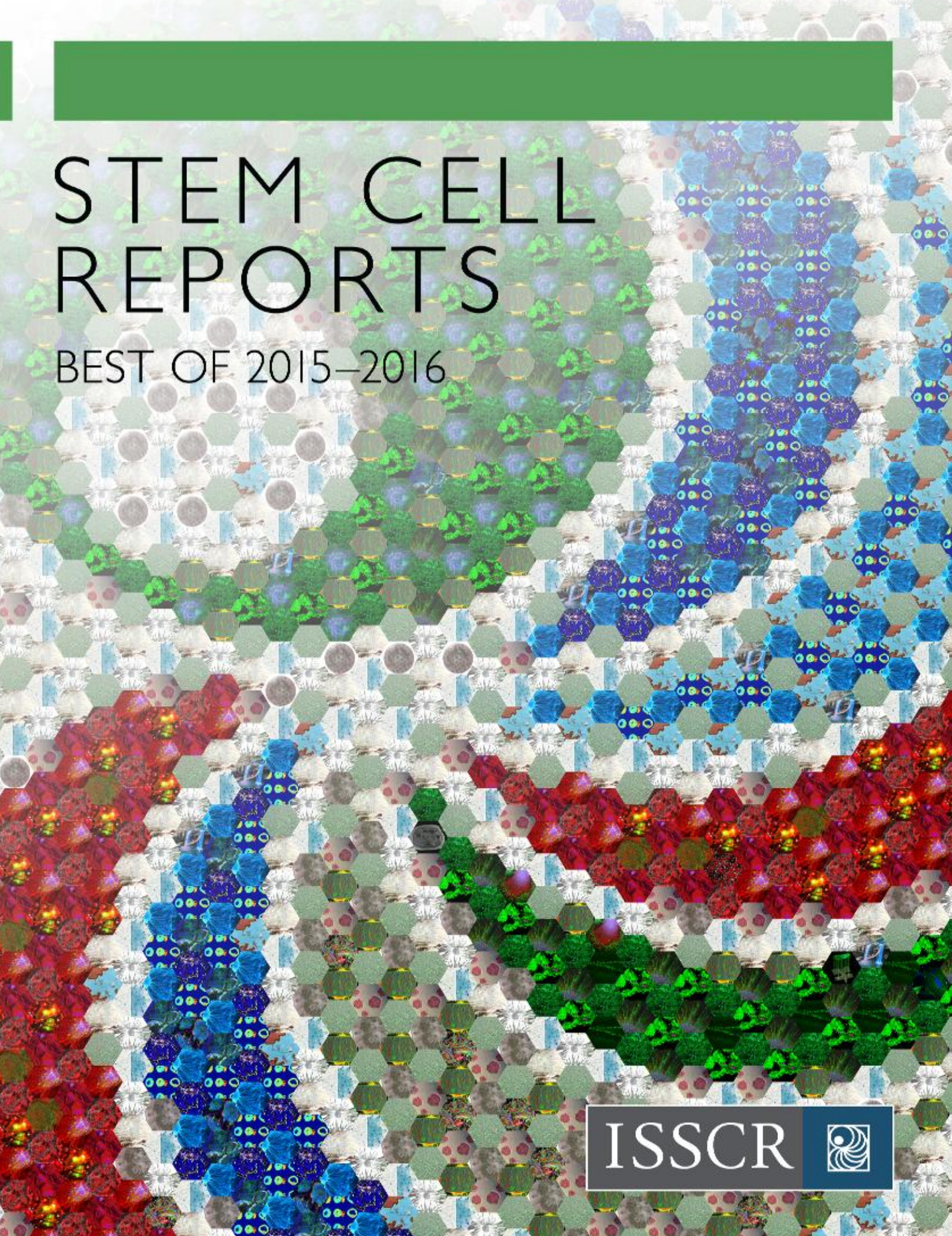

ISSCR

Seahorse Bioscience is now Agilent Technologies

A MAJOR LEAP FORWARD IN PHENOTYPING

Determine the functional impact of genes, proteins or compounds on metabolism in an hour

Agilent Seahorse XFp Cell Energy Phenotype Test Kit

Using as few as 15,000 live cells and an Agilent Seahorse XFp Analyzer, the Seahorse XFp Cell Energy Phenotype Test identifies your cells' metabolic phenotype as well as their metabolic potential — the utilization of mitochondrial respiration and glycolysis.

LEARN MORE at www.agilent.com

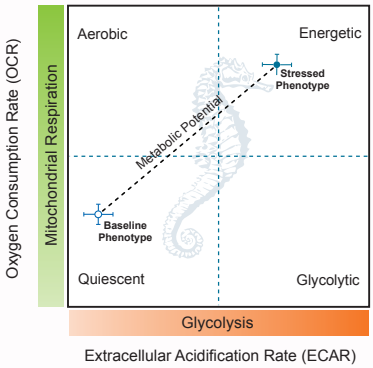

For Research Use Only. Not for use in diagnostic procedures.

Agilent Technologies

FOREWORD

Welcome to the *Best of Stem Cell Reports*, 2015–2016!

June 2016 is our third anniversary, and we are delighted to celebrate with this collection of editors' and readers' favorites from 2015 and early 2016. *Stem Cell Reports* is an open-access journal dedicated to stem cell research and its application to medicine, published for scientists by scientists: a forum for new data, dialogue about scientific issues, and a chance for researchers in the field to present their latest findings in short, single-message papers. The ISSCR leadership and the stem cell research community have been incredibly active in this endeavor, and we have welcomed growth over the past years that has surpassed our expectations. Our first impact factor in June 2015 was testimony that our articles continue to be downloaded, disseminated, and well-cited.

In the past year, we have established a strong foundation of authors, reviewers, and readers. Authors have continued to submit excellent manuscripts over the full breadth of our scope and from all parts of the world carrying out stem cell research. We receive many enthusiastic emails from our authors and share just a few of them with you here.

Personally, I feel that the review process was very positive, constructive, and a valuable experience. It was a privilege to have had such a sophisticated scientific discourse. We are truly grateful for your and the reviewers' kind work.

- Mike Karl, Dresden, Germany

It has been a rewarding experience to work with *Stem Cell Reports*. We have been impressed by the high efficiency and professionalism of *Stem Cell Reports*. We will share the positive experience with our colleagues and definitely consider submitting our manuscripts to *Stem Cell Reports* again in the future.

- Yibing Qyang, New Haven, USA

I would also like to thank you for your enthusiasm for this work and the painless process of publication in *Stem Cell Reports*.

- Jenny Nichols, Cambridge, UK

We have been happy with the review and publishing process at *Stem Cell Reports*. Your work is efficient, and [you] always reply in time. *Stem Cell Reports* is a good choice.

- Di Li, Guangzhou, China

It has been great to work with a journal that is very fast and good with deadlines.

- Marti Borkent, Boston, USA

We remain particularly grateful for the loyalty of our reviewers, many of whom review more than five papers each year. Our reviewers provide high-quality, constructive evaluations anonymously, altruistically, and with rapid turnaround, helping authors to improve their work and helping our editors to set standards in the field, crucial for the credibility of and support for stem cell research among a wider public. We also thank our many readers, who have helped to shape the collection of articles in this issue.

Our vision remains the publication of high-quality stem cell research. In our third year, our focus has been on attracting and publishing the best work we hear about and consolidating our position as a premier journal to publish stem cell research. We encourage you to talk to our editors and ISSCR board members at conferences. We continue to place emphasis on fair and expedient evaluation of all manuscripts and the inclusion of studies that debate or confirm existing literature. Our credo is that reproducibility strengthens the field and underlies its progress.

We also share the ISSCR publications committee's belief that keeping a journal exciting and lively means an organized turnover of those leading it. We as editors all have fixed terms in our roles, and a roll-on, roll-off system of replacement is in place to make sure we continue to have new

ideas and new people. David Scadden is the first to leave us, after more than three years working with us to start up the journal. He has been a superb associate editor, and while we are sad to see him leave, we are also pleased to introduce you to an excellent new associate editor: welcome to Amy Wagers! Many of you will know her for her ground-breaking work on aging and skeletal muscle, and we hope you will speak with her at the "Meet the Editors" session at the annual ISSCR meeting or elsewhere.

We will celebrate our fifth "century" this month, when the 500th article will be accepted for publication: a tremendous achievement and a testament to the support of the ISSCR board of directors and also of the society's membership and those beyond supporting this new format. Downloads of articles continue to grow, and mainstream media as well as scientific publications regularly highlight our articles; you may spot these in our "In the News" section on the website. Take a look to find out what is going on.

Just one poignant note, though: many of you will know that Paolo Bianco, one of our 2015 ISSCR Public Service Award laureates, a pioneer in mesenchymal stromal cell research and one of its most outspoken critics, died prematurely in November 2015. When he passed away, he had a paper in revision in *Stem Cell Reports*. His co-authors on that paper, led by Pam Robey and Mara Riminucci, managed to complete the requested revisions. You can read this important and critical contribution to the field in the June issue, of course dedicated to our good friend Paolo.

We also hope you have noticed our impressive covers! We encourage our authors to submit suggestions and have received the most beautiful imaging and illustrations you can imagine, as well as some fun and quirky variants; just take a look at the website, www.cell.com/stem-cell-reports.

Have you looked closely at the cover of this *Best of Stem Cell Reports* issue? Take a magnifying glass for a good peek. We are delighted to profile additional images from the many wonderful submissions that we have received since we started; perhaps you can spot yours built into the ISSCR logo! We encourage you to settle in and take this opportunity to catch up on—or re-read—a selection of the exciting research we have had the privilege to publish over the past year: the favorite papers of our editors and readers.

We hope you enjoy this *Best of Stem Cell Reports* compilation as much as we enjoyed putting it together. We thank you all for your tremendous support.

Cellular Dynamics international

a FUJIFILM company

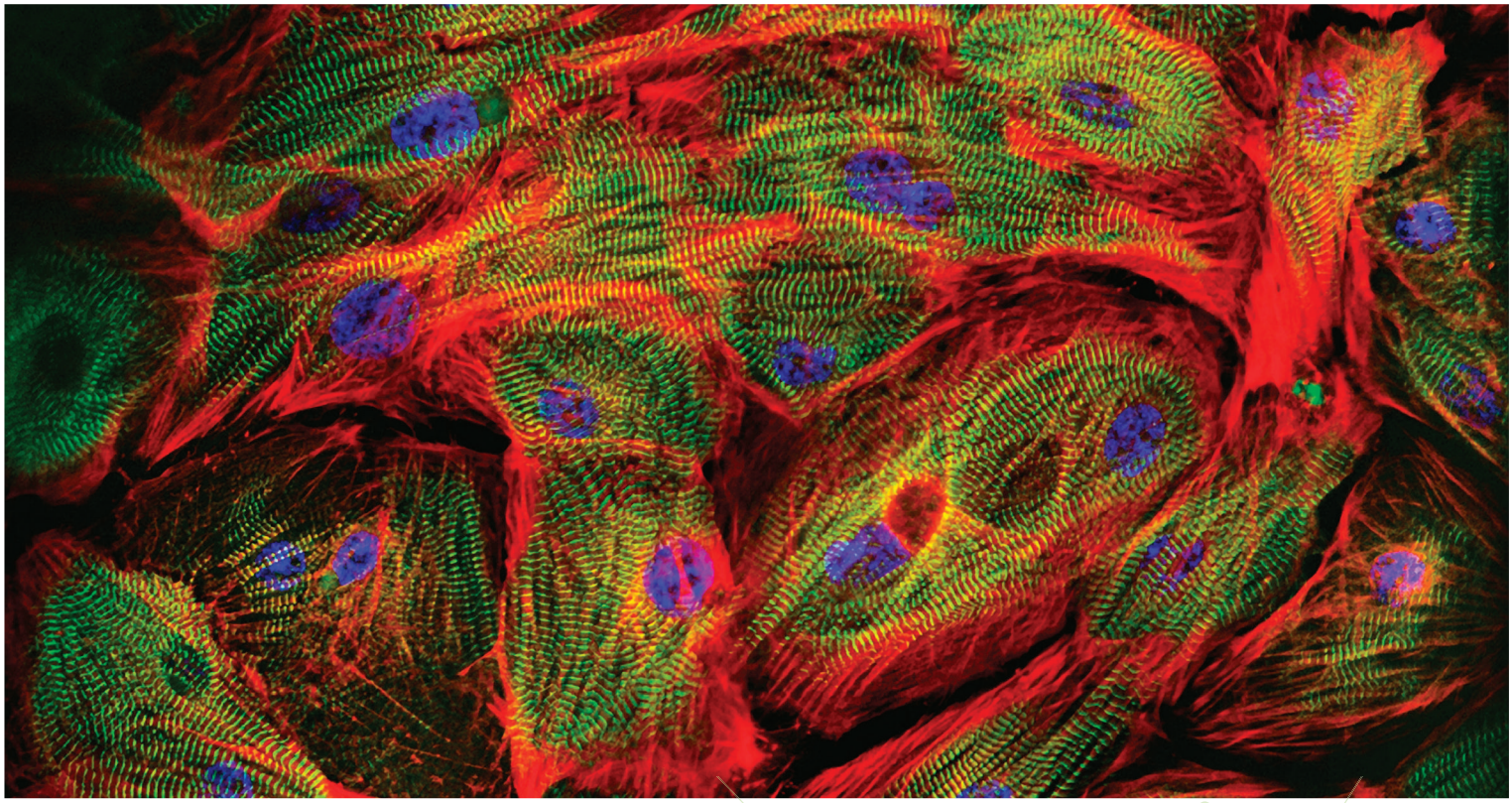

Human Cells

Endless Possibilities from Discovery to Regenerative Medicine.

Cellular Dynamics International (CDI), has designed an induced pluripotent stem cell (iPSC)-based technology platform that enables the large scale production of high-quality, fully functioning human cells. Stem cells are early stage, undifferentiated cells that are found in all multicellular organisms. They are unique because they can survive and replicate indefinitely. CDI's technology offers the potential to create iPSCs from anyone, starting with a standard blood draw, and followed by the powerful capability to develop into virtually any cell type in the human body.

Our iCell® and donor-specific MyCell® Products are highly pure, highly reproducible, and available in industrial quantity to enable drug discovery, toxicity testing, stem cell banking, and cell therapy development.

cellulardynamics.com

Culture of Excellence

ISSCR ANNUAL MEETING GOLD SUPPORTER

Visit BI booth
#1419

Redefining Stem Cell Excellence

and Advancing Clinical Applications

NutriStem® Family of Stem Cell Products

- Defined, serum-free, xeno-free, and feeder-free culture systems for hiPSC, hESC and hMSC
- Specially developed solutions for attachment, dissociation, cryopreservation and differentiation
- Hundreds of publications
- Complete protocols and application data
- FDA Drug Master File (DMF) available

Discover how our innovative, reliable, high performance products facilitate stem cell research and advancing cell-based therapies

Growth curve of hPSC

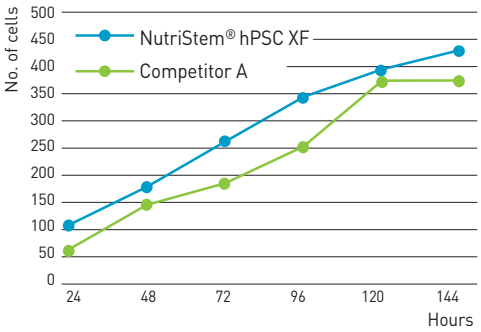

H1 cells (passage 6) were seeded in 96 well plates (Matrigel-coated) in the various media. Media were changed every 24 hours. The number of cells was determined using a CyQuant cell proliferation assay kit.

Growth Curve of hMSC

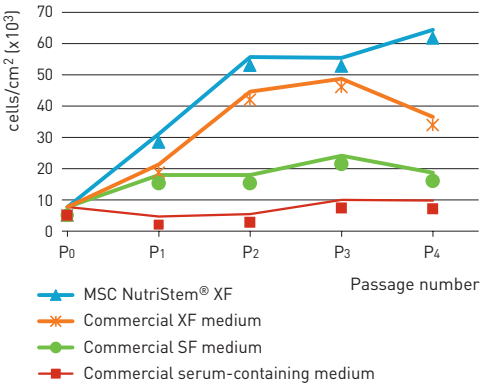

Expansion of hMSC-AT in MSC NutriStem® XF and commercial competitors XF, SF, and serum-containing media. Cells were cultured in plates, pre-coated with MSC Attachment Solution. Initial seeding was 5000 cells/cm² for each of the tested media (Day 0). Cells were counted at day 3 in each passage.

BI Biological Industries
Culture of Excellence

USA - Tel. 860-316-2702 | orders-usa@bioind.com
Global - Tel. 972-4-9960595 | info@bioind.com
www.bioind.com

CERTIFIED QMS ISO 9001 2008
CERTIFIED QMS ISO 13485 2003
CE
cGMP Manufacturing Facility

STEM CELL REPORTS

The Official Journal of the International Society for Stem Cell Research

Best of 2015–2016

REPORTS

MEETING REPORT

ARTICLES

(continued)

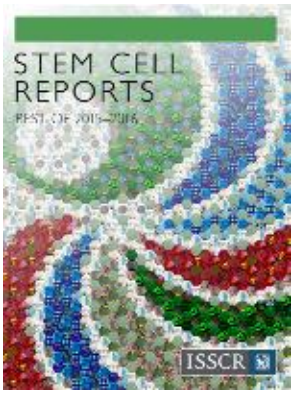

COVER

Designed by Kelly Hosman from a compilation of 2015–2016 cover submissions from: Susan Lindsay and Susan Barnett, Dominique Bonnet, Laura Kerosuo and Marianne Bronner, Jason Butler, Patrick Charnay, Andrew Cohen, Stephen Dalton, Ibrahim Domian, Camilla Forsberg, Yoko Nakai-Futatsugi, Wei-Qiang Gao, Shimpei Gotoh, Thomas Graf, Dave Hay, Marti Borkent, Rick Berry and Konrad Hochedlinger, Masaki Ieda, Mike Karl, Timothy Kieffer, Rohit Kulkarni, Michael Kyba, Wei Liu, Reema Korshed and Christina Lo Celso, Susana Chuva de Sousa Lopes, In Kyoung Mah and Francesca Mariani, Javier Menendez, Seji Okada, Hideyuki Okano, Jason Pomerantz, Thomas Rando, Mahendra Rao, Angel Raya, Laura Lasagni and Paola Romagnani, Laurent Roybon, Hugo Fernandes and Richard Wade-Martins, Wolfgang Wagner, Tara Walker, and Johannes Riegler and Joseph Wu.

ISSCR
INTERNATIONAL SOCIETY FOR STEM CELL RESEARCH

co-sponsored by:
HSCI Harvard Stem Cell Institute

THE GLOBAL STEM CELL EVENT

SAVE THE DATES

ISSCR 2017
ANNUAL MEETING
BOSTON | USA
14-17 JUNE
ISSCR2017.ORG

inspiring SCIENCE STEM CELL insightfully DELIVERED

Researchers around the world continue to advance the science of stem cells. The ISSCR Annual Meeting is where they come together, work together and find inspiration together. Plan now to experience inspiring stem cell science and technology delivered with the insight you need to meet your research goals.
Join us at ISSCR 2017 in Boston.

ISSCR

CONNECT WEBINARS

STEM CELL SCIENCE. ANYWHERE. ANYTIME.

Get connected to the latest research that inspires new perspectives on your work, the field, and the future of stem cell science.

Tune in to ISSCR Connect Webinars after the Annual Meeting to view select session rebroadcasts.

NEW TO CONNECT

CAREER DEVELOPMENT SERIES

Hear scientists talk about their careers, experiences and finding rewarding, career options in industry, business, government, publishing and advocacy.

Watch live presentations to interact directly with speakers, ask questions, and more!

GET IT ON Google Play

Download on the App Store

Download the Xpocast app to view ISSCR Connect Webinars from your mobile device.

LOG IN AT WWW.ISSCR.ORG/CONNECT

Stem Cell Reports
Report

ISSCR

OPEN ACCESS

Naive Pluripotent Stem Cells Derived Directly from Isolated Cells of the Human Inner Cell Mass

Ge Guo,[1] Ferdinand von Meyenn,[4] Fatima Santos,[4] Yaoyao Chen,[1] Wolf Reik,[4,5] Paul Bertone,[1] Austin Smith,[1,3,*] and Jennifer Nichols[1,2,*]

[1]Wellcome Trust – Medical Research Council Stem Cell Institute, University of Cambridge, Tennis Court Road, Cambridge CB2 1QR, UK
[2]Department of Physiology, Development and Neuroscience, University of Cambridge, Downing Street, Cambridge CB2 4BG, UK
[3]Department of Biochemistry, University of Cambridge, Tennis Court Road, Cambridge CB2 1GA, UK
[4]Epigenetics Programme, Babraham Institute, Cambridge CB22 3AT, UK
[5]Wellcome Trust Sanger Institute, Hinxton, Cambridge CB10 1SA, UK
*Correspondence: austin.smith@cscr.cam.ac.uk (A.S.), jn270@cam.ac.uk (J.N.)
http://dx.doi.org/10.1016/j.stemcr.2016.02.005

SUMMARY

Conventional generation of stem cells from human blastocysts produces a developmentally advanced, or primed, stage of pluripotency. In vitro resetting to a more naive phenotype has been reported. However, whether the reset culture conditions of selective kinase inhibition can enable capture of naive epiblast cells directly from the embryo has not been determined. Here, we show that in these specific conditions individual inner cell mass cells grow into colonies that may then be expanded over multiple passages while retaining a diploid karyotype and naive properties. The cells express hallmark naive pluripotency factors and additionally display features of mitochondrial respiration, global gene expression, and genome-wide hypomethylation distinct from primed cells. They transition through primed pluripotency into somatic lineage differentiation. Collectively these attributes suggest classification as human naive embryonic stem cells. Human counterparts of canonical mouse embryonic stem cells would argue for conservation in the phased progression of pluripotency in mammals.

INTRODUCTION

Human pluripotent stem cells (PSCs), whether derived from blastocysts or generated by somatic cell reprogramming, differ substantially from canonical mouse embryonic stem cells (ESCs) and are considered to represent a later phase of epiblast development, termed primed pluripotency (Hackett and Surani, 2014; Nichols and Smith, 2009; Rossant, 2015). Multiple claims of conversion of primed human PSCs into a more naive-like phenotype have been published (reviewed in (Davidson et al., 2015)). These reports are based on a shift in some attribute(s) in response to exogenous reprogramming factors and/or altered culture conditions. Evidence has been lacking, however, for a global state that correlates with mouse ESCs or human naive epiblast (Huang et al., 2014), or for presence of a functional gene regulatory network to sustain naive pluripotency (Boroviak et al., 2015; Dunn et al., 2014; Martello and Smith, 2014).

Two independent studies have described resetting of human PSCs to resemble mouse ESCs following short-term expression of *KLF2* and *NANOG* (Takashima et al., 2014; Theunissen et al., 2014). Reset cells are maintained in medium based on components used for mouse ESCs (Dutta et al., 2011; Ying et al., 2008) comprising titrated inhibition of glycogen synthase kinase-3 and blockade of the mitogen-activated protein kinase (MAPK/Erk) pathway (t2i) with leukemia inhibitory factor (LIF), plus protein kinase C (PKC) inhibition (Takashima et al., 2014). LIF and t2i have also been used to achieve resetting in combination with activin plus inhibitors of BRaf, Src family kinases, and Rho-associated kinase (ROCK) (Theunissen et al., 2014). Reset pluripotent cells are transcriptionally distinct from conventional PSCs and more similar to mouse ESCs and human ICM (Davidson et al., 2015; Huang et al., 2014). They have increased mitochondrial respiratory activity and exhibit global DNA hypomethylation (Takashima et al., 2014), properties consistent with pre-implantation identity. Perhaps most persuasively, reset cells have acquired expression of, and functional dependency on, transcription factors KLF4 and TFCP2L1 constituting part of the core gene regulatory network of naive pluripotency in mouse ESCs (Dunn et al., 2014; Martello et al., 2013; Niwa et al., 2009; Ye et al., 2013) and are expressed in the human ICM but negligible in the primed PSC (Takashima et al., 2014).

In rodents functional equivalence of ESCs with naive epiblast can be demonstrated by blastocyst colonization and extensive multilineage contribution to chimeras. Such an assay is not feasible in human. An alternative indicator of developmental identity is propagation directly from naive epiblast cells, as for derivation of mouse ESCs (Boroviak et al., 2014; Brook and Gardner, 1997; Nichols et al., 2009). In human the standard process for establishing PSC lines from embryos entails explant outgrowth to form an epithelial structure (Pickering et al., 2003), the

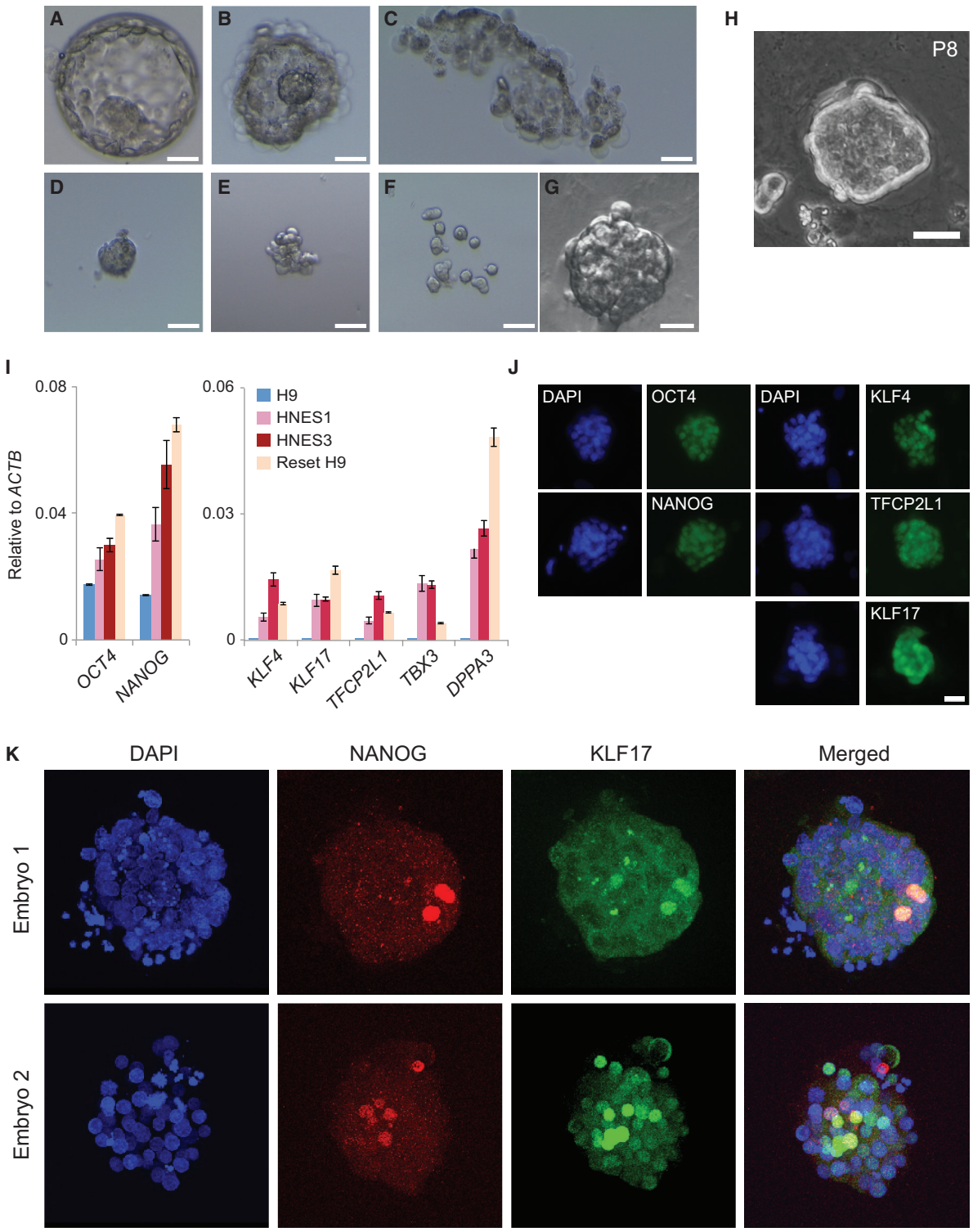

Figure 1. Cell Line Derivation from Dissociated Human Inner Cell Mass Cells

(A) Day-6 blastocyst.

(B) Trophoblast lysis.

(C) Discarded trophoblast.

(D) Isolated inner cell mass.

(legend continued on next page)

Table 1. Derivation of Naive Epiblast Stem Cell Lines

Experiment	Embryos Surviving Thaw	Blastocysts[a]	Dissociated ICMs	Cell Lines	Cumulative Passages
1	24	4	1	HNES1	P30
2	9	4	2	HNES2	P22
				HNES3	P29
3	20	4	4	HNES4[b]	P21
4	5	2	1	[c]	
Total	58	14	8	4	

[a]Embryos cavitated by day 6.
[b]Primary colonies lost in three cases associated with incubator humidity failure.
[c]Primary colonies emerged but failed to expand after five passages.

post-inner cell mass intermediate (PICMI) (O'Leary et al., 2012). This is thought to simulate development of the post-implantation embryonic disk (Van der Jeught et al., 2015), which may explain why derivative cell lines acquire characteristics of primed pluripotency. Naive pluripotency factors such as TFCP2L1 are downregulated during PICMI formation (O'Leary et al., 2012). We elected to test the ability of culture conditions that sustain human naive PSCs after resetting in vitro to support de novo derivation from dissociated human ICMs without PICMI transition.

RESULTS

Previous human embryo derivations of PSCs have been performed in the presence of fibroblast growth factor (FGF) and/or serum factors, conditions that support developmental progression. We avoided these and adopted the culture regime developed for human reset PSCs (Takashima et al., 2014), comprising serum-free N2B27 medium with LIF and t2i (inhibitors of GSK3 and MAPK/Erk signaling) plus the PKC inhibitor Gö6983. To safeguard viability of precious embryo cells, we added ascorbic acid and ROCK inhibitor (Y-27632), constituting t2iLGöY. Cultures were maintained throughout on fibroblast feeders in 5% O_2.

ICMs were isolated from blastocysts 6 days post-fertilization by immunosurgery (Solter and Knowles, 1975). Following dissociation, single cells or doublets were distributed on feeders in t2iLGöY. Up to half of the plated ICM cells formed compact colonies within 4–5 days (Figures 1A–1G), similar to mouse ESC primary colony formation (Nichols et al., 2009). For each embryo, colonies were manually picked, dissociated, and pooled. Replated cells proliferated (Figures 1H and S1A) and from a total of eight ICMs, four cell lines were established (Table 1) and provisionally termed human naive embryonic stem (HNES) cells.

HNES cells were expanded by passaging every 3–4 days, with ROCK inhibitor and ascorbic acid maintained throughout. HNES cells can be replated and maintained without ROCK inhibitor, albeit at lower efficiency, and propagated without ascorbic acid (Figures S1B–S1D). They can be cryopreserved and thawed with expected recovery efficiency using standard procedures. HNES1 cells exhibit a consistent 46XY karyotype with no abnormalities detected by G-banding (Figure S1E and Table S1), while HNES2 comprised both diploid and tetraploid cells on initial karyotyping but resolved to 46XY after flow sorting (Figures S1E and S1F). HNES3 is a mix of 46XX and cells with chr22 trisomy. HNES4 contains two isochromosomes of chromosome 12. Array comparative genomic hybridization at 200 kb genome-wide resolution confirmed lack of chromosomal abnormalities in HNES1. This line is described below with data from other lines where specified.

HNES cells expressed mRNAs for naive pluripotency markers *KLF4*, *TFCP2L1*, and *DPPA3*, along with elevated *NANOG* transcripts (Figure 1I) as seen in reset cells generated from conventional PSCs (Takashima et al., 2014). Immunostaining confirmed presence of NANOG, KLF4, TFCP2L1, and OCT4 (Figures 1J and S1G). Expression of *ESRRB* and *KLF2* was low in HNES cells, similar to reset cells. Both factors are also expressed at low levels in human and marmoset ICMs, indicating divergence between primates and rodents (Blakeley et al., 2015; Boroviak et al., 2015). Another Kruppel-like factor, KLF17, is observed at the transcript level in primate ICMs (Blakeley et al., 2015; Boroviak et al., 2015) and expressed in reset and HNES cells

(E) Decompacted ICM.
(F) Dissociated ICM.
(G) Primary stem cell clone grown from a single ICM cell.
(H) Colony at passage 8.
(I) qRT-PCR for pluripotency markers in HNES cells, conventional human PSCs (H9), and in vitro reset PSCs (Reset H9). Error bars indicate the SD of two independent reactions.
(J) Immunofluorescence of pluripotency markers in HNES1 cells.
(K) Immunofluorescence of KLF17 and NANOG in D6 human ICM cells.
Scale bars: 25 μm.

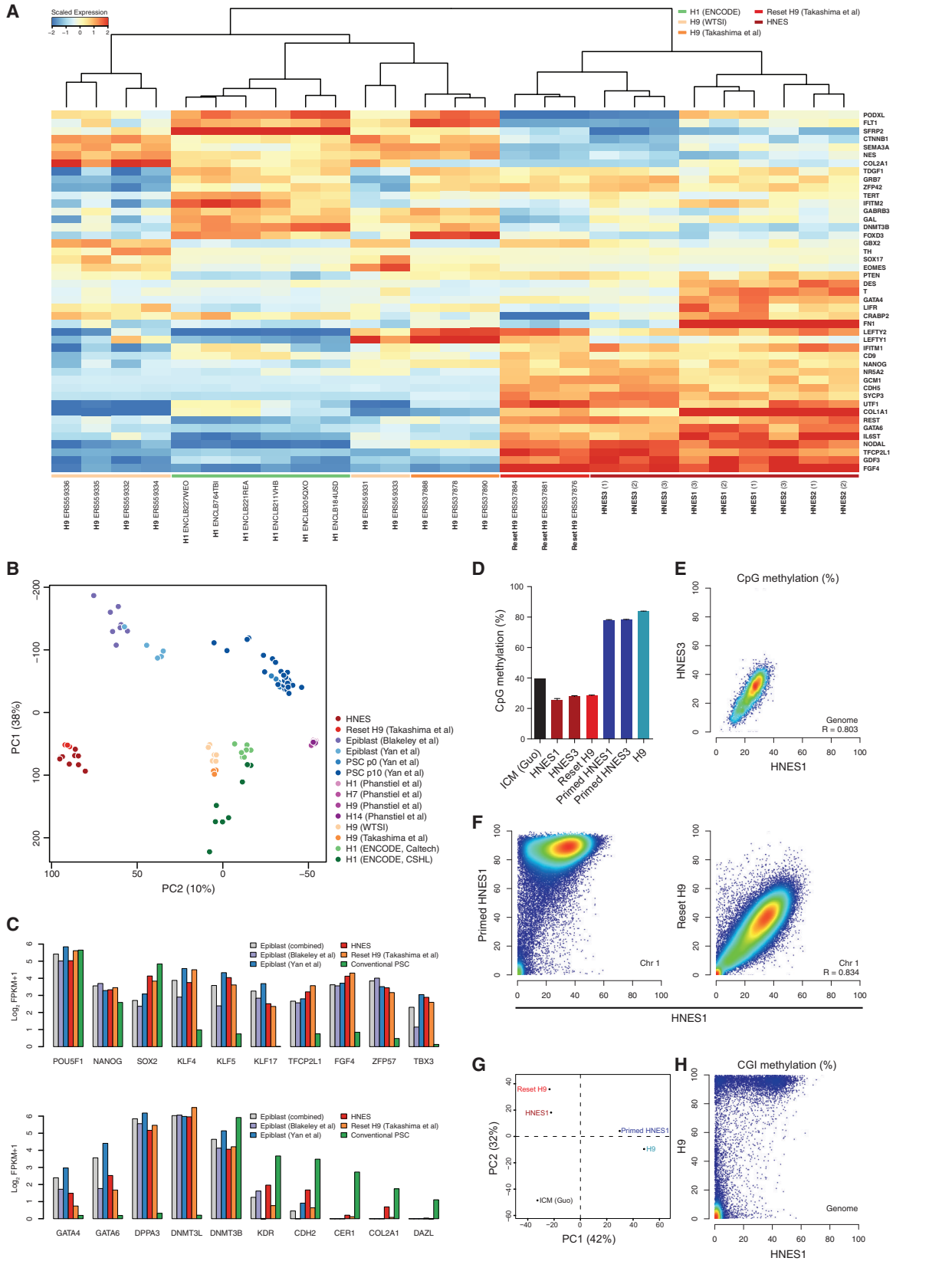

(legend on next page)

(Figure 1I). We detected KLF17 protein in HNES cells and human ICMs (Figures 1J and 1K).

Whole-transcriptome profiles were obtained by RNA-seq from replicate cultures of HNES1, HNES2, and HNES3. These were compared with reset and conventional human PSC datasets (Takashima et al., 2014) and to a wider panel of H1, H7, H9, and H14 data from the public domain. HNES cells feature a transcriptome distinct from other PSCs and close to the reset state (Figure 2A). They show consistent expression of naive pluripotency factors. Conventional PSCs exhibit wider variation in expression profiles with sporadic activation of naive factors such as *NANOG, ZFP42* (*REX1*), and *TFCP2L1*. HNES cells express a restricted complement of lineage markers compared with conventional PSCs. We performed principal component analysis (PCA), additionally incorporating published data (Blakeley et al., 2015; Yan et al., 2013) on human ICM cells and primary cultures generated by single-cell RNA-seq (Figure 2B). PC1 primarily discriminates between cells profiled by single-cell and bulk RNA-seq methods, suggesting a substantial contribution of global expression variance by sequencing protocol. Numerous transcripts present in conventional RNA-seq datasets register zero read counts in the single-cell libraries, in line with known detection limitations (Kharchenko et al., 2014). Biological replicates of the three HNES cells cluster together and adjacent to reset H9 cells. PC2 places HNES cells in relative proximity to the ICM cells and well separated from other PSCs. The degree of correspondence between HNES and embryo cells appears reasonable, considering the wider variation between samples profiled in the embryo studies, and that early ICM cells analyzed precede naive epiblast. Markers of naive pluripotency and lineage specification diverge between HNES and reset cells versus conventional PSC (Figure 2C).

Primed PSCs rely on anaerobic glycolysis with low mitochondrial respiration capacity (Zhou et al., 2012), whereas reset PSCs have active mitochondria and reduced glucose dependence (Takashima et al., 2014). We evaluated the capacity of HNES cells to form colonies in the presence of the competitive inhibitor of glycolysis, 2-deoxyglucose. Undifferentiated HNES cells readily formed colonies while primed HNES cells generated by passaging in FGF/KSR did not survive (Figure S2A). HNES cells also stained intensely with MitoProbe DiIC1, reflecting mitochondrial membrane potential (Figures S2B and S2C). Extracellular flux analysis indicated that HNES cells exhibit at least 2-fold higher respiratory capacity than primed cells (Figure S2D).

Global DNA hypomethylation is a distinguishing feature of mouse and human ICM cells (Guo et al., 2014; Smith et al., 2012), a property shared with naive ESCs (Ficz et al., 2013; Habibi et al., 2013; Leitch et al., 2013) and reset human PSCs (Takashima et al., 2014). Immunostaining for 5-methylcytosine (5mC) is fainter in HNES cell nuclei compared with primed HNES cells (Figure S3A). Like reset PSCs, HNES cells show appreciable expression of TET1 and downregulation of de novo methyltransferase DNMT3B (Figures S3B and S3C). We performed whole-genome bisulfite sequencing on two HNES lines and their primed derivatives. Analysis confirmed genome-wide hypomethylation in male and female HNES cells, similar to levels of 25%–40% observed in human ICM and in contrast to >70% CpG methylation in conventional PSCs and primed HNES cells (Figure 2D). Both HNES lines showed extensive overlap in the distribution of CpG methylation sites (Figure 2E), with substantial hypomethylation compared with primed HNES cells (Figure 2F). The methylomes of HNES and reset H9 cells are very similar, suggesting that the epigenetic state of conventional human PSCs can be accurately and consistently reprogrammed. We analyzed methylation levels of CpG islands (CGIs) and performed PCA, revealing clustering of HNES with reset H9 cells and conventional human PSCs (H9) with primed HNES cells (Figure 2G). PC1 captured most of the variation (42%), indicating high resemblance between HNES cells and human ICMs (Guo et al., 2014). Comparisons of CGI

Figure 2. Transcriptome and Methylome Analyses

(A) Clustered expression data from HNES cells, and reset and conventional human PSCs for a panel of pluripotency and lineage markers selected by the International Stem Cell Initiative (Adewumi et al., 2007). Displayed are $\log_2$ FPKM values (fragments per kilobase of exon per million reads mapped) scaled by the mean expression of each gene across samples. Published data are labeled with sample accession codes.

(B) PCA of HNES cells, and reset and conventional PSCs with single-cell RNA-seq data from early human ICMs (Blakeley et al., 2015; Yan et al., 2013) and PSC explants. Embryo single-cell samples are those assigned an epiblast identity in the respective studies.

(C) Pluripotency and lineage marker expression in human ICM, HNES cells, and reset and conventional PSC lines.

(D) Proportion of whole-genome CpG methylation measured by bisulfite sequencing (BS-seq) analysis from three biological replicates. Error bars indicate the SD of three biological replicates.

(E) Comparison of global methylation in HNES1 (male) and HNES3 (female) cells by averaging CpG methylation levels over 500-kb windows.

(F) Comparisons of CpG methylation in HNES1 cells and primed derivatives, and reset H9 and ICM cells.

(G) PCA of mean CpG island methylation.

(H) CGI methylation in HNES1 and conventional PSCs.

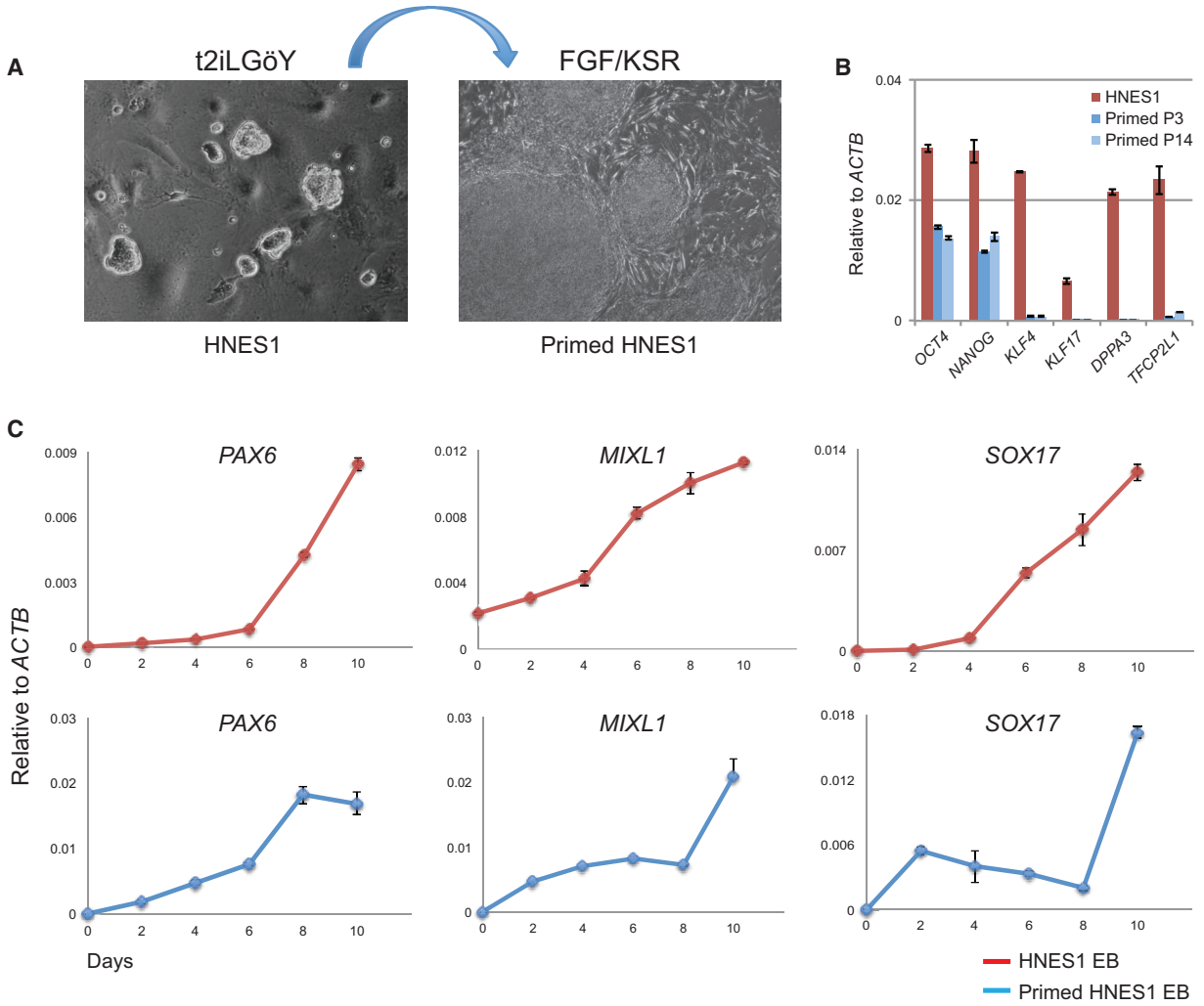

(legend on next page)

methylation in HNES and H9 cells (Figure 2H) showed that the majority of CGIs are hypomethylated in both HNES cells and conventional PSCs, while many CGIs gain methylation in primed cells. Only a subset of CGIs is methylated in both conditions. These data highlight similarity between HNES and human ICM methylomes and show that conventional human PSCs have gained methylation at a number of CGIs when compared with HNES cells.

We transferred HNES cells to conventional PSC culture medium containing FGF/KSR and lacking inhibitors. After one passage the domed colonies of HNES cells assumed flattened epithelial morphology, and after two passages resembled conventional PSC (Figure 3A). During this transition *OCT4* and *NANOG* were reduced, and naive markers, including *KLF17*, were extinguished (Figures 3B, S4A, and S4B).

We assessed whether HNES cells can undergo multilineage differentiation by generating embryoid bodies directly from naive and primed HNES cells. In both cases early lineage markers *PAX6*, *MIXL1*, and *SOX17* were upregulated (Figure 3C). Outgrowths from plated embryoid bodies displayed TuJ1-positive neuronal, FOXA2/AFP double-positive endoderm, and smooth muscle actin-positive cells (Figure 3D). We also applied a protocol for cardiomyocyte differentiation (van den Berg et al., 2016) to primed HNES cells and observed multiple regions of spontaneous contraction after 12 days (Movie S1). Cardiomyocyte identity was confirmed by expression of surface markers VCAM-1 and CD172a (SIRPα) (Figure S4C).

DISCUSSION

Hitherto, stem cell derivations from human embryos have yielded cells with features distinct from rodent ESCs and more similar to mouse post-implantation epiblast-derived stem cells (Brons et al., 2007; Tesar et al., 2007). This may be because the culture conditions used were inadequate to sustain naive pluripotency in the face of stimuli for developmental progression emanating from extraembryonic endoderm (Brook and Gardner, 1997) in ICM explants and/or provided by FGF and serum factors. Even for derivations commencing from single blastomeres, a blastocyst-like structure develops, followed by ICM outgrowth prior to cell line derivation (Taei et al., 2013). We show that after dissociation of the ICM to separate epiblast and primitive endoderm, stem cell colonies emerge directly in the presence of inhibitors of MAPK/Erk, GSK3, and PKC. Resulting HNES cell lines can be propagated by enzymatic dissociation to single cells, retain chromosomal integrity over many passages, exhibit features diagnostic of naive pluripotency, and are capable of multilineage differentiation.

Conventional human PSC cultures are heterogeneous, potentially comprising complex hierarchies (Davidson et al., 2015; Enver et al., 2009; Hough et al., 2014). Furthermore, pluripotency is an inherently plastic stage of development. It is unsurprising, therefore, that PSCs can adjust to alternative culture conditions with shifts in morphology and gene expression. Without objective criteria, these may be misinterpreted as a change in developmental status rather than accommodation to culture. In contrast, global transcriptome, metabolic properties, and DNA hypomethylation features align HNES cells with reset PSCs and distinguish them from conventional human PSCs. Of particular significance, HNES cells and reset PSCs express the naive pluripotency factors *KLF4*, *TFCP2L1*, *TBX3*, and *NANOG* found in the primate ICMs and functional in mouse ESC self-renewal. Additionally they express *KLF17*, which might compensate for lower expression of *KLF2*. Apart from NANOG, these factors are expressed at low levels or not at all in conventional human PSCs, including those variants purported to be naive by other criteria. We have shown that the reset PSC state is dependent on both KLF4 and TFCP2L1 (Takashima et al., 2014).

The naive gene regulatory network is not fully conserved between mouse and human. Absence of ESRRB marks a substantial distinction. Mouse ESCs can be maintained after deletion of *Esrrb* but are less stable (Martello et al., 2012). Lack of ESRRB may therefore render human naive PSC propagation inherently more demanding. Nonetheless, culture refinements and replacement of feeders with a defined substrate may be anticipated to facilitate their handling and possibly attainment of a ground state.

In summary, these findings suggest that it is possible to suspend human developmental progression at the pre-implantation epiblast phase and propagate a self-renewing pluripotent state analogous to mouse ESCs (Boroviak et al., 2014; Brook and Gardner, 1997). Derivation of equivalent cell lines from non-human primates and formation of high-contribution chimeras would provide further

Figure 3. Differentiation

(A) Colonies of naive HNES1 cells in t2iLGöY and primed HNES1 cells after 12 passages in FGF/KSR.

(B) qRT-PCR analysis of naive marker expression in naive HNES1 cells and derivatives after three passages in FGF/KSR. Error bars indicate the SD of two independent reactions.

(C) qRT-PCR analysis of embryoid bodies formed from HNES1 and primed HNES1 cells. Error bars indicate the SD two independent reactions.

(D) Immunofluorescence of embryoid body outgrowths: TuJ1, β-III tubulin; AFP, α-fetoprotein; SMA, α-smooth muscle actin (green); FOXA2 (red). Nuclei (DAPI; blue). Scale bars, 100 μm.

validation. However, our results support the case for naive pluripotency in human development and may reconcile the long-running debate about the difference between PSCs from mice and men.

EXPERIMENTAL PROCEDURES

Embryo Manipulation

Supernumerary frozen human embryos were donated with informed consent under license from the UK HFEA. Embryos were thawed using EmbryoThaw medium (FertiPro) and cultured in drops of pre-equilibrated medium (Origio): EmbryoAssist for 1–8 cell stage (days 0–2), and BlastAssist for 8 cell stage to blastocyst (days 3–6) under embryo-tested mineral oil (Sigma). Expanded blastocysts (day 6) were subjected to immunosurgery (Pickering et al., 2005) to isolate ICMs using anti-human serum (Sigma). ICMs were treated with Accutase (Sigma or Gibco) for 5–10 min, and placed in a drop of medium for mechanical separation using a finely drawn Pasteur pipette. ICM cells were scattered onto mitotically inactivated (irradiated) murine embryonic fibroblasts (MEFs). Immunostaining was performed as described by Takashima et al. (2014).

Naive Stem Cell Culture

Cells were propagated in modified N2B27 medium supplemented with PD0325901 (1 μM, prepared in-house), CHIR99021 (1 μM, prepared in-house), Gö6983 (2.5 μM, Sigma-Aldrich), rho-associated kinase inhibitor (Y-27632) (10 μM, Calbiochem), human LIF (10 ng/ml, prepared in-house), and ascorbic acid (250 μM, Sigma). N2B27 medium (1 l) comprised 490 ml of DMEM/F12 (Life Technologies), 490 ml of Neurobasal (Life Technologies), 10 ml of B27 (Life Technologies), 5 ml of N2 (prepared in-house), 10 μg/ml insulin (Sigma), 2 mM L-glutamine (Life Technologies), and 0.1 mM 2-mercaptoethanol (Sigma). N2 contains 100 μg/ml apo-transferrin (eBioscience, ABC2553), 3 μM sodium selenite (Sigma), 1.6 mg/ml putrescine (Sigma), and 2 μg/ml progesterone (Sigma) in DMEM/F12 (Life Technologies). Primary colonies and nascent cell lines were passaged manually as described above for ICMs. Established cells were passaged either manually with Accutase (Life Technologies) dissociation reagent or as a pool using TrypLE Express (Life Technologies). Cells were cultured in 5% O_2 and 7% CO_2 in a humidified incubator at 37°C. Cells were frozen in 50% t2iLGöY medium with 40% serum and 10% DMSO.

Conversion to Primed Pluripotency

HNES cells were seeded on MEFs in t2iLGöY for 24 hr, then transferred into FGF/KSR medium for 7–10 days before passaging with TrypLE Express. Y-27632 was added for the first passage. Thereafter cells were passaged as clusters using collagenase/dispase (Roche). FGF/KSR medium comprised 20% KnockOut Serum Replacement (Invitrogen), 1× non-essential amino acids (Invitrogen), 2 mM L-glutamine (Invitrogen), 100 μM 2-mercaptoethanol (Sigma), 10 ng/ml FGF2 (prepared in-house), and DMEM/F-12 basal medium (Sigma-Aldrich). Established primed HNES cultures can also be maintained in mTeSR1 or E8 media (StemCell Technologies) on Matrigel.

In Vitro Differentiation

HNES cells or primed derivatives were dissociated with TrypLE Express and placed in PrimeSurface 96V cell plates (Sumitomo Bakelite MS-9096V) at a density of 4,000–5,000 cells per well in medium containing 20% KSR. Y-27632 was added during the first 24 hr of aggregation. At day 7 aggregates were plated on gelatin in 20% FBS.

Cardiomyocyte differentiation was performed as described by van den Berg et al. (2016).

ACCESSION NUMBERS

Data from this study are available in ArrayExpress: E-MTAB-4461 (RNA-seq), E-MTAB-4462 (BS-seq) and E-MTAB-4463 (Affymetrix).

SUPPLEMENTAL INFORMATION

Supplemental Information includes Supplemental Experimental Procedures, four figures, seven tables, and one movie and can be found with this article online at http://dx.doi.org/10.1016/j.stemcr.2016.02.005.

AUTHOR CONTRIBUTIONS

J.N., A.S., and G.G. planned the study; G.G., F.v.M., F.S., Y.C., P.B., and J.N. carried out experiments and analyses; P.B. performed RNA sequencing and bioinformatics; W.R. supervised methylome studies; J.N., A.S., P.B., and G.G. prepared the manuscript in consultation with all authors.

ACKNOWLEDGMENTS

We are grateful to Sally Marchant, Karen Thompson, and the staff and patients at the Centres for Reproductive Medicine at Barts and Leeds hospitals. We thank Ken Jones, James Clarke, Rosalind Drummond, Agata Kurowski, and Sally Lees for valuable technical assistance, Christine Mummery for the cardiomyocyte protocol, and Thorsten Boroviak for helpful comments. This work was supported by the Medical Research Council, Biotechnology and Biological Sciences Research Council, Swiss National Science Foundation (SNF)/Novartis SNF (F.v.M.), and core funding to the Cambridge Stem Cell Institute from the Wellcome Trust and Medical Research Council. A.S. is a Medical Research Council Professor. A.S. and G.G. are inventors on a patent application relating to naive human PSCs filed by the University of Cambridge.

Received: August 13, 2015
Revised: February 7, 2016
Accepted: February 8, 2016
Published: March 3, 2016

REFERENCES

Adewumi, O., Aflatoonian, B., Ahrlund-Richter, L., Amit, M., Andrews, P.W., Beighton, G., Bello, P.A., Benvenisty, N., Berry, L.S., Bevan, S., et al. (2007). Characterization of human embryonic stem cell lines by the International Stem Cell Initiative. Nat. Biotechnol. *25*, 803–816.

Blakeley, P., Fogarty, N.M., Del Valle, I., Wamaitha, S.E., Hu, T.X., Elder, K., Snell, P., Christie, L., Robson, P., and Niakan, K.K.

(2015). Defining the three cell lineages of the human blastocyst by single-cell RNA-seq. Development *142*, 3151–3165.

Boroviak, T., Loos, R., Bertone, P., Smith, A., and Nichols, J. (2014). The ability of inner-cell-mass cells to self-renew as embryonic stem cells is acquired following epiblast specification. Nat. Cell Biol. *16*, 516–528.

Boroviak, T., Loos, R., Lombard, P., Okahara, J., Behr, R., Sasaki, E., Nichols, J., Smith, A., and Bertone, P. (2015). Lineage-specific profiling delineates the emergence and progression of naive pluripotency in mammalian embryogenesis. Dev. Cell *35*, 366–382.

Brons, I.G., Smithers, L.E., Trotter, M.W., Rugg-Gunn, P., Sun, B., Chuva de Sousa Lopes, S.M., Howlett, S.K., Clarkson, A., Ahrlund-Richter, L., Pedersen, R.A., et al. (2007). Derivation of pluripotent epiblast stem cells from mammalian embryos. Nature *448*, 191–195.

Brook, F.A., and Gardner, R.L. (1997). The origin and efficient derivation of embryonic stem cells in the mouse. Proc. Natl. Acad. Sci. USA *94*, 5709–5712.

Davidson, K.C., Mason, E.A., and Pera, M.F. (2015). The pluripotent state in mouse and human. Development *142*, 3090–3099.

Dunn, S.J., Martello, G., Yordanov, B., Emmott, S., and Smith, A.G. (2014). Defining an essential transcription factor program for naive pluripotency. Science *344*, 1156–1160.

Dutta, D., Ray, S., Home, P., Larson, M., Wolfe, M.W., and Paul, S. (2011). Self-renewal versus lineage commitment of embryonic stem cells: protein kinase C signaling shifts the balance. Stem Cells *29*, 618–628.

Enver, T., Pera, M., Peterson, C., and Andrews, P.W. (2009). Stem cell states, fates, and the rules of attraction. Cell Stem Cell *4*, 387–397.

Ficz, G., Hore, T.A., Santos, F., Lee, H.J., Dean, W., Arand, J., Krueger, F., Oxley, D., Paul, Y.L., Walter, J., et al. (2013). FGF signaling inhibition in ESCs drives rapid genome-wide demethylation to the epigenetic ground state of pluripotency. Cell Stem Cell *13*, 351–359.

Guo, H., Zhu, P., Yan, L., Li, R., Hu, B., Lian, Y., Yan, J., Ren, X., Lin, S., Li, J., et al. (2014). The DNA methylation landscape of human early embryos. Nature *511*, 606–610.

Habibi, E., Brinkman, A.B., Arand, J., Kroeze, L.I., Kerstens, H.H., Matarese, F., Lepikhov, K., Gut, M., Brun-Heath, I., Hubner, N.C., et al. (2013). Whole-genome bisulfite sequencing of two distinct interconvertible DNA methylomes of mouse embryonic stem cells. Cell Stem Cell *13*, 360–369.

Hackett, J.A., and Surani, M.A. (2014). Regulatory principles of pluripotency: from the ground state up. Cell Stem Cell *15*, 416–430.

Hough, S.R., Thornton, M., Mason, E., Mar, J.C., Wells, C.A., and Pera, M.F. (2014). Single-cell gene expression profiles define self-renewing, pluripotent, and lineage primed states of human pluripotent stem cells. Stem Cell Rep. *2*, 881–895.

Huang, K., Maruyama, T., and Fan, G. (2014). The naive state of human pluripotent stem cells: a synthesis of stem cell and preimplantation embryo transcriptome analyses. Cell Stem Cell *15*, 410–415.

Kharchenko, P.V., Silberstein, L., and Scadden, D.T. (2014). Bayesian approach to single-cell differential expression analysis. Nat. Methods *11*, 740–742.

Leitch, H.G., McEwen, K.R., Turp, A., Encheva, V., Carroll, T., Grabole, N., Mansfield, W., Nashun, B., Knezovich, J.G., Smith, A., et al. (2013). Naive pluripotency is associated with global DNA hypomethylation. Nat. Struct. Mol. Biol. *20*, 311–316.

Martello, G., and Smith, A. (2014). The nature of embryonic stem cells. Annu. Rev. Cell Dev. Biol. *30*, 647–675.

Martello, G., Sugimoto, T., Diamanti, E., Joshi, A., Hannah, R., Ohtsuka, S., Gottgens, B., Niwa, H., and Smith, A. (2012). Esrrb is a pivotal target of the Gsk3/Tcf3 axis regulating embryonic stem cell self-renewal. Cell Stem Cell *11*, 491–504.

Martello, G., Bertone, P., and Smith, A. (2013). Identification of the missing pluripotency mediator downstream of leukaemia inhibitory factor. EMBO J. *32*, 2561–2574.

Nichols, J., and Smith, A. (2009). Naive and primed pluripotent states. Cell Stem Cell *4*, 487–492.

Nichols, J., Silva, J., Roode, M., and Smith, A. (2009). Suppression of Erk signalling promotes ground state pluripotency in the mouse embryo. Development *136*, 3215–3222.

Niwa, H., Ogawa, K., Shimosato, D., and Adachi, K. (2009). A parallel circuit of LIF signalling pathways maintains pluripotency of mouse ES cells. Nature *460*, 118–122.

O'Leary, T., Heindryckx, B., Lierman, S., van Bruggen, D., Goeman, J.J., Vandewoestyne, M., Deforce, D., de Sousa Lopes, S.M., and De Sutter, P. (2012). Tracking the progression of the human inner cell mass during embryonic stem cell derivation. Nat. Biotechnol. *30*, 278–282.

Pickering, S.J., Braude, P.R., Patel, M., Burns, C.J., Trussler, J., Bolton, V., and Minger, S. (2003). Preimplantation genetic diagnosis as a novel source of embryos for stem cell research. Reprod. Biomed. Online *7*, 353–364.

Pickering, S.J., Minger, S.L., Patel, M., Taylor, H., Black, C., Burns, C.J., Ekonomou, A., and Braude, P.R. (2005). Generation of a human embryonic stem cell line encoding the cystic fibrosis mutation deltaF508, using preimplantation genetic diagnosis. Reprod. Biomed. Online *10*, 390–397.

Rossant, J. (2015). Mouse and human blastocyst-derived stem cells: vive les differences. Development *142*, 9–12.

Smith, Z.D., Chan, M.M., Mikkelsen, T.S., Gu, H., Gnirke, A., Regev, A., and Meissner, A. (2012). A unique regulatory phase of DNA methylation in the early mammalian embryo. Nature *484*, 339–344.

Solter, D., and Knowles, B.B. (1975). Immunosurgery of mouse blastocyst. Proc. Natl. Acad. Sci. USA *72*, 5099–5102.

Taei, A., Hassani, S.-N., Eftekhari-Yazdi, P., Rezazadeh Valojerdi, M., Nokhbatolfoghahai, M., Masoudi, N.-S., Pakzad, M., Gourabi, H., and Baharvand, H. (2013). Enhanced generation of human embryonic stem cells from single blastomeres of fair and poor-quality cleavage embryos via inhibition of glycogen synthase kinase β and Rho-associated kinase signaling. Hum. Reprod. *28*, 2661–2671.

Takashima, Y., Guo, G., Loos, R., Nichols, J., Ficz, G., Krueger, F., Oxley, D., Santos, F., Clarke, J., Mansfield, W., et al. (2014).

Resetting transcription factor control circuitry toward ground-state pluripotency in human. Cell *158*, 1254–1269.

Tesar, P.J., Chenoweth, J.G., Brook, F.A., Davies, T.J., Evans, E.P., Mack, D.L., Gardner, R.L., and McKay, R.D. (2007). New cell lines from mouse epiblast share defining features with human embryonic stem cells. Nature *448*, 196–199.

Theunissen, T.W., Powell, B.E., Wang, H., Mitalipova, M., Faddah, D.A., Reddy, J., Fan, Z.P., Maetzel, D., Ganz, K., Shi, L., et al. (2014). Systematic identification of culture conditions for induction and maintenance of naive human pluripotency. Cell Stem Cell *15*, 471–487.

van den Berg, C.W., Elliott, D.A., Braam, S.R., Mummery, C.L., and Davis, R.P. (2016). Differentiation of human pluripotent stem cells to cardiomyocytes under defined conditions. Methods Mol. Biol. *1353*, 163–180.

Van der Jeught, M., O'Leary, T., Duggal, G., De Sutter, P., Chuva de Sousa Lopes, S., and Heindryckx, B. (2015). The post-inner cell mass intermediate: implications for stem cell biology and assisted reproductive technology. Hum. Reprod. Update *21*, 616–626.

Yan, L., Yang, M., Guo, H., Yang, L., Wu, J., Li, R., Liu, P., Lian, Y., Zheng, X., Yan, J., et al. (2013). Single-cell RNA-Seq profiling of human preimplantation embryos and embryonic stem cells. Nat. Struct. Mol. Biol. *20*, 1131–1139.

Ye, S., Li, P., Tong, C., and Ying, Q.L. (2013). Embryonic stem cell self-renewal pathways converge on the transcription factor Tfcp2l1. EMBO J. *32*, 2548–2560.

Ying, Q.L., Wray, J., Nichols, J., Batlle-Morera, L., Doble, B., Woodgett, J., Cohen, P., and Smith, A. (2008). The ground state of embryonic stem cell self-renewal. Nature *453*, 519–523.

Zhou, W., Choi, M., Margineantu, D., Margaretha, L., Hesson, J., Cavanaugh, C., Blau, C.A., Horwitz, M.S., Hockenbery, D., Ware, C., et al. (2012). HIF1alpha induced switch from bivalent to exclusively glycolytic metabolism during ESC-to-EpiSC/hESC transition. EMBO J. *31*, 2103–2116.

Stem Cell Reports
Report

ISSCR

OPEN ACCESS

OSKM Induce Extraembryonic Endoderm Stem Cells in Parallel to Induced Pluripotent Stem Cells

Anthony Parenti,[1,2] Michael A. Halbisen,[2] Kai Wang,[3] Keith Latham,[3] and Amy Ralston[1,2,*]
[1]Program in Cell and Molecular Biology, Michigan State University, East Lansing, MI 48824, USA
[2]Department of Biochemistry and Molecular Biology, Michigan State University, East Lansing, MI 48824, USA
[3]Department of Animal Sciences, Michigan State University, East Lansing, MI 48824, USA
*Correspondence: aralston@msu.edu
http://dx.doi.org/10.1016/j.stemcr.2016.02.003

SUMMARY

The reprogramming factors OCT4, SOX2, KLF4, and MYC (OSKM) can reactivate the pluripotency network in terminally differentiated cells, but also regulate expression of non-pluripotency genes in other contexts, such as the mouse primitive endoderm. The primitive endoderm is an extraembryonic lineage established in parallel to the pluripotent epiblast in the blastocyst, and is the progenitor pool for extraembryonic endoderm stem (XEN) cells. We show that OSKM induce expression of endodermal genes, leading to formation of induced XEN (iXEN) cells, which possess key properties of blastocyst-derived XEN cells, including morphology, transcription profile, self-renewal, and multipotency. Our data show that iXEN cells arise in parallel to induced pluripotent stem cells, indicating that OSKM drive cells to two distinct cell fates during reprogramming.

INTRODUCTION

The pluripotency-promoting role of the reprogramming factors OCT4, SOX2, KLF4, and MYC (OSKM) is widely appreciated. However, these reprogramming factors also promote expression of non-pluripotency genes. For example, OCT4 (*Pou5f1*) directly promotes expression of genes important for mouse primitive endoderm (Aksoy et al., 2013; Frum et al., 2013; Le Bin et al., 2014), an extraembryonic lineage present in the blastocyst, SOX2 indirectly promotes expression of primitive endoderm genes in the mouse blastocyst (Wicklow et al., 2014), KLF4 may regulate expression of primitive endoderm genes in the mouse blastocyst (Morgani and Brickman, 2015), and MYC regulates endodermal genes in fibroblasts and embryonic stem cells (ESCs) (Neri et al., 2012; Smith et al., 2010). These observations raise the possibility that OSKM induce expression of endodermal genes in somatic cells. In support of this idea, several groups have reported that endodermal genes, such as *Gata6*, *Gata4*, and *Sox17*, are upregulated in protocols used to reprogram fibroblasts to induced pluripotent stem cells (iPSCs) (Hou et al., 2013; Serrano et al., 2013; Zhao et al., 2015).

However, there is no consensus as to whether endodermal gene expression promotes or antagonizes the acquisition of pluripotency. GATA4 and GATA6 can reportedly substitute for OCT4 to produce iPSCs (Shu et al., 2013, 2015), arguing that endodermal genes promote acquisition of pluripotency. Consistent with this, endodermal genes are reportedly expressed by cells as they become pluripotent during chemical reprogramming (Hou et al., 2013; Zhao et al., 2015). By contrast, other evidence suggests that endodermal genes oppose pluripotency during reprogramming. For example, *Gata4* interferes with the acquisition of pluripotency during *OSKM* reprogramming (Serrano et al., 2013), *Gata6* is expressed in some partially reprogrammed cells (Mikkelsen et al., 2008), which are thought to be trapped in a state between differentiated and pluripotent (Meissner et al., 2007), and *Gata6* knockdown led to increased expression of *Nanog* in these cells (Mikkelsen et al., 2008). Thus, endodermal genes have been described as indicators of incomplete reprogramming. Here, we show that OSKM drive cells along two distinct and parallel pathways, one pluripotent and one endodermal.

RESULTS AND DISCUSSION

iXEN Cells Display XEN Cell Morphology and Gene Expression

We infected mouse embryonic fibroblasts (MEFs) or adult tail tip fibroblasts (TTFs) with retroviruses carrying *OSKM* (Takahashi and Yamanaka, 2006). Eighteen days after infection, we observed domed colonies with smooth boundaries (Figure 1A), which could be propagated as stable iPSC lines (16 out of 28 colonies) and could contribute to normal development in chimeras (Figure S1A). In addition, we observed colonies that were large and flat, with ragged boundaries (Figure 1A), and roughly three times more abundant and three times larger than presumptive iPSC colonies (Figure 1B). These colonies were visible as early as 6 days after *OSKM* infection (Figure S1B). Here, we demonstrate extensive similarity between blastocyst-derived extraembryonic endoderm stem cell (XEN) cell lines and the MEF-derived cell lines that we hereafter refer to as induced XEN (iXEN) cells.

We manually isolated putative iXEN cell colonies and cultured these in ESC medium without leukemia inhibitory

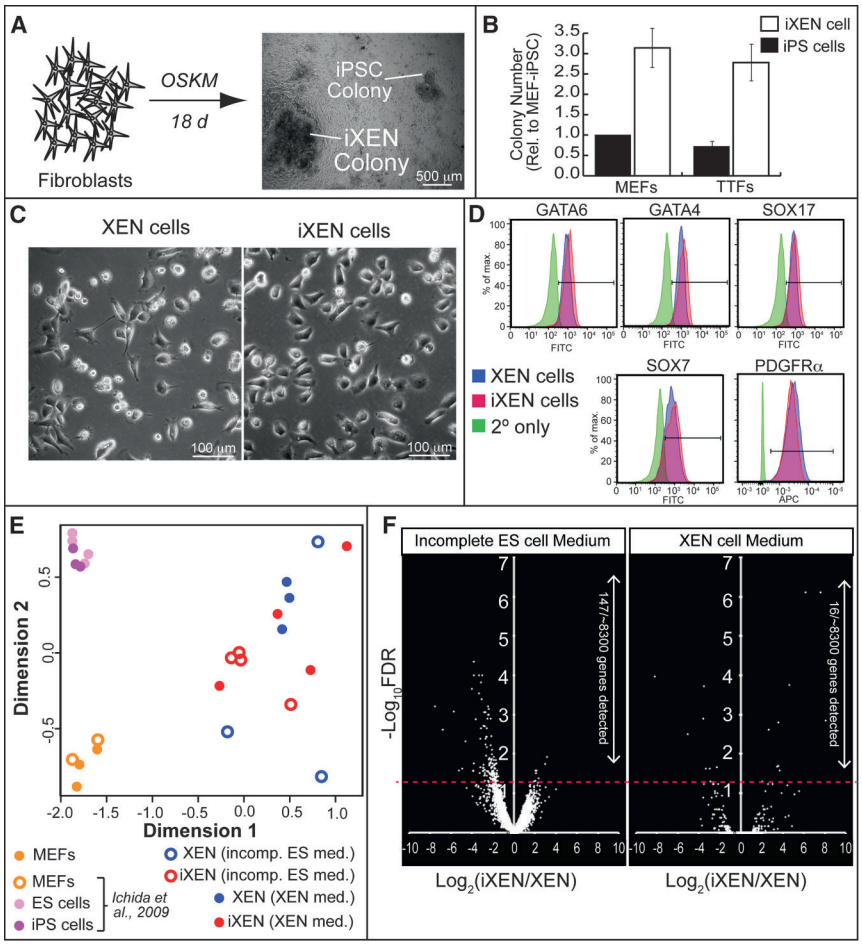

Figure 1. OSKM-Induced XEN Cells Arise during Reprogramming

(A) Fibroblasts were reprogrammed (Takahashi and Yamanaka, 2006), and examined 18 days after *OSKM* infection.

(B) Frequencies at which iPSC and iXEN cell colonies were observed. Error bars denote SE among three reprogrammings each.

(C) Morphology of iXEN cells is similar to that of blastocyst-derived XEN cells.

(D) Flow cytometric analysis shows that endodermal proteins are detected in essentially all XEN and iXEN cells (representative of three independently derived XEN and iXEN cell lines; brackets, see Figure S1C).

(E) Multidimensional scaling analysis of the 100 most variably expressed genes shows that iXEN and XEN cell lines are highly similar, regardless of culture medium, and dissimilar to MEFs and pluripotent stem cell lines (Ichida et al., 2009).

(F) Volcano plots show genes whose average expression level differs significantly (FDR > 0.05, red dotted line) between XEN and iXEN cell lines in each cell culture medium.

See also Table S1.

factor (LIF) (incomplete ESC medium) or in XEN cell medium, which includes FGF4 and HEPARIN, because both media support the expansion of blastocyst-derived XEN cells (Kunath et al., 2005). Most iXEN cell colonies maintained XEN cell morphology, growing as individual, dispersed, and apparently motile cells, in either medium (40 of 51 colonies) (Figure 1C). A minority of non-iPSC colonies (11 of 51 colonies) displayed a mixed mesenchymal morphology (not shown), reminiscent of partially reprogrammed or transformed cells (Meissner et al., 2007; Mikkelsen et al., 2008; Sridharan et al., 2009).

Next, we evaluated the expression of endodermal markers, including GATA6, GATA4, SOX17, SOX7, and PDGFRA, which were expressed to a similar degree in both XEN and iXEN cell lines (Figures 1D, S1C, and S1D). Notably, NANOG was not detected in iXEN cells (Figure S1D), indicating that iXEN cells are distinct from F-class ("fuzzy") cells, which exist in a state of alternative pluripotency (Tonge et al., 2014). These observations show that iXEN cells express XEN cell markers.

Finally, we compared iXEN and XEN cell transcriptomes by RNA sequencing independently derived cell lines, as well as MEF, iPSC, and ESC lines. Multidimensional scaling (MDS) analysis of the 100 most variably expressed genes showed that iXEN and XEN cell transcriptomes are more similar to each other than to MEF, ESC, or iPSC transcriptomes, regardless of the medium in which XEN/iXEN cell lines had been cultured (Figure 1E). Comparing XEN with iXEN cell lines, we observed significant (false discovery rate [FDR] < 0.05) differences in the expression levels of few (146) genes between XEN and iXEN cells cultured in incomplete ESC medium, and even fewer (16) differences in XEN cell medium (Figure 1F and Table S1). Expression of *OSKM* was not detected in iXEN cells, consistent with transgene silencing. Pathway and gene ontology (GO) term analysis of the differentially expressed genes identified deficiencies in expression of oxidative phosphorylation and glutathione metabolism genes in iXEN cells cultured in incomplete ESC medium relative to those grown in XEN cell medium (Table S1), which could indicate deficient iXEN cell proliferation in the absence of growth factor. No pathways were significantly enriched among the differentially expressed genes when XEN and iXEN cells had been cultured in XEN cell medium. Thus, while

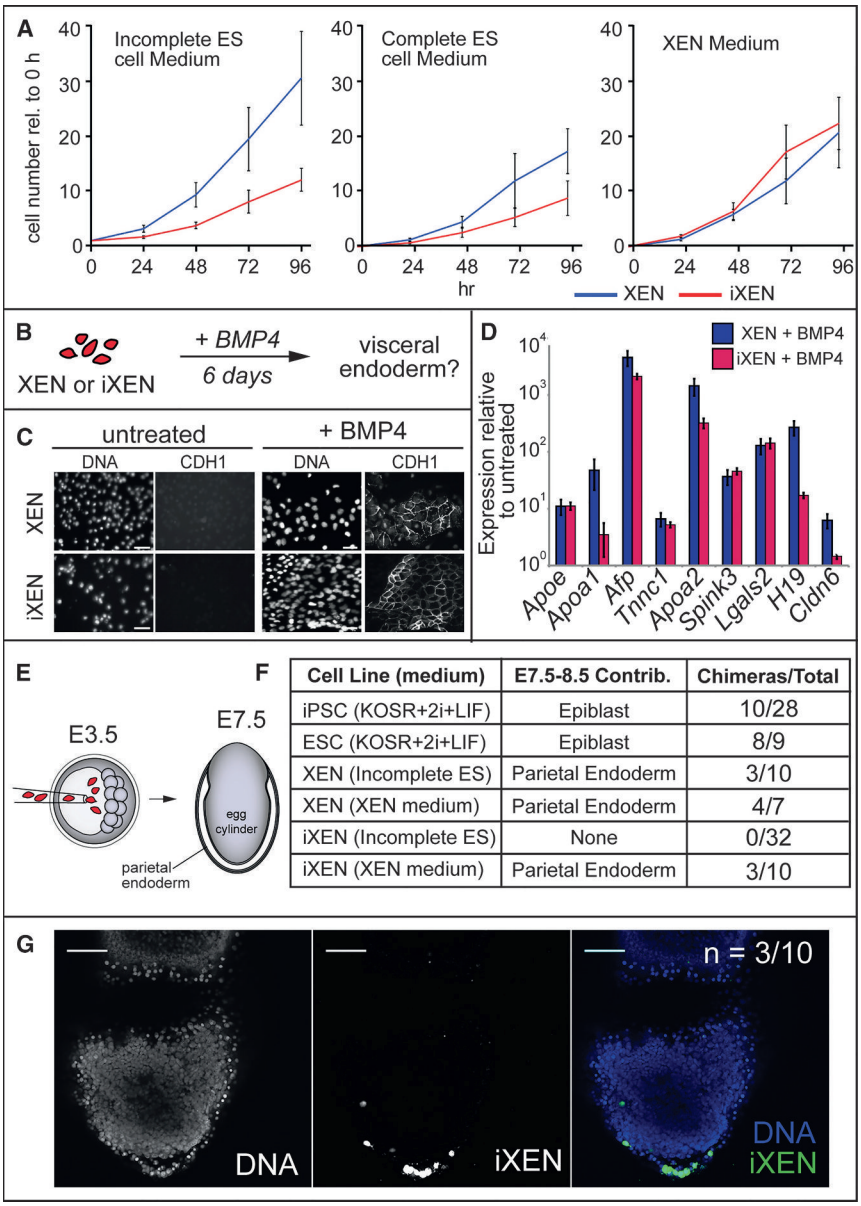

Cell Line (medium)	E7.5-8.5 Contrib.	Chimeras/Total
iPSC (KOSR+2i+LIF)	Epiblast	10/28
ESC (KOSR+2i+LIF)	Epiblast	8/9
XEN (Incomplete ES)	Parietal Endoderm	3/10
XEN (XEN medium)	Parietal Endoderm	4/7
iXEN (Incomplete ES)	None	0/32
iXEN (XEN medium)	Parietal Endoderm	3/10

Figure 2. iXEN Cells Are Self-Renewing and Multipotent

(A) Proliferation rates for cell lines grown in each cell culture medium. Error bars denote SE among three XEN and iXEN cell lines.

(B) VE differentiation assay.

(C) Immunofluorescence shows CDH1 at cell junctions in differentiated iXEN and XEN cells, but not in untreated cells (representative of five independent XEN/iXEN cell lines, DNA = DAPI). Scale bar, 100 μm.

(D) qPCR analysis of VE gene expression in differentiated XEN/iXEN cells, relative to untreated cell lines. Error bars denote SE for two differentiations and four qPCRs each.

(E) In vivo differentiation assay.

(F) Summary of chimera results.

(G) iXEN cells contribute to ParE (see Figure S2 for control chimeras). Scale bar, 100 μm.

more transcriptional differences between iXEN, XEN, MEF, and pluripotent cell lines could become apparent with deeper biological sampling, we conclude that iXEN and XEN cell transcriptomes are extremely similar, and that XEN cell medium better supports conversion of MEFs to XEN-like cells, consistent the role of FGF4 signaling in promoting primitive endoderm development in vivo (Chazaud et al., 2006; Kang et al., 2013; Nichols et al., 2009; Yamanaka et al., 2010).

MEF-Derived XEN Cells Exhibit Stem Cell Properties

Next, we evaluated the self-renewal and multipotency of iXEN cell lines. In terms of self-renewal, iXEN cell lines could be passaged >35 times in either medium. However, iXEN cells grew more slowly than XEN cells in incomplete ESC medium than in XEN cell medium (Figure 2A), consistent with transcriptional profiling predictions. Because LIF supports the expansion of totipotent ESCs that possess XEN-like properties (Morgani et al., 2013), we also examined the proliferation rate of iXEN cells in ESC medium with LIF, but iXEN cells did not proliferate as rapidly as XEN cells in this condition (Figure 2A).

Since blastocyst-derived XEN cells can differentiate into visceral endoderm (VE) or parietal endoderm (ParE) (Artus et al., 2012; Kunath et al., 2005; Paca et al., 2012), we evaluated the multipotency of iXEN cells. During the VE

differentiation assay (Figure 2B), iXEN cell lines were able to differentiate to VE, evidenced by epithelialization, localization of E-cadherin (CDH1) at cell boundaries (Figure 2C), and upregulation of VE markers (Figure 2D). To evaluate differentiation to ParE, we made chimeras with XEN and iXEN cell lines. ESC and iPSC lines were used in parallel positive controls. In chimeras examined between embryonic days 7.5 and 8.5, ESCs and iPSCs contributed to the epiblast lineage, while XEN cells contributed to ParE with expected degree and frequency (Figures 2F and S2) (Kunath et al., 2005; Wamaitha et al., 2015). iXEN cells cultured in incomplete ESC medium did not contribute to chimeras, even though XEN cells cultured in incomplete ESC medium did. However, iXEN cell lines cultured in XEN cell medium contributed to ParE (Figures 2F and 2G) to a similar extent as XEN cells, indicating that iXEN cells cultured in FGF4/HEP have XEN cell-like developmental potential in vivo. These observations underscore the importance of FGF4/HEP for acquisition of iXEN cell function. These results also indicate that iXEN cells are distinct from totipotent cells isolated from pluripotent cell cultures (Canham et al., 2010; Macfarlan et al., 2012; Morgani et al., 2013), because iXEN cells did not contribute to epiblast or trophoblast lineages.

iXEN Cells Are Not Derived from Pre-existing iPSC Colonies

In monolayers, ESCs can differentiate to XEN-like cells at low frequency in the presence of LIF (Niakan et al., 2010), or at high frequency in the absence of LIF and presence of retinoic acid and activin (RA/activin) (Cho et al., 2012; Niakan et al., 2013). These observations raised the possibility that iXEN cells were derived from iPSCs. However, this possibility seemed unlikely for several reasons. First, we derived iXEN cells in the presence of LIF and absence of RA/activin, and rare XEN-like cells that arise under these conditions arise adjacent to, or encircling, the ESC colony from which they are derived (Niakan et al., 2010). By contrast, iXEN cell colonies were often located far ($\geq$50 μm) from the nearest iPSC colony (29 of 48 colonies). In addition, we routinely observed nascent iXEN cell colonies on the sixth day of OSKM infection (Figures 3A and S1B), which is before we observed iPSCs. These observations argue that iXEN cells are derived from MEFs in parallel to iPSCs.

To query the cellular origins of iXEN cells experimentally, we infected ~100 wells each containing around ten tdTOMATO-labeled MEFs per 20,000 unlabeled MEFs with *OSKM* retroviruses (Figure 3B). Because MEFs were labeled sparsely, we predicted that labeled iPSC or iXEN cell colonies would be relatively rare, enabling us to discern iXEN cell origins. For example, if iXEN cells were derived from iPSC colonies, labeled iXEN cell colonies would always be coincident with labeled iPSC colonies. Alternatively, if iXEN cells were derived from MEFs, labeled iXEN cell colonies would be observed in wells lacking labeled iPSC colonies. As expected, most of the wells (85 of 93 wells) contained unlabeled colonies after 18 days of OSKM infection (Figure 3B). Of the wells containing labeled colonies, most (7 of 8) contained one labeled iXEN cell colony and no labeled iPSC colonies. Only in one well did we observe a labeled iXEN cell colony and a labeled iPSC colony (1 of 93 wells). Therefore, the majority of iXEN cells were not derived from iPSC colonies. We do not exclude the possibility that iXEN cells could be derived from a cell that transiently expressed pluripotency genes (Bar-Nur et al., 2015; Maza et al., 2015). Nevertheless, the presence of iXEN cells in conventional reprogramming experiments could influence the interpretation of reprogramming outcomes, and underscores the importance of evaluating cell fates at the clonal level.

All Four Reprogramming Factors Induce XEN Cell Fate

Next, we investigated whether iXEN cells and iPSCs are induced by similar or different combinations of OSKM. We evaluated the copy numbers of each transgene by qPCR analysis of genomic DNA from multiple iXEN cell and iPSC lines. We observed that the number of *OSKM* copies tended to be lower in iXEN cell than in iPSC lines, although average copy numbers did not differ significantly (Figure 3C). To determine whether the trend was meaningful, we overexpressed equal levels of *OSKM* by deriving MEFs by carrying a doxycycline (dox)-inducible *OSKM* cassette (Carey et al., 2010). Interestingly, we observed an increase in the efficiency of forming both iPSC and iXEN cell colonies (Figure 3D), indicating that all four reprogramming factors can induce formation of iXEN cells.

GATA6 and GATA4 Facilitate iXEN Cell, but Not iPSC, Formation

Endodermal genes are reportedly upregulated prior to pluripotency genes in cultures of MEFs undergoing small-molecule reprogramming, but not during *OSKM* reprogramming (Hou et al., 2013; Zhao et al., 2015). However, we observed GATA6-positive cells 6 days after *OSKM* infection (Figure 3A). Moreover, qPCR analysis showed that endodermal genes, like pluripotency genes, were increasingly upregulated during the 20-day time course of *OSKM* reprogramming (Figure 4A), but this did not resolve whether endodermal genes were expressed within iPSC progenitors or within a distinct population. We therefore used flow cytometry to determine whether NANOG-positive, pre-iPSCs (Bar-Nur et al., 2015) expressed endodermal (GATA6 or SOX17) proteins during reprogramming. We detected NANOG and endodermal proteins in two largely distinct populations that increased in size during reprogramming (Figures 4B and S3A–S3C). Neither

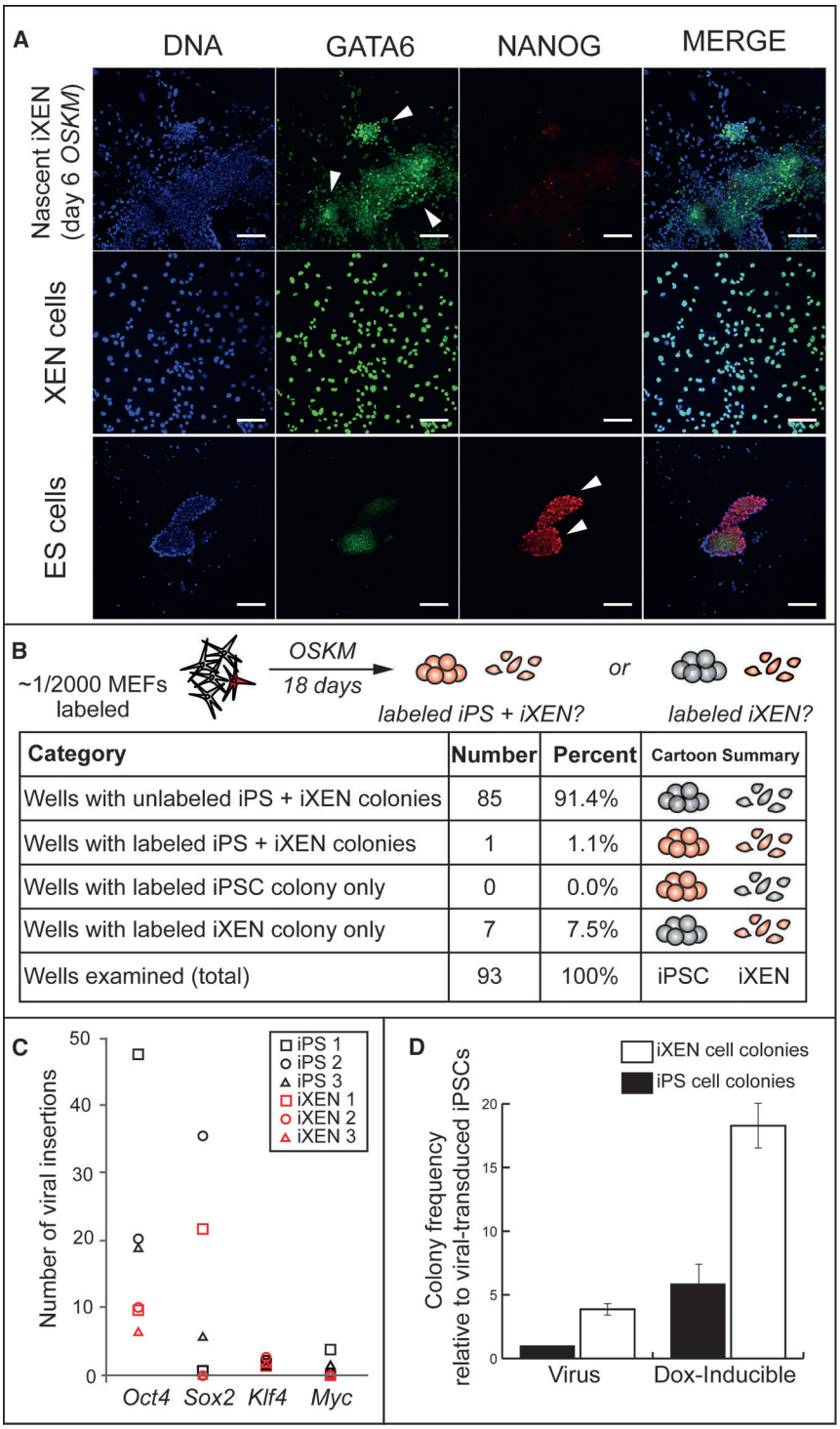

Category	Number	Percent	Cartoon Summary
Wells with unlabeled iPS + iXEN colonies	85	91.4%	
Wells with labeled iPS + iXEN colonies	1	1.1%	
Wells with labeled iPSC colony only	0	0.0%	
Wells with labeled iXEN colony only	7	7.5%	
Wells examined (total)	93	100%	iPSC iXEN

Figure 3. OSKM Induce iXEN Cell Fate in MEFs

(A) Nuclear GATA6, but not NANOG, in nascent iXEN colony on day 6 of *OSKM* reprogramming (compared with XEN cell and ESC controls). Arrowheads point to nuclear proteins. Scale bar, 100 μm.

(B) Lineage tracing shows that iXEN cells are not derived from iPSC colonies during *OSKM* reprogramming of MEFs (representative of two experiments).

(C) Absolute qPCR measurement of *OSKM* copy numbers in XEN/iXEN cell genomic DNA.

(D) Comparison of the frequency of iXEN cell/iPSC colonies after retroviral or transgenic overexpression of *OSKM* on day 18 of reprogramming. Error bars denote SE; two cell lines, four experiments each.

population was prevalent in MEFs undergoing mock reprogramming (Figure S4A), but both populations were present and distinct in TTFs during *OSKM* reprogramming (Figure S4B). These observations suggest that endodermal genes are not expressed in pluripotent cells during *OSKM* reprogramming, in contrast to evidence that MEFs undergoing chemical reprogramming transition through a XEN-like state (Zhao et al., 2015).

To investigate further whether iPSCs transition through a XEN-like state during *OSKM* reprogramming, we used

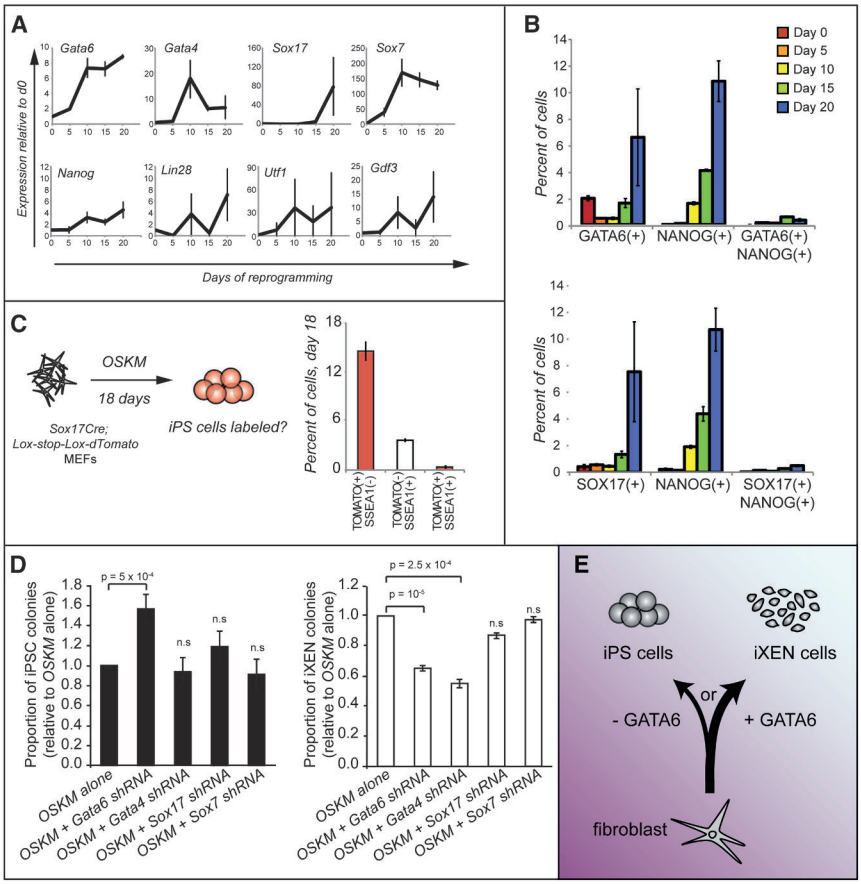

Figure 4. MEF-Expressed Endodermal Genes Promote iXEN Cell Fate

(A) Endodermal (top row) and pluripotency (lower row) genes are upregulated during retroviral *OSKM* reprogramming of MEFs, measured by qPCR. Error bars denote SE among three reprogrammings and four qPCRs.

(B) Flow cytometry analysis of MEFs during *OSKM* reprogramming shows that cells expressing endodermal and pluripotency proteins are largely distinct. Error bars denote SE between two experiments (see also Figures S3A–S3C and S4).

(C) *Sox17Cre* lineage tracing and flow cytometry analysis of cells 20 days after *OSKM* infection of MEFs, showing that most pluripotent (SSEA1-positive) cells never expressed *Sox17*. Error bars denote SE among three reprogrammings (see also Figure S3D).

(D) Proportions of iPSC and iXEN cell colonies after coinfection of MEFs with *OSKM* and shRNA constructs. Error bars denote SE among three reprogrammings (see also Figure S3E).

(E) Model proposing that endogenous GATA6 expression can push cells toward either iPSC or iXEN fate during reprogramming.

lineage tracing. We retrovirally reprogrammed MEFs carrying *Cre* under the control of the *Sox17* promoter (Liao et al., 2009) and a CRE-sensitive *lox-stop-lox-tdTomato* reporter (Madisen et al., 2010). We predicted that if iPSCs had expressed endodermal genes during reprogramming, then most iPSCs would be tdTOMATO-positive 20 days after *OSKM* infection because SOX17 is highly and homogeneously expressed in iXEN/XEN cells (Figure 1D). However, we observed that almost all SSEA1-positive cells were tdTOMATO negative (Figures 4C and S3D), indicating that most pluripotent cells had not expressed *Sox17* during reprogramming. Taken together, our observations indicate that during *OSKM* reprogramming, endodermal genes are upregulated in cells that are largely distinct from those becoming pluripotent. In addition, our observations indicate that pluripotency and XEN pathways are parallel during *OSKM* reprogramming, in contrast to the serial, XEN-to-iPSC pathway that predominates chemical reprogramming (Zhao et al., 2015). Moreover, XEN-like cells derived during chemical reprogramming cannot be maintained in XEN cell medium (Zhao et al., 2015), highlighting fundamental differences in cells produced by chemical and *OSKM* reprogramming.

Finally, we tested the requirement for endodermal genes in the formation of iXEN cells, with the expectation that decreasing endodermal gene expression would decrease the proportion of iXEN cells. We first confirmed substantial knockdown of *Gata6*, *Gata4*, *Sox17*, or *Sox7* in established XEN cells by transfection of small hairpin RNA (shRNA)-encoding plasmids (Figure S3E). We then infected MEFs with shRNAs during reprogramming. Knockdown of *Gata6* or *Gata4* led to a 2-fold decrease in the number of iXEN cell colonies obtained (Figure 4D), indicating that these genes are required for iXEN cell fate. Notably, knockdown of *Gata6* also led to a significant increase in the number of iPSC colonies. Thus, endodermal gene expression interferes with pluripotency during *OSKM* reprogramming. We propose that heterogeneous expression of GATA6 within the MEFs (Figure 4B) could contribute to different outcomes during reprogramming (Figure 4E). Alternatively, stochastic differences in the timing of translation or nuclear localization of the reprogramming factors could influence cell fates. Finally, our observations suggest that the parallel pluripotency and XEN pathways compete with, rather than support, each other during reprogramming. By contrast, paracrine signaling

from pluripotent epiblast cells supports the formation of XEN cell progenitors in the blastocyst (Frum and Ralston, 2015), but our evidence does not support this model during reprogramming. We anticipate that identification of additional mechanisms regulating the balance between iXEN cell and iPSC fates will inform future efforts to characterize the molecular steps of cell fate specification, and lead to establishment of new genetic models of reproductive disorders.

EXPERIMENTAL PROCEDURES

Mouse Work

All animal work conformed to the guidelines and regulatory standards of the Michigan State University Institutional Animal Care and Use Committee. See Supplemental Experimental Procedures for strains.

Cell Culture

See Supplemental Experimental Procedures for media recipes. *OSKM* retroviruses were produced by transfecting 293T cells with pCL-ECO and pMXs plasmids encoding *OSKM* (Addgene). 48 hr later, supernatant was harvested and qPCR was used to quantify virus (for primer sequence see Supplemental Experimental Procedures). Approximately 6×10^7 copies OSKM per 40,000 MEFs were added for 24 hr, and medium was then replaced with MEF medium, then ESC medium on days 2 and 4, and finally reprogramming medium on day 6 and every other day thereafter. For dox-induced reprogramming, dox-inducible MEFs were plated at a density of 50 cells/mm^2 on gelatin in MEF medium. After 24 hr and every 2 days for 16 days thereafter, wells received ESC medium with 2 μg/ml dox (Sigma). For sparse labeling, ten tdTOMATO-labeled MEFs and 20,000 unlabeled MEFs were seeded in each well of 24-well dishes, then infected with *OSKM* and examined 18 days later. For lineage tracing, MEFs carrying *Sox17*$^{tm1(icre)Heli}$ and *Gt(ROSA)26Sor*$^{tm14(CAG-tdTomato)Hze}$ were infected with *OSKM* retrovirus, as described above. shRNAs were cloned into pMXs and titrated by qPCR (for sequence see Supplemental Experimental Procedures).

Single-Cell Analyses

Immunostained cells were analyzed on a Becton Dickinson LSR II or Olympus Fluoview FV1000. Details are available in Supplemental Experimental Procedures.

RNA Sequencing and qPCR

cDNA libraries were sequenced to a depth of 25–50 million 50-bp single-end reads using an Illumina HiSeq 2500. See Supplemental Experimental Procedures for details on library preparation and data processing. The accession number is GEO: GSE77550.

XEN/iXEN Cell Differentiation

In vitro differentiation followed previously described techniques (Artus et al., 2012; Paca et al., 2012). To create chimeras, we injected ~15 fluorescently labeled cells into each blastocoel of unlabeled CD-1 blastocysts, and embryos were then transferred into the uterus of E2.5 pseudopregnant recipient females. See Supplemental Experimental Procedures for detailed protocols.

Statistical Analyses

Unless otherwise stated, t tests were performed for pairwise comparisons and ANOVA for multiple pairwise comparisons.

SUPPLEMENTAL INFORMATION

Supplemental Information includes Supplemental Experimental Procedures, four figures, and one table and can be found with this article online at http://dx.doi.org/10.1016/j.stemcr.2016.02.003.

AUTHOR CONTRIBUTIONS

A.P., M.A.H., K.W., K.L., and A.R. designed the experiments. A.P. and K.W. performed experiments, and M.A.H. performed the computational analysis. A.P., M.A.H., and A.R. interpreted the experiments. A.R. wrote the manuscript, with input from A.P., M.A.H., K.W., and K.L.

ACKNOWLEDGMENTS

We thank Jason Knott, Beronda Montgomery, David Arnosti, and Monique Floer for discussion. This work was supported by California Institute for Regenerative Medicine grant TG2-01157 to A.P., NIH grants R03 HD077112 to K.W., R01 HD075093 to K.L., R01 GM104009 to A.R., MSU AgBioResearch, and Michigan State University.

Received: November 2, 2015
Revised: February 3, 2016
Accepted: February 4, 2016
Published: March 3, 2016

REFERENCES

Aksoy, I., Jauch, R., Chen, J., Dyla, M., Divakar, U., Bogu, G.K., Teo, R., Leng Ng, C.K., Herath, W., Lili, S., et al. (2013). Oct4 switches partnering from Sox2 to Sox17 to reinterpret the enhancer code and specify endoderm. EMBO J. *32*, 938–953.

Artus, J., Douvaras, P., Piliszek, A., Isern, J., Baron, M.H., and Hadjantonakis, A.K. (2012). BMP4 signaling directs primitive endoderm-derived XEN cells to an extraembryonic visceral endoderm identity. Dev. Biol. *361*, 245–262.

Bar-Nur, O., Verheul, C., Sommer, A.G., Brumbaugh, J., Schwarz, B.A., Lipchina, I., Huebner, A.J., Mostoslavsky, G., and Hochedlinger, K. (2015). Lineage conversion induced by pluripotency factors involves transient passage through an iPSC stage. Nat. Biotechnol. *33*, 761–768.

Canham, M.A., Sharov, A.A., Ko, M.S., and Brickman, J.M. (2010). Functional heterogeneity of embryonic stem cells revealed through translational amplification of an early endodermal transcript. PLoS Biol. *8*, e1000379.

Carey, B., Markoulaki, S., Beard, C., Hanna, J., and Jaenisch, R. (2010). Single-gene transgenic mouse strains for reprogramming adult somatic cells. Nat. Methods *7*, 56–59.

Chazaud, C., Yamanaka, Y., Pawson, T., and Rossant, J. (2006). Early lineage segregation between epiblast and primitive endoderm in mouse blastocysts through the Grb2-MAPK pathway. Dev. Cell *10*, 615–624.

Cho, L.T., Wamaitha, S.E., Tsai, I.J., Artus, J., Sherwood, R.I., Pedersen, R.A., Hadjantonakis, A.K., and Niakan, K.K. (2012). Conversion from mouse embryonic to extra-embryonic endoderm stem cells reveals distinct differentiation capacities of pluripotent stem cell states. Development *139*, 2866–2877.

Frum, T., and Ralston, A. (2015). Cell signaling and transcription factors regulating cell fate during formation of the mouse blastocyst. Trends Genet. *31*, 402–410.

Frum, T., Halbisen, M.A., Wang, C., Amiri, H., Robson, P., and Ralston, A. (2013). Oct4 cell-autonomously promotes primitive endoderm development in the mouse blastocyst. Dev. Cell *25*, 610–622.

Hou, P., Li, Y., Zhang, X., Liu, C., Guan, J., Li, H., Zhao, T., Ye, J., Yang, W., Liu, K., et al. (2013). Pluripotent stem cells induced from mouse somatic cells by small-molecule compounds. Science *341*, 651–654.

Ichida, J.K., Blanchard, J., Lam, K., Son, E.Y., Chung, J.E., Egli, D., Loh, K.M., Carter, A.C., Di Giorgio, F.P., Koszka, K., et al. (2009). A small-molecule inhibitor of TGF-beta signaling replaces sox2 in reprogramming by inducing nanog. Cell Stem Cell *5*, 491–503.

Kang, M., Piliszek, A., Artus, J., and Hadjantonakis, A.K. (2013). FGF4 is required for lineage restriction and salt-and-pepper distribution of primitive endoderm factors but not their initial expression in the mouse. Development *140*, 267–279.

Kunath, T., Arnaud, D., Uy, G.D., Okamoto, I., Chureau, C., Yamanaka, Y., Heard, E., Gardner, R.L., Avner, P., and Rossant, J. (2005). Imprinted X-inactivation in extra-embryonic endoderm cell lines from mouse blastocysts. Development *132*, 1649–1661.

Le Bin, G.C., Muñoz-Descalzo, S., Kurowski, A., Leitch, H., Lou, X., Mansfield, W., Etienne-Dumeau, C., Grabole, N., Mulas, C., Niwa, H., et al. (2014). Oct4 is required for lineage priming in the developing inner cell mass of the mouse blastocyst. Development *141*, 1001–1010.

Liao, W.P., Uetzmann, L., Burtscher, I., and Lickert, H. (2009). Generation of a mouse line expressing Sox17-driven Cre recombinase with specific activity in arteries. Genesis *47*, 476–483.

Macfarlan, T.S., Gifford, W.D., Driscoll, S., Lettieri, K., Rowe, H.M., Bonanomi, D., Firth, A., Singer, O., Trono, D., and Pfaff, S.L. (2012). Embryonic stem cell potency fluctuates with endogenous retrovirus activity. Nature *487*, 57–63.

Madisen, L., Zwingman, T.A., Sunkin, S.M., Oh, S.W., Zariwala, H.A., Gu, H., Ng, L.L., Palmiter, R.D., Hawrylycz, M.J., Jones, A.R., et al. (2010). A robust and high-throughput Cre reporting and characterization system for the whole mouse brain. Nat. Neurosci. *13*, 133–140.

Maza, I., Caspi, I., Zviran, A., Chomsky, E., Rais, Y., Viukov, S., Geula, S., Buenrostro, J.D., Weinberger, L., Krupalnik, V., et al. (2015). Transient acquisition of pluripotency during somatic cell transdifferentiation with iPSC reprogramming factors. Nat. Biotechnol. *33*, 769–774.

Meissner, A., Wernig, M., and Jaenisch, R. (2007). Direct reprogramming of genetically unmodified fibroblasts into pluripotent stem cells. Nat. Biotechnol. *25*, 1177–1181.

Mikkelsen, T.S., Hanna, J., Zhang, X., Ku, M., Wernig, M., Schorderet, P., Bernstein, B.E., Jaenisch, R., Lander, E.S., and Meissner, A. (2008). Dissecting direct reprogramming through integrative genomic analysis. Nature *454*, 49–55.

Morgani, S.M., and Brickman, J.M. (2015). LIF supports primitive endoderm expansion during pre-implantation development. Development *142*, 3488–3499.

Morgani, S.M., Canham, M.A., Nichols, J., Sharov, A.A., Migueles, R.P., Ko, M.S., and Brickman, J.M. (2013). Totipotent embryonic stem cells arise in ground-state culture conditions. Cell Rep. *3*, 1945–1957.

Neri, F., Zippo, A., Krepelova, A., Cherubini, A., Rocchigiani, M., and Oliviero, S. (2012). Myc regulates the transcription of the PRC2 gene to control the expression of developmental genes in embryonic stem cells. Mol. Cell Biol. *32*, 840–851.

Niakan, K.K., Ji, H., Maehr, R., Vokes, S.A., Rodolfa, K.T., Sherwood, R.I., Yamaki, M., Dimos, J.T., Chen, A.E., Melton, D.A., et al. (2010). Sox17 promotes differentiation in mouse embryonic stem cells by directly regulating extraembryonic gene expression and indirectly antagonizing self-renewal. Genes Dev. *24*, 312–326.

Niakan, K.K., Schrode, N., Cho, L.T., and Hadjantonakis, A.K. (2013). Derivation of extraembryonic endoderm stem (XEN) cells from mouse embryos and embryonic stem cells. Nat. Protoc. *8*, 1028–1041.

Nichols, J., Silva, J., Roode, M., and Smith, A. (2009). Suppression of Erk signalling promotes ground state pluripotency in the mouse embryo. Development *136*, 3215–3222.

Paca, A., Séguin, C.A., Clements, M., Ryczko, M., Rossant, J., Rodriguez, T.A., and Kunath, T. (2012). BMP signaling induces visceral endoderm differentiation of XEN cells and parietal endoderm. Dev. Biol. *361*, 90–102.

Serrano, F., Calatayud, C.F., Blazquez, M., Torres, J., Castell, J.V., and Bort, R. (2013). Gata4 blocks somatic cell reprogramming by directly repressing Nanog. Stem Cells *31*, 71–82.

Shu, J., Wu, C., Wu, Y., Li, Z., Shao, S., Zhao, W., Tang, X., Yang, H., Shen, L., Zuo, X., et al. (2013). Induction of pluripotency in mouse somatic cells with lineage specifiers. Cell *153*, 963–975.

Shu, J., Zhang, K., Zhang, M., Yao, A., Shao, S., Du, F., Yang, C., Chen, W., Wu, C., Yang, W., et al. (2015). GATA family members as inducers for cellular reprogramming to pluripotency. Cell Res. *25*, 169–180.

Smith, K.N., Singh, A.M., and Dalton, S. (2010). Myc represses primitive endoderm differentiation in pluripotent stem cells. Cell Stem Cell *7*, 343–354.

Sridharan, R., Tchieu, J., Mason, M.J., Yachechko, R., Kuoy, E., Horvath, S., Zhou, Q., and Plath, K. (2009). Role of the murine

reprogramming factors in the induction of pluripotency. Cell *136*, 364–377.

Takahashi, K., and Yamanaka, S. (2006). Induction of pluripotent stem cells from mouse embryonic and adult fibroblast cultures by defined factors. Cell *126*, 663–676.

Tonge, P.D., Corso, A.J., Monetti, C., Hussein, S.M., Puri, M.C., Michael, I.P., Li, M., Lee, D.S., Mar, J.C., Cloonan, N., et al. (2014). Divergent reprogramming routes lead to alternative stem-cell states. Nature *516*, 192–197.

Wamaitha, S.E., del Valle, I., Cho, L.T., Wei, Y., Fogarty, N.M., Blakeley, P., Sherwood, R.I., Ji, H., and Niakan, K.K. (2015). Gata6 potently initiates reprograming of pluripotent and differentiated cells to extraembryonic endoderm stem cells. Genes Dev. *29*, 1239–1255.

Wicklow, E., Blij, S., Frum, T., Hirate, Y., Lang, R.A., Sasaki, H., and Ralston, A. (2014). HIPPO pathway members restrict SOX2 to the inner cell mass where it promotes ICM fates in the mouse blastocyst. PLoS Genet. *10*, e1004618.

Yamanaka, Y., Lanner, F., and Rossant, J. (2010). FGF signal-dependent segregation of primitive endoderm and epiblast in the mouse blastocyst. Development *137*, 715–724.

Zhao, Y., Zhao, T., Guan, J., Zhang, X., Fu, Y., Ye, J., Zhu, J., Meng, G., Ge, J., Yang, S., et al. (2015). A XEN-like state bridges somatic cells to pluripotency during chemical reprogramming. Cell *163*, 1678–1691.

Cell SnapShot archive

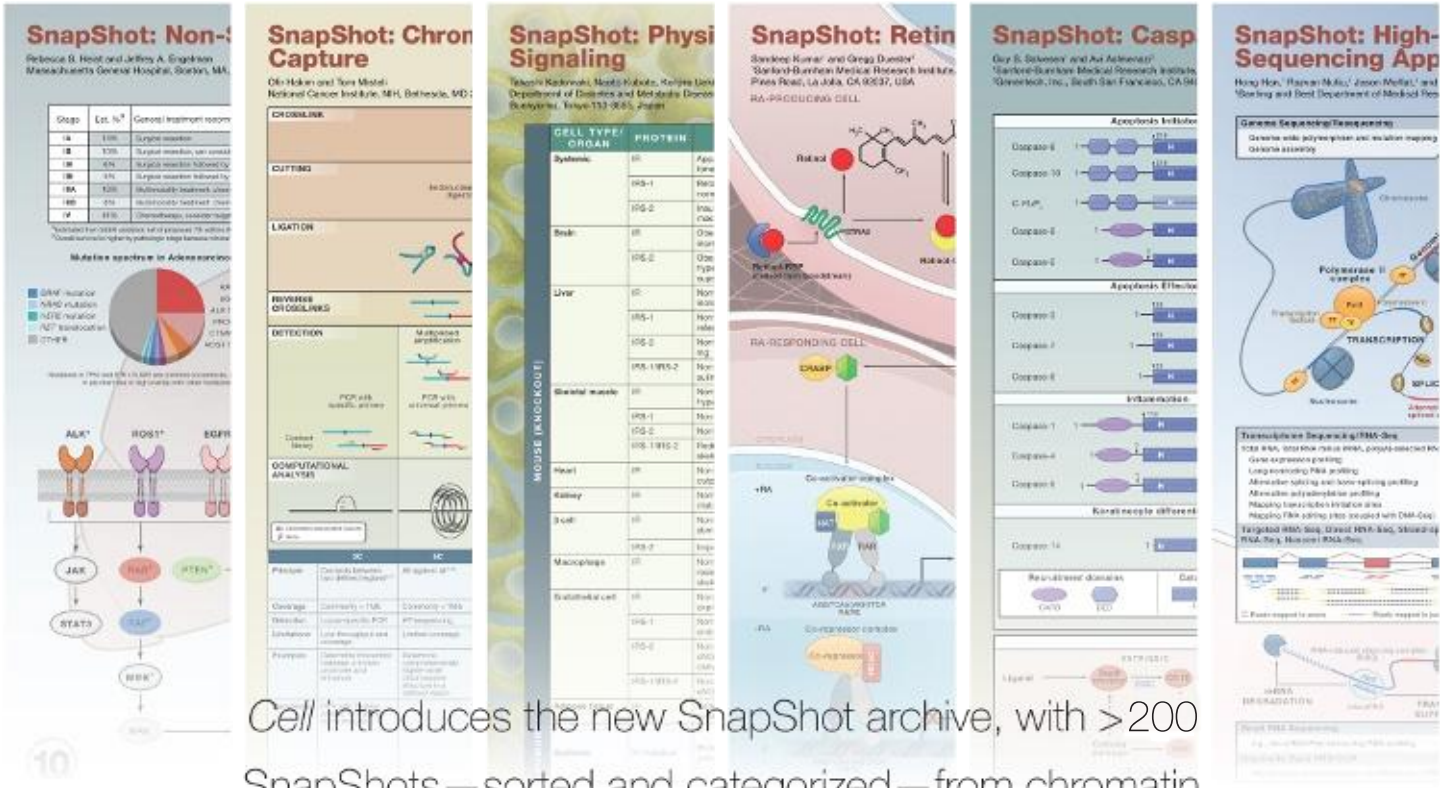

Cell introduces the new SnapShot archive, with >200 SnapShots—sorted and categorized—from chromatin remodelers and autophagy to cancer and autism. All SnapShots published from a year ago or more are open access and freely available.

Sponsored By

R&D SYSTEMS
a bio-techne brand

view the archive

cell.com/snapshots

Stem Cell Reports
Meeting Report
OPEN ACCESS

Creating Patient-Specific Neural Cells for the In Vitro Study of Brain Disorders

Kristen J. Brennand,[1,23] M. Carol Marchetto,[2,23] Nissim Benvenisty,[3] Oliver Brüstle,[4] Allison Ebert,[5] Juan Carlos Izpisua Belmonte,[6] Ajamete Kaykas,[7] Madeline A. Lancaster,[8] Frederick J. Livesey,[9] Michael J. McConnell,[10] Ronald D. McKay,[11] Eric M. Morrow,[12] Alysson R. Muotri,[13] David M. Panchision,[14] Lee L. Rubin,[15] Akira Sawa,[16] Frank Soldner,[17] Hongjun Song,[18] Lorenz Studer,[19] Sally Temple,[20] Flora M. Vaccarino,[21] Jun Wu,[6] Pierre Vanderhaeghen,[22] Fred H. Gage,[2,*] and Rudolf Jaenisch[17,*]

[1]Department of Psychiatry, Icahn School of Medicine at Mount Sinai, 1425 Madison Avenue, New York, NY 10029, USA
[2]Laboratory of Genetics, Salk Institute for Biological Studies, 10010 North Torrey Pines Road, San Diego, CA 92037, USA
[3]Department of Genetics, Hebrew University of Jerusalem, Jerusalem 91904, Israel
[4]Institute of Reconstructive Neurobiology, LIFE & BRAIN Center, University of Bonn, Bonn 53127, Germany
[5]Department of Cell Biology, Neurobiology & Anatomy, Medical College of Wisconsin, 8701 Watertown Plank Road, Milwaukee, WI 53226, USA
[6]Gene Expression Laboratory, Salk Institute for Biological Studies, 10010 North Torrey Pines Road, San Diego, CA 92037, USA
[7]Department of Neurobiology, Novartis Institute for BioMedical Research, Inc., 100 Technology Square, Cambridge, MA 02139, USA
[8]Laboratory of Molecular Biology, Francis Crick Avenue, Cambridge Biomedical Campus, Cambridge CB2 0QH, UK
[9]Gurdon Institute, University of Cambridge, Tennis Court Road, Cambridge CB2 1QN, UK
[10]Department of Biochemistry and Molecular Genetics, Center for Brain Immunology and Glia, University of Virginia School of Medicine, 1340 Jefferson Park Avenue, Charlottesville, VA 22908, USA
[11]Brain Development, Lieber Institute for Brain Development, 855 North Wolfe Street, Baltimore, MD 21205, USA
[12]Department of Molecular Biology, Cell Biology and Biochemistry, Brown University, 70 Ship Street, Providence, RI 02912, USA
[13]Department of Cellular & Molecular Medicine, University of California, San Diego, 9500 Gilman Drive, La Jolla, CA 92037, USA
[14]Developmental Neurobiology Program, National Institute of Mental Health, 6001 Executive Boulevard, Bethesda, MD 20892, USA
[15]Department of Stem Cell and Regenerative Biology, Harvard University, 16 Divinity Avenue, Cambridge, MA 02138, USA
[16]Department of Psychiatry and Behavioral Sciences, The Johns Hopkins Hospital, 600 North Wolfe Street, Baltimore, MD 21287, USA
[17]Whitehead Institute for Biomedical Research, 9 Cambridge Center, Cambridge, MA 02142, USA
[18]Institute for Cell Engineering, Johns Hopkins University School of Medicine, 733 North Broadway, Baltimore, MD 21205, USA
[19]Stem Cell and Tumor Biology, Memorial Sloan-Kettering Cancer Center, 1275 York Avenue, Box 256, New York, NY 10021, USA
[20]Neural Stem Cell Institute, One Discovery Drive, Rensselaer, NY 12144, USA
[21]Child Study Center, Yale University, 230 South Frontage Road, New Haven, CT 06520, USA
[22]Institute of Interdisciplinary Research (IRIBHM), University of Brussels ULB, 808, Route de Lennik, 1070 Brussels, Belgium
[23]Co-first author
*Correspondence: fgage@salk.edu (F.H.G.), jaenisch@wi.mit.edu (R.J.)
http://dx.doi.org/10.1016/j.stemcr.2015.10.011

SUMMARY

As a group, we met to discuss the current challenges for creating meaningful patient-specific in vitro models to study brain disorders. Although the convergence of findings between laboratories and patient cohorts provided us confidence and optimism that hiPSC-based platforms will inform future drug discovery efforts, a number of critical technical challenges remain. This opinion piece outlines our collective views on the current state of hiPSC-based disease modeling and discusses what we see to be the critical objectives that must be addressed collectively as a field.

Just 10 years since the development of human induced pluripotent stem cell (hiPSC) technology (Takahashi et al., 2007), the use of these cells to model brain disorders and obtain disease-relevant information is becoming a tangible reality. Not only are we now able to better detect relevant genetic changes in a patient's cells using high-throughput genome sequencing technology but also we can establish a direct phenotypic correlation between genetic mutations and an aberrant neuronal phenotype or developmental trajectory. The latest improvements in generating relevant neural cell types by either differentiation of hiPSC lines or by direct conversion of somatic cells (e.g., fibroblasts) now allow researchers to make cells from different areas of the central nervous system (CNS) and peripheral nervous system (PNS) and probe effects on the cell type where disease manifests. This represents a significant improvement of previous experimental tools, including animal models and in vitro cultures of non-relevant cell lines (such as 293T or HeLa cells), which recapitulate only some of the specific traits of human disease (Eglen and Reisine, 2011; Pouton and Haynes, 2005), with the potential to reverse the current trend of huge investments by the pharmaceutical industry yielding few therapeutic compounds entering the market (Mullard, 2015; Scannell et al., 2012).

In April 2015, a group of stem cell researchers, neuroscientists, genomic and computational biologists, clinicians, and industry partners met for 4 days at the Banbury Center at Cold Spring Harbor, New York, to discuss the current challenges for creating meaningful patient-specific in vitro

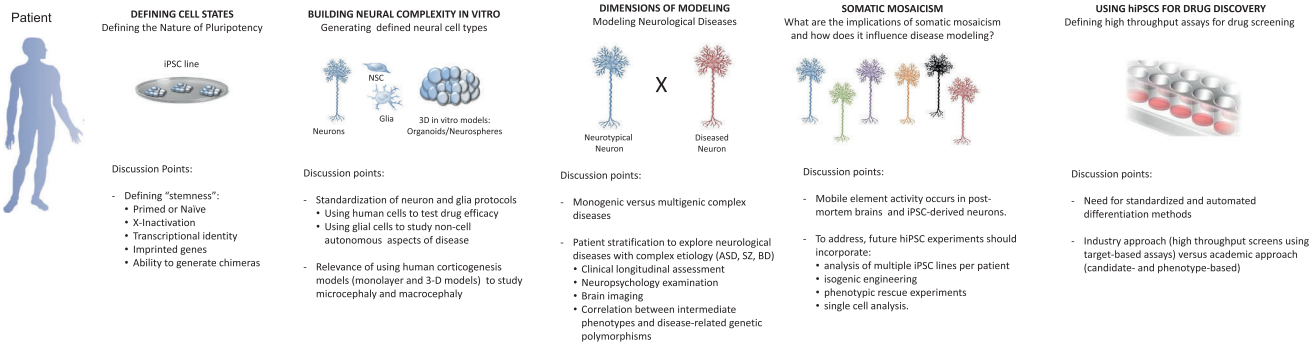

Figure 1. Current Challenges for Creating Meaningful Patient-Specific In Vitro Models to Study Brain Disorders

A critical limitation of the field at present is the inherent difficulty in accurately defining cell states, particularly concerning the temporal and regional identity of pluripotent cells, neurons, and glial cells. A next step for hiPSC-based models of brain disorders will be building neural complexity in vitro, incorporating cell types and 3D organization to achieve network- and circuit-level structures. As the level of cellular complexity increases, new dimensions of modeling will emerge, and modeling neurological diseases that have a more complex etiology will be accessible. An important caveat to hiPSC-based models is the possibility that epigenetic factors and somatic mosaicism may contribute to neurological and neuropsychiatric disease, risk factors that may be difficult to capture in reprogramming or accurately recapitulate in vitro differentiation. A critical next step, in order to enable the use of hiPSCs for drug discovery, will be improving the scalability and reproducibility of in vitro differentiations and functional assays.

models to study brain disorders (Figures 1 and 2). This opinion piece outlines the current state of the field and discusses the main challenges that should drive future research initiatives.

Defining Cell States

The initial discussion at the Banbury meeting addressed the basic properties of stem cells and the increasing appreciation of the heterogeneity of the pluripotent state. The most basic definition of "pluripotency" is the ability of a single cell to differentiate into cells from all three germ layers; however, an improved understanding of the varieties of stem cells and pluripotent states available will broaden the types of cells used as sources for disease modeling and potentially improve production of specific cell types. While we now understand that a variety of artificial stem cell states may be possible during the reprogramming process (Benevento et al., 2014; Clancy et al., 2014; Lee et al., 2014; Tonge et al., 2014), originally, two distinct states of pluripotency were apparent: (1) a "naive" ground state, which was leukemia inhibitory factor (LIF)-dependent, capable of generating both embryonic and extra-embryonic cell lineages, and resembled the properties of mouse embryonic stem cells (mESCs); and (2) a "primed" state, which was FGF2-dependent, reminiscent of "epiblast" identity, and resembled human embryonic stem cells (hESCs) (reviewed by Stadtfeld and Hochedlinger, 2010). In mice, it is well established that inhibition of ERK1/ERK2 and GSK3β (2i/LIF) is necessary to maintain the naive state (Marks et al., 2012; Ying et al., 2008); withdrawal of 2i/LIF is sufficient to drift naive cells to the primed state (Brons et al., 2007). Recently, several groups have described culture conditions for maintaining transgene-independent hESCs that share various properties with mESCs (Chan et al., 2013; Gafni et al., 2013; Marinho et al., 2015; Valamehr et al., 2014; Ware et al., 2014). Most compellingly, Hanna and colleagues reported that 2i/LIF, together with EGF, FGF2, JNKi, ROCKi, and p38I, not only converted primed hESCs to the naive state but also conferred competence to form cross-species chimeric mouse embryos (Gafni et al., 2013). While culture of mouse cells in 2i/LIF can convert cells from the primed into the naive ground state, this is not sufficient to convert primed human cells into a naive state. A number of different protocols have been published using a variety of cytokines and inhibitors, with gene expression analyses used to characterize the state of pluripotency. The transcriptome of naive cells generated by some protocols resembled that of mouse naive cells and cleavage human embryos (Takashima et al., 2014; Theunissen et al., 2014), whereas the transcriptome of naive cells produced by other protocols more closely resembled that of primed cells (Brons et al., 2007; Chan et al., 2013; Gafni et al., 2013; Valamehr et al., 2014; Ware et al., 2014). Thus, no consensus on what constitutes the naive human state has been reached, and it is possible that different states of pluripotency exist in human cells. Within this context, a number of presenters considered the importance of carefully defining cell states, in particular the nature of pluripotency.

Rudolf Jaenisch, from the Whitehead Institute for Biomedical Research, reported on iterative chemical screening to evaluate alternative culture conditions

Figure 2. Banbury Meeting Attendees

for naive human pluripotency, ultimately yielding an improved combination of five kinase inhibitors (5i/L/FA) that induces and maintains *OCT4* distal enhancer activity when applied directly to conventional hESCs (Theunissen et al., 2014). Using these optimized conditions, his group demonstrated direct conversion of primed to naive ESCs in the absence of transgenes and isolation of novel hESCs from human blastocysts. They noted, however, that naive hESCs showed upregulated *XIST* and evidence of X inactivation, raising the possibility that X inactivation in naive stem cells in mouse and human may be different. Critically, transplantation of GFP-positive human naive hESCs into mouse blastocysts yielded no GFP-positive E10.5 embryos, either by their original method (n = 860 embryos) or by published methods (Gafni et al., 2013) (n = 436+ embryos). PCR for human mitochondria is a more sensitive assay, identifying even the presence of 1/10,000 human cells, but this also failed to detect mouse-human chimerism. Although the generation of interspecies chimeras by injection of human ESCs into mouse morulae was proposed as a stringent assay for naive human pluripotency (Gafni et al., 2013), the assay may be too inefficient for use as a routine functional assay. Instead, Jaenisch suggested that expression profiling is the best method to define naive versus primed ESCs, noting that principal component analysis (PCA) of gene expression from naive hESCs clusters close to mESCs and far from primed hESCs.

Jun Wu, from the Izpisua Belmonte lab at the Salk Institute of Biological Studies, also spoke briefly of recent difficulties in generating viable chimeras following injection of naive human iPSCs tagged with a GFP reporter (hiPSC-GFP). Fortuitously, these studies led to media formulations that allowed his group to expand and propagate mouse epiblast stem cell cells (mEpiSCs) from embryonic day 5.75 (E5.75) embryos. When cultured with both FGF2 and WNT inhibition (IWR1), in the absence of serum, these mouse epiblast stem cells showed high cloning efficiency, comparable to that observed in mESCs. Careful characterization revealed a surprising regional specification of these cells (now termed rsEpiSCs); upon transplantation into mouse embryos, although they could contribute to all three germ layers, they could only incorporate into the posterior of the embryo, but not the distal or anterior regions (Wu et al., 2015). Similar culture conditions yielded human

rsPSCs, which also contributed to all three germ layers, exclusively in the posterior region, of chimeric mouse embryos (Wu et al., 2015). This is in sharp contrast to conventional human PSCs, which failed to incorporate in E7.5 mouse epiblast; global genome-wide expression analysis confirmed that these stem cell states have unique molecular signatures.

Ronald McKay, of the Lieber Institute for Brain Studies, further considered molecular regulation of stem cell identity. Sophisticated immunohistochemical analyses revealed unexpected dynamics in the level of pluripotent gene expression, which was high immediately following passaging and declined between splitting and varied between colonies and cultures, relative to their location within the colony (Chen et al., 2014). The transcriptional identity of each stem cell line, however, was stable across datasets and between laboratories, evidence that the dynamic variation between PSCs is defined by our individual human genomes (Adamo et al., 2015). This transcriptional identity not only is conserved in replicate cell lines derived from the same genome but also is stable throughout differentiation; the signature can be detected in post-mortem brain tissue matched to individual stem cell lines. Such signatures may provide a useful means to both classify and assess risk within stratified patient populations without requiring advance knowledge of the target neural cell type(s).

Nissim Benvenisty, from Hebrew University of Jerusalem, discussed epigenetic regulation of stem cells. By generating parthogenetic hiPSCs from female teratomas that harbor two sets of maternal chromosomes, his group was able to identify novel imprinted genes, including many miRNAs (Stelzer et al., 2011). Rather than observing decreased expression in all paternally expressed genes in parthogenetic hiPSCs, he reported that about half of the known paternally expressed genes were unexpectedly not downregulated. Two classes of imprinted genes were resolved: the first was downregulated in all parthenogenetic cell types and included classical imprinted genes such as PEG10, whereas the second was not downregulated in some or all examined parthenogenetic cell types and showed overlapping imprinted and non-imprinted isoforms; this resulted from expression from two promoters, only one of which was imprinted (Stelzer et al., 2015). In this context, Benvenisty considered whether parthenogenetic hiPSCs could be used to model epigenetic human disorders such as the neurological Prader-Willi Syndrome (PWS), which results from maternal uniparental disomy of chromosome 15. Characterization of the parthogenetic PSCs and iPSCs from PWS patients revealed specific maternal expression of the *DLK1-DIO3* locus in chromosome 14. The data suggest that an imprinted gene can work in *trans*, because the loss of expression of *IPW*, an imprinted long noncoding RNA in the PWS region, is a regulator of *DLK1-DIO3* region. This supports a working model that paternal chromosome 15 mutation in PWS leads to loss of *IPW* and subsequent upregulation of maternal genes (Stelzer et al., 2014).

From these talks arose a discussion of the various tools by which one could define cell states. There was general agreement that genome-wide transcription analysis, both of populations or cells, and particularly at the single-cell level to resolve heterogeneity, was highly informative. Moreover, genetic and epigenetic editing, combined with selective use of cell-line derivation methods, could be tailored to the unique requirements for mechanistic studies of any particular disorder. Finally, as one considers modeling neurological and psychiatric diseases, it is critical that the field as a whole establishes whether or not there is an ideal starting somatic cell type, reprogramming methodology, and/or pluripotency cell state from which to initiate hiPSC-based disease modeling experiments of brain disorders.

Building Complexity to Neuronal Development In Vitro

From here, the focus of discussions turned toward novel methods to generate defined cell types and their application toward a number of highly penetrant neurodevelopmental and neurodegenerative disorders. There was consistent discussion of the critical need to build complexity into hiPSC-based models of neuronal development, first, by more efficiently differentiating and maturing pure populations of neurons, astrocytes, and other neural cell types, and, second, by allowing these populations to self-organize into defined circuits and three-dimensional (3D) systems (organoids) (Eiraku et al., 2008; Kadoshima et al., 2013; Mariani et al., 2012). Earlier work had shown that organoids recapitulate morphogen gradients, cell polarity, layer formation, and other essential features of morphogenesis. Ultimately, there is a need to return to the in vivo environment, and a number of researchers discussed early work in transplanting human hiPSC neurons back into either fetal or adult mouse brains (chimeras), in order to track connectivity and systems-level functionality of these cells in vivo (Muotri et al., 2005), on the basis of early evidence that hESC-derived human neurons can cross-talk with mouse neurons.

Oliver Brüstle, from the University of Bonn, reported on several stable intermediate neural stem cell populations, which reflect different stages of CNS development and thus facilitate standardized generation of neurons and glia from human pluripotent stem cells (for review, see Karus et al., 2014). The latest addition to this assortment is radial glia-like neural stem cells, which, in contrast to developmentally earlier neural stem cell (NSC) populations, are

endowed with a stable regional identity and enable efficient and more rapid oligodendroglial differentiation (Gorris et al., 2015). Brüstle also gave an update on the StemCell-Factory project, an automated platform for parallelized industrial-scale cell reprogramming and neural differentiation (http://www.stemcellfactory.de/). He discussed several applications of PSC-derived NSCs. First, he presented recent comparisons of gamma secretase modulators, finding that amyloid precursor protein (APP) processing in hiPSC neurons is resistant to non-steroidal anti-inflammatory drug (NSAID)-based gamma-secretase modulation (Mertens et al., 2013). This is in contrast to results from transgenic cell lines and mouse models, indicating the need to validate compound efficacy directly in the human cell type affected by disease. Second, Brüstle developed an hiPSC-based model of the polyglutamine disorder Machado-Joseph disease (spinocerebellar ataxia type 3) to illustrate how the earliest steps in protein aggregation can be modeled in patient-derived cells (Koch et al., 2011). Aggregates of ataxin-3 were observed specifically in hiPSC-derived neurons, but not in primary patient fibroblasts, hiPSCs, or hiPSC-derived glial cells. His group's findings indicate that pronounced neuronal intranuclear inclusions are specific to neurons and help to explain the reason for neuron-specific degeneration in this disease. Finally, he also discussed latest developments in studying in vivo integration and connectivity phenotypes of transplanted iPSC-derived neurons with rabies-virus-based monosynaptic tracing and light sheet microscopy of whole-brain preparations.

Allison Ebert, from the Medical College of Wisconsin, described methods for generating astrocyte cultures of improved purity from hiPSCs. In contrasting other recent reports (Emdad et al., 2012; Krencik et al., 2011; Serio et al., 2013), she noted the lengthy duration of existing protocols, which required months to differentiate and expand astrocytes, and she reported on recent attempts to use magnetic activated cell sorting (MACS)-based methods, and even simple cellular passaging, to positively select for astrocyte fate within weeks. Despite some successes, she challenged the field to thoughtfully consider which type of astrocyte each protocol in fact yields and the relevance of these astrocytes to those occurring in vivo. Ebert closed by discussing recent findings from hiPSC astrocyte studies regarding the cell non-autonomous effects underlying reduced synaptic puncti in spinal muscular atrophy (SMA) hiPSC-derived motor neurons (Ebert et al., 2009; Sareen et al., 2012). SMA is a genetic childhood disease characterized by motor neuron loss that is believed to be due to a reduction in the amount of survival motor neuron (SMN) protein in motor neurons. She reported that astrocyte activation could be a non-cell-autonomous contributor to disease, as when *SMN* is reduced in hiPSC astrocytes and there is increased astrocyte reactivity, and that co-culture of neurons with SMA astrocytes leads to neuronal phenotype. Together, this work begins to answer why motor neurons are uniquely vulnerable in SMA when SMN is a ubiquitously expressed protein, as it may be that increased astrocyte reactivity ultimately leads to the reduced synaptic puncti observed in SMA hiPSC motor neurons.

Pierre Vanderhaeghen, from the University of Brussels, described efforts to generate defined cortical circuits from hiPSCs (Espuny-Camacho et al., 2013). Their differentiation methods seemed to closely mirror embryonic development, as hiPSCs differentiated first to cortical progenitors, then to pioneer neurons, then to deep layer pyramidal neurons, and finally to upper-layer pyramidal neurons. Although the human timeline was drastically extended, this same pattern was observed in both mouse (1-week) and human (3-month) cells (Nagashima et al., 2014). Using a 3D default differentiation protocol in Matrigel (3DDM differentiation), which yields spheres for analysis within 21 days, Vanderhaegen's group analyzed lines from subjects with autosomal recessive primary microcephaly (mutations in the *ASPM* gene) (also termed microcephaly primary hereditary [MCPH]). Just as *ASPM* mutations disrupt corticogenesis in the earliest stages, he reported increased neuronal differentiation, although with reduced cortical marker expression, as well as mitotic spindle deviations, in the mutant cells compared to controls. Such phenotypes were not detected in ASPM mutant mice, which display only mild microcephaly, suggesting that ASPM mechanisms of action may be in part species-specific, underscoring the importance of studying human health in human cells. Moreover, this impairment was not due to the hypothesized defect in proliferation but was more likely the result of perturbed cellular patterning, which could be corrected by applying WNT inhibitor; hence, these models can truly generate novel unexpected mechanistic insights. Finally, Vanderhaegen reported that PSC-derived cortical cells can be transplanted in neonatal mice, where human neurons develop normally but mature at a considerably slower pace than their mouse counterparts (over 9 months instead of 4 weeks), reminiscent of the neoteny that characterizes neuronal maturation in human cortex.

Madeline Lancaster, from the Institute of Molecular Biotechnology (IMBA) and the MRC Laboratory of Molecular Biology, discussed using cerebral organoids to examine pathogenesis of neurodevelopmental disorders (Lancaster et al., 2013). She noted the many advantages of these self-organizing 3D mixed cultures of human cells, including organized progenitor zones and sequential generation of neuronal layer identities. These organoids comprise radial glia progenitor cells and neurons with good cortical pyramidal morphology. Nonetheless, these

mixed cultures lack axis patterning, show high variability (line to line and batch to batch), and show a loss of neurons with extended differentiation. At their current state of development, organoid assays are likely ideal for studying disorders of neurodevelopment (particularly microencephaly), neurogenesis, and fate specification. Noting that microencephaly is not adequately modeled in rodents, Lancaster, in work performed in the lab of Juergen Knoblich, generated hiPSCs from a microencephaly patient with a null mutation in centrosomal protein *CDK5RAP2* (independent mutations at either allele). She observed a depleted progenitor population and premature neuronal differentiation, demonstrating the precision of this platform in resolving microencephalic phenotypes.

Using a similar strategy, Flora Vaccarino, from Yale University, described applying telencephalic organoids to model early developmental trajectories in autism spectrum disorders (ASD). She noted that human-based studies are critical, owing to fundamental differences in cortical development and timing between humans and mice. Concerns with hiPSCs remain, of course, particularly concerning the potential genetic instability of hiPSCs, which show an accumulation of mutations, tracing back in large part to the original fibroblast population: 30% of skin fibroblasts carry one to two large somatic copy number variants (CNVs), and there is wide variability in the frequency of different mosaic mutations among fibroblast cells (15%–0.3%) (Abyzov et al., 2012). Nonetheless, by applying a neuronal differentiation strategy based upon 3D cortical organoids, Vaccarino demonstrated patient-specific molecular and cellular phenotypes in ASD hiPSC-derived neurons. She reported a methodology for generating cortical organoids that are more homogeneous in structure, composed of repeating units of rosettes, and for which RNA sequencing comparison to the BrainSpan dataset revealed closest similarity to early fetal brain tissue. She cautioned that specific transcriptome differences exist between isogenic intact organoids and dissociated progenitors. Noting that an increase in brain and head size (i.e., macrocephaly) characterizes a subset of ASD patients with poorer outcome, Vaccarino described a study where organoids from patients were systematically compared to those from their fathers in transcriptomics and cellular phenotypes. She reported that ASD hiPSC-derived organoids show a complex cellular phenotype that includes decreased cell cycle length, upregulation of genes directing gamma-amino butyric acid (GABA) neuron fate, increased synaptogenesis and dendrite outgrowth, and changes in synaptic activity. Global gene co-expression network analysis of cortical organoids resolved a number of gene modules that were differentially expressed in ASD individuals, including one potentially driven by *FOXG1*, a master regulatory transcription factor that was greatly upregulated in ASD. Interestingly, knockdown of *FOXG1* in ASD-derived iPSCs normalized the shift in GABA phenotype in ASD cortical organoids, suggesting a potential causal pathway in the ASD GABAergic imbalance phenotype (Mariani et al., 2015).

Dimensions of Modeling

As the disease modeling field is developing both more reliable in vitro protocols for neural differentiation and more accurate phenotypical functional readouts, researchers are beginning to explore neurological diseases that have more complex etiologies. While highly penetrant monogenic disorders such as Rett and Fragile X syndromes remain among the most tractable areas for iPSC research, the majority of CNS diseases are multigenic, have incomplete penetrance, and are subject to significant environmental influences. One way to circumvent the variability in phenotypes is to stratify the population of patients. Selecting for specific clinical cohorts such as biologically relevant measures, i.e., the brain size phenotype, drug responsiveness, endophenotypes, or specific genetic cohorts containing specific genetic variations with clinical relevance, can provide valuable information toward patient-tailored biomarkers and therapies.

Carol Marchetto, from the Salk Institute of Biological Studies, extended her previous characterization of a monogenic form of ASD (Rett syndrome) (Marchetto et al., 2010) by recruiting a genetically heterogeneous cohort of patients with ASD, characterized by an endophenotype of transient macrocephaly, and comparing them to gender- and age-matched unrelated controls. ASD-derived neural progenitor cells (NPCs) display increased cell proliferation due to a dysregulation of a β-catenin/BRN2 transcriptional cascade, while ASD-derived neurons displayed premature differentiation, reduced synaptogenesis, and altered levels of excitatory and inhibitory neurotransmitters, leading to functional defects in neuronal networks, measured by multielectrode arrays. Interestingly, RNA analysis also revealed increased expression of *FOXG1* in ASD NPCs, in agreement with Flora Vaccarino's data in a completely independent set of experiments, suggesting that there may be common features in macrocephalic ASD and pointing to a potential target of therapeutic intervention.

Kristen Brennand, from the Icahn School of Medicine at Mount Sinai, spoke about the inherent value of modeling predisposition, rather than end-stage disease, in the context of schizophrenia (SZ), noting that gene expression patterns characteristic of SZ hiPSC neurons (Brennand et al., 2011) are conserved in SZ-hiPSC-derived NPCs (Brennand et al., 2015). She presented several phenotypical readouts that would be predictive for SZ predisposition in vitro, such as migration defects (Brennand et al., 2015), WNT signaling defects (Topol et al., 2015), and perturbations in

neuronal connectivity (Brennand et al., 2011) and activity (Yu et al., 2014). By studying the disease phenotype in vitro, she also gained some insight on the disease biology; through the analysis of global expression profiles from SZ-derived NPCs, she reported differential expression of genes and microRNAs related to the migration changes observed in vitro. Additionally, Brennand is working with patient families and a cohort of childhood-onset SZ patients to correlate SZ-related genetic mutations with gene expression levels.

Given the vast clinical heterogeneity of major mental illness, Akira Sawa, from John Hopkins University School of Medicine, advocated careful patient stratification when selecting cohorts for hiPSC-based disease modeling. He argued that traditional *Diagnostic and Statistical Manual of Mental Disorders (DSM-IV)* (American Psychiatric Association, 1994) diagnosis does not provide enough neurobiologically relevant information for patient recruitment for basic research and proposed that other criteria such as clinical longitudinal assessment, neuropsychology examination, brain imaging, and correlation between intermediate phenotypes and disease-related genetic polymorphisms should be considered. By screening olfactory NPCs obtained from a larger clinical cohort of patients with SZ and bipolar disorder (BD) with psychotic features, he identified those patients with reduced phosphorylation (pS713) of disrupted in schizophrenia 1 (DISC1), independent of clozapine treatment, and selected them for further hiPSC-based characterizations. Reduced (pS713) DISC1 phosphorylation was replicated in hiPSC neurons, and levels of p713-DISC1 correlated to neuropsychological and anatomical changes, highlighting the importance of patient stratification in complex neuropsychiatric diseases. He proposed that such clinical phenotype-based stratification of the subjects for hiPSC research could also be applied for unique subsets of SZ and mood disorders, such as psychotic depression and rapid-cycling BD.

Hongjun Song, from Johns Hopkins University School of Medicine, generated hiPSC-derived cortical neurons from four members of a SZ family pedigree defined by a deletion mutation of *DISC1* gene (4-base-pair frameshift deletion on exon 12) (Chiang et al., 2011), observing decreased excitatory postsynaptic current (EPSC) frequencies and synaptic vesicle protein 2 (SV2) puncta density in patients with the mutation, which were rescued by both transcription activator-like effector nucleases (TALEN)-mediated genetic correction (Wen et al., 2014). Subsequent RNA sequencing showed *DISC1*-associated changes in expression of genes involved in neuronal development, synaptic transmission, and those related to mental disorders. Complementary data obtained from genetically modified mice with this same *DISC1* mutation highlighted the continued value of mouse models to study the role of specific mutations independent of genetic background, as a means of cross-paradigm validation of results obtained with hiPSCs, at the levels of neuronal circuits and behavior, and for in vivo drug testing.

Eric Morrow, from Brown University, showed data from patients with a recently described condition termed Christianson syndrome (CS), a monogenetic X-linked disorder caused by mutations in the endosomal sodium/hydrogen exchanger 6 protein (*NHE6*) (Pescosolido et al., 2014). His laboratory has engineered iPSCs from peripheral blood mononuclear cells from patients with CS and their unaffected male siblings. His studies are investigating a variety of endosomal phenotypes in iPSC-derived neurons as well as cellular phenotypes related to abnormal neuronal differentiation. They are using these cellular assays as platforms to screen candidate treatments. His study emphasized several themes, including pursuing various paths to assemble control cells as well as using statistical methods on experiments on multiple mutations with different subclonal lines. Further, Morrow's studies capitalize on his access to patient clinical assessments, a mouse model, as well as iPSCs. Combining these in vivo studies with the in vitro iPSC studies may prove to be a powerful approach.

Frank Soldner, from the Whitehead Institute for Biomedical Research, having previously generated isogenic hiPSCs at two-point mutations in early-onset Parkinson's disease (PD) (Soldner et al., 2011), now presented studies on the penetrance of non-coding PD risk alleles. Meta-analysis of genome-wide association study (GWAS) data from 13,708 PD cases has identified 26 significant PD-associated loci; however, there is a lack of mechanistic insight in how such sequence variants functionally contribute to complex disease. Soldner proposed that functional disruption of distal enhancer elements leads to the deregulation of gene expression and confers susceptibility to PD. As a proof of principle to study the consequence of these mutations on gene expression, he conducted functional analysis of *cis*-regulatory elements in the *SNCA* locus via genome editing tools in order to precisely disrupt regulatory elements in isogenic pairs. He used quantitative allele-specific assays as readouts and showed that common single nucleotide polymorphisms (SNPs) with small effect size can contribute to PD risk. This work highlights the importance of correlating previously identified disease-related mutations (SNPs and CNVs) with changes in expression profile in vitro in order to identify functional disease-relevant risk variants and determine the mutation's impact.

Rick Livesey, from the Gurdon Institute, provided insights into mechanisms of Alzheimer's disease (AD) pathogenesis using human stem cell models (Shi et al., 2012). The cellular hallmarks of AD are the accumulation of amyloid precursor protein (APP) protein-derived Aβ peptide fragments and neurofibrillary tangles of the

microtubule-associated protein tau. Livesey described the characterization of hiPSC neurons derived from patients with different familial AD mutations in the APP gene or Presenilin1 (PSEN1), the enzymatic subunit of the γ-secretase complex that processes APP. All of the different mutations increased the release of pathogenic longer forms of Aβ peptides. However, while increased APP gene dosage and APP mutations all increased total and phosphorylated tau in neurons, PSEN1 mutations did not (Moore et al., 2015). Manipulating γ-secretase activity in human neurons, using available drugs, identified that APP processing is linked to regulating levels of tau protein, hinting that extracellular Aβ may not be the only process relevant to disease pathogenesis. His work proposes a cell-autonomous link between APP processing and tau.

Lorenz Studer, from Memorial Sloan-Kettering Cancer Center, described work modeling two rare human diseases, familial dysautonomia (FD) and Hirschsprung's disease (colonic aganglionosis). FD is a rare recessive disorder, occurring when a T → C point mutation leads to skipping of exon 20 in *iKBKAP/ELP1*. Deriving hiPSCs from patients with both severe (S1 and S2) and mild (M1 and M2) FD, he found that patient-derived hiPSC neurons clearly modeled clinical outcome; relative to unaffected controls, severe FD patients had difficulty generating BRN3A sensory neurons, whereas mild FD patients did not (sensory neurons from both classes of patients die within 28 days). To study Hirschsprung's disease, a fatal if untreated disease in which there is incomplete migration of the enteric nervous system, Studer described a differentiation protocol that successfully generates vagal and enteric neural crest from hESCs that express appropriate cell-type-specific BRN3A/ISL1 markers, produce slow wave activity in vitro, and properly innervate the colon when transplanted into mice (Chambers et al., 2013). hESC-derived $ENRB^{-/-}$ and $RET^{-/-}$ enteric neural crest cells showed reduced migration in vitro and in vivo. A high-throughput screening (HTS) assay for compounds that rescue these migration deficits identified Pepstatin A. Studer concluded by discussing the technical challenges in studying disorders that require cell types that require significant maturation and aging, some of which are potentially addressable through overexpression of progerin (Miller et al., 2013), as well as methods and assays under-development to address these challenges. For example, he described combining a method to rapidly differentiate cortical neurons with in vivo cell engraftment, in collaboration with Marc Tessier-Lavigne, to yield substantial morphological integration of neurons when imaged by iDISCO, a novel 3D immunohistological processing and imaging technique (Renier et al., 2014); this strategy will allow mapping of the connectivity of human neurons derived from patients with a variety of neurodevelopmental disorders.

Sally Temple, from the Neural Stem Cell Institute, has applied a robust hiPSC differentiation protocol to retinal pigment epithelium (RPE) to understand molecular mechanisms underlying age-related macular degeneration (AMD) (Stanzel et al., 2014), a highly prevalent neurodegenerative disease affecting one in five people older than age 75. A characteristic sign of the early, dry form of AMD is the appearance of large extracellular deposits termed drusen in the macula. Proteomic analysis has demonstrated that drusen share many molecular characteristics with senile plaques in AD. Observing significantly higher expression of AMD and drusen-associated transcripts, particularly Aβ42 and Aβ40, in AMD iPSC-RPE than in controls, the group took a candidate-based approach and identified several small molecules that reduce AMD-associated transcripts in iPSC-RPE, in some cases irrespective of original AMD disease status. These findings suggest that this in vitro model may be valuable to identify dry AMD therapeutics.

In aggregate, it has become obvious that by more accurately modeling human neurodevelopmental and neurodegenerative diseases in vitro, a number of insights into the cellular and molecular mechanisms underlying the disease state have already arisen. hiPSC-based platforms, combined with genome-scale analyses of sequence variations and transcripts, are increasingly facilitating studies of the temporal dynamics of human disease and allowing researchers to study human-specific elements of disease, asking when critical changes occur in the disease process. From insights into the mechanisms of tau changes in AD, to increased FOXG1 expression in two hiPSC cohorts of ASD, to the critical role of ASPN in microencephaly, cellular models are revealing convergent mechanisms underlying genetically heterogeneous neurological conditions.

Somatic Mosaicism

An emerging issue in the stem cell field is somatic mosaicism, the presence of DNA structural and/or sequence variation from cell to cell in a given individual. This raises interesting questions about not only the role of this form of cellular heterogeneity in health and disease but also the utility of any single patient-derived iPSC line in accurately representing that patient's disease state. Alysson Muotri, from University of California, San Diego, presented data on iPSC-derived neurons from patients with Aicardi-Goutieres syndrome (AGS), a neurodevelopmental disease characterized by intellectual and physical problems with neuroinflammation. Muotri made iPSCs from AGS patients with mutations on *TREX1* gene related to clearance of L1 mobile elements from the cytosol and compared them with isogenic controls. *TREX1*-mutant cells have high levels of single-stranded DNA (ssDNA) derived from mobile retroelements (Alus and L1s) in the cytoplasm and

decreased expression of neuronal markers TLG4, MAP2, TUJ1, and SYN. These features were partially rescued by treatment with reverse transcriptase inhibitors (such as anti-HIV drugs), indicating clinical relevance on this extreme neurological condition. Additionally, *TREX1*-deficient astrocytes also increased ssDNA and triggered an inflammatory response that affected neurons, suggesting a non-cell-autonomous inflammatory effect that may be contributing to neuronal loss in AGS. The *TREX1* mutation highlights the importance of human models, since mouse models for the disease don't present any neurological symptoms.

Mike McConnell, from University of Virginia School of Medicine, presented the use of hiPSC-based neurogenesis to study brain mosaicism (McConnell et al., 2013). His strategy is to perform single cell genomic sequencing. His data from primary brain showed that 45/110 human frontal cortex neurons had megabase-scale CNVs. Similarly, he detected similar levels of mosaic CNVs in hiPSC-derived neurons but very low levels of mosaicism in hiPSC-derived NPCs or human fibroblasts. These data suggest that some aspects of primary brain somatic mosaicism are recapitulated during hiPSC-based neurogenesis. His laboratory is currently defining the levels of genetic mosaicism in neuronal cultures to understand the impact of mosaicism on disease modeling. New data were presented using hiPSC-based neurogenesis to investigate the cause and consequence of brain somatic mosaicism.

It is increasingly clear that somatic mosaicism occurs in both post-mortem and hiPSC neurons. What remains to be determined is the precise extent of this phenomenon in the human brain, its mechanisms, and the precise role that mosaicism contributes to evolution, human behavior and disease, and even the "normal" physiological condition. Moving forward, future hiPSC experiments should be designed with a consideration of the existence of somatic mosaicism, incorporating (1) analysis of multiple iPSC lines per patient, (2) isogenic engineering, and (3) phenotypic rescue experiments.

Using hiPSCs for Drug Discovery

A major goal in the still nascent human stem cell field is to utilize improved cell-based assays in the service of small-molecule therapeutics discovery and virtual early-phase clinical trials. Ajamete Kaykas, from the Novartis Institute for BioMedical Research, discussed the pharmaceutical pipeline to identify phenotypes in human pluripotent stem cell (hPSC)-derived neurons. He demonstrated that in a non-academic setting, it is possible to establish a library of more than 100 transgene-free hiPSCs as well as a clustered regularly interspaced short palindromic repeats (CRISPR) pipeline to create and screen clones for indels, knockout, and point mutation via high-throughput sequencing methods. In parallel, his group has tested the feasibility of scaling both directed differentiation as well as NGN2-induction protocols into 384-well plate format for high-throughput screening. Overall, both a robust hPSC pipeline for hiPSC-based modeling as well as standardized and automated differentiation methods are being established at Novartis, in collaboration with the Stanley Center, for the characterization and drug screening of SZ patients.

Lee Rubin, from Harvard University, discussed the challenges and successes his laboratory has encountered, in the academic setting, while establishing hiPSC-based high-throughput drug screening for SMA. Given that there are three types of SMA, fatal within the first year of life (type 1), by the teenage years (type 2), and characterized by chronic immobility (type 3), Lee asked whether SMA is in fact one disease or three. To determine why motor neurons from some SMA patients are more sensitive than others, he generated hiPSCs from patients with all three types of SMA, observing that SMA iPSCs have an increased propensity to generate NPCs and a slightly decreased propensity to yield endoderm, consistent with clinical observations that children with SMA have other defects, particularly in endodermal and cardiac tissues. Compared to controls, SMA motor neurons show increased cell death, apoptotic station, reduced neuronal outgrowth, and decreased neuronal firing (SMA3 > SMA2 > SMA1), and regardless of diagnosis, non-motor neurons do not die. Lee conducted three high-throughput screens for compounds to prevent cell death in SMA (ES-derived motor neurons from SMN-deficient mice, SMA patient fibroblasts, and SMA hiPSC-derived motor neurons). Unbiased screens in mouse motor neurons, human motor neurons, and human fibroblasts identified many compounds that increased SMN levels, only some of which overlapped between platforms: while some compounds that block SMN degradation were hits in all three screens, proteasome inhibitors were found in the fibroblast screen but proved toxic to motor neurons (MNs). On the basis of high content imaging data generated through the various screens, his group also observed that at the level of single cells, whether from control or SMA hiPSCs, there is cell-to-cell variation in SMN levels; individual cells with high SMN are the fittest and survive better than neighboring cells with lower SMN, implying that SMN is a general regulator of motor neuron survival, likely owing to reducing activation of the endoplasmic reticulum (ER) stress response. Moreover, inhibitors of the degradation process do not promote survival of SMN neurons below a defined basal level but shift the distribution of SMN, producing more neurons with levels that support survival. On the other hand, compounds that reduce ER stress don't affect SMN levels at all but still promote motor neuron survival. Lee summarized problems

that arise in high-throughput screening of hiPSC-derived cells as those arising due to issues of neuronal variability, immaturity, and non-cell-autonomous disease-relevant interactions.

In discussions among attendees, it became apparent that pharmaceutical and academic scientists approach drug discovery with different perspectives. Traditionally, most academics seek to test the cell type most relevant to disease, pursuing a candidate-based approach to test effects on phenotypes, whereas industry scientists have historically conducted high-throughput screens on entrenched industry-standard screening cell lines using target-based assays. While academics have typically been willing to develop more "risky" assays, the strengths of pharma have historically been in assay selection, scalability, and optimization, as well as drug chemistry and target optimization. Now, research strategies are converging, and both types of researchers are moving toward hiPSC-based screening platforms, drifting toward a hybrid model of testing medium-throughput libraries, screening ~30,000 compound libraries with known targets. New collaborations between academic and pharma researchers promise a future of parallel screening for both targets and phenotypes. Additional hurdles will be encountered if academics are to be the new drivers of drug discovery, including replication (across platforms/reproducibility across sites), documentation (to the rigor of record keeping in industry), and investments to increase automation.

Perspectives and Summary

In line with many of these themes, David Panchision, from the National Institute of Mental Health (NIMH), discussed recent funding initiatives to facilitate cell-based research on mental illness, including those supporting technology development and academic-industry partnerships for developing validated assays. He solicited feedback on NIMH priorities for advancing the field, which involve investigators working together to: (1) implement centralized sharing of patient and reference cell lines with genetic and clinical data, such as through the NIMH Repository and Genomics Resource (https://www.nimhgenetics.org/); (2) arrive at common cell-line quality control methods and standards for validating hiPSCs and differentiated cell types; (3) keep improving hiPSC-based technology, including developing easier and quicker targeting methods, optimizing the fidelity of "in vivo" surrogate assays like chimeras and organoids, improving assay miniaturization, and scaling up to increase the number of individuals who can be contrasted by these strategies; (4) focus on robustness and reproducibility, which can include studying genetic variants of large effect from fully characterized patients and maintaining consistency and transparency in protocols/samples across labs; and (5) remain mindful of the critical value of collaboration and training and supporting the rapid dissemination of best practices (Panchision, 2013).

There was agreement that, although it was important to maximize the rapid sharing and adoption of resources/methods for patient-based disease studies, it was critical that this be balanced with the need for innovation at this early stage in the field. For example, although reprogramming technologies had advanced tremendously, some participants cautioned funding organizations to not restrict iPSC production to a single method or provider, since questions still remained about best practices. Additionally, analysis of specific biological processes or disorders may benefit from tailored cell derivation technologies (e.g., parthenogenesis), stem cell patterning (e.g., naive versus primed hiPSCs), and strategies for genetic manipulation (e.g., CRISPR-Cas9 versus TALEN).

The meeting highlighted the diverse array of cell-based approaches that are being pursued to study human biology and disease, including those (e.g., somatic mosaicism) that illustrated the possibilities and potential limitations of these technologies. Our group was heartened that we are seeing clear disease-related phenotypes in the dish, giving some confidence that discoveries (such as those reflecting early stages in disease processes) would be clinically relevant. Moreover, as such discoveries are being made, unexpected findings are emerging, but the convergence and reproduction among labs improve our group's optimism that these are robust results and that human cells will be a powerful tool in the therapeutic development armament. Moving forward, a critical application of hiPSC-based studies will be in providing a platform for defining the cellular, molecular, and genetic mechanisms of disease risk, which will be an essential first step toward target discovery. Toward this goal, the case studies discussed demonstrated that different assay systems could yield a surprising convergence of phenotypes, leading to some optimism that the considerable remaining technical challenges to modeling disease are still surmountable.

AUTHOR CONTRIBUTIONS

All authors contributed to the writing of this report.

REFERENCES

Abyzov, A., Mariani, J., Palejev, D., Zhang, Y., Haney, M.S., Tomasini, L., Ferrandino, A.F., Rosenberg Belmaker, L.A., Szekely, A., Wilson, M., et al. (2012). Somatic copy number mosaicism in human skin revealed by induced pluripotent stem cells. Nature *492*, 438–442.

Adamo, A., Atashpaz, S., Germain, P.L., Zanella, M., D'Agostino, G., Albertin, V., Chenoweth, J., Micale, L., Fusco, C., Unger, C., et al. (2015). 7q11.23 dosage-dependent dysregulation in human

pluripotent stem cells affects transcriptional programs in disease-relevant lineages. Nat. Genet. *47*, 132–141.

American Psychiatric Association. (1994). Diagnostic and Statistical Manual of Mental Disorders: DSM-IV, Fourth Edition (American Psychiatric Press).

Benevento, M., Tonge, P.D., Puri, M.C., Hussein, S.M., Cloonan, N., Wood, D.L., Grimmond, S.M., Nagy, A., Munoz, J., and Heck, A.J. (2014). Proteome adaptation in cell reprogramming proceeds via distinct transcriptional networks. Nat. Commun. *5*, 5613.

Brennand, K.J., Simone, A., Jou, J., Gelboin-Burkhart, C., Tran, N., Sangar, S., Li, Y., Mu, Y., Chen, G., Yu, D., et al. (2011). Modelling schizophrenia using human induced pluripotent stem cells. Nature *473*, 221–225.

Brennand, K., Savas, J.N., Kim, Y., Tran, N., Simone, A., Hashimoto-Torii, K., Beaumont, K.G., Kim, H.J., Topol, A., Ladran, I., et al. (2015). Phenotypic differences in hiPSC NPCs derived from patients with schizophrenia. Mol. Psychiatry *20*, 361–368.

Brons, I.G., Smithers, L.E., Trotter, M.W., Rugg-Gunn, P., Sun, B., Chuva de Sousa Lopes, S.M., Howlett, S.K., Clarkson, A., Ahrlund-Richter, L., Pedersen, R.A., and Vallier, L. (2007). Derivation of pluripotent epiblast stem cells from mammalian embryos. Nature *448*, 191–195.

Chambers, S.M., Mica, Y., Lee, G., Studer, L., and Tomishima, M.J. (2013). Dual-SMAD inhibition/WNT activation-based methods to induce neural crest and derivatives from human pluripotent stem cells. Methods Mol. Biol. *1307*, 329–343.

Chan, Y.S., Göke, J., Ng, J.H., Lu, X., Gonzales, K.A., Tan, C.P., Tng, W.Q., Hong, Z.Z., Lim, Y.S., and Ng, H.H. (2013). Induction of a human pluripotent state with distinct regulatory circuitry that resembles preimplantation epiblast. Cell Stem Cell *13*, 663–675.

Chen, K.G., Mallon, B.S., Johnson, K.R., Hamilton, R.S., McKay, R.D., and Robey, P.G. (2014). Developmental insights from early mammalian embryos and core signaling pathways that influence human pluripotent cell growth and differentiation. Stem Cell Res. (Amst.) *12*, 610–621.

Chiang, C.H., Su, Y., Wen, Z., Yoritomo, N., Ross, C.A., Margolis, R.L., Song, H., and Ming, G.L. (2011). Integration-free induced pluripotent stem cells derived from schizophrenia patients with a DISC1 mutation. Mol. Psychiatry *16*, 358–360.

Clancy, J.L., Patel, H.R., Hussein, S.M., Tonge, P.D., Cloonan, N., Corso, A.J., Li, M., Lee, D.S., Shin, J.Y., Wong, J.J., et al. (2014). Small RNA changes en route to distinct cellular states of induced pluripotency. Nat. Commun. *5*, 5522.

Ebert, A.D., Yu, J., Rose, F.F., Jr., Mattis, V.B., Lorson, C.L., Thomson, J.A., and Svendsen, C.N. (2009). Induced pluripotent stem cells from a spinal muscular atrophy patient. Nature *457*, 277–280.

Eglen, R., and Reisine, T. (2011). Primary cells and stem cells in drug discovery: emerging tools for high-throughput screening. Assay Drug Dev. Technol. *9*, 108–124.

Eiraku, M., Watanabe, K., Matsuo-Takasaki, M., Kawada, M., Yonemura, S., Matsumura, M., Wataya, T., Nishiyama, A., Muguruma, K., and Sasai, Y. (2008). Self-organized formation of polarized cortical tissues from ESCs and its active manipulation by extrinsic signals. Cell Stem Cell *3*, 519–532.

Emdad, L., D'Souza, S.L., Kothari, H.P., Qadeer, Z.A., and Germano, I.M. (2012). Efficient differentiation of human embryonic and induced pluripotent stem cells into functional astrocytes. Stem Cells Dev. *21*, 404–410.

Espuny-Camacho, I., Michelsen, K.A., Gall, D., Linaro, D., Hasche, A., Bonnefont, J., Bali, C., Orduz, D., Bilheu, A., Herpoel, A., et al. (2013). Pyramidal neurons derived from human pluripotent stem cells integrate efficiently into mouse brain circuits in vivo. Neuron *77*, 440–456.

Gafni, O., Weinberger, L., Mansour, A.A., Manor, Y.S., Chomsky, E., Ben-Yosef, D., Kalma, Y., Viukov, S., Maza, I., Zviran, A., et al. (2013). Derivation of novel human ground state naive pluripotent stem cells. Nature *504*, 282–286.

Gorris, R., Fischer, J., Erwes, K.L., Kesavan, J., Peterson, D.A., Alexander, M., Nöthen, M.M., Peitz, M., Quandel, T., Karus, M., and Brüstle, O. (2015). Pluripotent stem cell-derived radial glia-like cells as stable intermediate for efficient generation of human oligodendrocytes. Glia *63*, 2152–2167.

Kadoshima, T., Sakaguchi, H., Nakano, T., Soen, M., Ando, S., Eiraku, M., and Sasai, Y. (2013). Self-organization of axial polarity, inside-out layer pattern, and species-specific progenitor dynamics in human ES cell-derived neocortex. Proc. Natl. Acad. Sci. USA *110*, 20284–20289.

Karus, M., Blaess, S., and Brüstle, O. (2014). Self-organization of neural tissue architectures from pluripotent stem cells. J. Comp. Neurol. *522*, 2831–2844.

Koch, P., Breuer, P., Peitz, M., Jungverdorben, J., Kesavan, J., Poppe, D., Doerr, J., Ladewig, J., Mertens, J., Tüting, T., et al. (2011). Excitation-induced ataxin-3 aggregation in neurons from patients with Machado-Joseph disease. Nature *480*, 543–546.

Krencik, R., Weick, J.P., Liu, Y., Zhang, Z.J., and Zhang, S.C. (2011). Specification of transplantable astroglial subtypes from human pluripotent stem cells. Nat. Biotechnol. *29*, 528–534.

Lancaster, M.A., Renner, M., Martin, C.A., Wenzel, D., Bicknell, L.S., Hurles, M.E., Homfray, T., Penninger, J.M., Jackson, A.P., and Knoblich, J.A. (2013). Cerebral organoids model human brain development and microcephaly. Nature *501*, 373–379.

Lee, D.S., Shin, J.Y., Tonge, P.D., Puri, M.C., Lee, S., Park, H., Lee, W.C., Hussein, S.M., Bleazard, T., Yun, J.Y., et al. (2014). An epigenomic roadmap to induced pluripotency reveals DNA methylation as a reprogramming modulator. Nat. Commun. *5*, 5619.

Marchetto, M.C., Carromeu, C., Acab, A., Yu, D., Yeo, G.W., Mu, Y., Chen, G., Gage, F.H., and Muotri, A.R. (2010). A model for neural development and treatment of Rett syndrome using human induced pluripotent stem cells. Cell *143*, 527–539.

Mariani, J., Simonini, M.V., Palejev, D., Tomasini, L., Coppola, G., Szekely, A.M., Horvath, T.L., and Vaccarino, F.M. (2012). Modeling human cortical development in vitro using induced pluripotent stem cells. Proc. Natl. Acad. Sci. USA *109*, 12770–12775.

Mariani, J., Coppola, G., Zhang, P., Abyzov, A., Provini, L., Tomasini, L., Amenduni, M., Szekely, A., Palejev, D., Wilson, M., et al. (2015). FOXG1-Dependent Dysregulation of GABA/Glutamate Neuron Differentiation in Autism Spectrum Disorders. Cell *162*, 375–390.

Marinho, P.A., Chailangkarn, T., and Muotri, A.R. (2015). Systematic optimization of human pluripotent stem cells media using Design of Experiments. Sci. Rep. *5*, 9834.

Marks, H., Kalkan, T., Menafra, R., Denissov, S., Jones, K., Hofemeister, H., Nichols, J., Kranz, A., Stewart, A.F., Smith, A., and Stunnenberg, H.G. (2012). The transcriptional and epigenomic foundations of ground state pluripotency. Cell *149*, 590–604.

McConnell, M.J., Lindberg, M.R., Brennand, K.J., Piper, J.C., Voet, T., Cowing-Zitron, C., Shumilina, S., Lasken, R.S., Vermeesch, J.R., Hall, I.M., and Gage, F.H. (2013). Mosaic copy number variation in human neurons. Science *342*, 632–637.

Mertens, J., Stüber, K., Wunderlich, P., Ladewig, J., Kesavan, J.C., Vandenberghe, R., Vandenbulcke, M., van Damme, P., Walter, J., Brüstle, O., and Koch, P. (2013). APP processing in human pluripotent stem cell-derived neurons is resistant to NSAID-based γ-secretase modulation. Stem Cell Reports *1*, 491–498.

Miller, J.D., Ganat, Y.M., Kishinevsky, S., Bowman, R.L., Liu, B., Tu, E.Y., Mandal, P.K., Vera, E., Shim, J.W., Kriks, S., et al. (2013). Human iPSC-based modeling of late-onset disease via progerin-induced aging. Cell Stem Cell *13*, 691–705.

Moore, S., Evans, L.D., Andersson, T., Portelius, E., Smith, J., Dias, T.B., Saurat, N., McGlade, A., Kirwan, P., Blennow, K., et al. (2015). APP metabolism regulates tau proteostasis in human cerebral cortex neurons. Cell Rep. *11*, 689–696.

Mullard, A. (2015). 2014 FDA drug approvals. Nat. Rev. Drug Discov. *14*, 77–81.

Muotri, A.R., Nakashima, K., Toni, N., Sandler, V.M., and Gage, F.H. (2005). Development of functional human embryonic stem cell-derived neurons in mouse brain. Proc. Natl. Acad. Sci. USA *102*, 18644–18648.

Nagashima, F., Suzuki, I.K., Shitamukai, A., Sakaguchi, H., Iwashita, M., Kobayashi, T., Tone, S., Toida, K., Vanderhaeghen, P., and Kosodo, Y. (2014). Novel and robust transplantation reveals the acquisition of polarized processes by cortical cells derived from mouse and human pluripotent stem cells. Stem Cells Dev. *23*, 2129–2142.

Panchision, D.M. (2013). Meeting report: using stem cells for biological and therapeutics discovery in mental illness, April 2012. Stem Cells Transl. Med. *2*, 217–222.

Pescosolido, M.F., Stein, D.M., Schmidt, M., El Achkar, C.M., Sabbagh, M., Rogg, J.M., Tantravahi, U., McLean, R.L., Liu, J.S., Poduri, A., and Morrow, E.M. (2014). Genetic and phenotypic diversity of NHE6 mutations in Christianson syndrome. Ann. Neurol. *76*, 581–593.

Pouton, C.W., and Haynes, J.M. (2005). Pharmaceutical applications of embryonic stem cells. Adv. Drug Deliv. Rev. *57*, 1918–1934.

Renier, N., Wu, Z., Simon, D.J., Yang, J., Ariel, P., and Tessier-Lavigne, M. (2014). iDISCO: a simple, rapid method to immunolabel large tissue samples for volume imaging. Cell *159*, 896–910.

Sareen, D., Ebert, A.D., Heins, B.M., McGivern, J.V., Ornelas, L., and Svendsen, C.N. (2012). Inhibition of apoptosis blocks human motor neuron cell death in a stem cell model of spinal muscular atrophy. PLoS ONE *7*, e39113.

Scannell, J.W., Blanckley, A., Boldon, H., and Warrington, B. (2012). Diagnosing the decline in pharmaceutical R&D efficiency. Nat. Rev. Drug Discov. *11*, 191–200.

Serio, A., Bilican, B., Barmada, S.J., Ando, D.M., Zhao, C., Siller, R., Burr, K., Haghi, G., Story, D., Nishimura, A.L., et al. (2013). Astrocyte pathology and the absence of non-cell autonomy in an induced pluripotent stem cell model of TDP-43 proteinopathy. Proc. Natl. Acad. Sci. USA *110*, 4697–4702.

Shi, Y., Kirwan, P., Smith, J., MacLean, G., Orkin, S.H., and Livesey, F.J. (2012). A human stem cell model of early Alzheimer's disease pathology in Down syndrome. Sci. Transl. Med. *4*, 124ra29.

Soldner, F., Laganière, J., Cheng, A.W., Hockemeyer, D., Gao, Q., Alagappan, R., Khurana, V., Golbe, L.I., Myers, R.H., Lindquist, S., et al. (2011). Generation of isogenic pluripotent stem cells differing exclusively at two early onset Parkinson point mutations. Cell *146*, 318–331.

Stadtfeld, M., and Hochedlinger, K. (2010). Induced pluripotency: history, mechanisms, and applications. Genes Dev. *24*, 2239–2263.

Stanzel, B.V., Liu, Z., Somboonthanakij, S., Wongsawad, W., Brinken, R., Eter, N., Corneo, B., Holz, F.G., Temple, S., Stern, J.H., and Blenkinsop, T.A. (2014). Human RPE stem cells grown into polarized RPE monolayers on a polyester matrix are maintained after grafting into rabbit subretinal space. Stem Cell Reports *2*, 64–77.

Stelzer, Y., Yanuka, O., and Benvenisty, N. (2011). Global analysis of parental imprinting in human parthenogenetic induced pluripotent stem cells. Nat. Struct. Mol. Biol. *18*, 735–741.

Stelzer, Y., Sagi, I., Yanuka, O., Eiges, R., and Benvenisty, N. (2014). The noncoding RNA IPW regulates the imprinted DLK1-DIO3 locus in an induced pluripotent stem cell model of Prader-Willi syndrome. Nat. Genet. *46*, 551–557.

Stelzer, Y., Bar, S., Bartok, O., Afik, S., Ronen, D., Kadener, S., and Benvenisty, N. (2015). Differentiation of human parthenogenetic pluripotent stem cells reveals multiple tissue- and isoform-specific imprinted transcripts. Cell Rep. *11*, 308–320.

Takahashi, K., Tanabe, K., Ohnuki, M., Narita, M., Ichisaka, T., Tomoda, K., and Yamanaka, S. (2007). Induction of pluripotent stem cells from adult human fibroblasts by defined factors. Cell *131*, 861–872.

Takashima, Y., Guo, G., Loos, R., Nichols, J., Ficz, G., Krueger, F., Oxley, D., Santos, F., Clarke, J., Mansfield, W., et al. (2014). Resetting transcription factor control circuitry toward ground-state pluripotency in human. Cell *158*, 1254–1269.

Theunissen, T.W., Powell, B.E., Wang, H., Mitalipova, M., Faddah, D.A., Reddy, J., Fan, Z.P., Maetzel, D., Ganz, K., Shi, L., et al. (2014). Systematic identification of culture conditions for induction and maintenance of naive human pluripotency. Cell Stem Cell *15*, 471–487.

Tonge, P.D., Corso, A.J., Monetti, C., Hussein, S.M., Puri, M.C., Michael, I.P., Li, M., Lee, D.S., Mar, J.C., Cloonan, N., et al. (2014). Divergent reprogramming routes lead to alternative stem-cell states. Nature *516*, 192–197.

Topol, A., Zhu, S., Tran, N., Simone, A., Fang, G., and Brennand, K. (2015). Altered WNT signaling human induced pluripotent stem

cell neural progenitor cells derived from four schizophrenia patients. Biol. Psychiatry *78*, e29–e34.

Valamehr, B., Robinson, M., Abujarour, R., Rezner, B., Vranceanu, F., Le, T., Medcalf, A., Lee, T.T., Fitch, M., Robbins, D., and Flynn, P. (2014). Platform for induction and maintenance of transgene-free hiPSCs resembling ground state pluripotent stem cells. Stem Cell Reports *2*, 366–381.

Ware, C.B., Nelson, A.M., Mecham, B., Hesson, J., Zhou, W., Jonlin, E.C., Jimenez-Caliani, A.J., Deng, X., Cavanaugh, C., Cook, S., et al. (2014). Derivation of naive human embryonic stem cells. Proc. Natl. Acad. Sci. USA *111*, 4484–4489.

Wen, Z., Nguyen, H.N., Guo, Z., Lalli, M.A., Wang, X., Su, Y., Kim, N.S., Yoon, K.J., Shin, J., Zhang, C., et al. (2014). Synaptic dysregulation in a human iPS cell model of mental disorders. Nature *515*, 414–418.

Wu, J., Okamura, D., Li, M., Suzuki, K., Luo, C., Ma, L., He, Y., Li, Z., Benner, C., Tamura, I., et al. (2015). An alternative pluripotent state confers interspecies chimaeric competency. Nature *521*, 316–321.

Ying, Q.L., Wray, J., Nichols, J., Batlle-Morera, L., Doble, B., Woodgett, J., Cohen, P., and Smith, A. (2008). The ground state of embryonic stem cell self-renewal. Nature *453*, 519–523.

Yu, D.X., Di Giorgio, F.P., Yao, J., Marchetto, M.C., Brennand, K., Wright, R., Mei, A., McHenry, L., Lisuk, D., Grasmick, J.M., et al. (2014). Modeling hippocampal neurogenesis using human pluripotent stem cells. Stem Cell Reports *2*, 295–310.

Stem Cell Reports
Article

ISSCR

OPEN ACCESS

Lysophosphatidic Acid Receptor Is a Functional Marker of Adult Hippocampal Precursor Cells

Tara L. Walker,[1] Rupert W. Overall,[1] Steffen Vogler,[2] Alex M. Sykes,[3] Susann Ruhwald,[1] Daniela Lasse,[2] Muhammad Ichwan,[1] Klaus Fabel,[1,2] and Gerd Kempermann[1,2,*]

[1]CRTD – Center for Regenerative Therapies Dresden, Technische Universität Dresden, Dresden 01307, Germany
[2]German Center for Neurodegenerative Diseases (DZNE) Dresden, Dresden 01307, Germany
[3]Max Planck Institute for Molecular Cell Biology and Genetics, Dresden 01307, Germany
*Correspondence: gerd.kempermann@crt-dresden.de
http://dx.doi.org/10.1016/j.stemcr.2016.03.002

SUMMARY

Here, we show that the lysophosphatidic acid receptor 1 (LPA_1) is expressed by a defined population of type 1 stem cells and type 2a precursor cells in the adult mouse dentate gyrus. LPA_1, in contrast to Nestin, also marks the quiescent stem cell population. Combining LPA_1-GFP with EGFR and prominin-1 expression, we have enabled the prospective separation of both proliferative and non-proliferative precursor cell populations. Transcriptional profiling of the isolated proliferative precursor cells suggested immune mechanisms and cytokine signaling as molecular regulators of adult hippocampal precursor cell proliferation. In addition to LPA_1 being a marker of this important stem cell population, we also show that the corresponding ligand LPA is directly involved in the regulation of adult hippocampal precursor cell proliferation and neurogenesis, an effect that can be attributed to LPA signaling via the AKT and MAPK pathways.

INTRODUCTION

Neurogenesis in the adult mouse hippocampus has by now been very well characterized; however, despite considerable effort, the identification and isolation of the underlying neural stem cells has been hampered by the lack of appropriate markers. Nestin is the most widely used marker of the stem cell population in the adult dentate gyrus and subventricular zone (SVZ). However, in Nestin-GFP transgenic mice the GFP expression is not restricted to the neural stem cells (Kawaguchi et al., 2001; Mignone et al., 2004). Nestin-GFP expression can also be found in immature neurons and when cultured in vitro as neurospheresf, only 0.4% of cells formed neurospheres (Mignone et al., 2004). SOX2 is another widely used stem cell marker, but its cell-type specificity is also not sufficient for many concerns. A large fraction of classical astrocytes ($S100\beta^+$), for example, expresses SOX2 (Couillard-Despres et al., 2006; Suh et al., 2007), with a recent study showing that approximately 30% of all SOX2-GFP^+ cells in the dentate gyrus are positive for S100β, a marker that is not expressed by the stem cells (Bracko et al., 2012). While several workable hippocampal stem cell isolation protocols have been proposed (Jhaveri et al., 2010; Walker et al., 2007, 2013), there is agreement in the field that there is still much room for further improvement.

Based on its expression pattern, we identified the lysophosphatidic acid receptor 1 (LPA_1)-GFP transgenic mouse as a potential tool for the isolation of adult hippocampal stem cells (Heintz, 2004). The importance of lipid metabolism in neural stem cell biology was highlighted with the identification of a direct function of lipid signaling in stem cell-based neural plasticity. The key enzyme for de novo lipidogenesis, fatty acid synthase (FASN), is not only active in neural stem cells, but its inhibition also impairs adult hippocampal neurogenesis (Knobloch et al., 2013). Among the potential lipid-based regulatory molecules, phospholipids are the primary candidates. Phospholipids are found in large amounts in the brain as the key components of the cellular lipid bilayer. Lysophosphatidic acid (LPA) is a membrane-synthesized phospholipid that acts as an intercellular signaling molecule through six G-protein receptor subtypes (LPA_{1-6}; Choi et al., 2010). The first of these receptors to be described, LPA_1, mediates the proliferation, migration, and survival of neural progenitor cells during development (Estivill-Torrus et al., 2008). There have also been reports that LPA_1 deletion reduces adult hippocampal neurogenesis (Matas-Rico et al., 2008) and causes spatial memory deficits (Castilla-Ortega et al., 2011; Santin et al., 2009). These findings suggested to us that LPA_1 might play a functional role in adult hippocampal neurogenesis. In addition, the nature of LPA_1 as a surface receptor made it a potential candidate for the prospective isolation of hippocampal precursor cells.

Given the possible functional links between LPA_1 and adult neurogenesis, we undertook the present study to determine whether the receptor LPA_1 might indeed serve as a marker for the identification and prospective isolation of adult hippocampal stem cells and whether its ligand, the phospholipid LPA, might exert specific pro-neurogenic effects.

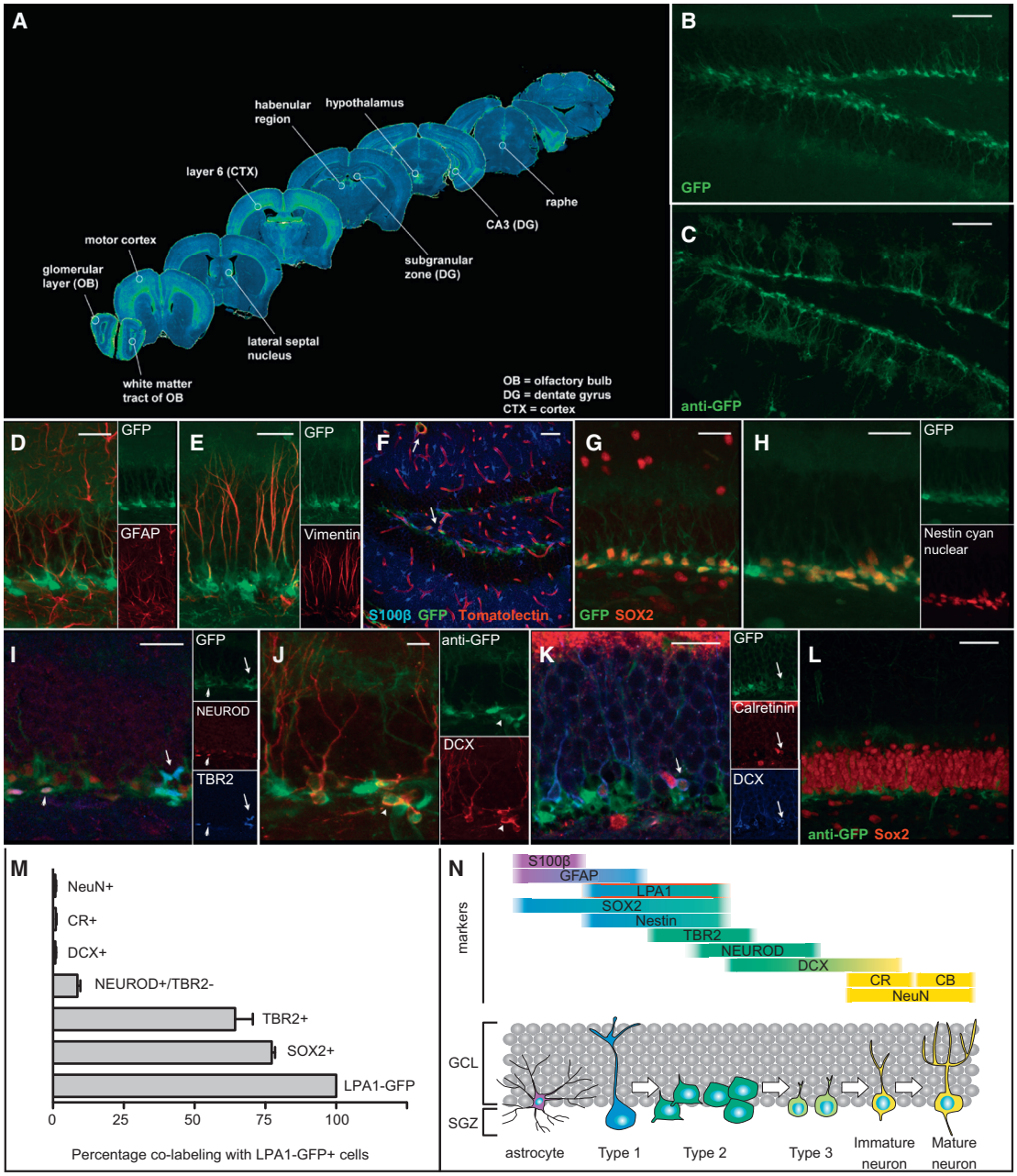

Figure 1. LPA_1-GFP Is Expressed in the Precursor Cells of the Adult Dentate Gyrus

(A–E) GFP^+ cells in the adult brain are detected in various brain regions (A) including the adult dentate gyrus (B). The GFP signal in the dentate gyrus resembles that in the Nestin-GFP mouse (C); however, the processes of the radial-glia-like stem cells show less prominent GFP immunofluorescence (D). The processes of some LPA_1-GFP^+ cells (green) co-express GFAP (red) and vimentin (red, E).

(F–L) We could not detect co-localization of LPA_1-GFP with S-100β (F, blue) in the dentate gyrus. LPA_1-GFP rarely co-localized with tomato lectin-stained blood vessels (F, red, arrows). Abundant co-localization of SOX2 (red) and GFP (green) is observed (G). (H) Linear unmixing of LPA_1-GFP (green) and Nestin-cyan nuclear (red) shows almost complete overlap in the progenitors in the SGZ. (I) GFP^+ cells in the dentate gyrus express TBR2 (blue, arrow) and several cells express GFP, TBR2, and NeuroD (red, arrowhead). Very few cells are DCX^+ and GFP^+ (J [red, arrowheads] and K [blue, arrow]). In general, GFP^+ cells (G, green) do not express NeuN (L, red) or calretinin (K, red). Double-positive cells were very rarely found (K).

(legend continued on next page)

RESULTS

LPA_1 Is Expressed by Radial-Glia-like Precursor Cells of the Adult Dentate Gyrus but Shows Limited Expression in the SVZ

Using the LPA_1-GFP reporter mouse line (Gong et al., 2003), we first mapped LPA_1-GFP expression along the entire ventral-dorsal axis of the adult brain (Figures 1A and S1). LPA_1-GFP expression was detected in the subgranular zone (SGZ) of the dentate gyrus (Figure 1B) and very closely resembled the characteristic Nestin-GFP signal (Figure 1; Yamaguchi et al., 2000). Glial fibrillary acidic protein (GFAP) immunofluorescence revealed co-localization in the processes of $GFAP^+$ and LPA_1-GFP^+ cells in the SGZ (Figure 1D), indicating that they are radial-glia-like type 1 cells (Kempermann et al., 2004). This was confirmed by staining for another astrocytic marker, vimentin (Figure 1E). No co-localization of LPA_1-GFP^+ was detected with S100β, a marker of post-mitotic astrocytes in the murine hippocampus (Figure 1F). As expected, there was significant overlap in expression between LPA_1 and the precursor marker Sox2 (77.25% ± 1.2%; Figure 1G). Crossing LPA_1-GFP mice with nuclear Nestin-Cyan mice (Encinas and Enikolopov, 2008) revealed that almost all GFP^+ cells were also $Cyan^+$ (Figure 1H). The majority of LPA_1-GFP^+ cells were early progenitors (LPA_1-GFP^+Tbr2^+: 64.5% ± 6.3%; Figure 1; Hodge et al., 2008). LPA_1-GFP^+ expression also identified a fraction of type 2b cells (LPA_1-$GFP^+NeuroD^+Tbr2^-$: 4.3% ± 0.1%). Only very few LPA_1-GFP^+ cells co-expressed doublecortin (DCX) (0.9% ± 0.2%; Figures 1J and 1K) or NeuN (0.9% ± 0.2%; Figure 1L) and calretinin (0.1% ± 0.1%; Figure 1K). Outside the dentate gyrus, LPA_1-GFP^+ expression was not restricted to precursor cells (Figure S2). These data indicate that LPA_1 in the dentate gyrus is a specific marker of type 1 stem cells and early progenitor cells.

LPA_1-GFP Mice Can Be Used to Directly Quantify the Exercise-Induced Increase in Precursor Proliferation

To determine whether LPA_1-GFP mice could be used to directly detect in vivo changes in precursor cell numbers, we used the physical activity paradigm (van Praag et al., 1999). Quantification of bromodeoxyuridine (BrdU)-labeled cells revealed the expected increase in proliferation following physical activity (standard housing 2,977 ± 162.8 $BrdU^+$ cells, n = 11 mice versus running 4,869 ± 475.8 $BrdU^+$ cells, n = 12 mice, p = 0.0016; Figures 2B and 2C). Similarly this could be directly quantified by counting LPA_1-GFP^+ cells (standard housing 7,176 ± 512 LPA_1-GFP^+ cells, n = 11 mice versus running 10,220 ± 562.9 LPA_1-GFP^+ cells, n = 12 mice, p = 0.0007; Figures 2D and 2E). The running-induced increase in proliferation could also be directly detected by flow cytometric quantification of LPA_1-GFP^+ cells (Figures 2F–2H: standard housing 14.2% ± 0.7%, n = 4 mice versus running 20.4% ± 1.7%, n = 4 mice, p = 0.0142), thus confirming that LPA_1-GFP mice are a useful tool to directly detect in vivo changes in hippocampal precursor proliferation.

Sorting LPA_1-GFP^+ Cells Allows the Prospective Isolation of Hippocampal Precursor Cells

Given that we could detect LPA_1-GFP expression in the precursor cells of the adult DG by immunofluorescence, we next examined whether we could prospectively isolate hippocampal precursor cells on the basis of LPA_1-GFP expression. Firstly, the baseline precursor frequency of unfractionated cells, gating only on forward and side scatter and propidium iodide (live cells), was determined (2.4 ± 1.3 neurospheres per 1,000 total cells). Sorting on the basis of LPA_1-GFP expression enhanced the frequency of precursor cells to 19.9 ± 5.5 neurospheres per 1,000 cells, and neurospheres formed almost exclusively from the LPA_1-GFP^+ population (LPA_1-GFP^+ 99.8% ± 0.2% versus LPA_1-GFP^- 0.2% ± 0.2% of total neurospheres, n = 4 experiments; p = 0.0001; Figures 3A–3D). Plating the LPA_1-GFP^+ population in the presence of depolarizing levels of KCl, which we have previously shown activates a latent stem cell population (Walker et al., 2008), increased the number of neurospheres (LPA_1-GFP^+, no KCl 19.9 ± 5.5 versus KCl 24.4 ± 6.4 neurospheres per 1,000 cells, n = 4 experiments, p = 0.03) but had no effect on the LPA_1-GFP^- cells (LPA_1-GFP^- no KCl 0.03 ± 0.03 versus KCl 0.02 ± 0.02 neurospheres per 1,000 cells, n = 4 experiments, p = 0.9).

Given that Nestin is a commonly used marker of neural precursor cells, we next compared the efficacy of precursor isolation using the LPA_1-GFP transgenic mice with that of Nestin-GFP mice. Although the majority of the neurospheres were formed from the Nestin-GFP^+ population (Nestin-GFP^+ 33.8 ± 6.1 versus Nestin-GFP^- 2.0 ± 0.4 neurospheres per 1,000 cells, n = 6 experiments, p = 0.0022; Figure 3D), a large percentage of the total neurosphere formation was from the Nestin-GFP^- cells (Nestin-GFP^+ 73.5% ± 9.6% versus Nestin-GFP^- 26.5% ± 9.6%). In

(M) A summary plot of the fraction of LPA_1-GFP^+ cells that co-localize with other markers (n = 4 individual mice with a total of 800 cells for each antibody combination).

(N) Schematic illustration of expression of individual markers in relation to LPA_1-GFP expression.

Scale bars represent 50 μm in (B), (C), (F), and (L) and 25 μm in all other panels. (A) is a compilation of images of coronal sections, (I) and (K) are single planes of z stacks, and the other panels are maximum-intensity projections of z stacks.

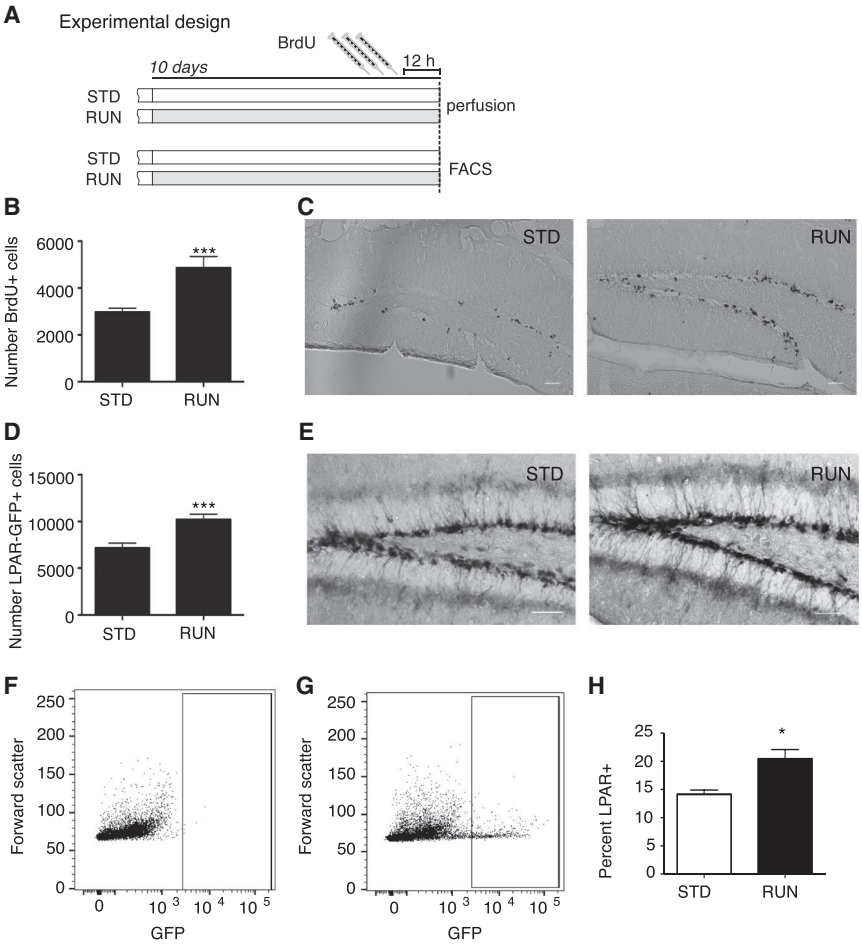

Figure 2. A Running-Induced Increase in Proliferation Can Be Measured Directly in LPA_1-GFP Mice

(A and B) Experimental design (A) and histogram (B) representing the number of BrdU-labeled cells in running (RUN) and standardly housed (STD) LPA_1-GFP mice. n = 11 mice per group, ***p < 0.001, Student's t test.

(C) Representative images of BrdU labeling in the dentate gyrus. Scale bars represent 50 μm.

(D) Histogram representing the number of LPA_1-GFP^+ cells in RUN and STD housed LPA_1-GFP mice. n = 11 mice per group, ***p < 0.001, Student's t test.

(E) Representative image of LPA_1-GFP labeling in the dentate gyrus. Scale bars represent 50 μm.

(F–H) FACS plot of a wild-type littermate used to set the GFP gates (F). LPA_1-GFP^+ cells were analyzed from RUN (G) or STD housed mice with the gates set to count total GFP^+ cells. Histograms representing the percentage of total LPA_1-GFP^+ cells (H, n = 4 mice per group, *p < 0.05, student's t-test) in RUN or STD mice.

All data represent the mean ± SEM.

contrast to the LPA_1-GFP^- population, the Nestin-GFP^- population contained a population of latent stem cells that could be activated by depolarizing levels of KCl (Nestin-GFP^+, no KCl 30.32 ± 5.9 versus KCl 27.9 ± 4.0, p = 0.9 versus Nestin-GFP^-, no KCl 2.0 ± 0.2 versus KCl 2.5 ± 0.2 neurospheres per 1,000 cells, n = 6 experiments, p = 0.04). Therefore, compared with Nestin-GFP, LPA_1-GFP can be used to isolate both the active and quiescent precursor cells from the adult dentate gyrus.

LPA_1-GFP^+ Precursor Cells Show Stem Cell Properties

In agreement with the results generated from the neurosphere assays, cells grown as adherent monolayers showed proliferation only from the LPA_1-GFP^+ cultures (Figures 3E and 3F). After four passages under proliferative conditions, >95% of cells were positive for Nestin and LPA_1-GFP (Figure 3G). Following differentiation, all three neural cell types (neurons, astrocytes, and oligodendrocytes) were generated from LPA_1-GFP^+ primary neurospheres (Figures 3H–3J), supporting multipotency. The majority of the cells were astrocytes (91.2% ± 1.3%), a small number were neurons (6.0% ± 1.3%), and few oligodendrocytes (1.1% ± 0.3%) were generated (n = 4 experiments). To examine self-renewal, we dissociated individual large (>200 μm) primary neurospheres, which we have previously shown to be stem cell derived (Walker et al., 2008), into single cells, replated them into neurosphere medium, and cultured them as individual cell lines. Approximately 20% of the primary neurospheres could be maintained over five passages (11 of 56 neurospheres), indicating their ability to self-renew. In addition, the adherent monolayer cultures generated both $GFAP^+$ astrocytes and βIII-$tubulin^+$ neurons following differentiation. Taken together, these results support the idea that the LPA_1-GFP-expressing cells from the dentate gyrus include multipotent, self-renewing stem cells.

LPA_1-GFP in Combination with EGF-Receptor and Prominin-1 Expression Effectively Separates the Proliferative from the Non-proliferative Precursor Cells

The LPA_1-GFP^+ population was relatively large and had a neurosphere-forming frequency of approximately 1 in 50

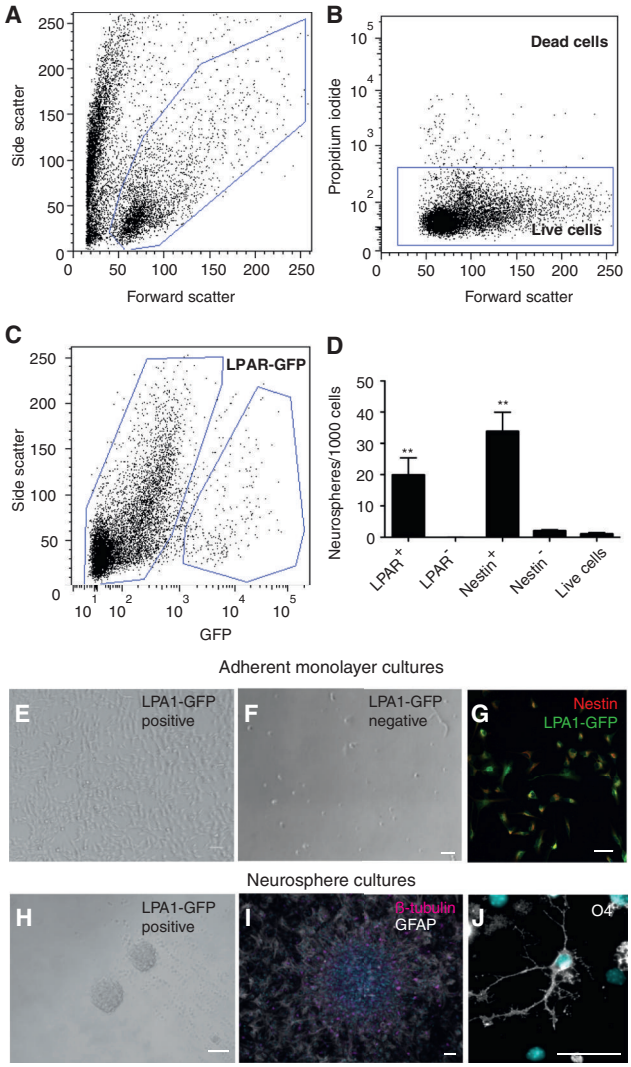

Figure 3. LPA_1-GFP^+ Precursor Cells Can Be Prospectively Isolated from the Adult Dentate Gyrus and Are Multipotent In Vitro

(A–C) Cells isolated from the dentate gyrus of LPA_1-GFP^+ mice are first gated on the basis of forward and side scatter (A) and excluding dead cells (B). Approximately 5% of cells in the adult dentate gyrus are LPA_1-GFP^+ (C).

(D) Histogram representing the number of neurospheres generated per 1,000 cells for each isolated population. $F_9 = 13.3$, $^{**}p < 0.01$, one-way ANOVA with Tukey's multiple comparison test, n = 4 experiments.

(E–J) LPA_1-GFP^+ and LPA_1-GFP^- cells were sorted and cultured independently as adherent monolayer cultures (E–G) or neurospheres (H–J). Cell proliferation was observed only from the LPA_1-GFP^+ cultures (E), with no growth from the LPA_1-GFP^- cells (F). After five passages under proliferative conditions, the majority of the cells remained positive for the precursor markers LPA_1-GFP (green) and Nestin (red) (G). The primary neurospheres generated from the LPA_1-GFP^+ cells (H) can differentiate into βIII-tubulin$^+$ (I, magenta) neurons, $GFAP^+$ astrocytes (I, white), and $O4^+$ oligodendrocytes (white, J). $DAPI^+$ cell nuclei are cyan (I, J).

Data represent the mean ± SEM. Scale bars, 50 μm.

cells. This was increased to approximately 1 in 7 by isolating cells with high levels of LPA_1-GFP expression (LPA_1-GFP^{high} 135.5 ± 30.5 versus LPA_1-GFP^{low} 13.7 ± 2.3 neurospheres per 1,000 cells, n = 3 experiments, p = 0.05; Figure S3A). Activated stem cells and proliferative progenitor cells can also be isolated from the adult SVZ (Pastrana et al., 2009) and dentate gyrus (Walker et al., 2013) on the basis of epidermal growth factor receptor (EGFR) expression. As expected, the LPA_1-GFP^+EGFR^+ population contained most of the proliferative cells (205.2 ± 32.8 neurospheres per 1,000 cells) compared with the LPA_1-GFP^+EGFR^- (4.5 ± 0.02 neurospheres per 1,000 cells), the LPA_1-GFP^-EGFR^+ (2.8 ± 0.05 neurospheres per 1,000 cells), and the LPA_1-GFP^-EGFR^- (0.1 ± 0.03 neurospheres per 1,000 cells; n = 3 experiments, p = 0.0021; Figure S3B) populations. The neurosphere-forming frequency of the LPA_1-GFP^+EGFR^+ population increased to 1 in 4.9 cells.

Finally, we have previously shown that adult hippocampal stem cells express prominin-1 (Walker et al., 2013). A combination of all three markers (LPA_1-GFP, EGFR, and prominin-1) increased the purity of the proliferative population to one neurosphere formed per 3.2 cells plated (LPA_1-GFP^+EGFR^+prominin-1^+ 310.6 ± 31.7, LPA_1-GFP^+EGFR^-prominin-1^+ 13.3 ± 4.9; LPA_1-GFP^+EGFR^+ prominin-1^- 102.0 ± 39.8 neurospheres per 1,000 cells, n = 3 experiments, p = 0.001; Figure S3C). The expected theoretical maximum frequency of acutely counted, potential neurosphere-forming cells that survive the sorting procedure has been estimated to be between 1 in 2 (our observations) and 1 in 6 (Kawaguchi et al., 2001). The above combination of markers therefore allows us to isolate an essentially pure population of proliferating neurosphere-forming cells.

Proliferative Precursor Cells from the Adult Dentate Gyrus Have a Distinct Transcriptional Profile

Using the combination of LPA_1-GFP, prominin-1, and EGF-647, we are able to separate the highly proliferative (i.e., neurosphere-forming) LPA_1^+ cells from the non-proliferative population. To gain insight into the underlying molecular regulation of these distinct subpopulations of LPA_1^+ cells, we performed RNA sequencing on three fluorescence-activated cell sorting (FACS)-isolated primary cell populations; "proliferative LPA_1^+ cells" (LPA_1-GFP^+EGFR^+prominin-1^+), "non-proliferative LPA_1^+ cells" (LPA_1-GFP^+EGFR^+prominin-1^-, LPA_1-GFP^+EGF^-prominin-1^+, and LPA_1-GFP^+EGFR^-prominin-1^-), and "niche cells" (LPA_1-GFP^-), a heterogeneous population that is composed predominantly of neurons ($NeuN^+$: 46.8% ± 2.7%, n = 4 experiments; Figures 4A–4C).

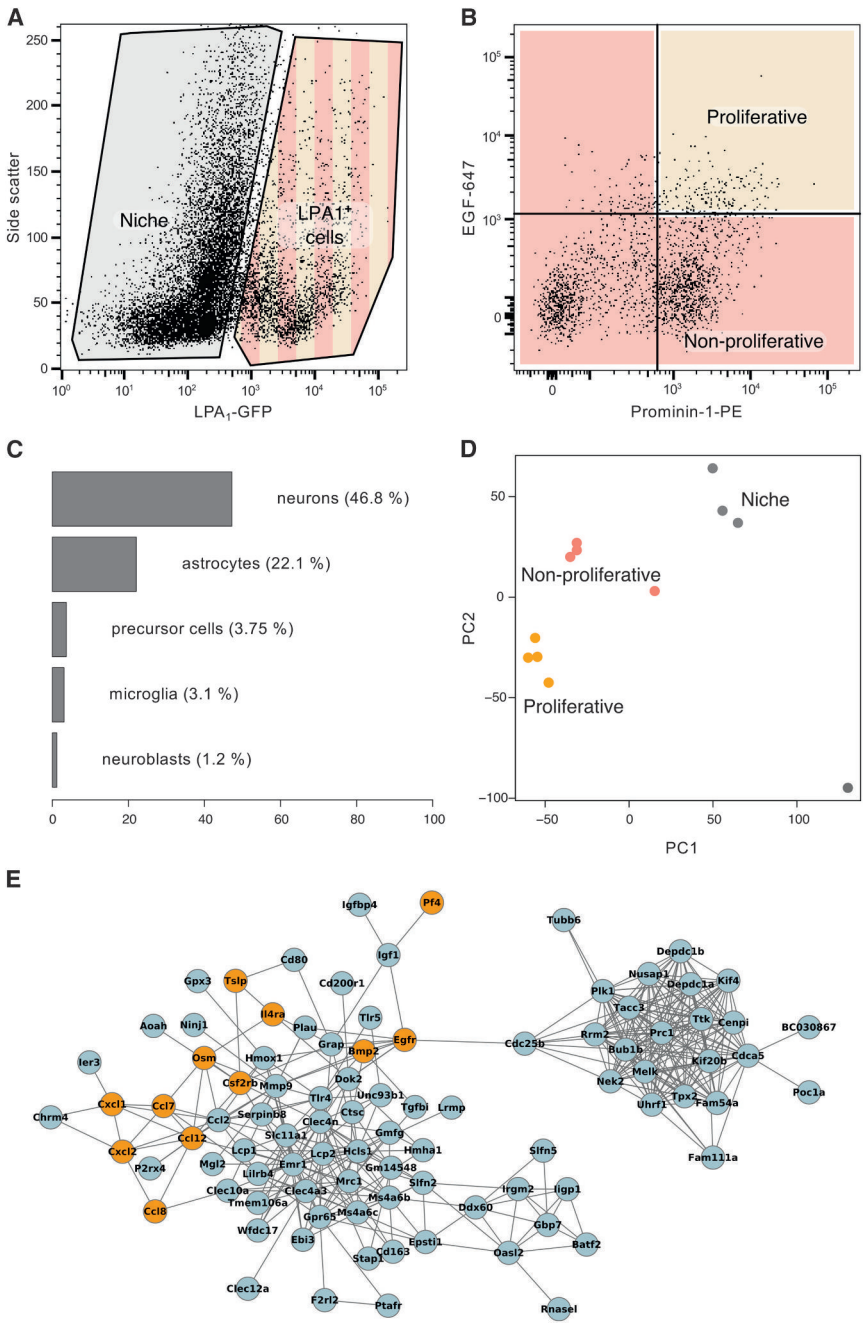

Figure 4. RNA Sequencing of the Proliferative Precursor Population Reveals Enrichment in Immune-Response-Associated Genes

(A–E) Dissociated dentate gyrus was sorted into LPA_1-GFP^- (non-precursor "niche" cells) and LPA_1-GFP^+ (precursor cells) populations (A), and a subset of the precursors were further enriched for proliferative cells based on EGFR and prominin-1 expression, with the remainder being classed as non-proliferative precursor cells (B, n = 4 independent experiments). The LPA_1-GFP^- population was a mixture of other cell types, predominantly neurons, comprising the niche (C). A principal component analysis showed samples to cluster by cell population (D). A pathway enrichment analysis of the proliferative population using the KEGG database revealed a significant association with "cytokine-cytokine receptor interaction," and genes from this pathway (orange nodes) cluster together when highlighted on a STRING interaction network (E). The STRING network was generated using the list of proliferative cell genes, but genes with no connections were not drawn.

A principal component analysis showed that, as expected, the samples cluster by cell population (Figure 4D). We identified a set of 255 genes expressed only in the precursor cells (all LPA_1^+ cells compared with LPA_1^- cells) and a subset of 145 genes with specific expression only in the proliferative neurosphere-forming cells (LPA_1-GFP^+EGFR^+prominin-1^+; Tables S1 and S2). As expected, the combined precursor population was enriched in the gene ontology (GO) categories of "cell division" (GO:0051301, $p = 3.9 \times 10^{-15}$) and "cell cycle" (GO:0007049, $p = 3.9 \times 10^{-15}$), confirming its highly proliferative nature (Table S3). A GO analysis of the proliferative LPA_1^+ cells revealed a unique functional profile, with an enrichment in terms related to the immune response such as "immune system process" (GO:0002376, $p = 1.6 \times 10^{-10}$), "immune response" (GO:0006955, $p = 4 \times 10^{-9}$), and "inflammatory response" (GO:0006954, $p = 5.3 \times 10^{-7}$; Table S4). A survey of the KEGG database revealed that our set of proliferative precursor cell genes was enriched in the pathways "cytokine-cytokine receptor interaction" ($p = 1.3 \times 10^{-5}$) and "chemokine signaling pathway"

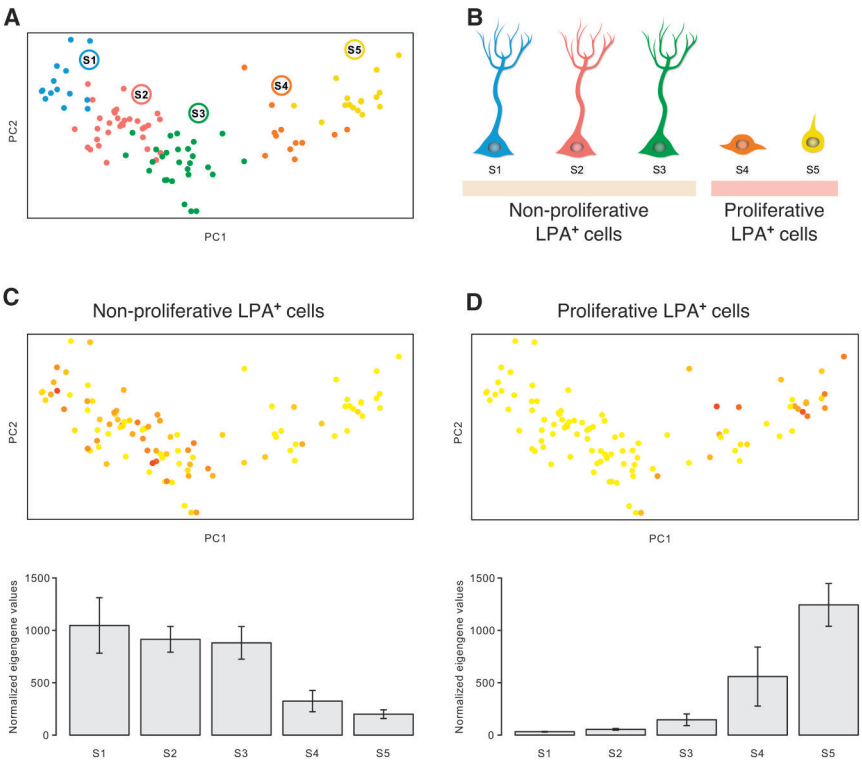

Figure 5. The Two LPA_1-GFP$^+$ Populations Correspond to Subpopulations Proposed by Existing Single-Cell Sequencing Data

(A) Clustering of single cells identified by principal component analysis of RNA-sequencing data from Shin et al. (2015) (figure adapted from original manuscript).

(B) The five subpopulations (S1–S5) correspond to the proliferative and non-proliferative LPA_1^+ populations identified in the current study.

(C and D) Normalized eigengene expression profiles in the Shin et al. dataset for the genes we found enriched in non-proliferative (C) and proliferative (D) LPA_1^+ cells are plotted on the clustering graph (upper panels) and as mean ± SD for each subpopulation (lower panels; n = 4 experiments).

($p = 3 \times 10^{-3}$). Interestingly, when viewed as a STRING protein-protein interaction network (Franceschini et al., 2013), many of the KEGG pathway-enriched genes clustered together, further suggesting that they are functionally similar (Figure 4E). This same network also contains a tight cluster of genes involved in cell division. Given that these GO and KEGG profiles are also characteristic of circulating immune cells, we had to exclude potential contamination with blood cells. Using flow cytometry, we confirmed that our proliferative cell population did not contain any lymphocytes ($CD45^+$) or endothelial cells ($CD31^+$; Figure S4). Together these results show that, while the total precursor cell population exhibited the expected mitotic phenotype, the highly proliferative neurosphere-forming population is distinguished by an unexpected transcription profile, suggesting a role for cytokine signaling in these cells.

A recent study further differentiated hippocampal Nestin-positive cells into five subpopulations (S1–S5) based on their molecular profiles, with characteristics ranging from quiescent stem cells to actively dividing precursors (Shin et al., 2015) (Figures 5A and 5B). Comparison of the expression profiles of our proliferative and non-proliferative precursor cells with the expression data from that study showed that our non-proliferative cells exhibited a profile similar to that of the S1–S3 stages, identified by Shin et al. (2015) as the non-dividing putative stem cell subpopulations (Figure 5C), whereas our proliferative population corresponded to the actively dividing S4 and S5 stages (Figure 5D).

CXCL1 Increases Hippocampal Neurosphere Number

As a case study to investigate the role of immune-associated genes in adult hippocampal precursor proliferation, we chose three cytokines that were highly expressed in our stem cell population, CXCL1, CXCL2, and CCL8. Whether these three cytokines play a role in neural precursor cell proliferation was unknown. CXCL2 and CCL8 had no effect on the size or number of neurospheres generated from either SVZ or dentate gyrus primary cells (Figure S5). CXCL1, however, significantly increased the number of neurospheres generated from both the SVZ (30 ng/ml CXCL1 137.1% ± 6.2% of control, p = 0.009, n = 4 experiments) and the dentate gyrus (3 ng/ml CXCL1 173.0% ± 10.8% of control, p = 0.02, n = 3 experiments; Figure S5). This exemplary result confirms the regulatory role of one of the identified immune-related cytokines in adult hippocampal precursor proliferation.

LPA Increases Hippocampal Precursor Proliferation In Vitro

In combination, the data presented above suggest that LPA_1-GFP is expressed with high specificity on type 1 and type 2a hippocampal precursor cells in vivo. However, the direct effect of LPA on the proliferation and survival

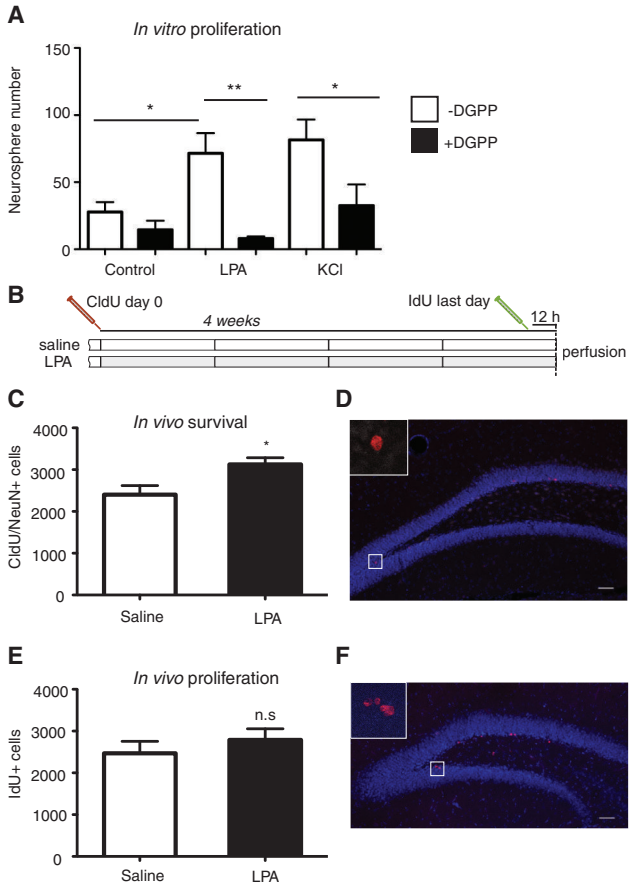

Figure 6. LPA Increases Precursor Proliferation In Vitro and In Vivo

(A) Histogram representing the number of neurospheres formed from primary adult dentate gyrus cells treated with 10 μM LPA or 15 mM KCl in the presence or absence of the LPA inhibitor DGPP. F_{23} = 8.3, *p < 0.05, **p < 0.01, one-way ANOVA with Tukey's multiple comparison test, n = 4 experiments.

(B) Experimental design for in vivo LPA infusion and thymidine analog labeling.

(C–F) Histograms representing the number of surviving neurons (C) and the number of proliferating precursor cells (E) following 28 days of LPA infusion. Two-tailed Student's t test, *p < 0.05, n = 11 animals (control group) and n = 12 animals (LPA group). Representative images of CldU (red) and NeuN (white) double-labeled cells (D) and IdU (red) single-labeled cells (F), DAPI-labeled nuclei (blue).

Data represent the mean ± SEM. Scale bars, 50 μm.

of these cells has not yet been examined. To investigate this, we first added LPA (10 μM) to cultured primary hippocampal precursor cells. Exogenous LPA significantly increased the number of neurospheres, as did the addition of depolarizing levels of KCl, a response that could be blocked by the specific LPA_1/LPA_3 antagonist diacylglycerol pyrophosphate (DGPP) (control 27.75 ± 7.39, LPA 71.50 ± 15.06, LPA + DGPP 8.00 ± 1.58, KCl 81.5 ± 15.2, KCl + DGPP 32.5 ± 15.8, n = 4 experiments, p = 0.0006; Figure 6A). LPA treatment also increased neurosphere size (control 51.5 ± 1.5 μm, LPA 69.3 ± 3.3 μm, n = 3 experiments, p = 0.04) but had no effect on the percentage of neurons (control 8.6% ± 2.3% versus LPA 11.5% ± 5.2%, p = 0.57, n > 8 coverslips) or astrocytes (control 82.1% ± 7.3% versus LPA 87.0% ± 4.8%, p = 0.62, n > 8 coverslips) after differentiation.

LPA Increases Net Neurogenesis without Changing Proliferation In Vivo

To confirm that the effect of LPA on hippocampal precursor cells in vivo, we used osmotic minipumps to continuously infuse LPA directly into the hippocampus for 28 days. To measure neuronal survival, we injected 5-chloro-2′-deoxyuridine (CldU) at the beginning of the experiment, and to label proliferating cells 5-iodo-2′-deoxyuridine (IdU) was injected 12 hr prior to perfusion (Figure 6B). We found an increase in neuronal survival ($CldU^+NeuN^+$ cells; saline 2,402 ± 215.1, n = 11 animals versus LPA 3,125 ± 161.6, n = 12 animals, p = 0.01; Figures 6C and 6D), indicating a significant effect of LPA on adult hippocampal neurogenesis. Interestingly, this effect did not appear to be due to a pro-proliferative effect, as we saw only a small but non-significant increase in proliferating (IdU^+) precursor cells in the 28-day LPA-infused group (saline 2,469 ± 286.4, n = 10 animals versus LPA 2,732 ± 266.5, n = 12 animals, p = 0.42; Figures 6E and 6F). Similarly, we also observed no significant increase in IdU^+ cells following 7 days of LPA infusion (saline 2,553 ± 302.9, n = 6 animals versus 2,656 ± 140.0, n = 7 animals, p = 0.8). These data show a specific effect of LPA on survival of newborn neurons.

LPA Signals through the AKT and the MAPK Pathways In Vitro and Ex Vivo

LPA can signal through several G-protein-coupled receptors ($LPA_{1–6}$) and multiple signaling pathways including AKT, mitogen-activated protein kinase (MAPK), or protein kinase C (PKC) to induce cell proliferation, differentiation, or survival of many cell types (Ye et al., 2002). We first performed a time-course experiment with LPA stimulations of between 2 and 60 min (Figure 7A). In these experiments, we found that LPA stimulation of adherent neural precursor cells in vitro rapidly and transiently induced phosphorylation of AKT (S473) 2 min after stimulation (ratio pAKT/AKT unstimulated 0.52 ± 0.02 versus 2 min 0.66 ± 0.09, n = 4 experiments, p = 0.02; Figure 7B) and ERK1/2 (ratio pERK/ERK unstimulated 0.23 ± 0.04, 2 min 1.41 ± 0.23, p = 0.0025, 5 min 1.47 ± 0.24, p = 0.0025, 10 min 0.83 ± 0.08, p = 0.0006; Figure 7C), an effect that was reduced to basal levels at 5 min (for AKT) and 30 min (for ERK1/2) after LPA administration. A similar effect was observed following

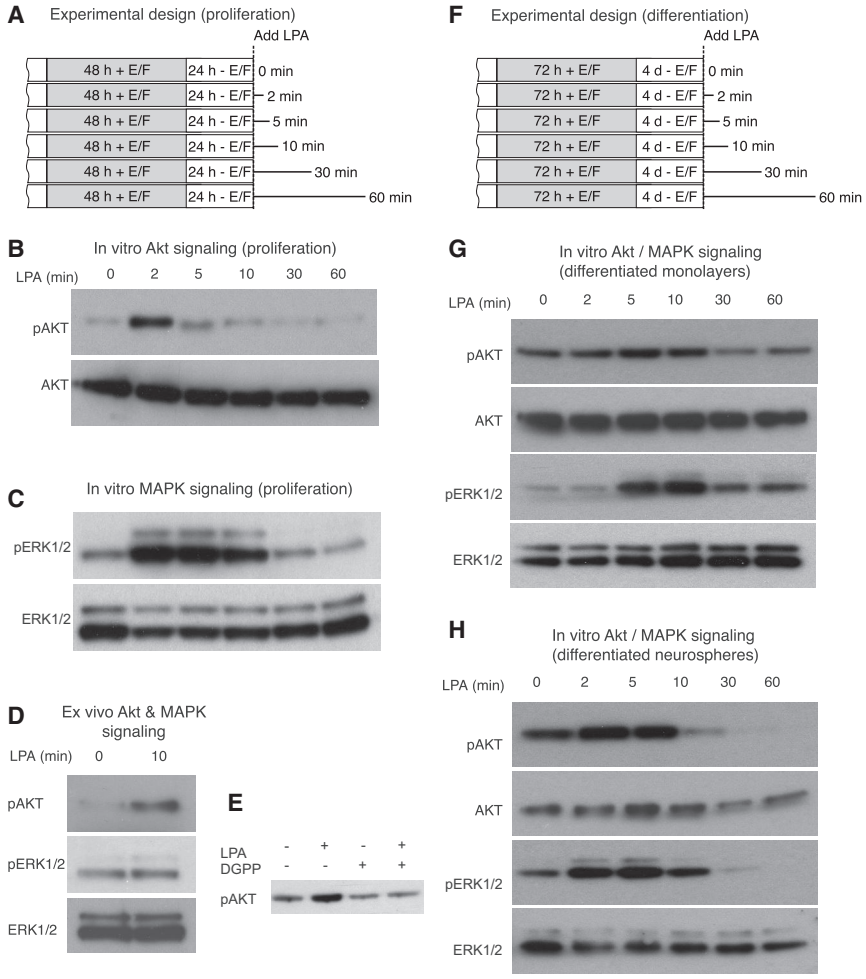

Figure 7. LPA Signals via the AKT and MAPK Pathways In Vitro

(A) Experimental design for in vitro LPA signaling under proliferation conditions.

(B–D) There is a rapid phosphorylation of AKT (B) and MAPK (C) in response to LPA treatment of adherent neural precursor cells in vitro and primary dentate gyrus cells in vivo (D, n = 4 experiments).

(E) The activation of AKT signaling can be blocked by the specific $LPA_{1/3}$ antagonist DGPP.

(F) Experimental design for in vitro LPA signaling under proliferation conditions.

(G and H) There is a rapid phosphorylation of AKT and MAPK in response to LPA treatment in both differentiated adherent monolayers (G) and differentiated neurospheres (H, n = 3 experiments).

10 min of LPA stimulation of primary isolated dentate gyrus cells ex vivo (Figure 7D). We confirmed that this signaling was occurring via the $LPA_{1/3}$ receptor as AKT phosphorylation was inhibited when the cells were pre-treated with the $LPA_{1/3}$-specific antagonist DGPP for 1 hr prior to the addition of LPA (Figure 7E). In addition, we confirmed that phosphorylation of AKT and MAPK in response to LPA stimulation also occurs in differentiated cells generated from both adherent monolayers (Figures 7F and 7G) and neurospheres (Figure 7H). These results demonstrate that LPA signals via the AKT and MAPK pathways, providing a functional context for this marker.

DISCUSSION

In the present study we show that LPA_1 is expressed by stem and progenitor cells (predominantly type 1 and type 2a) within the neurogenic niche of the dentate gyrus of adult mice, and that it outperforms Nestin, the current gold standard, as a marker for prospective isolation of cells that exhibit precursor cell properties ex vivo. Sorting LPA_1-GFP^+ cells in combination with prominin-1 and EGFR allows the separation of the non-proliferative from the proliferative precursor cells, the latter of which was revealed by RNA sequencing to have an unexpected immune-cell-like transcriptional profile.

The intermediate filament Nestin is the most commonly used marker of neural stem cells. Although all four commonly accessible transgenic Nestin-GFP lines show expression in the adult neurogenic regions, they differ in the extent of GFP expression (Beech et al., 2004; Kawaguchi et al., 2001; Mignone et al., 2004; Yamaguchi et al., 2000). It was recently demonstrated that Nestin expression is absent from the quiescent stem cell population of the adult SVZ (Codega et al., 2014), being upregulated only after the stem cells are activated. In the present study, we demonstrate that LPA_1-GFP is a more sensitive marker than Nestin-GFP and can be used to effectively isolate the proliferative hippocampal precursor population, with >99% of

the neurospheres generated from the LPA_1-GFP^+ cells. Importantly, LPA_1-GFP appears to also mark the quiescent stem cell population in the dentate gyrus. In contrast to the Nestin-GFP^- population, no quiescent stem cells could be activated from the LPA_1-GFP^- population following in vitro depolarization, a treatment which we have previously shown to mimic neural activity (Walker et al., 2008). Combining LPA_1-GFP expression with two other markers, EGFR and prominin-1, we were able to further separate the proliferative (neurosphere-forming) from the non-proliferative cells.

Our flow cytometric isolation strategy has allowed the molecular characterization of proliferative, as distinct from the non-proliferative precursor cells. This distinction could previously not be made using broader markers such as Nestin and SOX2. Indeed, comparison of our list of 145 proliferative precursor-cell-enriched genes with the SOX2-enriched genes generated by Bracko et al. (2012) revealed only three common genes (*Igf1*, *Dab2*, and *Txnip*), and when our threshold was decreased to 2-fold enrichment only two additional commonly expressed genes were detected (*Ucp2* and *Hmgb2*). The fact that SOX2 also marks post-mitotic astrocytes and the presence of known choroid plexus markers in their stem cell gene list highlights the limitation of sorting using a single marker. In contrast, our division of proliferative versus non-proliferative corresponds well with subpopulations identified by transcript functional profiling in another recent study (Shin et al., 2015). Our present study extends on this work by enabling prospective isolation of the proliferative and non-proliferative precursor cell populations. This will allow downstream manipulation in vitro for further characterization of factors capable of activating the quiescent stem cells, as well as for potential applications such as transplantation.

Transcriptomic analysis of our isolated proliferative precursor population revealed a profile with immune-like characteristics. The presence of cytokine receptors on neural precursor cells, as well as the production of cytokines and other inflammatory molecules, supports the existence of bidirectional crosstalk between the neural stem cells and the immune system (Zhang et al., 2015). Indeed, there is emerging evidence for a direct and synergistic interaction between neural stem cells and peripheral T cells to maintain baseline neurogenesis levels as well as to promote recovery following insult (Niebling et al., 2014; Wolf et al., 2009; Zhang et al., 2015). Our analysis revealed a number of immune molecules expressed by the proliferative precursor cells, most of which have no known role in the regulation of adult neural stem cells. We had, however, previously identified one of these molecules, Oncostatin M, as a regulator of neural precursor activity (Beatus et al., 2011). In addition, as a proof of concept, we confirmed a regulatory role of one of the identified immune-related proteins in adult hippocampal precursor proliferation. More detailed studies, however, are required to further investigate the specific role that CXCL1 and the other stem-cell-specific cytokines play in this process.

The definition of marker combinations in neural stem cell biology has been hampered by the dearth of information linking markers and the underlying lineage-defining biology. LPA is of particular interest as it suggests lipids as a new class of molecules co-defining stem cell entities, and indeed lipids are emerging as key signaling molecules in neural stem cell biology. The most abundant brain lipid, DHA (docosahexaenoic acid), is consistently released from phospholipids, and its presence is inversely linked to brain aging and neurodegenerative diseases. DHA supplementation leads to enhanced hippocampal long-term potentiation (Kawashima et al., 2010) and, combined with physical activity, enhances synaptic plasticity and spatial learning (Wu et al., 2008). DHA increases neurogenesis in vitro and in vivo (Kawakita et al., 2006). Another dietary polyunsaturated fatty acid, arachidonic acid, has also been shown to enhance hippocampal neurogenesis (Maekawa et al., 2009). We show that exogenous LPA affects in vitro precursor cell potential as well as proliferative capacity. This is in contrast to a previous report of reduced neurosphere size from LPA-treated cortical cells (Fukushima et al., 2007). Neurosphere numbers were not quantified in that study. Another study, using 10 μM LPA, showed inhibition of neurosphere formation and neuronal differentiation of human embryonic stem cells without affecting proliferation, apoptosis, or astrocytic differentiation (Dottori et al., 2008). Conversely, in embryonic brain cultures ex vivo, LPA promoted survival and differentiation of cortical precursor cells (Kingsbury et al., 2003). We found a significant stimulatory effect of LPA on adult hippocampal neurogenesis in vivo. Interestingly, only a small and statistically non-significant increase in proliferating precursor cell number in the LPA-infused group was seen. This is consistent with data showing that LPA can promote differentiation and cell survival without eliciting a strong proliferative response (Tang et al., 2014). Lipids have a critical role in cell signaling, with LPA binding G-protein-coupled receptors of the LPA receptor family (LPA_{1-6}) which signal via the PI3K-AKT, Ras-ERK, and PLC-PKC cell-signaling pathways. Cell survival is largely mediated by AKT signaling whereas the MAPK pathway generally regulates differentiation and cell specification, and the Rho and PKC pathways mediate proliferation (Gude et al., 2006; Miyamoto et al., 2009; Ye et al., 2002). Our present data showing an activation of AKT and MAPK pathway signaling explains the pro-survival effect observed in response to exogenous LPA. However, the exact mechanism through which LPA_1 activation is involved in the control of precursor cell activity and adult neurogenesis remains to be explored.

In summary, we show that LPA_1 is expressed by a defined population of neural precursor cells in the hippocampus, and provide evidence for the involvement of LPA in the regulation of these cells both in vitro and in vivo. In addition, we present a marker combination that allows the separation of proliferative and non-proliferative precursor cells and present the transcriptional profile of the proliferative cells, providing insight into their immune-like characteristics and further supporting the hypothesis of a bidirectional crosstalk between neural stem cells and the immune system.

EXPERIMENTAL PROCEDURES

For a more detailed description, see Supplemental Experimental Procedures.

Animals

LPA_1-GFP (Gong et al., 2003), Nestin-GFP (Yamaguchi et al., 2000), and Nestin-Cyan nuclear (Encinas and Enikolopov, 2008) mice were maintained on a 12-/12-hr light/dark cycle with food and water provided ad libitum. All experiments were conducted in accordance with the applicable European and national regulations (Tierschutzgesetz) and were approved by the responsible authority (Landesdirektion Sachsen). All animals were 8 weeks old at the time of the experiment except for the Nestin-Cyan/LPA_1-GFP mice, which were 3 weeks old.

Fluorescence Immunohistochemistry of Tissue Sections

Fluorescence immunohistochemistry was performed using the following primary antibodies: GFP, GFAP, vimentin, SOX2, TBR2, NeuN, calretinin, DCX, NeuroD, or S100β. The appropriate DyLight and cyanine secondary antibodies (1:500; Dianova) were used. For visualization of the blood vessels, biotinylated *Lycopersicon esculentum* (tomato lectin; 1:2,000; Vector Laboratories, Linaris) was added for 48 hr at 4°C, followed by incubation with streptavidin-Cy3 (1:500; Jackson ImmunoResearch Laboratories) and DAPI (1:10,000; Invitrogen). Fluorescence immunohistochemistry for the detection of CldU, IdU, and NeuN was performed as described previously (Overall et al., 2013).

Fluorescence-Activated Cell Sorting and In Vitro Cell Culture

Dentate gyrus tissue from Nestin-GFP or LPA_1-GFP mice (eight per experiment) was microdissected (Hagihara et al., 2009) and enzymatically dissociated using the Neural Tissue Dissociation Kit (Miltenyi). Cells were stained with a prominin-1-specific antibody (13A4-phycoerythrin [PE]; eBioscience) and/or EGF-647 (Molecular Probes). Prior to adding the prominin-1-PE or EGF-647, a small proportion of the cells were removed and stained with an isotype control (rat IgG1-PE; eBioscience) as a control for non-specific staining. Dead cells were excluded by staining with propidium iodide (1 μg/ml). Sorted populations of cells were collected directly into neurosphere growth medium, and each population was plated into 48 wells of a 96-well plate as described elsewhere (Walker and Kempermann, 2014). Primary hippocampal neurospheres were passaged from wells containing single large neurospheres. For differentiation, neurospheres were plated onto poly-D-lysine (PDL) and laminin-coated coverslips in medium without growth factors for 8 days. The primary cells from each sorted population were plated into one well of a PDL/laminin-coated 24-well plate in 1 ml of growth medium to generate adherent monolayer cultures. The cells were stained for βIII-tubulin, MAP2ab, GFAP, the oligodendrocyte marker O4, or the precursor cell antigen Nestin.

For the in vitro neurosphere experiments, primary dentate gyrus cells were isolated and either LPA (18:1 1-oleoyl-2-hydroxy-sn-glycero-3-phosphate, 10 μM; Avanti Polar Lipids), DGPP (8:0 dioctanoylglycerol pyrophosphate, 50 μM; Avanti Polar Lipids), KCl (15 mM), CXCL1 (3 ng/ml or 30 ng/ml; R&D Systems), CXCL2 (0.1 ng/ml, 1 ng/ml, or 10 ng/ml; R&D Systems), or CCL8 (10 ng/ml or 100 ng/ml; BioLegend) were added at the time of plating.

BrdU and GFP Immunohistochemistry and Quantification

For assessment of cell proliferation in the dentate gyrus, LPA_1-GFP mice were given three intraperitoneal injections of 50 mg/kg BrdU (Sigma) spaced 6 hr apart, and were perfused 12 hr after the last injection.

For quantification of $BrdU^+$ and GFP^+ cells in the dentate gyrus, sections were stained for either BrdU or GFP, followed by incubation with anti-rat-biotin or anti-rabbit-biotin secondary antibodies (both 1:500; Dianova). Detection was performed using the Vectastain ABC-Elite reagent (Vector Labs, Linaris) with diaminobenzidine (Sigma) and 0.04% NiCl as the chromogen.

Next-Generation Sequencing

Three populations of primary dentate gyrus cells, "proliferative LPA_1^+ cells" (LPA_1-GFP^+EGFR^+prominin-1^+), "non-proliferative LPA_1^+ cells" (LPA_1-GFP^+EGFR^+prominin-1^-, LPA_1-GFP^+EGF^-prominin-1^+, and LPA_1-GFP^+EGFR^-prominin-1^-), and "niche cells" (LPA_1-GFP^-), were isolated by FACS and pools of approximately 1,000 cells were sequenced on the Illumina HiSeq 2000 platform providing on average 35 Mio reads per sample. The raw sequence data are deposited in the GEO under accession number GEO: GSE68270. Reads were mapped to the latest mouse genome build (mm10) and counts per gene were $\log_2$-transformed for downstream analysis. Population-specific transcripts were identified by first using an ANOVA filter (adjusted $p < 0.05$) and then selecting transcripts with more than 4-fold difference in expression between groups. Comparison with single-cell data (Shin et al., 2015) employed an eigengene derived from transcripts corresponding to the genes differentially regulated in this study (Table S1).

In Vivo LPA Infusion

Micro-osmotic pumps (Alzet, #1004; 28 days of infusion at a flow rate of 0.11 μl/hr) were loaded with LPA (200 nM) supplemented with 0.1% BSA or vehicle solution (0.9% sterile PBS, containing 0.1% BSA), and the cannula inserted to enable unilateral infusion directly into the hilus region of the hippocampus (anterior/posterior −1.3, dorsal/lateral +1.0, dorsal/ventral −2.2, relative to

Bregma). Mice were injected with CldU (42.5 mg/kg) immediately following surgery on day 1 and with IdU (57.5 mg/kg) on the evening of the 28th day, 12 hr prior to perfusion.

Protein Preparation and Western Blot Analysis

LPA_1-GFP$^+$ adherent cultures were transferred to mitogen-free medium for 24 hr, after which LPA (25 μM) was added and the cells were incubated for 2, 5, 10, 30, or 60 min at 37°C. For the ex vivo experiments primary dentate gyrus cells were isolated and treated with either PBS or LPA (25 μM) for 10 min in either the presence or absence of the LPA_1-specific inhibitor DGPP (50 μM). They were then lysed immediately on ice and clarified by centrifugation at 16,000 × *g* for 10 min at 4°C. Lysates were separated on 4%–12% NuPage gels and transferred to polyvinylidene fluoride membranes, and probed with either rabbit anti-AKT, rabbit anti-phospho AKT-S473, or mouse anti-phospho ERK1/2 antibodies. Immunoreactive bands were detected using either donkey anti-rabbit horseradish peroxidase or goat anti-mouse secondary antibodies and the Super-Signal West Dura Chemiluminescent Substrate (Thermo Scientific).

ACCESSION NUMBERS

The accession number for the next generation sequence data reported in this paper is GEO: GSE68270.

SUPPLEMENTAL INFORMATION

Supplemental Information includes Supplemental Experimental Procedures, five figures, and four tables and can be found with this article online at http://dx.doi.org/10.1016/j.stemcr.2016.03.002.

AUTHOR CONTRIBUTIONS

T.L.W., K.F., and G.K. designed the study. T.L.W., A.M.S., S.V., D.L., S.R., M.I., and K.F. performed the experiments. T.L.W. and R.W.O. analyzed the data. T.L.W., R.W.O., K.F., and G.K. wrote the manuscript.

ACKNOWLEDGMENTS

T.L.W. was supported by a Marie Curie International Incoming Fellowship. This work was partly funded by Deutsche Forschungsgemeinschaft SFB 655. The project was otherwise financed from basic institutional funding. We thank Anne Karasinsky for care and maintenance of animals, Katja Schneider and Nicole Rund for assistance with FACS, Masuhiro Yamaguchi for providing the Nestin-GFP mice, Grigori Enikolopov for providing Nestin-Cyan nuclear mice, Ronald Naumann for the in vitro fertilization to generate the LPA_1-GFP mice, Silke White for microscopy assistance, Maciej Paszkowski-Rogacz for making his fpkem software available, and Andreas Dahl, Sylvia Klemroth, and Annekathrin Kränkel from the Deep Sequencing Group SFB 655 for technical support in performing the RNA-sequencing experiments.

Received: December 17, 2015
Revised: March 3, 2016
Accepted: March 3, 2016
Published: March 31, 2016

REFERENCES

Beatus, P., Jhaveri, D.J., Walker, T.L., Lucas, P.G., Rietze, R.L., Cooper, H.M., Morikawa, Y., and Bartlett, P.F. (2011). Oncostatin M regulates neural precursor activity in the adult brain. Dev. Neurobiol. *71*, 619–633.

Beech, R.D., Cleary, M.A., Treloar, H.B., Eisch, A.J., Harrist, A.V., Zhong, W., Greer, C.A., Duman, R.S., and Picciotto, M.R. (2004). Nestin promoter/enhancer directs transgene expression to precursors of adult generated periglomerular neurons. J. Comp. Neurol. *475*, 128–141.

Bracko, O., Singer, T., Aigner, S., Knobloch, M., Winner, B., Ray, J., Clemenson, G.D., Jr., Suh, H., Couillard-Despres, S., Aigner, L., et al. (2012). Gene expression profiling of neural stem cells and their neuronal progeny reveals IGF2 as a regulator of adult hippocampal neurogenesis. J. Neurosci. *32*, 3376–3387.

Castilla-Ortega, E., Hoyo-Becerra, C., Pedraza, C., Chun, J., Rodriguez De Fonseca, F., Estivill-Torrus, G., and Santin, L.J. (2011). Aggravation of chronic stress effects on hippocampal neurogenesis and spatial memory in LPA(1) receptor knockout mice. PLoS One *6*, e25522.

Choi, J.W., Herr, D.R., Noguchi, K., Yung, Y.C., Lee, C.W., Mutoh, T., Lin, M.E., Teo, S.T., Park, K.E., Mosley, A.N., et al. (2010). LPA receptors: subtypes and biological actions. Annu. Rev. Pharmacol. Toxicol. *50*, 157–186.

Codega, P., Silva-Vargas, V., Paul, A., Maldonado-Soto, A.R., Deleo, A.M., Pastrana, E., and Doetsch, F. (2014). Prospective identification and purification of quiescent adult neural stem cells from their in vivo niche. Neuron *82*, 545–559.

Couillard-Despres, S., Winner, B., Karl, C., Lindemann, G., Schmid, P., Aigner, R., Laemke, J., Bogdahn, U., Winkler, J., Bischofberger, J., et al. (2006). Targeted transgene expression in neuronal precursors: watching young neurons in the old brain. Eur. J. Neurosci. *24*, 1535–1545.

Dottori, M., Leung, J., Turnley, A.M., and Pebay, A. (2008). Lysophosphatidic acid inhibits neuronal differentiation of neural stem/progenitor cells derived from human embryonic stem cells. Stem Cells *26*, 1146–1154.

Encinas, J.M., and Enikolopov, G. (2008). Identifying and quantitating neural stem and progenitor cells in the adult brain. Methods Cell Biol. *85*, 243–272.

Estivill-Torrus, G., Llebrez-Zayas, P., Matas-Rico, E., Santin, L., Pedraza, C., De Diego, I., Del Arco, I., Fernandez-Llebrez, P., Chun, J., and De Fonseca, F.R. (2008). Absence of LPA1 signaling results in defective cortical development. Cereb. Cortex *18*, 938–950.

Franceschini, A., Szklarczyk, D., Frankild, S., Kuhn, M., Simonovic, M., Roth, A., Lin, J., Minguez, P., Bork, P., von Mering, C., et al. (2013). STRING v9.1: protein-protein interaction networks, with increased coverage and integration. Nucleic Acids Res. *41*, D808–D815.

Fukushima, N., Shano, S., Moriyama, R., and Chun, J. (2007). Lysophosphatidic acid stimulates neuronal differentiation of cortical neuroblasts through the LPA1-G(i/o) pathway. Neurochem. Int. *50*, 302–307.

Gong, S., Zheng, C., Doughty, M.L., Losos, K., Didkovsky, N., Schambra, U.B., Nowak, N.J., Joyner, A., Leblanc, G., Hatten,

M.E., et al. (2003). A gene expression atlas of the central nervous system based on bacterial artificial chromosomes. Nature *425*, 917–925.

Gude, N., Muraski, J., Rubio, M., Kajstura, J., Schaefer, E., Anversa, P., and Sussman, M.A. (2006). Akt promotes increased cardiomyocyte cycling and expansion of the cardiac progenitor cell population. Circ. Res. *99*, 381–388.

Hagihara, H., Toyama, K., Yamasaki, N., and Miyakawa, T. (2009). Dissection of hippocampal dentate gyrus from adult mouse. J. Vis. Exp. http://dx.doi.org/10.3791/1543.

Heintz, N. (2004). Gene expression nervous system atlas (GENSAT). Nat. Neurosci. *7*, 483.

Hodge, R.D., Kowalczyk, T.D., Wolf, S.A., Encinas, J.M., Rippey, C., Enikolopov, G., Kempermann, G., and Hevner, R.F. (2008). Intermediate progenitors in adult hippocampal neurogenesis: Tbr2 expression and coordinate regulation of neuronal output. J. Neurosci. *28*, 3707–3717.

Jhaveri, D.J., Mackay, E.W., Hamlin, A.S., Marathe, S.V., Nandam, L.S., Vaidya, V.A., and Bartlett, P.F. (2010). Norepinephrine directly activates adult hippocampal precursors via beta3-adrenergic receptors. J. Neurosci. *30*, 2795–2806.

Kawaguchi, A., Miyata, T., Sawamoto, K., Takashita, N., Murayama, A., Akamatsu, W., Ogawa, M., Okabe, M., Tano, Y., Goldman, S.A., et al. (2001). Nestin-EGFP transgenic mice: visualization of the self-renewal and multipotency of CNS stem cells. Mol. Cell Neurosci. *17*, 259–273.

Kawakita, E., Hashimoto, M., and Shido, O. (2006). Docosahexaenoic acid promotes neurogenesis in vitro and in vivo. Neuroscience *139*, 991–997.

Kawashima, A., Harada, T., Kami, H., Yano, T., Imada, K., and Mizuguchi, K. (2010). Effects of eicosapentaenoic acid on synaptic plasticity, fatty acid profile and phosphoinositide 3-kinase signaling in rat hippocampus and differentiated PC12 cells. J. Nutr. Biochem. *21*, 268–277.

Kempermann, G., Jessberger, S., Steiner, B., and Kronenberg, G. (2004). Milestones of neuronal development in the adult hippocampus. Trends Neurosci. *27*, 447–452.

Kingsbury, M.A., Rehen, S.K., Contos, J.J., Higgins, C.M., and Chun, J. (2003). Non-proliferative effects of lysophosphatidic acid enhance cortical growth and folding. Nat. Neurosci. *6*, 1292–1299.

Knobloch, M., Braun, S.M., Zurkirchen, L., von Schoultz, C., Zamboni, N., Arauzo-Bravo, M.J., Kovacs, W.J., Karalay, O., Suter, U., Machado, R.A., et al. (2013). Metabolic control of adult neural stem cell activity by Fasn-dependent lipogenesis. Nature *493*, 226–230.

Maekawa, M., Takashima, N., Matsumata, M., Ikegami, S., Kontani, M., Hara, Y., Kawashima, H., Owada, Y., Kiso, Y., Yoshikawa, T., et al. (2009). Arachidonic acid drives postnatal neurogenesis and elicits a beneficial effect on prepulse inhibition, a biological trait of psychiatric illnesses. PLoS One *4*, e5085.

Matas-Rico, E., Garcia-Diaz, B., Llebrez-Zayas, P., Lopez-Barroso, D., Santin, L., Pedraza, C., Smith-Fernandez, A., Fernandez-Llebrez, P., Tellez, T., Redondo, M., et al. (2008). Deletion of lysophosphatidic acid receptor LPA1 reduces neurogenesis in the mouse dentate gyrus. Mol. Cell Neurosci. *39*, 342–355.

Mignone, J.L., Kukekov, V., Chiang, A.S., Steindler, D., and Enikolopov, G. (2004). Neural stem and progenitor cells in nestin-GFP transgenic mice. J. Comp. Neurol. *469*, 311–324.

Miyamoto, S., Murphy, A.N., and Brown, J.H. (2009). Akt mediated mitochondrial protection in the heart: metabolic and survival pathways to the rescue. J. Bioenerg. Biomembr. *41*, 169–180.

Niebling, J., E Rünker, A., Schallenberg, S., Kretschmer, K., and Kempermann, G. (2014). Myelin-specific T helper 17 cells promote adult hippocampal neurogenesis through indirect mechanisms. F1000Res. *3*, 169.

Overall, R.W., Walker, T.L., Leiter, O., Lenke, S., Ruhwald, S., and Kempermann, G. (2013). Delayed and transient increase of adult hippocampal neurogenesis by physical exercise in DBA/2 mice. PLoS One *8*, e83797.

Pastrana, E., Cheng, L.C., and Doetsch, F. (2009). Simultaneous prospective purification of adult subventricular zone neural stem cells and their progeny. Proc. Natl. Acad. Sci. USA *106*, 6387–6392.

Santin, L.J., Bilbao, A., Pedraza, C., Matas-Rico, E., Lopez-Barroso, D., Castilla-Ortega, E., Sanchez-Lopez, J., Riquelme, R., Varela-Nieto, I., de la Villa, P., et al. (2009). Behavioral phenotype of maLPA1-null mice: increased anxiety-like behavior and spatial memory deficits. Genes Brain Behav. *8*, 772–784.

Shin, J., Berg, D.A., Zhu, Y., Shin, J.Y., Song, J., Bonaguidi, M.A., Enikolopov, G., Nauen, D.W., Christian, K.M., Ming, G.L., et al. (2015). Single-cell RNA-Seq with waterfall reveals molecular cascades underlying adult neurogenesis. Cell Stem Cell *17*, 360–372.

Suh, H., Consiglio, A., Ray, J., Sawai, T., D'Amour, K.A., and Gage, F.H. (2007). In vivo fate analysis reveals the multipotent and self-renewal capacities of Sox2+ neural stem cells in the adult hippocampus. Cell Stem Cell *1*, 515–528.

Tang, N., Zhao, Y., Feng, R., Liu, Y., Wang, S., Wei, W., Ding, Q., An, M.S., Wen, J., and Li, L. (2014). Lysophosphatidic acid accelerates lung fibrosis by inducing differentiation of mesenchymal stem cells into myofibroblasts. J. Cell Mol. Med. *18*, 156–169.

van Praag, H., Kempermann, G., and Gage, F.H. (1999). Running increases cell proliferation and neurogenesis in the adult mouse dentate gyrus. Nat. Neurosci. *2*, 266–270.

Walker, T.L., and Kempermann, G. (2014). One mouse, two cultures: isolation and culture of adult neural stem cells from the two neurogenic zones of individual mice. J. Vis. Exp. e51225.

Walker, T.L., Yasuda, T., Adams, D.J., and Bartlett, P.F. (2007). The doublecortin-expressing population in the developing and adult brain contains multipotential precursors in addition to neuronal-lineage cells. J. Neurosci. *27*, 3734–3742.

Walker, T.L., White, A., Black, D.M., Wallace, R.H., Sah, P., and Bartlett, P.F. (2008). Latent stem and progenitor cells in the hippocampus are activated by neural excitation. J. Neurosci. *28*, 5240–5247.

Walker, T.L., Wierick, A., Sykes, A.M., Waldau, B., Corbeil, D., Carmeliet, P., and Kempermann, G. (2013). Prominin-1 allows prospective isolation of neural stem cells from the adult murine hippocampus. J. Neurosci. *33*, 3010–3024.

Wolf, S.A., Steiner, B., Akpinarli, A., Kammertoens, T., Nassenstein, C., Braun, A., Blankenstein, T., and Kempermann, G. (2009). CD4-positive T lymphocytes provide a neuroimmunological link in the

control of adult hippocampal neurogenesis. J. Immunol. *182*, 3979–3984.

Wu, A., Ying, Z., and Gomez-Pinilla, F. (2008). Docosahexaenoic acid dietary supplementation enhances the effects of exercise on synaptic plasticity and cognition. Neuroscience *155*, 751–759.

Yamaguchi, M., Saito, H., Suzuki, M., and Mori, K. (2000). Visualization of neurogenesis in the central nervous system using nestin promoter-GFP transgenic mice. Neuroreport *11*, 1991–1996.

Ye, X., Fukushima, N., Kingsbury, M.A., and Chun, J. (2002). Lysophosphatidic acid in neural signaling. Neuroreport *13*, 2169–2175.

Zhang, H., Shao, B., Zhuge, Q., Wang, P., Zheng, C., Huang, W., Yang, C., Wang, B., Su, D.M., and Jin, K. (2015). Cross-talk between human neural stem/progenitor cells and peripheral blood mononuclear cells in an allogeneic co-culture model. PLoS One *10*, e0117432.

Stem Cell Reports
Article

OPEN ACCESS

Establishment of In Vitro FUS-Associated Familial Amyotrophic Lateral Sclerosis Model Using Human Induced Pluripotent Stem Cells

Naoki Ichiyanagi,[1,8] Koki Fujimori,[1,8] Masato Yano,[1,2,*] Chikako Ishihara-Fujisaki,[1] Takefumi Sone,[1] Tetsuya Akiyama,[3] Yohei Okada,[1,4] Wado Akamatsu,[5] Takuya Matsumoto,[1] Mitsuru Ishikawa,[1] Yoshinori Nishimoto,[1] Yasuharu Ishihara,[1] Tetsushi Sakuma,[6] Takashi Yamamoto,[6] Hitomi Tsuiji,[7] Naoki Suzuki,[3] Hitoshi Warita,[3] Masashi Aoki,[3] and Hideyuki Okano[1,*]

[1]Department of Physiology, School of Medicine, Keio University, 35 Shinanomachi, Shinjuku-ku, Tokyo 160-8582, Japan
[2]Division of Neurobiology and Anatomy, Graduate School of Medical and Dental Sciences, Niigata University, 1-757, Asahimachidori, Chuo-ku, Niigata 951-8510, Japan
[3]Department of Neurology, Tohoku University Graduate School of Medicine, 1-1 Seiryo-machi, Aoba-ku, Sendai, Miyagi 980-8574, Japan
[4]Department of Neurology, Aichi Medical University School of Medicine, 1-1 Yazako Karimata, Nagakute, Aichi 480-1195, Japan
[5]Center for Genomic and Regenerative Medicine, Graduated School of Medicine, Juntendo University, 2-1-1 Hongo, Bunkyo-ku, Tokyo 113-8421, Japan
[6]Department of Mathematical and Life Sciences, Graduate School of Science, Hiroshima University, 1-3-1 Kagamiyama, Higashihiroshima, Hiroshima 739-8526, Japan
[7]Department of Biomedical Science, Graduate School of Pharmaceutical Sciences, Nagoya City University, 3-1 Tanabe-dori, Mizuho-ku, Nagoya, Aichi 467-8603, Japan
[8]Co-first author
*Correspondence: myano@med.niigata-u.ac.jp (M.Y.), hidokano@a2.keio.jp (H.O.)
http://dx.doi.org/10.1016/j.stemcr.2016.02.011

SUMMARY

Amyotrophic lateral sclerosis (ALS) is a late-onset motor neuron disorder. Although its neuropathology is well understood, the cellular and molecular mechanisms are yet to be elucidated due to limitations in the currently available human genetic data. In this study, we generated induced pluripotent stem cells (iPSC) from two familial ALS (FALS) patients with a missense mutation in the *fused-in sarcoma* (*FUS*) gene carrying the heterozygous FUS H517D mutation, and isogenic iPSCs with the homozygous FUS H517D mutation by genome editing technology. These cell-derived motor neurons mimicked several neurodegenerative phenotypes including mis-localization of FUS into cytosolic and stress granules under stress conditions, and cellular vulnerability. Moreover, exon array analysis using motor neuron precursor cells (MPCs) combined with CLIP-seq datasets revealed aberrant gene expression and/or splicing pattern in FALS MPCs. These results suggest that iPSC-derived motor neurons are a useful tool for analyzing the pathogenesis of human motor neuron disorders.

INTRODUCTION

Amyotrophic lateral sclerosis (ALS) is a neurodegenerative disease resulting in the selective death of motor neurons (Cleveland and Rothstein, 2001). ALS symptoms are associated with muscle weakness and paralysis and approximately 80% of ALS patients die within 3–5 years after the onset of these symptoms. The prevalence of ALS is two per 100,000 people per year (Bruijn et al., 2004) and approximately 10% of patients have a familial history of the disease (Gros-Louis et al., 2006). Familial ALS (FALS) is identified by mutations in several genes, including *SOD1*, *TARDBP* and *FUS* (Chen et al., 2013).

Several efforts including animal and in vitro culture models have been undertaken to understand the pathogenic mechanism of ALS. In animal models, neurobiological phenotypes of ALS are observed, which are due to multiple pathogenic mechanisms, including protein degradation, oxidative stress, inflammation, paraspeckle formation, mitochondrial dysfunction and apoptotic pathways (Lanson and Pandey, 2012; Nishimoto et al., 2013; Robberecht and Philips, 2013; Tsao et al., 2012). In addition, the use of recently developed induced pluripotent stem cell (iPSC) technologies also enables understanding of the disease pathogenesis (Mattis and Svendsen, 2011; Okano and Yamanaka, 2014). Indeed, iPSCs have been generated from ALS patients with mutations in SOD1 (Chestkov and Vasilieva, 2014; Dimos et al., 2008), TDP-43 (Bilican et al., 2012; Egawa et al., 2012), C9ORF72 (Almeida et al., 2013; Sareen et al., 2013) and recent publications of FUS (Lenzi et al., 2015; Liu et al., 2015; Di Salvio et al., 2015) suggest a useful tool for pursuing the cellular pathogenesis and mechanism underlying FALS.

FUS, also known as Translocated in Liposarcoma (TLS), is a DNA/RNA-binding protein containing a glycine-rich region, an RNA recognition motif and a nuclear localization signal (Lattante et al., 2013; Yang et al., 2010). In FALS, more than 50 mutations in the *FUS* gene have been reported (Lattante et al., 2013). Some mutant FUS proteins form nuclear/cytosolic protein aggregations that shift from the nucleus to the cytoplasm (Dormann et al., 2010; Suzuki et al., 2012; Vance et al., 2013; Zhou et al., 2013). This sequestration of FUS into aggregations is thought to be a potential cue for the initiation of motor neuron degeneration.

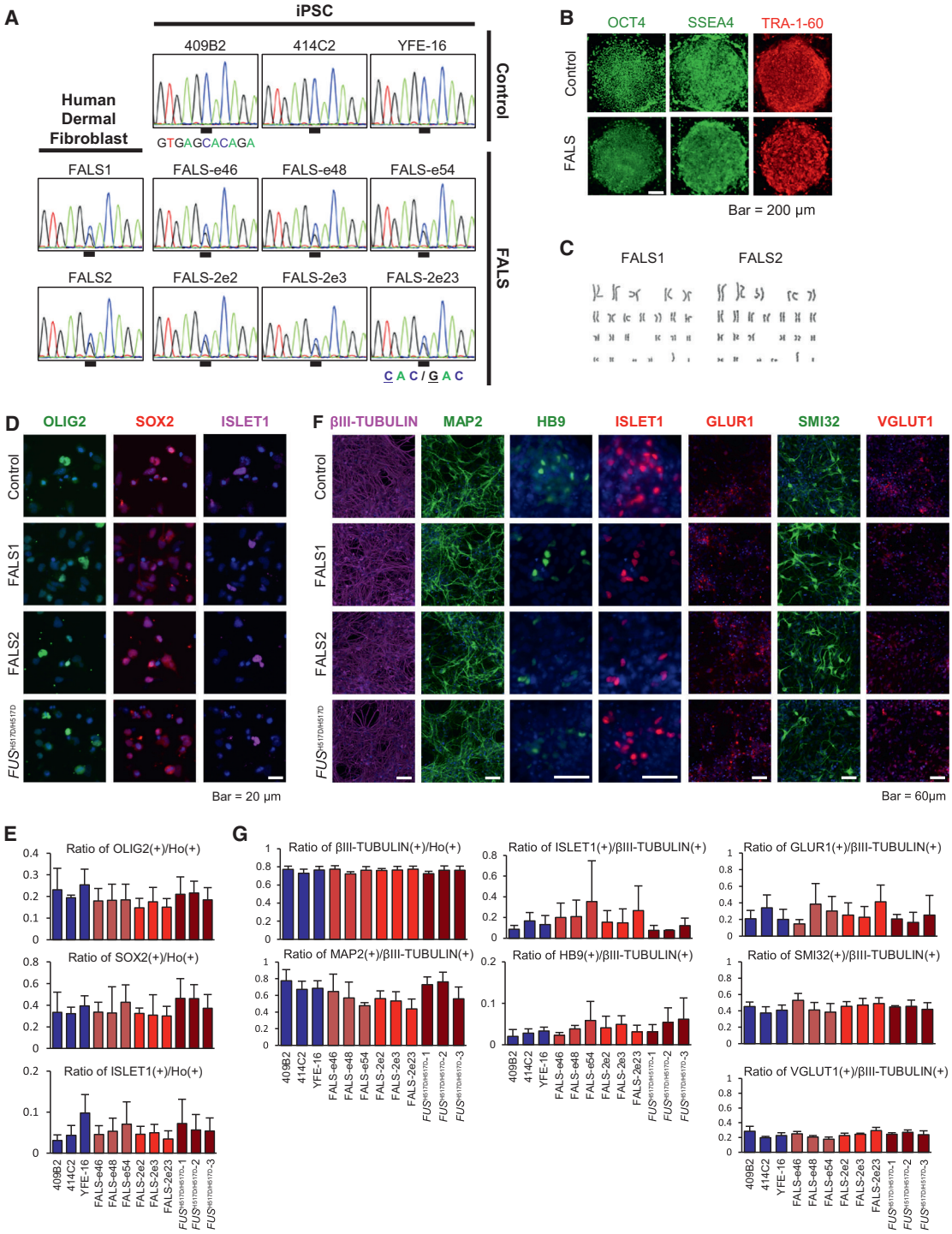

Figure 1. Characterization of iPSCs and Differentiation into Motor Neurons

(A) Human dermal fibroblasts from two ALS patients who carried the FUS H517D heterozygous mutation (C-to-G heterozygous mutation); the mutation was maintained in the generated iPSCs.

(B) Representative image of immunochemical analysis of pluripotent markers, OCT4, SSEA4 and TRA-1-60. Control, YFE-16; FALS, FALS-2e2. The same images are shown in Figure S1B. The scale bar represents 200 μm.

(C) Representative karyotypes of the generated FALS1 and FALS2 iPSC lines are shown.

(legend continued on next page)

In the present study, we generated iPSCs from two ALS patients carrying the FUS H517D mutation, healthy volunteers and isogenic iPSCs with FUS H517D mutation using the TALEN system and investigated the multifaceted cellular phenotypes of their motor neurons in vitro. We differentiated these iPSCs into the motor neuron cell lineage and observed significant mis-localization of mutant FUS to the cytosol and the accumulation of FUS in stress granules under various stresses, which has never been reported for wild-type FUS protein. Furthermore, using two comprehensive analyses, exon array combined with previous CLIP-seq data (Lagier-Tourenne et al., 2012), we identified transcripts showing aberrant gene expression, which may be involved in FUS-dependent pathology, even in motor neuron precursor cells (MPCs) derived from FALS iPSCs. The subsequent analysis using the IN Cell Analyzer revealed an increase in neuronal cell death and a decrease in neurite length in FALS iPSC-derived HB9-positive motor neurons compared with controls under stress conditions. In contrast, in our analysis on βIII-TUBULIN-positive neurons, there were nearly no changes in FUS mis-localization, FUS accumulation in stress granules, occurrence of neuronal cell death, or neurite length. Thus, the present report describes the in vitro modeling of human ALS with the *FUS* mutation to uncover the pathogenetic history of this disease.

RESULTS

Generation of FUS-ALS-iPSCs and Differentiation into Motor Neurons

We generated FALS iPSCs derived from skin fibroblasts isolated from two FALS patients (Figure S1A and Table S1), both with a point mutation in the gene encoding the C-terminal domain of the FUS protein (Akiyama et al., 2016). To reprogram the skin cells into FUS-ALS-iPSCs, we used episomal vectors carrying *OCT4*, *SOX2*, *KLF4*, *L-MYC*, *LIN28* and *p53* shRNA. The two ALS patients had a heterozygous C-to-G transition at nucleotide 1,550 (c.1550C>G) in the exon 15 coding sequence of the *FUS* gene (hereafter referred to as patient-1, FALS-e46, FALS-e48, and FALS-e54; and patient-2, FALS-2e2, FALS-2e3, and FALS-2e23). We confirmed that FALS iPSCs also harbored the heterozygous C-to-G point mutation in the *FUS* gene (Figure 1A) and had no other mutations in the *FUS* gene (data not shown). This point mutation causes a single amino acid substitution (histidine to aspartic acid) at amino acid position 517 in the C-terminal domain of the FUS protein, termed H517D. Furthermore, we established another control iPSC line, YFE-16 (Shimojo et al., 2015), in addition to the two control human iPSC lines, 409B2 and 414C2, which were established previously (Table S1) (Okita et al., 2011). These three control lines were derived from two individuals who were diagnosed as clinically healthy and did not have the C-to-G point mutation in the *FUS* gene (Figure 1A). Importantly, these iPSC lines showed the typical morphology of colonies similar to human embryonic stem cell lines, based on the expression of pluripotent stem cell markers (SSEA4, OCT4, and TRA-1-60) by immunocytochemical analysis (Figures 1B and S1B; control and FALS in Figure 1B represented YFE-16 and FALS-2e2 respectively and the same images are shown in Figure S1B), normal karyotypes by the G-band staining method (Figure 1C) and no exogenous transgene expression by qRT-PCR (Figure S1C) or *oriP* genomic PCR (Figure S1D). We also confirmed the pluripotency of differentiation potentials into three germ layers (Figure S1E). In addition, we generated isogenic iPSCs with FUS H517D homozygous mutation (hereafter referred to as $FUS^{H517D/H517D}$-1, -2, and -3) using the TALEN genome editing systems on 409B2 control iPSCs (Figure S2).

All iPSCs were differentiated into neural lineages including motor neurons based on a previously described protocol but with slight modifications (Bilican et al., 2012; Chambers and Fasano, 2009; Egawa et al., 2012; Hester et al., 2011; Hu and Zhang, 2009; Imaizumi et al., 2015; Nizzardo et al., 2010; Surmacz et al., 2012; Matsumoto et al., 2016). The iPSCs were transferred into a suspension culture to form the neurosphere in neural progenitor maintenance media containing retinoic acid and the hedgehog signaling activator, purmorphamine, to promote the commitment of MPCs. All MPCs were constructed from motor neuron progenitor marker, OLIG2 and SOX2 double-positive cells, and an early marker of motor neuron differentiation, ISLET1 positive cells (Figure 1D). Quantitative analysis for the ratio of marker expression using IN Cell Analyzer revealed that there was no significant difference in the differentiation ratio between control, FALS, and $FUS^{H517D/H517D}$ MPCs (Figure 1E). MPCs

(D) Representative image of immunocytochemistry for the neural stem cell marker (SOX2) and motor neuron progenitor markers (OLIG2 and ISLET1). The scale bar represents 20 μm.

(E) Quantitative data of the ratio of each MPC marker-positive cell/Hoechst-positive cell (n = 3 independent experiments; means ± SD; Tukey's test).

(F) Representative image of immunocytochemistry for motor neuron markers (HB9, ISLET1 and SMI32) and other neural markers (βIII-TUBULIN, MAP2, VGLUT1 and GLUR1). The scale bars represent 60 μm.

(G) Quantitative data of the ratio of each marker-positive cell/βIII-TUBULIN-positive cell (n = 3 independent experiments; mean ± SD; Tukey's test).

were passaged twice and then adhered on poly-ornithine/laminin-coated plates. Neurons were differentiated after 20 days in adherent culture. These neuronal cell populations contained motor neurons (i.e., HB9, ISLET1 and SMI32), glutamatergic neurons (i.e., VGLUT1) and glutamate-responsive neurons (i.e., GLUR1) (Figure 1F) and there was no significant difference in the ratio of these markers between control, FALS, and *FUS*$^{H517D/H517D}$ neurons (Figure 1G).

Aberrant Gene Expression in FALS Motor Neuron Progenitor Cells

We performed exon array analysis using an Affymetrix GeneChip Human Exon 1.0 ST Array to analyze RNA profiles in control and FALS-derived MPCs, which efficiently differentiate into motor neurons. We compared 18,738 genes using core probes to observe fold changes (FCs) in gene expression between the three control and six FALS-derived cell types. A scatterplot of FCs showed a very high correlation coefficient of more than 0.9, suggesting our in vitro culture model was stable regarding their transcriptome. Next, we prepared a list of FUS-regulated genes, which were differentially expressed for each cell, by filtering the gene-level signal intensities with Bayes statistics p values <0.001. Of the 159 differently expressed genes we identified, 124 genes were upregulated and 35 genes were downregulated in FALS MPCs as summarized in plots and a heatmap (Figures 2A and 2B). We analyzed the Gene Ontology (GO) terms (Figure 2C) of the genes, including *SLITRK4*, *DST*, *GNAO1*, *ALCAM*, *NFASC*, *NEUROD4* and *ONECUT2* that were aberrantly expressed in FALS-derived cells. We found that these genes were associated with neuron differentiation, neuron development and cell adhesion and were enriched compared with the profiles of control MPCs (Aruga and Mikoshiba, 2003).

We reanalyzed a previous FUS CLIP-seq (crosslinking and immunoprecipitation, followed by high-throughput sequencing) dataset (Lagier-Tourenne et al., 2012) to determine whether this gene regulation is involved in direct regulation of the FUS protein. Among 10,159 FUS CLIP clusters, we defined 1,558 genes with tag number ≥ 20 and peak height ≥ 10; approximately 75% were located in intronic sequences (Figure 2D), which is consistent with previously reported FUS binding sites. We found that 23 genes were significantly overlapped using the exon array of 159 genes and potential FUS targets, as well as 1,558 genes based on the CLIP-seq dataset (Figures S3A, S3B, and Table S2). Most of these differently expressed genes were validated by qRT-PCR analysis (Figure 2E), indicating consistency between qRT-PCR and exon array analyses (Table S3).

We also analyzed the alternative splicing changes in control and FALS MPCs by exon array. We identified altered expression of exons between control and FALS MPCs including *RSU1* (Ras suppressor protein 1), *RPH3AL* (rabphilin 3A-like) and *EFCAB13* (EF-hand calcium binding domain 13), which had differences in expression levels on the core probes (Figure 3A). To validate these results by semi-quantitative RT-PCR assay (Figure 3B), we designed the primers flanking the splicing target exons in these genes and validated alternative splicing changes using total RNA obtained from tertiary MPC-specific cells by semi-quantitative RT-PCR analysis. As expected, these three genes showed dramatic splicing changes in FALS MPCs (Figure 3C). To confirm whether the splicing changes between control and FALS-derived cells depend on the mutation of the FUS protein, we analyzed the splicing patterns of these three genes in the MPCs derived from *FUS*$^{H517D/H517D}$-iPSCs carrying the FUS H517D homozygous mutation. We confirmed that differential splicing changes also occur in the *RPH3AL* and *EFCAB13* genes between control and *FUS*$^{H517D/H517D}$ MPCs (Figures 3D and S3C). Semi-quantitative analysis of splicing variants revealed that *FUS*$^{H517D/H517D}$ MPCs express higher levels of the *RPH3AL* 377-bp band than 409B2 control MPCs, but express similar levels of *RSU1* and *EFCAB13* splicing bands (Figure 3E). These results suggest that aberrant gene expressions and/or splicing changes are associated partially with mutant FUS.

Mutant FUS Is Localized in Stress Granules under Stress Conditions

The H517D mutation in FUS lies in a nuclear localization signal (NLS) (Figure 4A). Previous reports revealed that the FUS protein localizes to the nucleus; however, the mutations in the NLS sequences of the FUS protein cause mis-localization in the cytoplasm, even under normal conditions. To address the possibility that the FUS protein from FALS iPSC-derived cells harboring the H517D mutation also mis-localizes to the cytoplasm, we performed immunocytochemical analysis. The data confirmed that there is cytoplasmic mis-localization of the FUS protein in FALS and *FUS*$^{H517D/H517D}$ iPSCs (Figure 4B) and we determined the ratio of cytosolic FUS using IN Cell Analyzer (Figure 4C). The FUS proteins in FALS and *FUS*$^{H517D/H517D}$ iPSC-derived neuronal lineage cells (Figures 4D and 4E) and HB9-positive motor neurons (Figures 4D and 4F) were also mis-localized into cytosol. In addition, we performed biochemical analysis to measure the expression levels of *FUS* mRNA. Control, FALS and *FUS*$^{H517D/H517D}$ MPCs and neurons expressed similar levels of the *FUS* gene (Figure S4).

It has been reported that mutant FUS localizes into cytoplasmic stress granules (SGs) upon various stimuli (Aulas et al., 2012; Bentmann et al., 2012; Vance et al., 2013). SGs are cytosolic structures that transiently form upon exposure of cells to environmental stress, such as heat, oxidative stress, or hypoxia functions in the cellular defense

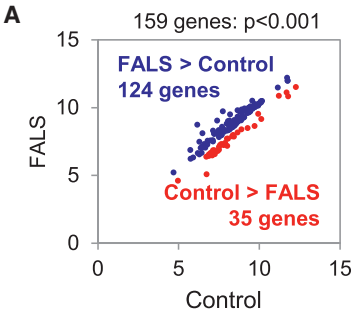

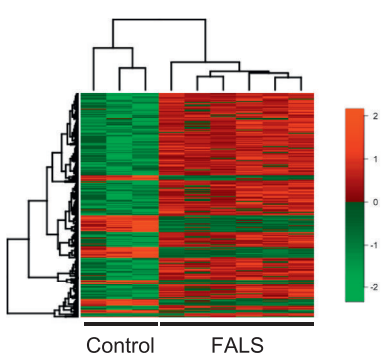

C

Biological Process

Control > FALS (35 genes)

GO ID	Term	P-Value
GO:0030203	glycosaminoglycan metabolic process	0.070749497
GO:0006022	aminoglycan metabolic process	0.083094059

FALS > Control (124 genes)

GO ID	Term	P-Value
GO:0010107	potassium ion import	0.015224803
GO:0030182	neuron differentiation	0.023999308
GO:0016050	vesicle organization	0.028859089
GO:0048666	neuron development	0.029235602
GO:0032438	melanosome organization	0.044992331
GO:0048753	pigment granule organization	0.049866621
GO:0007155	cell adhesion	0.065129708
GO:0022610	biological adhesion	0.065527162
GO:0006163	purine nucleotide metabolic process	0.069365159
GO:0006119	oxidative phosphorylation	0.089210024
GO:0051607	defense response to virus	0.097280821

D

Percentage of intervals in each region (adjusted)	
Region	%
CDS exon	6.4
5' UTR exon	1.9
Upstream 10K	0
3' UTR exon	13.6
Downstream 10K	2.6
Intron	72.6
Deep intergenic	2.8

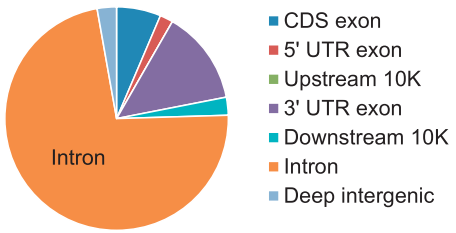

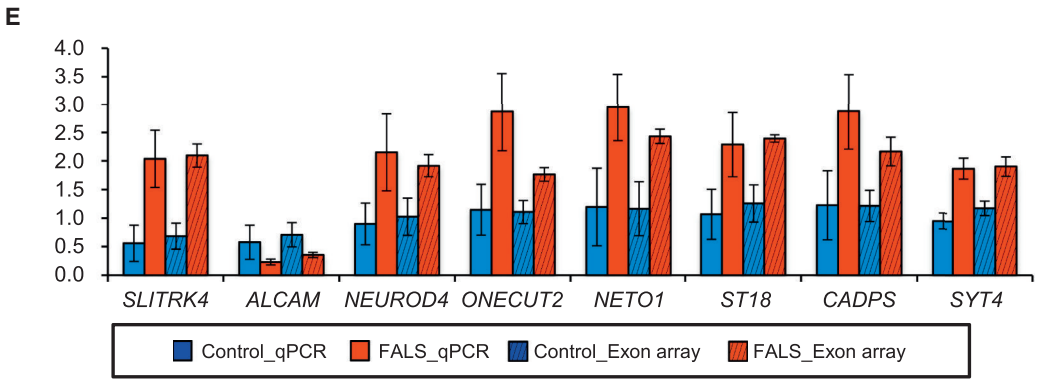

Figure 2. Exon Array Analysis Using MPCs and Comparison with FUS CLIP-Seq

(A) Scatterplot analysis of gene expression using control and FALS MPCs. A total of 124 genes were upregulated (blue) and 35 were downregulated (red) in FALS MPCs compared with control MPCs.

(B) The heatmap of correlation coefficients.

(C) Major GO terms showed both increases and decreases in gene expression in FALS versus control MPCs.

(D) Reanalysis of previously reported CLIP-seq (Lagier-Tourenne et al., 2012).

(E) Quantitative RT-PCR analysis of the expression levels for eight randomly selected genes in control and FALS iPSC-derived MPCs. Solid and hatched bars show qRT-PCR and exon array data, respectively (n = 3–6 independent samples; mean ± SD; Dunnett's test).

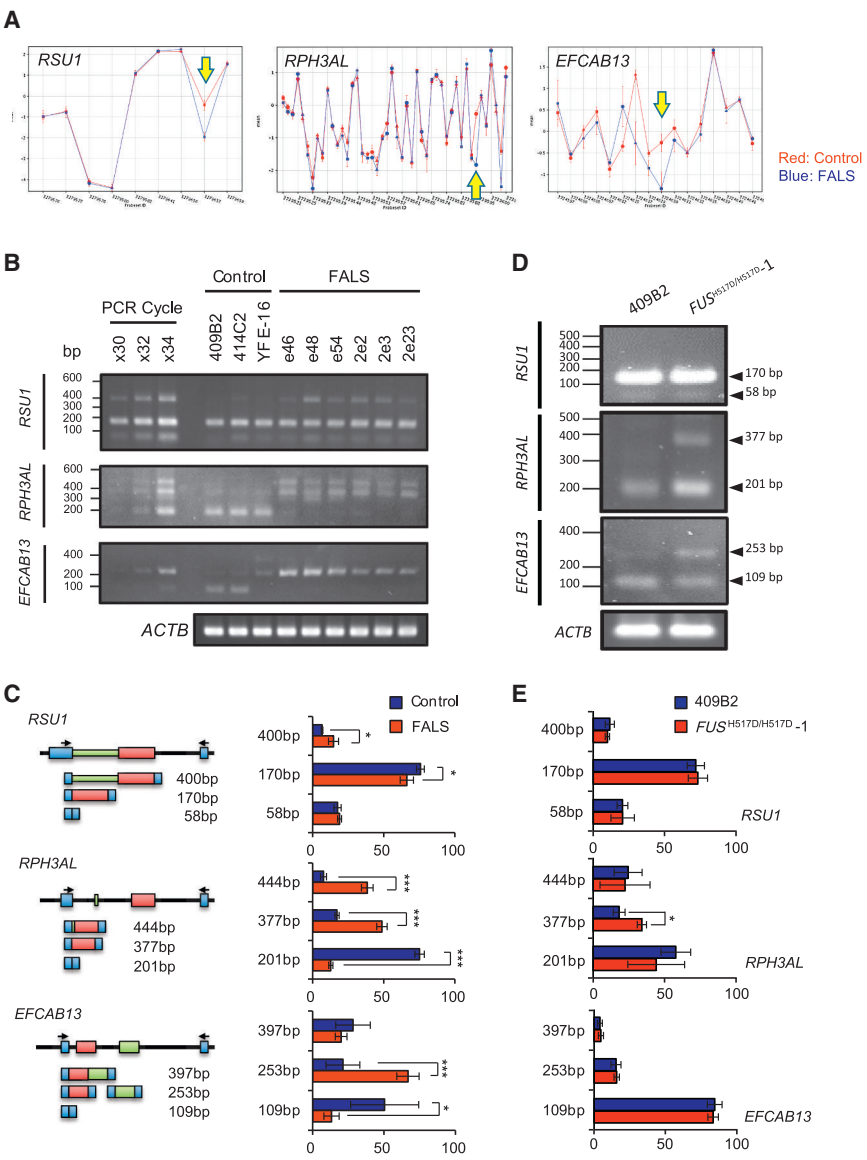

Figure 3. Alternative Splicing Analysis on MPCs

(A) The plots of the expression levels in exon probes. Red and blue lines show control and FALS expression levels, respectively. The yellow arrows show the change points of splicing between controls and FALS in each gene.

(B) RT-PCR of splicing variants in *RSU1*, *RPH3AL* and *EFCAB13* in iPSC-derived MPCs. The PCR cycle validated the PCR cycle numbers.

(C) Schematic figure of alternative splicing in each gene (left) and the measurement of the expression level of each of the spliced bands in (B) (right) (n = 3–6 independent samples; mean ± SD; *p < 0.05; ***p < 0.001; Student's t test).

(D) RT-PCR of splicing variants in *RSU1*, *RPH3AL* and *EFCAB13* in 409B2 and $FUS^{H517D/H517D}$-1 iPSC-derived MPCs.

(E) Expression levels of each of the spliced bands in (D) (n = 3 independent experiments; mean ± SD; *p < 0.05; Student's t test).

against stress, as well as translational repression of a subset of mRNAs (Nishimoto et al., 2010). We induced oxidative stress in iPSCs and iPSC-derived neurons by treatment with 0.5 mM sodium arsenite for 60 min to observe the formation of SGs using anti-G3BP (Ras GTPase-activating protein-binding protein) as a marker of SGs for immunocytochemistry. First we found that FUS proteins from FALS and $FUS^{H517D/H517D}$ iPSCs and iPSC-derived neurons leak and form aggregates in the cytosol, and that their aggregates co-localize with SGs (Figure S5A). In contrast, wild-type FUS remained in the nucleus and did not form G3BP-positive cytoplasmic granules (Figures 5A and 5F). Next, we determined the number of all SGs and FUS-positive SGs per OCT4-positive iPSCs or HB9-positive motor neurons using IN Cell Analyzer. The number of all SGs in iPSCs was unchanged in all lines (Figure 5B); however, the levels of FUS-positive SGs are significantly higher in FALS- and $FUS^{H517D/H517D}$-iPSCs than in controls (Figure 5C). We next examined similar assays in neuronal lineages. Importantly, we confirmed that the number of neuronal cell populations and all SGs in the differentiating cells in our culture was not significantly changed among all the lines (Figures 5D, 5E and 5G). FALS- and $FUS^{H517D/H517D}$-iPSC-derived neuronal lineage cells and HB9-positive motor neurons showed higher levels of FUS-positive SGs than did controls with significant changes (Figures 5H and 5I). We obtained similar results under the condition of 44°C heat shock (Figures S5B–S5E). In addition, FALS iPSC lines expressed both H517D-mutant and normal *FUS*; therefore, we used a transient expression assay to confirm whether the H517D

mutant FUS protein is localized into cytoplasmic SGs under stress conditions. The 293T cell lines were transfected with plasmids encoding either wild-type FUS or H517D mutated FUS (Figure S5F). Expectedly, only the H517D FUS mutant was co-localized with G3BP-positive SGs under the treatment with arsenite but not wild-type FUS, reflecting our observation in FUS iPSC lines (Figure S5G).

Stress Vulnerability in FALS Motor Neurons

While ALS is an adult-onset neurodegenerative disease that specifically targets motor neurons, GO analysis and overlapping genes with CLIP-seq predicted that FALS motor neurons are involved in neural development (Table S2). To address the possibility that FALS iPSC-derived neurons display any defects of neuronal maturation, we measured neurite length on motor neurons. Neural cell populations derived from iPSCs included various neuronal subtypes. Therefore, to label only motor neurons, HB9-venus reporter lentivirus (HB9:Venus) (Shimojo et al., 2015) was infected into the iPSC-derived cells. Motor neurons were visualized by Venus fluorescent protein (Figure 6A); we identified motor neurons labeled by the Venus fluorescent protein with the anti-GFP antibody to determine the length of neurites by IN Cell Analyzer (Figure 6B). As a result, there were no differences between controls, FALS, and *FUS*$^{H517D/H517D}$-derived βIII-TUBULIN-positive neurons under all conditions: unstressed, sodium arsenite treatment and glutamate treatment (Figure 6C). In HB9:Venus-positive motor neurons, however, FALS and *FUS*$^{H517D/H517D}$ neurons showed significantly shorter neurites than controls by treatment with both sodium arsenite and glutamate (Figure 6D). These results suggest that FALS-derived neurons might show not only neuronal maturation (in this case, neurite maintenance) but also cellular vulnerability especially in motor neurons. Therefore, we next pursued the cell viability of FALS-derived neurons and HB9-positive motor neurons under normal and stress conditions by immunostaining with cleaved-CASPASE3, which is a marker for apoptosis (Figure 7A). In all neurons labeled with βIII-TUBULIN, we found significant differences between control and *FUS*$^{H517D/H517D}$ lines; this may be due to homozygous mutation of FUS protein (Figure 7B). However, we were unable to confirm this as a single population of the FALS line also has a significant change. On the other hand, in HB9-positive motor neurons, the changes in the apoptotic cell population were much greater between control and all FALS and *FUS*$^{H517D/H517D}$ lines (Figure 7C). These results suggest that iPSC-derived HB9-positive motor neurons with FUS H517D mutation are vulnerable to stress and even with normal conditions rather than other types of neurons, this phenomenon reflects the ALS-like malady phenotype. Therefore we conclude that our in vitro FALS model is a useful tool to pursue the mechanism underlying the disease phenotype and treatment.

DISCUSSION

In the present study, we established ALS-specific human iPSCs from two patients with a point mutation in the *FUS* gene and isogenic iPSCs with FUS H517D homozygous mutations derived from healthy 409B2 iPSCs using the TALEN genome editing system. In addition, we differentiated into patient derived neurons to observe the disease history of FALS during neuronal differentiation in vitro. FALS-derived motor neuron lineage cells and HB9-positive mature motor neurons showed several ALS-related phenotypes such as neuronal cell death, pathological cellular structure and altered gene regulation, including steady-state transcript levels and alternative splicing. Our in vitro model may thus enable an investigation into the correlations between the molecular pathophysiology of ALS and various cell biological phenomena.

RNA-mediated mechanisms in ALS originated from the first discovery of ubiquitinated TDP43 protein, which is an RNA-binding protein (Neumann et al., 2006). Subsequent studies found the mutation in this gene among FALS (Ricketts et al., 2014; Rutherford et al., 2008; Sreedharan et al., 2008). TDP43-containing protein inclusions in cells ultimately came to be recognized as a pathological hallmark in ALS and frontotemporal lobar degeneration (FTLD). The other RNA-binding protein, the FUS/TLS protein coding gene, also contains potential causative mutations in FALS and in FTLD (Kwiatkowski et al., 2009; Vance et al., 2009). In the present study, the mutant FUS protein was co-localized with the stress marker protein G3BP in our cultured iPSCs, HB9-positive motor neurons derived from them, and fibroblast cell line overexpressing FUS protein responding to stress conditions, arsenite and heat shock (Figures 5F and S5). In general, the stress granule is a mechanism for avoiding stress and has been implicated in the cellular stress defense. These granules are in equilibrium between assembly and disassembly to manage correct gene regulation with cellular conditions. One such pathological hypothesis considers that once this equilibrium is disrupted, these stress granules form irreversible protein inclusions, named "pathological aggregates." In our in vitro model, we observed that FUS mutant proteins localize to SGs in iPSC-derived HB9-positive motor neurons, even under unstressed conditions; the co-localization of FUS and G3BP has not been observed in wild-type cells expressing normal FUS. This suggests the possibility that over-migration of FUS into SGs potentially causes aberrant gene expression and/or splicing, and that these granules may eventually form pathological aggregates, leading to neuronal cell death.

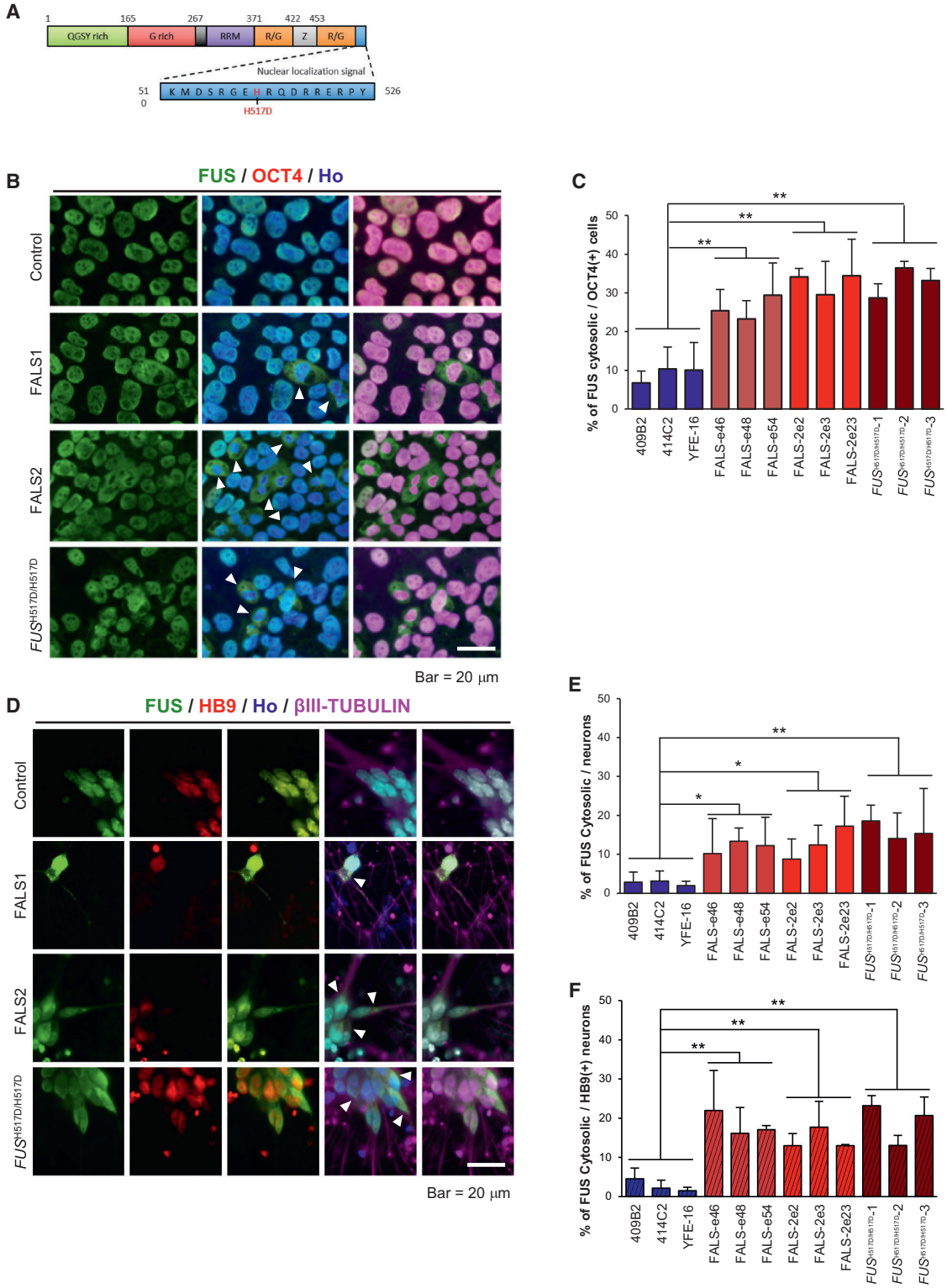

Figure 4. FUS Localization in iPSCs and iPSC-Derived Neurons

(A) Schematic diagram of FUS. The H517D mutation is located in the nuclear localization signal; RRM, RNA recognition motif; R/G, R/G rich region; Z, zinc finger domain.

(B) Representative images of immunocytochemistry for FUS in iPSCs. Arrowheads indicate cytosolic FUS. The scale bar represents 20 μm.

(legend continued on next page)

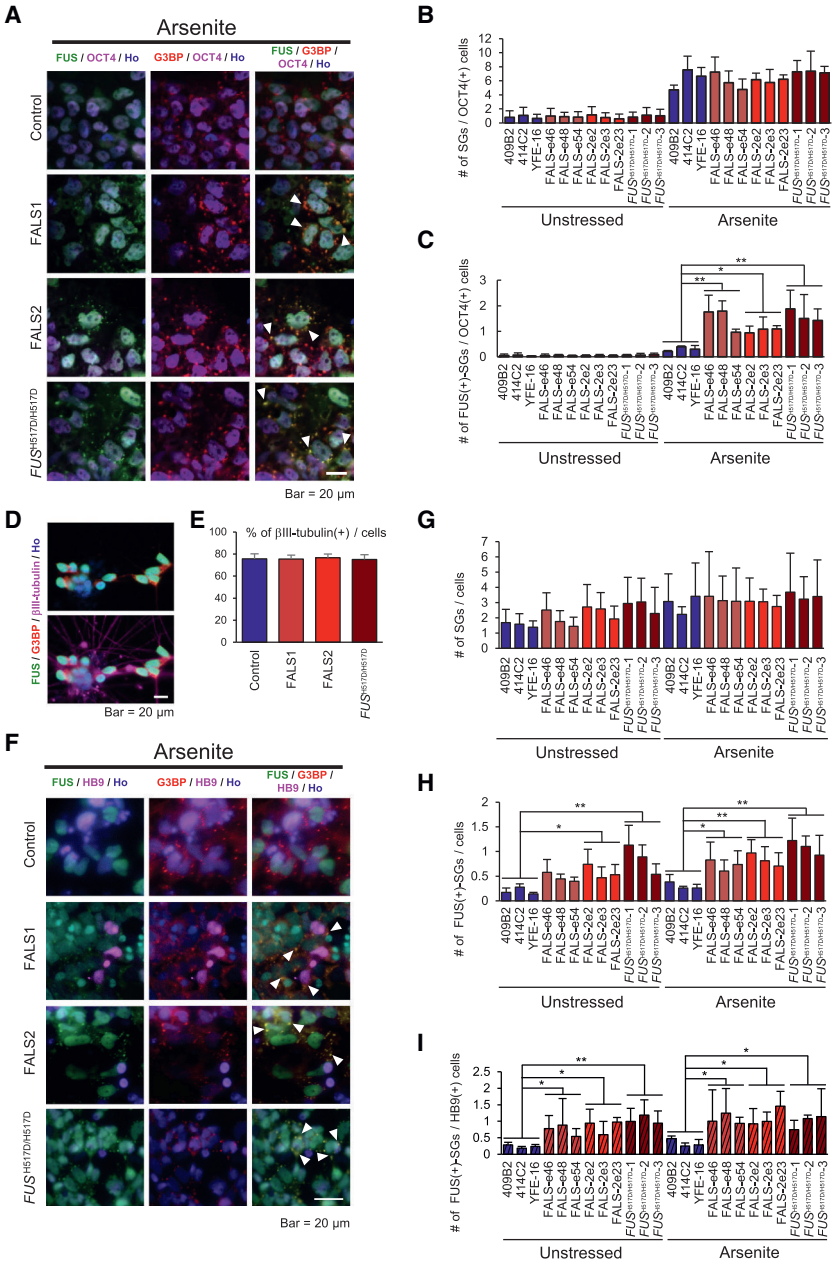

Figure 5. FUS Protein Localization into Stress Granules

(A) Representative images of immunocytochemistry for SG in iPSCs under 0.5 mM sodium arsenite stress conditions. FUS in FALS and *FUS*$^{H517D/H517D}$ iPSCs co-localized with the SG marker G3BP (arrowhead), whereas FUS in control iPSCs remained in the nucleus. The scale bar represents 20 μm. In (A)–(I) images or graphs, Arsenite means addition of 0.5 mM sodium arsenite, 1 hr treatment.

(B) Quantitative data of the number of SGs per OCT4-positive cell in iPSCs (n = 3 independent experiments; mean ± SD; Dunnett's test).

(C) Quantitative data of the number of FUS-positive SGs per OCT4-positive cell in iPSCs (n = 3 independent experiments; mean ± SD; *p < 0.05, **p < 0.01; Dunnett's test).

(D) Representative images of immunocytochemistry for βIII-TUBULIN-positive neurons. The scale bar represents 20 μm.

(E) Quantitative data of the percentage of βIII-TUBULIN-positive neurons (n = 3 independent experiments; mean ± SD; Dunnett's test).

(F) Representative images of immunocytochemistry for SG in iPSC-derived neurons under 0.5 mM sodium arsenite stress conditions. FUS co-localized with the SG marker G3BP (arrowhead). The scale bar represents 20 μm.

(G) Quantitative data of the number of SGs per Hoechst-positive cell in iPSC-derived neurons (n = 3 independent experiments; mean ± SD; Dunnett's test).

(H) Quantitative data of the number of FUS-positive SGs per Hoechst-positive cell in iPSC-derived neurons (n = 3 independent experiments; mean ± SD; *p < 0.05, **p < 0.01; Dunnett's test).

(I) Quantitative data of the number of FUS-positive SGs per HB9-positive cell in iPSC-derived neurons (n = 3 independent experiments; mean ± SD; *p < 0.05, **p < 0.01; Dunnett's test).

FUS binds to DNA as well as to RNA and regulates the expression of many transcripts in multiple steps of the gene regulation process (Dormann and Haass, 2013). In this study, we used FALS MPCs efficiently oriented into neuronal lineages including HB9-positive motor neurons to observe altered gene regulation in FALS-derived cells

(C) Quantitative data of the percentages of cytosolic FUS ratio per OCT4-positive cells in iPSCs (n = 3 independent experiments; mean ± SD; **p < 0.01; Dunnett's test).

(D) Representative images of immunocytochemistry for FUS in iPSC-derived neurons. Arrowheads indicate cytosolic FUS. The scale bar represents 20 μm.

(E) Quantitative data of the percentage of cytosolic FUS ratio per Hoechst-positive cell in iPSC-derived neurons (n = 3 independent experiments; mean ± SD; *p < 0.05, **p < 0.01; Dunnett's test).

(F) Quantitative data of the percentage of cytosolic FUS ratio per HB9-positive cell in iPSC-derived neurons (n = 3 independent experiments; mean ± SD; **p < 0.01; Dunnett's test).

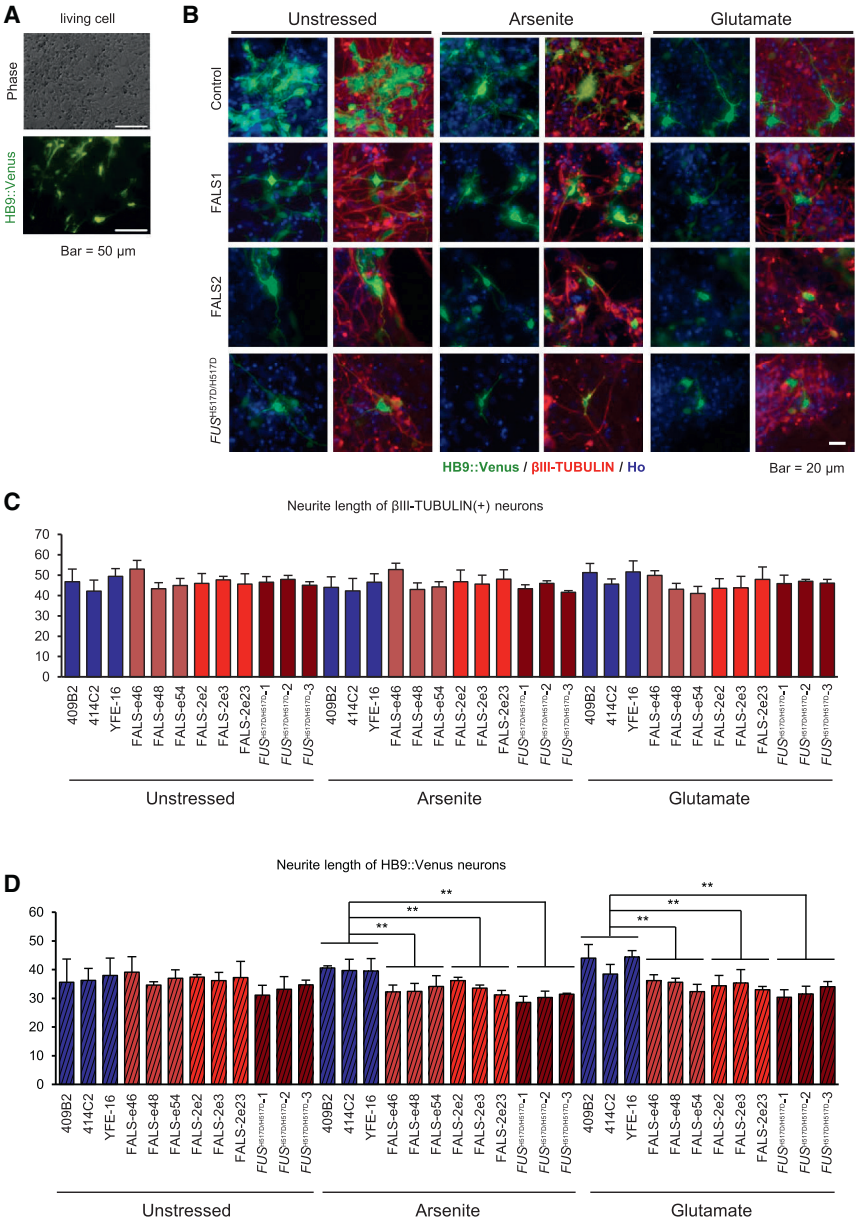

Figure 6. Shorter Neurites in FALS iPSC-Derived Motor Neurons

(A) Representative images of HB9::Venus-positive living motor neurons. The scale bars represent 50 μm.

(B) Representative images of immunocytochemistry for HB9::Venus-positive motor neurons with anti-GFP antibody. The scale bar represents 20 μm. In (B)–(D) images or graphs, Arsenite means 1.0 mM sodium arsenite, 1 hr treatment; Glutamate means 1.0 mM glutamate, 24 hr treatment.

(C) Quantitative data of the neurite length of βIII-TUBULIN-positive neurons (n = 3 independent experiments; mean ± SD; Dunnett's test).

(D) Quantitative data of the neurite length of GFP-positive motor neurons (n = 3 independent experiments; mean ± SD; **p < 0.01; Dunnett's test).

and to discover an early disease-related diagnostic marker. FUS has been shown to associate with RNA polymerase II and TFIID, thereby participating in the general transcriptional regulation process (Bertolotti et al., 1996). In addition, FUS binds to TBP and TFIID to repress transcription by RNAPIII, suggesting that FUS controls the cross-regulation between RNA polymerases (Tan and Manley, 2010). Recent studies, however, have shown that the recruitment of FUS proteins to promoter regions with lncRNA represses transcription (Wang et al., 2008). Furthermore, FUS binding to the antisense RNA transcribed by RNAPIII from promoter regions downregulates transcription (Ishigaki et al., 2012). These past studies suggest that FUS regulates transcriptional repression by various mechanisms in specific target genes. This finding could reflect our observations from our microarray assay that 78% (124 out of 159 genes) of the significantly changed genes in transcript levels are upregulated in FALS MPCs. Furthermore, with more specific analysis that focused on FUS direct targets that we defined by using the CLIP-seq dataset, we found that 95.6% of genes (of 23 genes) are upregulated in FALS.

In one proteomics study, FUS/TLS proteins were also identified as general splicing factors, which may be an early stage of the splicing process (Hartmuth et al., 2002). Our exon array analysis also revealed aberrant

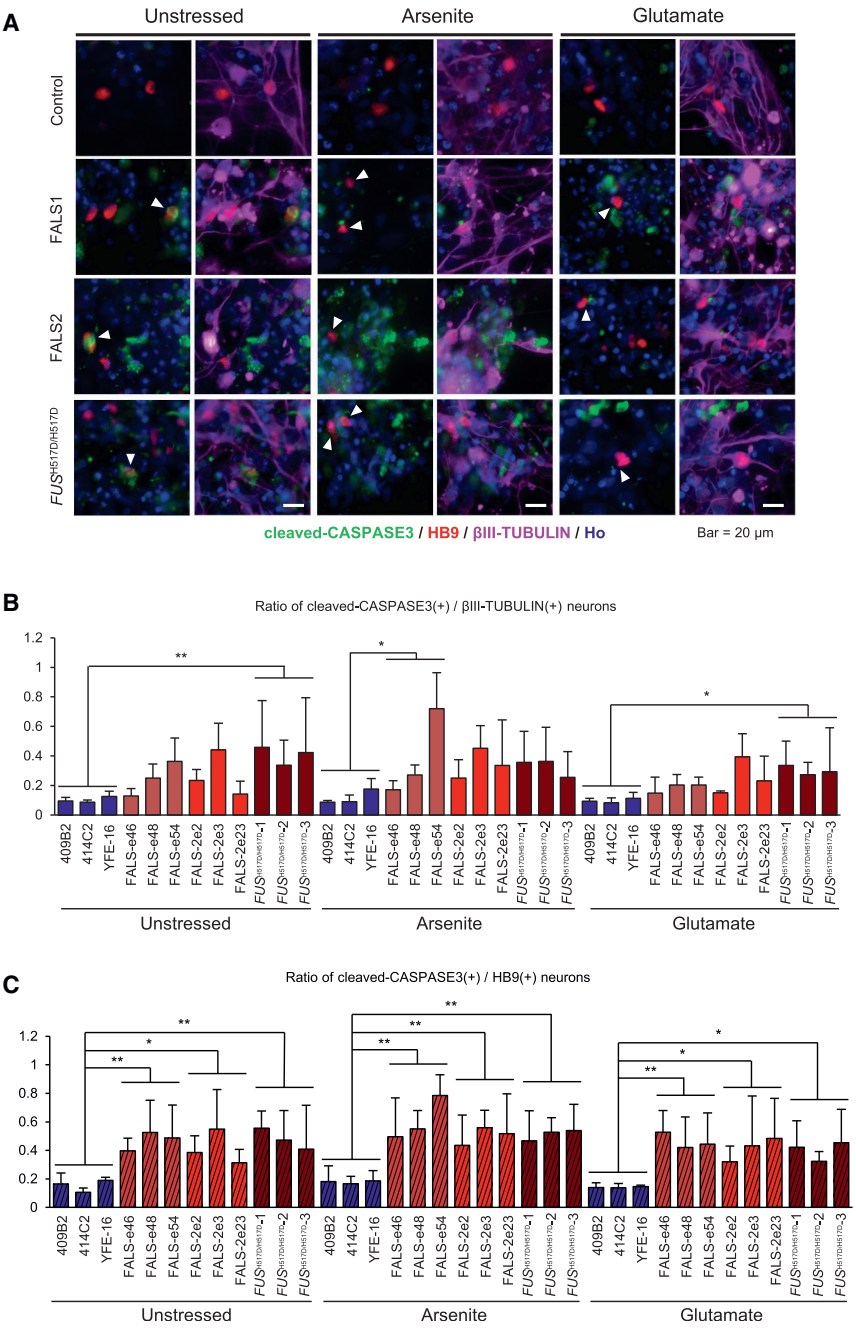

Figure 7. Enhanced Apoptosis in FALS iPSC-Derived Motor Neurons

(A) Representative images of immunocytochemistry for apoptotic HB9-positive motor neurons using markers for apoptosis (cleaved-CASPASE3), immature neurons (βIII-TUBULIN), and motor neurons (HB9). Arrowheads indicate HB9 positive cells. The scale bars represent 20 μm. In (A)–(C) images or graphs, Arsenite means 0.5 mM sodium arsenite, 1 hr treatment; Glutamate means 3.0 mM glutamate, 24 hr treatment.

(B) Quantitative data of the ratio of cleaved-CASPASE3-positive cells in βIII-TUBULIN-positive neurons (n = 3 independent experiments; mean ± SD; *p < 0.05, **p < 0.01; Dunnett's test).

(C) Quantitative data of the ratio of cleaved-CASPASE3-positive cells in HB9-positive motor neurons (n = 3 independent experiments; mean ± SD; *p < 0.05, **p < 0.01; Dunnett's test).

gene splicing events in *RSU1*, *RPH3AL*, and *EFCAB13* genes in the FALS patients. Of these, aberrant RNA processing of *RPH3AL* was also confirmed by our isogenic *FUS*$^{H517D/H517D}$ lines, suggesting the direct effects of FUS H517D mutation. However, in the other two alternative exons, we did not detect significant differences between control and isogenic *FUS*$^{H517D/H517D}$ lines, suggesting that FUS H517D mutation is not likely to have direct effects on their splicing regulation. RPH3AL is an associated protein of RAB3A (Haynes et al., 2001) and RAB27A (Fukuda, 2003) and regulates exocytosis in dense-core granules from endocrine cells (Haynes et al., 2001). In addition, mutant RPH3AL is mis-localized throughout the cytosol, whereas WT-RPH3AL is localized in the distal portion of the neurites (Fukuda et al., 2004). To date, there has been no reports of functional analyses of products from each alternative splicing event in these three genes. This may be involved in the pathological features of FUS-mediated pathologies and may also be useful as early diagnostic markers for ALS. Our iPSC model for FALS may thus

represent a useful tool for observing gene expression levels in the motor neuron lineage, as gene expression analysis in motor progenitor cells oriented into HB9-positive motor neurons cannot be achieved using conventional disease models.

We also addressed whether pathological features observed in other ALS models are observed in our in vitro FALS model. Motor neurons in patients with sporadic ALS express abundant unedited GLUA2 forms in the AMPA receptor subunit (Kawahara et al., 2004; Kwak et al., 2010), but the unedited GLUA2 form in FALS MPCs and neurons derived from iPSCs was not detected (Figure S6). ER stress is increasingly recognized as an important pathway leading to cell death in animal and cellular disease models based on mutant SOD1 (Atkin et al., 2006; Saxena et al., 2009), and mutant FUS proteins would also be predicted to induce ER stress and to interact with protein disulfide isomerase, similar to mutant SOD1 (Farg et al., 2012). In this study, however, the expression of ER stress-related genes (*BIP*, *CHOP*, spliced *XBP1*, *CASP4*, and *ASK1*) almost did not change in FALS and *FUS*$^{H517D/H517D}$ MPCs and neurons (Figure S7).

Our study showed that neurite length and the ratio of apoptotic cells in FALS- and *FUS*$^{H517D/H517D}$ iPSC-derived neurons were the same as in control motor neurons. With several stresses especially in glutamate treatment, however, FALS- and *FUS*$^{H517D/H517D}$ HB9-positive motor neurons exhibited shorter neurites and an increased cleaved-CASPASE3-positive cell ratio compared with control HB9-positive motor neurons. These results suggest that FALS iPSC-derived motor neurons are vulnerable to oxidative and excitatory stresses and there is a possibility that these phenomena are relevant to ALS-like phenotypes. We thus determined that these ALS patient-specific iPSC-derived motor neurons recapitulate disease phenotypes.

Recently, other groups also established in vitro FUS iPSCs models showing the inclusion of the stress granule of FUS mutant proteins (Lenzi et al., 2015; Liu et al., 2015). In addition to these findings, we observed additional ALS-like phenotypes and motor neuron vulnerability under some stress conditions and discovered potential biologically relevant aberrant gene expressions. Importantly, these events are also confirmed by the use of genome editing technology to generate isogenic mutant FUS H517D, suggesting that the present in vitro FALS model is able to recapitulate the ALS-like phenotypes. Based on these results, our mutant FUS-associated iPSC-derived HB9-positive motor neurons can be added to the list of model systems that may provide general tools for use in the analysis of the pathogenic process and drug screening studies in human motor neuron disorders.

EXPERIMENTAL PROCEDURES

Isolation of Human Skin Fibroblasts and Generation of iPSCs

The 409B2 and 414C2 iPSCs were kindly provided by Dr. Shinya Yamanaka (Okita et al., 2011). A skin-punch biopsy from a healthy 24-year-old Japanese man obtained after written informed consent (Keio University School of Medicine) was used to generate the control YFE-16 (Shimojo et al., 2015) iPSCs. FALS-1 and FALS-2 iPSCs were generated from a 39-year-old Japanese man and 43-year-old Japanese man, respectively. All the human iPSC clones were established by episomal vector transduction of transcription factors (SOX2, OCT4, KLF4, L-MYC, LIN28 and short hairpin RNA of p53) into human dermal fibroblasts (Okita et al., 2011). The cells were evaluated as described previously (Egawa et al., 2012; Müller et al., 2011; Okita et al., 2011). All the experimental procedures for skin biopsy and iPSC production were approved by the Keio University School of Medicine Ethics committee (approval number, 20080016) and Tohoku University School of Medicine Ethics committee (approval number, 2010-306).

Motor Neuron Differentiation

Motor neuron differentiation of iPSCs was performed as previously described with slight modifications (Imaizumi et al., 2015). Briefly, iPSCs were exposed to a medium including 3 μM dorsomorphin (Sigma), 3 μM SB431542 (Tocris Bioscience), and 3 μM CHIR99021 (Stemgent) over 5 consecutive days. Next, iPSCs were detached from feeder layers and then enzymatically dissociated into single cells. The dissociated cells were cultured in suspension in media hormone mix (MHM) (Okada et al., 2008) including 2% B27 supplement (Life Technologies), 2 ng/ml basic fibroblast growth factor (PeproTech), 3 μM CHIR99021 (Stemgent), 2 μM SB431542 (Tocris Bioscience), 10 μM Y27632 (Wako), 1 μM retinoic acid (Sigma), 1 μM purmorphamine (Calbiochem), and 10 ng/ml recombinant human leukemia inhibitory factor (Millipore) for 5–24 days to allow the formation of MPCs. MPCs were passaged repeatedly by dissociation into single cells followed by culture in the same manner. Typically, MPCs at three passages were used for analysis. The starting cell density was 1×10^4 cells/ml in primary MPC culture and 1×10^5 cells/ml in secondary and tertiary MPC cultures. For terminal differentiation, dissociated MPCs were allowed to adhere to poly-L-ornithine- and laminin-coated dishes with 5×10^4 cells/well in 96-well plate in MHM/B27 including 1× N2 supplement (Gibco), 1× GlutaMAX (Gibco), 10 ng/ml recombinant human brain-derived neurotrophic factor (R&D Systems), 10 ng/ml recombinant human glial cell line-derived neurotrophic factor (R&D Systems), 50 ng/ml recombinant hSHH (R&D Systems), 10 ng/ml insulin growth factor 1 (R&D Systems), 200 ng/ml ascorbic acid, 50 nM retinoic acid (Sigma), and 1 μM dibutyryl cyclic AMP (Sigma), and cultured for 20 days. Glutamate was added in the last 24 hr and sodium arsenite was added in the last 1 hr.

Immunocytochemistry

Immunocytochemistry was performed as described previously (Imaizumi et al., 2015). Detailed conditions are given in the Supplemental Information (Table S4). Fluorescence images were

acquired on AxioVision (Zeiss), BZ-9000 (Keyence), or IN Cell Analyzer (GE Healthcare).

High-Content Analysis

For the MPC population assay, neuronal subtype assay, neurite length analysis and cleaved-CASPASE3 analysis, stained plates were imaged on the high-content cellular analysis system IN Cell Analyzer 6000 (GE Healthcare) and a set of 5 × 5 fields were collected from each well using the 20× objective, resulting in over 10,000 cells being scored per well. For FUS mis-localization analysis and stress granule analysis, stained plates were imaged on IN Cell Analyzer 6000 and a set of 6 × 6 fields were collected from each well using the 60× objective, resulting in over 9,000 cells being scored per well. Analysis (IN Cell Developer Toolbox v1.9; GE Healthcare) began by identifying intact nuclei stained by Hoechst, which were defined as traced nuclei that were larger than 50 μm^2 in surface area and with intensity levels that were typical and lower than the threshold brightness of pyknotic cells. Each traced nucleus region was then expanded by 50% and cross-referenced with MPC markers (OLIG2, SOX2 and ISLET1), motor neuron markers (ISLET1, SMI32 and HB9), glutamatergic neuron marker (VGLUT1), glutamate-responsive neuron marker (GLUR1), neuron markers (MAP2 and βIII-TUBULIN), and pluripotent marker (OCT4) to identify them; from these images, the percentages of these were calculated. By setting areas on each cell type or neural subtype, the ratio of FUS mis-localization into cytosol, the number of stress granules, or the number of FUS-positive stress granules in OCT4-positve iPSCs, βIII-TUBULIN-positive neurons or HB9-positive motor neurons were analyzed. Using the above-described traced images of each cell, neurite length and the cleaved-CASPASE3-positive cell ratio in βIII-TUBULIN-positive neurons or HB9-positive motor neurons were analyzed.

Quantitative RT-PCR

RNA was isolated using an RNeasy kit (Qiagen) and reverse transcription using iScript cDNA Synthesis Kit (Bio-Rad). Quantitative RT-PCR was performed using SYBR Premix Ex Taq II (TaKaRa) on the ViiA 7 Real-Time PCR System (Life Technologies) (Table S5).

Sequence Analysis

Genomic DNA was isolated using a DNeasy kit (Qiagen) and amplified using intronic primers and direct nucleotide sequencing (Table S5). Both sense and antisense strands of all amplicons were sequenced using the Big Dye 3.1 dideoxy terminator methods (Applied Biosystems) and ABI Prism 3130xL Genetic Analyzer (Applied Biosystems).

Exon Array for MPCs

Exon array analysis was performed using an Affymetrix GeneChip Human Exon 1.0 ST Array. Data were analyzed using the GeneSpring GX7.3.1 software (Agilent), UCSC Genome browser (http://genome.ucsc.edu/index.html), and DAVID Bioinformatics Resources (http://david.abcc.ncifcrf.gov/). Exon array data have been registered in the Gene Expression Omnibus under accession number GEO: GSE76698.

SUPPLEMENTAL INFORMATION

Supplemental Information includes Supplemental Experimental Procedures, seven figures, and five tables and can be found with this article online at http://dx.doi.org/10.1016/j.stemcr.2016.02.011.

AUTHOR CONTRIBUTIONS

N.I., K.F., M.Y., and H.O. conceived and designed the experiments and wrote the manuscript. N.I. and K.F. performed most of the experiments and analyzed the data. N.I., C.I.-F., T.S., T.A., Y.O., W.A., T.M., M.I., Y.I., T.S., and T.Y. contributed to generate the patient-derived hiPSCs, isogenic hiPSCs, and analyzed the culture assay results. N.I., Y.N., H.T., and M.Y. analyzed and validated the microarray data and helped with in vitro analysis. N.S., H.W., and M.A. contributed to clinical and genetic analyses of the patient-coordinated study. All the authors read and approved the final version of the manuscript.

ACKNOWLEDGMENTS

We thank the members of the Okano laboratory for helpful comments and discussion. The research described in this study was supported by grants from the Program for Intractable Disease Research Utilizing Disease-specific iPS Cells funded by the Japan Science and Technology Agency (JST)/Japan Agency for Medical Research and Development (A-MED) to H.O., Ministry of Health, Labor and Welfare (MHLW) of Japan to H.O., Translational Research Network Program from A-MED to Keio University, the New Energy and Industrial Technology Development Organization (NEDO), and the Ministry of Education, Science, Sports and Culture (MEXT) (Scientific Research on Innovative Area, a MEXT Grant-in-Aid Project FY2014-2018 "Brain Protein Aging and Dementia Control"). H.O. is a scientific consultant for San Bio Co., Ltd.

Received: May 20, 2015
Revised: February 17, 2016
Accepted: February 18, 2016
Published: March 17, 2016

REFERENCES

Akiyama, T., Warita, H., Kato, M., Nishiyama, A., Izumi, R., Ikeda, C., Kamada, M., Suzuki, N., and Aoki, M. (2016). Genotype-phenotype relationships in familial ALS with FUS/TLS mutations in Japan. Muscle Nerve. http://dx.doi.org/10.1002/mus.25061.

Almeida, S., Gascon, E., Tran, H., Chou, H.J., Gendron, T.F., Degroot, S., Tapper, A.R., Sellier, C., Charlet-Berguerand, N., Karydas, A., et al. (2013). Modeling key pathological features of frontotemporal dementia with C9ORF72 repeat expansion in iPSC-derived human neurons. Acta Neuropathol. *126*, 385–399.

Aruga, J., and Mikoshiba, K. (2003). Identification and characterization of Slitrk, a novel neuronal transmembrane protein family controlling neurite outgrowth. Mol. Cell. Neurosci. *24*, 117–129.

Atkin, J.D., Farg, M.A., Turner, B.J., Tomas, D., Lysaght, J.A., Nunan, J., Rembach, A., Nagley, P., Beart, P.M., Cheema, S.S., et al. (2006). Induction of the unfolded protein response in familial amyotrophic

lateral sclerosis and association of protein-disulfide isomerase with superoxide dismutase 1. J. Biol. Chem. *281*, 30152–30165.

Aulas, A., Stabile, S., and Vande Velde, C. (2012). Endogenous TDP-43, but not FUS, contributes to stress granule assembly via G3BP. Mol. Neurodegener. *7*, 54.

Bentmann, E., Neumann, M., Tahirovic, S., Rodde, R., Dormann, D., and Haass, C. (2012). Requirements for stress granule recruitment of fused in sarcoma (FUS) and TAR DNA-binding protein of 43 kDa (TDP-43). J. Biol. Chem. *287*, 23079–23094.

Bertolotti, A., Lutz, Y., Heard, D.J., Chambon, P., and Toral, L. (1996). hTAF(II)68, a novel RNA/ssDNA-binding protein with homology to the pro-oncoproteins TLS/FUS and EWS is associated with both TFIID and RNA polymerase II. EMBO J. *15*, 5022–5031.

Bilican, B., Serio, A., Barmada, S.J., Nishimura, A.L., Sullivan, G.J., Carrasco, M., Phatnani, H.P., Puddifoot, C.a, Story, D., Fletcher, J., et al. (2012). Mutant induced pluripotent stem cell lines recapitulate aspects of TDP-43 proteinopathies and reveal cell-specific vulnerability. Proc. Natl. Acad. Sci. USA *109*, 5803–5808.

Bruijn, L.I., Miller, T.M., and Cleveland, D.W. (2004). Unraveling the mechanisms involved in motor neuron degeneration in ALS. Annu. Rev. Neurosci. *27*, 723–749.

Chambers, S., and Fasano, C. (2009). Highly efficient neural conversion of human ES and iPS cells by dual inhibition of SMAD signaling. Nat. Biotechnol. *27*, 275–280.

Chen, S., Sayana, P., Zhang, X., and Le, W. (2013). Genetics of amyotrophic lateral sclerosis: an update. Mol. Neurodegener. *8*, 28.

Chestkov, I., and Vasilieva, E. (2014). Patient-specific induced pluripotent stem cells for SOD1-associated amyotrophic lateral sclerosis pathogenesis studies. Acta Naturae *6*, 54–60.

Cleveland, D., and Rothstein, J. (2001). From Charcot to Lou Gehrig: deciphering selective motor neuron death in ALS. Nat. Rev. Neurosci. *2*, 806–819.

Di Salvio, M., Piccinni, V., Gerbino, V., Mantoni, F., Camerini, S., Lenzi, J., Rosa, A., Chellini, L., Loreni, F., Carrì, M.T., et al. (2015). Pur-alpha functionally interacts with FUS carrying ALS-associated mutations. Cell Death Dis. *6*, e1943.

Dimos, J.T., Rodolfa, K.T., Niakan, K.K., Weisenthal, L.M., Mitsumoto, H., Chung, W., Croft, G.F., Saphier, G., Leibel, R., Goland, R., et al. (2008). Induced pluripotent stem cells generated from patients with ALS can be differentiated into motor neurons. Science *321*, 1218–1221.

Dormann, D., and Haass, C. (2013). Fused in sarcoma (FUS): an oncogene goes awry in neurodegeneration. Mol. Cell. Neurosci. *56*, 475–486.

Dormann, D., Rodde, R., Edbauer, D., Bentmann, E., Fischer, I., Hruscha, A., Than, M.E., Mackenzie, I.R.A., Capell, A., Schmid, B., et al. (2010). ALS-associated fused in sarcoma (FUS) mutations disrupt Transportin-mediated nuclear import. EMBO J. *29*, 2841–2857.

Egawa, N., Kitaoka, S., Tsukita, K., Naitoh, M., Takahashi, K., Yamamoto, T., Adachi, F., Kondo, T., Okita, K., Asaka, I., et al. (2012). Drug screening for ALS using patient-specific induced pluripotent stem cells. Sci. Transl. Med. *4*, 145ra104.

Farg, M.A., Soo, K.Y., Walker, A.K., Pham, H., Orian, J., Horne, M.K., Warraich, S.T., Williams, K.L., Blair, I.P., and Atkin, J.D. (2012). Mutant FUS induces endoplasmic reticulum stress in amyotrophic lateral sclerosis and interacts with protein disulfide-isomerase. Neurobiol. Aging *33*, 2855–2868.

Fukuda, M. (2003). Distinct Rab binding specificity of Rim1, Rim2, rabphilin, and Noc2. Identification of a critical determinant of Rab3A/Rab27A recognition by Rim2. J. Biol. Chem. *278*, 15373–15380.

Fukuda, M., Kanno, E., and Yamamoto, A. (2004). Rabphilin and Noc2 are recruited to dense-core vesicles through specific interaction with Rab27A in PC12 cells. J. Biol. Chem. *279*, 13065–13075.

Gros-Louis, F., Gaspar, C., and Rouleau, G.A. (2006). Genetics of familial and sporadic amyotrophic lateral sclerosis. Biochim. Biophys. Acta *1762*, 956–972.

Hartmuth, K., Urlaub, H., Vornlocher, H., Will, C.L., Gentzel, M., Wilm, M., and Lührmann, R. (2002). Protein composition of human prespliceosomes isolated by a tobramycin affinity-selection method. Proc. Natl. Acad. Sci. USA *99*, 16719–16724.

Haynes, L.P., Evans, G.J., Morgan, A., and Burgoyne, R.D. (2001). A direct inhibitory role for the Rab3-specific effector, Noc2, in Ca2+-regulated exocytosis in neuroendocrine cells. J. Biol. Chem. *276*, 9726–9732.

Hester, M.E., Murtha, M.J., Song, S., Rao, M., Miranda, C.J., Meyer, K., Tian, J., Boulting, G., Schaffer, D.V., Zhu, M.X., et al. (2011). Rapid and efficient generation of functional motor neurons from human pluripotent stem cells using gene delivered transcription factor codes. Mol. Ther. *19*, 1905–1912.

Hu, B.-Y., and Zhang, S.-C. (2009). Differentiation of spinal motor neurons from pluripotent human stem cells. Nat. Protoc. *4*, 1295–1304.

Imaizumi, K., Sone, T., Ibata, K., Fujimori, K., Yuzaki, M., Akamatsu, W., and Okano, H. (2015). Controlling the regional identity of hPSC-derived neurons to uncover neuronal subtype specificity of neurological disease phenotypes. Stem Cell Rep. *5*, 1–13.

Ishigaki, S., Masuda, A., Fujioka, Y., Iguchi, Y., Katsuno, M., Shibata, A., Urano, F., Sobue, G., and Ohno, K. (2012). Position-dependent FUS-RNA interactions regulate alternative splicing events and transcriptions. Sci. Rep. *2*, 529.

Kawahara, Y., Ito, K., Sun, H., Aizawa, H., Kanazawa, I., and Kwak, S. (2004). Glutamate receptors: RNA editing and death of motor neurons. Nature *427*, 801.

Kwak, S., Hideyama, T., Yamashita, T., and Aizawa, H. (2010). AMPA receptor-mediated neuronal death in sporadic ALS. Neuropathology *30*, 182–188.

Kwiatkowski, T.J., Bosco, D.A., Leclerc, A.L., Tamrazian, E., Vanderburg, C.R., Russ, C., Davis, A., Gilchrist, J., Kasarskis, E.J., Munsat, T., et al. (2009). Mutations in the FUS/TLS gene on chromosome 16 cause familial amyotrophic lateral sclerosis. Science *323*, 1205–1208.

Lagier-Tourenne, C., Polymenidou, M., Hutt, K.R., Vu, A.Q., Baughn, M., Huelga, S.C., Clutario, K.M., Ling, S.-C., Liang, T.Y., Mazur, C., et al. (2012). Divergent roles of ALS-linked proteins FUS/TLS and TDP-43 intersect in processing long pre-mRNAs. Nat. Neurosci. *15*, 1488–1497.

Lanson, N.A., and Pandey, U.B. (2012). FUS-related proteinopathies: lessons from animal models. Brain Res. *1462*, 44–60.

Lattante, S., Rouleau, G.A., and Kabashi, E. (2013). TARDBP and FUS mutations associated with amyotrophic lateral sclerosis: summary and update. Hum. Mutat. *34*, 812–826.

Lenzi, J., De Santis, R., de Turris, V., Morlando, M., Laneve, P., Calvo, A., Caliendo, V., Chio, A., Rosa, A., and Bozzoni, I. (2015). ALS mutant FUS proteins are recruited into stress granules in induced pluripotent stem cell-derived motoneurons. Dis. Model. Mech. *8*, 755–766.

Liu, X., Chen, J., Liu, W., Li, X., Chen, Q., Liu, T., Gao, S., and Deng, M. (2015). The fused in sarcoma protein forms cytoplasmic aggregates in motor neurons derived from integration-free induced pluripotent stem cells generated from a patient with familial amyotrophic lateral sclerosis carrying the FUS-P525L mutation. Neurogenetics *16*, 223–231.

Matsumoto, T., Fujimori, K., Andoh-Noda, T., Ando, T., Kuzumaki, N., Toyoshima, M., Tada, H., Imaizumi, K., Ishikawa, M., Yamaguchi, R., et al. (2016). Functional neurons generated from T cell-derived induced pluripotent stem cells for neurological disease modeling. Stem Cell Rep. *6*, 1–14.

Mattis, V.B., and Svendsen, C.N. (2011). Induced pluripotent stem cells: a new revolution for clinical neurology? Lancet Neurol. *10*, 383–394.

Müller, F.-J., Schuldt, B.M., Williams, R., Mason, D., Altun, G., Papapetrou, E.P., Danner, S., Goldmann, J.E., Herbst, A., Schmidt, N.O., et al. (2011). A bioinformatic assay for pluripotency in human cells. Nat. Methods *8*, 315–317.

Neumann, M., Sampathu, D.M., and Kwong, L.K. (2006). Ubiquitinated TDP-43 in frontotemporal lobar degeneration and amyotrophic lateral sclerosis. Science *314*, 130–133.

Nishimoto, Y., Ito, D., Yagi, T., Nihei, Y., Tsunodo, Y., and Suzuki, N. (2010). Characterization of alternative isoforms and inclusion body of the TAR DNA-binding protein-43. J. Biol. Chem. *285*, 608–619.

Nishimoto, Y., Nakagawa, S., Hirose, T., Okano, H.J., Takao, M., Shibata, S., Suyama, S., Kuwako, K.-I., Imai, T., Murayama, S., et al. (2013). The long non-coding RNA nuclear-enriched abundant transcript 1_2 induces paraspeckle formation in the motor neuron during the early phase of amyotrophic lateral sclerosis. Mol. Brain *6*, 31.

Nizzardo, M., Simone, C., Falcone, M., Locatelli, F., Riboldi, G., Comi, G.P., and Corti, S. (2010). Human motor neuron generation from embryonic stem cells and induced pluripotent stem cells. Cell. Mol. Life Sci. *67*, 3837–3847.

Okada, Y., Matsumoto, A., Shimazaki, T., Enoki, R., Koizumi, A., Ishii, S., Itoyama, Y., Sobue, G., and Okano, H. (2008). Spatiotemporal recapitulation of central nervous system development by murine embryonic stem cell-derived neural stem/progenitor cells. Stem Cells *26*, 3086–3098.

Okano, H., and Yamanaka, S. (2014). iPS cell technologies: significance and applications to CNS regeneration and disease. Mol. Brain *7*, 22.

Okita, K., Matsumura, Y., Sato, Y., Okada, A., Morizane, A., Okamoto, S., Hong, H., Nakagawa, M., Tanabe, K., Tezuka, K., et al. (2011). A more efficient method to generate integration-free human iPS cells. Nat. Methods *8*, 409–412.

Ricketts, T., McGoldrick, P., Fratta, P., de Oliveira, H.M., Kent, R., Phatak, V., Brandner, S., Blanco, G., Greensmith, L., Acevedo-Arozena, A., et al. (2014). A nonsense mutation in mouse Tardbp affects TDP43 alternative splicing activity and causes limb-clasping and body tone defects. PLoS One *9*, e85962.

Robberecht, W., and Philips, T. (2013). The changing scene of amyotrophic lateral sclerosis. Nat. Rev. Neurosci. *14*, 248–264.

Rutherford, N.J., Zhang, Y., Baker, M., Gass, J.M., Finch, N.A., Xu, Y., Stewart, H., Kelley, B.J., Kuntz, K., Crook, R.J.P., et al. (2008). Novel mutations in TARDBP (TDP-43) in patients with familial amyotrophic lateral sclerosis. PLoS Genet. *4*, e1000193.

Sareen, D., O'Rourke, J.G., Meera, P., Muhammad, A.K., Grant, S., Simpkinson, M., Bell, S., Carmona, S., Ornelas, L., Sahabian, A., et al. (2013). Targeting RNA foci in iPSC-derived motor neurons from ALS patients with a C9ORF72 repeat expansion. Sci. Transl. Med. *5*, 208ra149.

Saxena, S., Cabuy, E., and Caroni, P. (2009). A role for motoneuron subtype-selective ER stress in disease manifestations of FALS mice. Nat. Neurosci. *12*, 627–636.

Shimojo, D., Onodera, K., Doi-torii, Y., Ishihara, Y., Hattori, C., Miwa, Y., Tanaka, S., Okada, R., Ohyama, M., Shoji, M., et al. (2015). Rapid, efficient and simple motor neuron differentiation from human pluripotent stem cells. Mol. Brain *8*, 79.

Sreedharan, J., Blair, I.P., Tripathi, V.B., Hu, X., Vance, C., Rogelj, B., Ackerley, S., Durnall, J.C., Williams, K.L., Buratti, E., et al. (2008). TDP-43 mutations in familial and sporadic amyotrophic lateral sclerosis. Science *319*, 1668–1672.

Surmacz, B., Fox, H., Gutteridge, A., Fish, P., Lubitz, S., and Whiting, P. (2012). Directing differentiation of human embryonic stem cells toward anterior neural ectoderm using small molecules. Stem Cells *30*, 1875–1884.

Suzuki, N., Kato, S., Kato, M., Warita, H., Mizuno, H., Kato, M., Shimakura, N., Akiyama, H., Kobayashi, Z., Konno, H., et al. (2012). FUS/TLS-immunoreactive neuronal and glial cell inclusions increase with disease duration in familial amyotrophic lateral sclerosis with an R521C FUS/TLS mutation. J. Neuropathol. Exp. Neurol. *71*, 779–788.

Tan, A.Y., and Manley, J.L. (2010). TLS inhibits RNA polymerase III transcription. Mol. Cell. Biol. *30*, 186–196.

Tsao, W., Jeong, Y.H., Lin, S., Ling, J., Price, D.L., Chiang, P.-M., and Wong, P.C. (2012). Rodent models of TDP-43: recent advances. Brain Res. *1462*, 26–39.

Vance, C., Rogelj, B., Hortobágyi, T., De Vos, K.J., Nishimura, A.L., Sreedharan, J., Hu, X., Smith, B., Ruddy, D., Wright, P., et al. (2009). Mutations in FUS, an RNA processing protein, cause familial amyotrophic lateral sclerosis type 6. Science *323*, 1208–1211.

Vance, C., Scotter, E.L., Nishimura, A.L., Troakes, C., Mitchell, J.C., Kathe, C., Urwin, H., Manser, C., Miller, C.C., Hortobágyi, T., et al. (2013). ALS mutant FUS disrupts nuclear localization and sequesters wild-type FUS within cytoplasmic stress granules. Hum. Mol. Genet. *22*, 2676–2688.

Wang, X., Arai, S., Song, X., Reichart, D., Du, K., Pascual, G., Tempst, P., Rosenfeld, M.G., Glass, C.K., and Kurokawa, R. (2008). Induced ncRNAs allosterically modify RNA-binding proteins in cis to inhibit transcription. Nature *454*, 126–130.

Yang, S., Warraich, S.T., Nicholson, G.A., and Blair, I.P. (2010). Fused in sarcoma/translocated in liposarcoma: a multifunctional DNA/RNA binding protein. Int. J. Biochem. Cell Biol. *42*, 1408–1411.

Zhou, Y., Liu, S., Liu, G., Oztürk, A., and Hicks, G.G. (2013). ALS-associated FUS mutations result in compromised FUS alternative splicing and autoregulation. PLoS Genet. *9*, e1003895.

Stem Cell Reports
Article

OPEN ACCESS

Retinal Organoids from Pluripotent Stem Cells Efficiently Recapitulate Retinogenesis

Manuela Völkner,[1] Marlen Zschätzsch,[1] Maria Rostovskaya,[2] Rupert W. Overall,[3] Volker Busskamp,[3] Konstantinos Anastassiadis,[2] and Mike O. Karl[1,3,*]

[1]German Center for Neurodegenerative Diseases (DZNE) Dresden, 01307 Dresden, Germany
[2]Stem Cell Engineering, Biotechnology Center (BIOTEC), TU Dresden, 01307 Dresden, Germany
[3]CRTD - Center for Regenerative Therapies Dresden, Technische Universität Dresden, 01307 Dresden, Germany
*Correspondence: mike.karl@dzne.de
http://dx.doi.org/10.1016/j.stemcr.2016.03.001

SUMMARY

The plasticity of pluripotent stem cells provides new possibilities for studying development, degeneration, and regeneration. Protocols for the differentiation of retinal organoids from embryonic stem cells have been developed, which either recapitulate complete eyecup morphogenesis or maximize photoreceptor genesis. Here, we have developed a protocol for the efficient generation of large, 3D-stratified retinal organoids that does not require evagination of optic-vesicle-like structures, which so far limited the organoid yield. Analysis of gene expression in individual organoids, cell birthdating, and interorganoid variation indicate efficient, reproducible, and temporally regulated retinogenesis. Comparative analysis of a transgenic reporter for PAX6, a master regulator of retinogenesis, shows expression in similar cell types in mouse in vivo, and in mouse and human retinal organoids. Early or late Notch signaling inhibition forces cell differentiation, generating organoids enriched with cone or rod photoreceptors, respectively, demonstrating the power of our improved organoid system for future research in stem cell biology and regenerative medicine.

INTRODUCTION

Pluripotent embryonic stem cells (PSCs) facilitate research on mammalian neuronal development, neurodegenerative disorders, and regenerative therapies. It has been shown in the retina that developmental processes such as optic-vesicle (OV) and optic-cup (OC) morphogenesis and signaling cascades can be reproduced using mouse and human embryonic stem cells (mESCs and hESCs) (Eiraku et al., 2011; Nakano et al., 2012; Hiler et al., 2015; La Torre et al., 2015). Retinal organoid (Boucherie et al., 2013; Decembrini et al., 2014; Gonzalez-Cordero et al., 2013) and 2D culture approaches (Lamba et al., 2006; Osakada et al., 2008) have been used for cell replacement therapy studies because efficient derivation of sufficient numbers of integration-competent cells remains a major limitation for regenerative medicine. The first reports on cell-based disease-modeling approaches (Phillips et al., 2014), retinal neuronal morphogenesis (Busskamp et al., 2014), and function in organoids (Zhong et al., 2014) are promising. Yet, in this evolving field, benefits and limitations have not been fully explored and many questions remain.

For example, the question of efficient generation of large, stratified, retinal tissues has not been addressed. Sasai and colleagues pioneered a protocol that allows the self-organization of eyecup-like structures (Eiraku et al., 2011; Nakano et al., 2012). This entails a series of complex tissue interactions, such as eyefield evagination and subsequent invagination, resulting in neural retina opposed by retinal pigment epithelium (RPE). However, this protocol relies on the evagination of the neuroepithelium and its live visualization, preferably using transgenic RAX (retina and anterior neural fold homeobox) reporter gene expression, for reliable manual isolation of the prospective retinal organoids. RAX is part of a group of transcription factors sufficient and necessary for the specification of the eyefield, which gives rise to the eye primordia and the retina. Although eyefield formation has been shown to be efficient in mouse PSC lines, the yield of retinal organoids depends on and is highly limited by a low frequency of neuroepithelial evagination (Eiraku et al., 2011; Hiler et al., 2015). Others have adapted protocols to maximize and simplify rod photoreceptor production by omitting the evagination dissection step. This results in larger organoids, with retinal and non-retinal structures intertwined within the starting organoid, and comes at the expense of inner-retina cell types (Decembrini et al., 2014; Gonzalez-Cordero et al., 2013). Therefore, we speculated that unbiased neuroepithelium trisection at the eyefield stage overcomes these limitations and enables production of more numerous retinal organoids.

Another question is the heterogeneity within and between organoids, which seems common to all the protocols developed so far but has not yet been studied in detail. Several processes, such as progenitor proliferation, cell differentiation, and ontogenetic cell death, could be potential sources of organoid variation. Transgenic animals with fluorescently labeled cells have been instrumental in visualizing major processes in the developing and adult retina. However, it is unknown whether reporter expression is

comparable between retinal organoids and in vivo. Thus, we investigated PAX6 transgenic reporter expression to gain an insight into retinal organoidogenesis. PAX6 is a highly conserved master regulator of neurogenesis (Shaham et al., 2012), playing several roles in eye and retinal development, e.g., eyefield specification, stemness control, and cell-fate specification. PAX6 reporter expression might also provide an insight into the formation of retinal structure because it remains expressed in postmitotic horizontal and amacrine cells, whose synaptic processes are part of the outer and inner plexiform layer, respectively.

Here, we have developed a protocol to facilitate efficient organoidogenesis of large, complex, 3D retinas derived from wild-type mESCs without requiring the formation and isolation of OV/OC-like structures. Gene-expression profile analyses of individual organoids and retinal cell birthdating experiments indicate efficient, reproducible, and temporally regulated retinogenesis. We have established retinal organoidogenesis from mESC and hESC lines carrying a human *PAX6* transgenic GFP reporter, hPAX6GFP BAC, and respective transgenic mice to assess GFP-expressing cells in a comparative approach. Our results suggest that our protocol is a valuable addition to the existing organoid technologies, and will facilitate future retina research and regenerative medicine.

RESULTS

Identifying the Limitations of Retinal Organoidogenesis

Taking advantage of the original retina organoid protocol (Eiraku and Sasai, 2011; Eiraku et al., 2011), we started the investigation using our transgenic hPAX6GFP mESC reporter lines and the respective wild-type mESC (E14TG2a). We generated the hPAX6GFP mESC lines by transposon-mediated BAC transgenesis. The reporter is composed of the human *PAX6* gene, with a GFP inserted in exon 4, and contains genomic sequences 108 kb upstream and 9.5 kb downstream of the gene body (Figure S1A). Two mESC clones were selected and tested positive for expression of pluripotency markers (Figure S1B; unless otherwise stated, clone 1 was used hereafter). Upon aggregation, mESCs formed continuous epithelial structures by day (D) 4–5 (Figure 1A), and by D10 we detected the first expression of hPAX6GFP (Figure 1B). However, although organoids had expanded in size and formed a neuroepithelial structure, the frequency of OV formation was as low as had been reported previously (Eiraku and Sasai, 2011; Hiler et al., 2015), which severely limited the number of retinal organoids generated. Furthermore, we did not observe any two-walled OC-like morphologies as previously described (Figure S1C and Table S1; Eiraku and Sasai, 2011). The protocol with ongoing culture of entire starting aggregates led to large heterogeneous organoids with intertwined retinal and non-retinal structures and rosette formation at D21 (Figures S1D and S1F; Table S1), comparable with previous reports (Decembrini et al., 2014; Gonzalez-Cordero et al., 2013). Specifically, the inner retinal cell types were not well developed: this substantially limited retinal organoid research and hPAX6GFP reporter analysis.

To overcome the observed limitations and to enable efficient retinal organoidogenesis, we devised an approach (Figures 1C and S1E) based on the following data on eyefield formation and neuroepithelium evagination efficiency. PAX6 and NESTIN expression at D5 indicated development of a polarized neuroepithelium with the apical surface inside (Figures S2A and S2B). Between D5 and D10, efficient eyefield induction and retinal determination occurred based on expression of the eyefield transcription factors RAX, PAX6, and LHX2 in predominant parts of the majority of organoids (D7, 81% ± 10% RAX^+ organoids, N = 7, n > 10; unless stated otherwise, data are given as mean ± SD of organoids [n] scored for marker expression by immunostaining per independent experiment [N]; Figures 2A–2C). At the same time, eyefield regions self-patterned into presumptive RPE ($MITF^+$ $OTX2^+$ $VSX2^-$ RAX^-) and neural retina (RAX^+ $VSX2^+$ $MITF^-$ $OTX2^-$) regions, reminiscent of an OC-like stage in vivo. RAX^+ regions co-expressed VSX2, indicating the onset of retinogenesis, while regions adjacent to the RAX^+ $VSX2^+$ areas expressed RPE markers (Figures 2B, S2D, and S2E). However, OC-like morphology due to tissue invagination was not observed; rather, the RPE regions that lie adjacent to the neural retina part either within the organoid main body (Figure 2B) or at the base of an evagination (Figure S2E). This suggested that self-patterning of the eyefield into presumptive neural retina and RPE occurred at the molecular, but not structural, level.

Next, we tested whether the cell-seeding density influences the evagination and eyefield differentiation efficiency: lower (1,500–3,000/well) compared with higher (6,000–9,000/well) cell-seeding numbers led to a higher percentage of organoids developing one or more evaginations by D7 (Figures 2D and 2E). The majority of organoids generated from lower seeding densities had eyefield areas (80% ± 4% RAX^+, N = 4, n = 24 organoids per seeding density and independent experiment [N]; Figures 2D and 2F), whereas organoids from higher seeding densities rarely had RAX^+ (10% ± 4% RAX^+, N = 4, n = 24), but regularly $LHX2^+$ areas. RAX^+ eyefield regions ranged from small parts to almost the entire organoid neuroepithelium (Figures 2A, 2D, and S2C). These quantitative data confirm and extend previous observations (Decembrini et al., 2014; Eiraku and Sasai, 2011), showing that eyefield differentiation efficiency is highly dependent on cell-seeding densities. Our

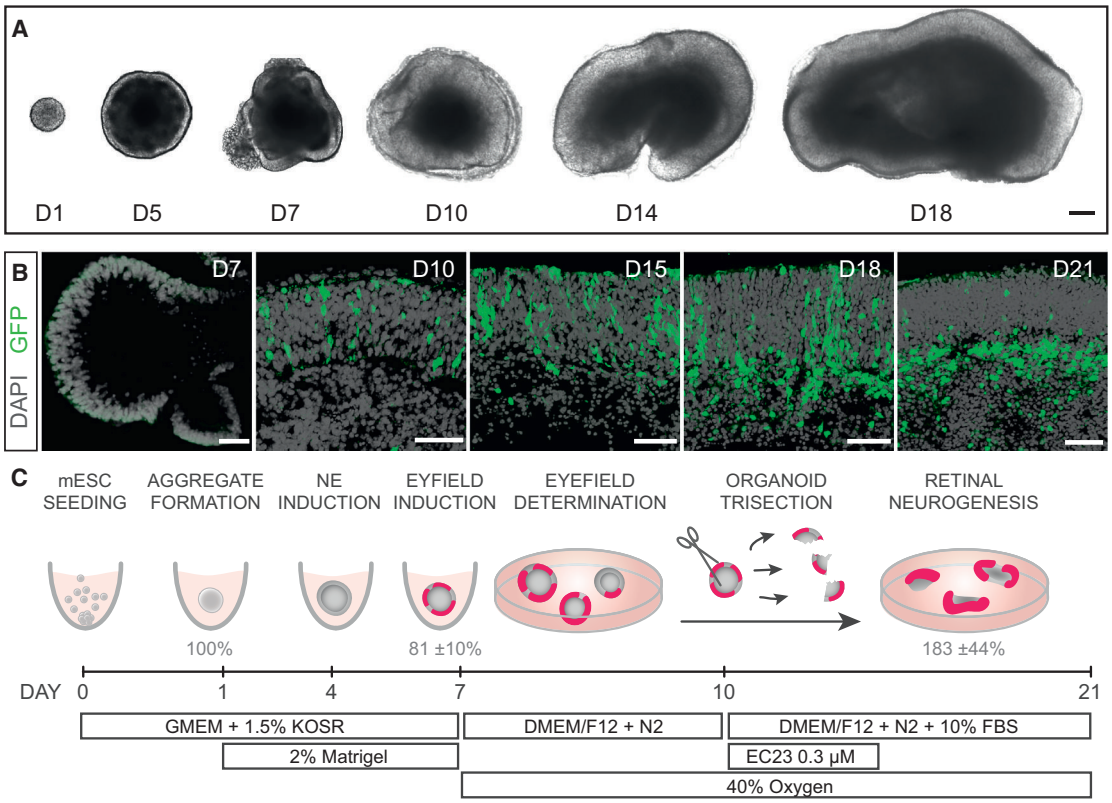

Figure 1. Description of the Retinal Organoidogenesis Trisection Protocol and the Generation of Wild-Type and hPAX6GFP mESC-Derived Retinal Organoids

(A and B) Representative phase contrast images of entire mESC-derived aggregates (A) and transgenic hPAX6GFP expression in organoid cryosections (B) at different days (D) of our trisection protocol. Aggregates are shown before (D1–10) and after (D14–18) organoid trisection.

(C) Schematic overview and timeline of the trisection protocol. mESC-derived starting (mother) aggregates are formed with 100% efficiency, out of which eyefield induction occurs in 81%, so that trisection increases the yield of retinal organoids to 183% ($N \geq 4$, $n \geq 20$). Magenta indicates eyefield tissue on D7–10 and retina thereafter. KOSR, knockout serum replacement; N2, N-2 supplement.

n = individual organoids per independent experiment (N). Scale bars, 200 μm (A) and 50 μm (B). See also Figure S1.

data indicate that aggregates with eyefield regions localized only in the aggregate main body were more frequent (65% ± 10%, n = 67) than aggregates with RAX^+ evaginations (35% ± 10%, N = 7, n = 67, $p < 0.0001$). Moreover, not all evaginations expressed eyefield markers (31% ± 7% RAX^-, 69% ± 7% RAX^+, N = 7, n = 57 evaginations analyzed; Figures 2G and S2C). Following the former protocol (Figures S1C and 2G) only 28% ± 8% (n = 25) of the starting aggregates could be used to harvest OV-like tissue, although their disposed main bodies frequently contained eyefield tissue. In addition, the majority of the starting organoids developed eyefield neuroepithelia within the main body without ever evaginating (53% ± 8%, N = 7, n = 42, $p < 0.0001$). These data imply that the default selection for evaginations omits numerous eyefield regions within mother aggregates. Consequently, merely isolating evaginations is a waste of potential retinal tissue. Also, evaginations are not reliable eyefield predictors. We reasoned that unbiased manual dissection of organoids at the eyefield stage into three evenly sized independent portions (trisection step), with potentially all of them containing eyefield-determined neuroepithelium, could enable the growth of three retinal organoids per starting aggregate (Figures S1E, 2G, and S2C).

Efficient Retinal Organoidogenesis from mESC

Following neuroepithelium trisection, the majority of organoids developed into large, continuous epithelial structures, resulting in the efficient formation of high numbers of large, stratified retinal organoids within 21 days (Figures 1, 2, 3, and S3; Table S1). Immunostaining analysis revealed organoid commitment to retinal fate, and indicated a synchronized onset and progression of retinogenesis. Quantitative analysis of cell proliferation and expression of the

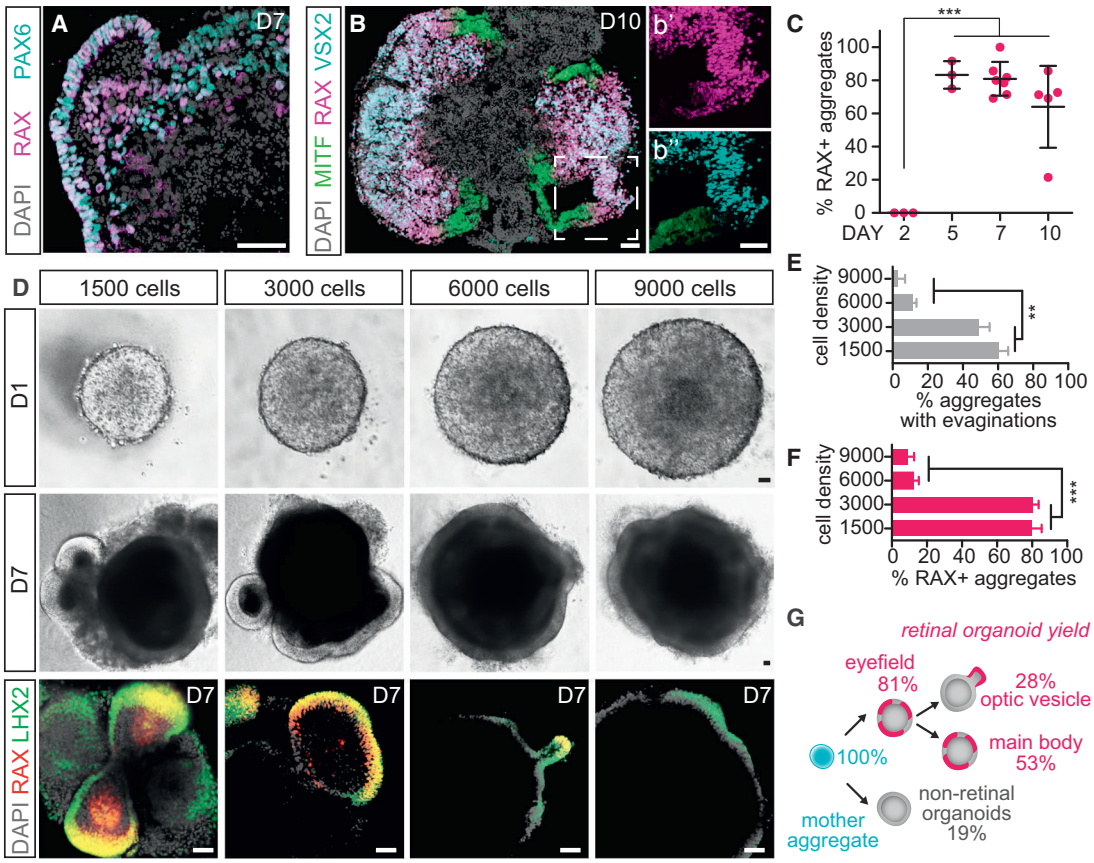

Figure 2. Low Frequency in Potential Optic-Vesicle Formation, but Not Eyefield Induction, Limits Retinal Organoidogenesis Efficiency

(A) RAX and PAX6 co-expression, indicating eyefield identity, was detected at day (D) 7.

(B) At D10, large neural retinal areas (RAX^+ $VSX2^+$) with adjacent RPE areas ($MITF^+$ RAX^- $VSX2^-$) were observed. Dashed square indicates region-of-interest shown at higher magnification: RAX^+ (b′) and $MITF^+VSX2^+$ (b″).

(C) Quantitative analysis of eyefield induction: the number of RAX^+ aggregates increases over time, based on scoring immunostained aggregate sections at D2–10 ($N \geq 3$, $n \geq 10$; 3,000 mESCs seeding density).

(D–F) Eyefield induction efficiency was dependent on cell-seeding density and did not correlate with evaginations (see also Figure S2).

(D) Phase-contrast images and immunostaining images for eyefield transcription factors RAX and LHX2 of aggregates developing from different cell-seeding densities at D1 and D7 as indicated. (E) Quantification of aggregates with evaginations and (F) RAX^+ aggregates, developed from different cell-seeding densities ($N = 4$, $n = 24$).

(G) Scheme of eyefield and optic-vesicle formation efficiency ($N = 7$, $n \geq 10$). mESC-derived starting (mother) aggregates are formed with 100% efficiency, out of which 81% develop eyefields and 28% form optic vesicles. Thus, according to the first protocol, aggregate evagination and optic-vesicle formation limit the efficiency of retinogenesis, and the majority of eyefield-containing tissues are frequently discarded.

n = individual organoids per independent experiment (N). Data shown are means ± SD. $^{**}p < 0.01$, $^{***}p < 0.001$. Scale bars, 50 μm. See also Figure S2.

neurogenic transcription factor ASCL1 (Figures 3A and 3B) suggested a regulated temporal process of organoidogenesis. The number of cells positive for the mitosis marker phosphohistone H3 (PHH3) significantly decreased from D12 to D25 ($N = 3$, $n = 5/N$, $p < 0.0001$). $ASCL1^+$ cells significantly increased from D12 to D16 ($N \geq 3$, $n = 5/N$, $p < 0.0001$) and decreased thereafter, indicating progenitor expansion followed by depletion, similar to retinogenesis in vivo. The vast majority of organoid neuroepithelia express VSX2, the earliest specific marker of retinal progenitors, at D10 (67% ± 8% $VSX2^+$ organoids) versus D7 (7% ± 2% $VSX2^+$ organoids) ($N \geq 5$, $n > 30$ per time point, $p < 0.0001$; Figures 3C and S3A). Photoreceptor-specific marker CRX was expressed in 89% ± 3% of organoids at D15, but not at D12 ($N \geq 3$, $n > 30$ scored per time point, $p < 0.0001$; Figure 3C). ELAVL3/4 (HUC/D), an early marker

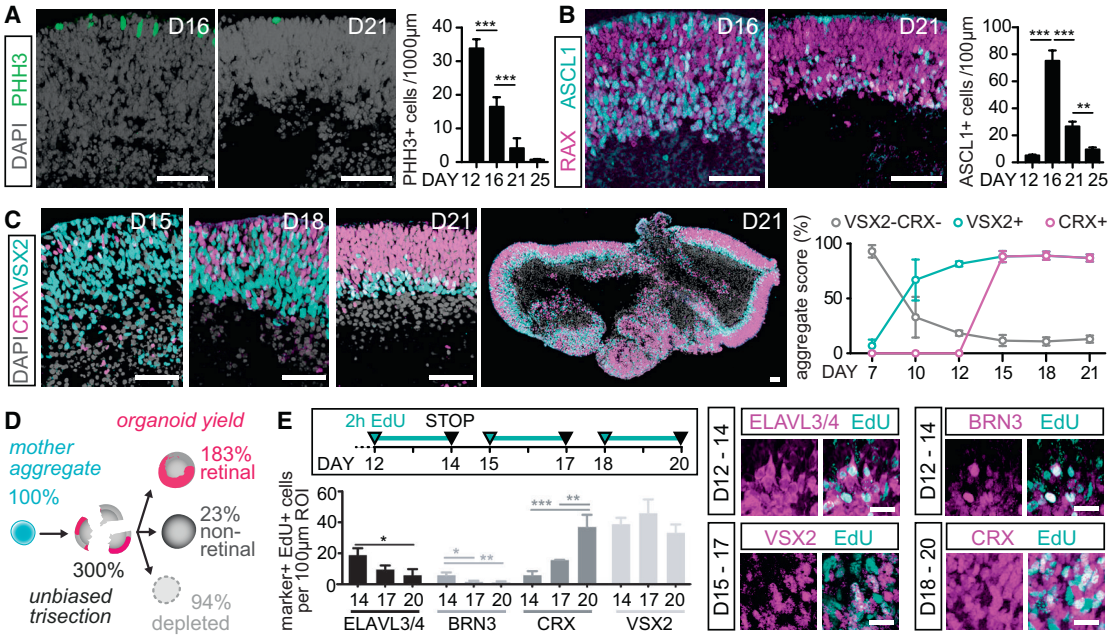

Figure 3. Efficient Retinal Histogenesis from Trisected Day-10 Aggregates

(A and B) Organoid development followed a temporal program, as evidenced by (A) mitotic marker phosphohistone H3 (PHH3) and (B) expression of the neurogenic marker ASCL1 (N = 3, n = 5).

(C) Developing large epithelial structures express markers for retinal progenitors (VSX2) and photoreceptors (CRX), indicating retinal identity. Photoreceptors were localized at the outer (apical) side of the aggregate. VSX2 is also expressed in postmitotic bipolars. Scoring analysis of (retinal) aggregates immunostained for VSX2 and CRX (N $\geq$ 4, n > 20).

(D) The trisection approach increased the total yield of retinal organoids at D21. Each starting aggregate was trisected at D10 into three evenly sized portions, out of which 183% ± 44% developed into retinal organoids (score of RAX$^+$ organoid section at D21; N = 4, n $\geq$ 20; see Supplemental Experimental Procedures and Table S1), the minority developed as non-retinal organoids (23%), and the remainder degraded by D21.

(E) Cell birthdating showed a defined timing of retinogenesis. The scheme shows 2-hr EdU pulses (open triangle) analyzed after a 2-day chase period (closed triangle). Graphs represent quantitative analysis of birthdated cells (N = 3, n = 3/N). Representative images of birthdated ELAVL3/4$^+$ (amacrine, horizontal, ganglion cells), BRN3$^+$ (ganglion cells), VSX2 (progenitors, bipolar cells), and CRX$^+$ (photoreceptors) cells.

n = individual organoids per independent experiment (N). Data are represented as means ± SD. *p < 0.05, **p < 0.01, ***p < 0.001. Scale bars, 50 µm (A–C) and 20 µm (E). See also Figure S3.

of ganglion and amacrine cells, was first detected at D10 in most of the RAX$^+$ regions (Figure S3B), marking the onset of retinal neurogenesis (50% ± 12% ELAVL3/4$^+$ RAX$^+$ organoids at D10 versus D7, N $\geq$ 5, n $\geq$ 8/N, p < 0.0001), whereas earlier, at D7, ELAVL3/4 was only found in some non-retinal organoid parts (RAX$^-$). Organoid scoring of immunostained sections revealed that markers of retinal ganglion (BRN3, ELAVL3/4) and amacrine cells (ELAVL3/4, TFAP2A, BHLHB5) were upregulated between D10 and D15, and photoreceptor (CRX, RCVRN, OTX2, RHO), bipolar (OTX2, VSX2), and Müller glia (glutamine synthetase, GLUL) cells by D15–18 (Figures S3B–S3G). Structurally, photoreceptors (CRX$^+$, RCVRN$^+$) were located on the outer (apical) surface of the organoid, and PAX6$^+$ cells (amacrine and ganglion cells) accumulated toward the organoid center, while VSX2-expressing cells (bipolar cells, Müller glia) were localized in an intermediate layer (Figures 3C and S3E), indicating that retinal organoids by D21 display a stratified architecture comparable with early postnatal retina in vivo. In comparison with previous protocols, the trisection of the starting (mother) aggregate at D10 resulted in a 3-fold increase in organoids that continued to develop. This resulted in twice as many differentiated large stratified retinal organoids at D21 as starting aggregates (183% ± 44%, N = 4, p < 0.05, number of RAX$^+$ retinal organoids scored at D21 compared with number of starting organoids; Figures 3D and S1C–S1E); only a minority were non-retinal (23%). Each D21 retinal organoid contained a major proportion of retinal tissue with a circumference of 1.2 ± 0.4 mm (N = 2, n = 10; Figures S1F and S3E), which is about one-third the size of a postmitotic mouse retina in vivo at postnatal day 10 (Löffler et al., 2015).

Approximately one-third of trisected organoids degraded before D21 by falling apart during media changes or at specimen fixation. Commonly, these organoids had no compact neuroepithelium, suggesting non-retinal phenotypes.

Reproducibility of Retinal Organoidogenesis Indicated by Cell Birthdating, and Comparative Temporal Gene Expression Analysis of Individual Organoids

To investigate the variability of retinal histogenesis among individual organoids and over time, we first conducted 5-ethynyl-2′-deoxyuridine (EdU) pulse-chase birthdating experiments (Figures 3E, S3H, and S3I). EdU was applied for 2 hr at D12, D15, or D18 and EdU-retaining cells were quantified 2 days later (data given as mean ± SD [range] per 100 μm random organoid regions of interest [ROI], N = 3, n = 3/N, 1 ROI/n). We found, on average, a total of 88 ± 20 (49–121) ELAVL3/4$^+$ (amacrine, horizontal, ganglion cells) and 18 ± 5 (4–28) BRN3$^+$ cells (ganglion cells) in developing D14 organoids. Both markers birthdate cell types that appear early in retinogenesis and the majority were also born early in the organoids, before D15 (Figure 3E, D14 versus D20, $p < 0.05$ and $p < 0.01$). The total number of BRN3$^+$ cells significantly increased over time (D20 40 ± 4 [24–58], $p < 0.01$ compared with D14) and ELAVL3/4 cells remained rather constant. The variability of birthdated ELAVL3/4 and BRN3 cells were high at all three time points according to the coefficient of variation (CV) (ratio of SD to mean; mean CV 40% and 59%, respectively). VSX2$^+$ EdU$^+$ cell numbers remained similar at all three time points (mean CV 17%): initially, they most likely represented progenitors and later bipolar cells. In contrast, significantly more CRX$^+$ (photoreceptors) appeared later, at D18 rather than D12 or D15 (D12 versus D18, $p < 0.001$). The total number of CRX$^+$ photoreceptors increased strongly over time (D14, 30 ± 2 [18–39] versus D17, $p < 0.05$, and versus D20, $p < 0.0001$; CRX$^+$ 170 ± 22 [132–219]). The low variability of CRX$^+$ EdU$^+$ cells at D17 (16 ± 0.2 [14–17], CV 1%) suggested robust photoreceptor genesis, but the variability strongly increased at D20 (37 ± 8 [20–54], CV 22%). In conclusion, the total number of BRN3 and CRX cells increased significantly over time, BRN3 and ELAV3/4 cells being born earlier and CRX cells later, indicating temporally regulated and robust retinogenesis. The birthdating data suggest differential variabilities in retina organoidogenesis, and that the variation of total cell numbers at the end of retinal organoidogenesis (D20) is higher than the variation reported in the adult mouse retina in vivo (Jeon et al., 1998).

To determine how synchronous organoids develop and to reveal potential variation at the molecular level, we performed real-time qPCR gene profiling of individual organoids. We collected 12 single organoids at each of five different time points (D7, D10, D15, D18, and D21; 60 organoids in total) and analyzed the expression of 21 genes in each organoid (normalized to *Actb*; Figures 4 and S4, Tables S2 and S3). We detected significant changes in genes associated with developing and mature retinal cells, including progenitors (proneural and stemness genes), ganglion cells, interneurons, photoreceptors, and Müller glia. Temporal gene-expression profiles indicated an early and late phase of organoidogenesis (see dashed vertical lines in Figure 4A). For example, there was a large and stable increase in *Crx*, the earliest known regulator of photoreceptor genesis, from D10 to D21 ($p < 0.00001$), whereas *Rcvrn*, indicating mature photoreceptors, increased later, at D18 ($p < 0.00001$ compared with D7). Hierarchical clustering (Figure 4B) revealed groups of genes increasing significantly before D15, indicating functions in early retinogenesis (clusters I, II, and V), such as those related to ganglion cell genesis (*Atoh7*, *Isl1*, and *Brn3*). In contrast, genes regulating late retinogenesis, such as *Nrl* (earliest known marker of postmitotic photoreceptors) and *Rlbp1* (Müller glia), became upregulated after D15 (clusters VI–VII). Many genes changed continuously (interneuron related, such as *Foxn4*, *Meis2*, *Neurod1/6*) and a few underwent smaller changes (such as *Rax*, *Pax6*, *Sox9*, *Vsx2*, mostly progenitor related). Low levels of *Mitf* suggested limited RPE cell fate.

The CV for each gene was used to capture relative variability in interindividual organoid gene expression (Mason et al., 2014) (CV include data with $\Delta\Delta$Cq values $\geq \pm 1.0$; Table S3). For example, neurogenic transcription factor *Ascl1* increased 120-fold up to D21, with a low mean variability (D10–21 mean CV 15%), indicating effective neurogenesis. *Crx* expression had a relatively low variability in the main phase of organoidogenesis (CV 12% at D15 and D18), suggesting robust photoreceptor production. However, *Crx* became more variable at D21 (CV 51%), and *Rcvrn*, indicative of further differentiated photoreceptors, was also quite variable at D18–21 (mean CV 26%). Given that retinal cell genesis is completed at D21 (Figure 3A), the observed variability might be due to processes such as ongoing cell maturation. The molecular data matched those for related proteins well (Figures 3 and S3). Photoreceptor birthdating indicated less variability during the main phase compared with the end of retinogenesis, and RCVRN protein was more heterogeneously expressed than CRX throughout a given organoid at D21 (Figures 3E, S3E, S3H, and S3I). In contrast, although ganglion and amacrine cell birthdating showed interorganoid variation throughout retinogenesis, expression of related genes (D10–18 mean CV of *Atoh7*, *Brn3b*, and *Foxn4* 14%) was less variable during neurogenesis, but stronger at the end of retinogenesis (D21 mean CV 41%). The average CV for all 21 genes at D10–21 was 35%. Overall, most genes analyzed show reproducible

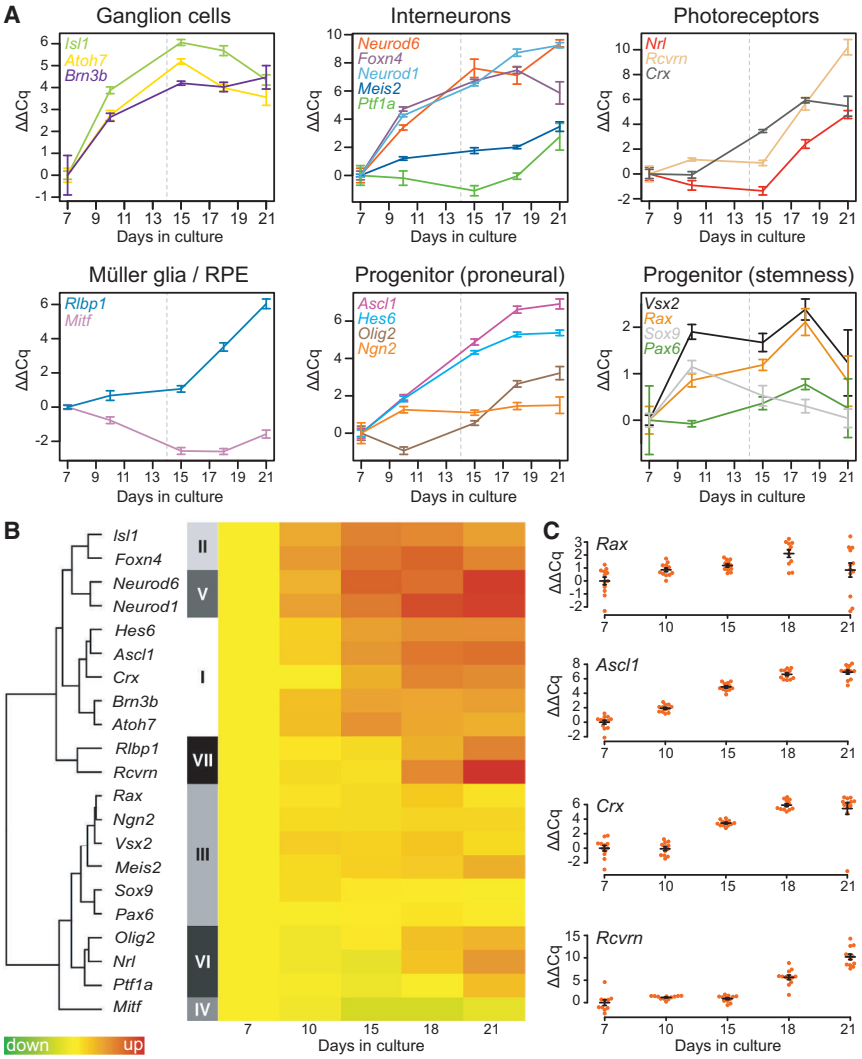

Figure 4. Temporal Gene Expression Comparison of Multiple Individual Organoids Indicated Reproducible mESC-Derived Retinogenesis

(A) Real-time qPCR analysis of retinal differentiation genes in individual organoids during organoidogenesis. At each of five different time points (days [D]), 12 single organoids were randomly sampled and analyzed individually for 21 genes (normalized to *Actb*). Average expression values (line graphs) for each gene were further normalized to D7 (ΔΔCq method) to yield relative expression values (log2 scale). Vertical dashed lines facilitate visualization of gene-expression changes before and after D15, which potentially correspond to early and late retinogenesis.

(B) Heatmap of gene-expression data shown in (A). Hierarchical clustering based on the Euclidean distance between genes (yellow-red scale corresponds to the lowest to highest value for each gene and reveals clusters I–VII).

(C) Scatterplots show gene expression of individual organoids (red dots) and thereby provide insight into interorganoid variability. Per time point, n = 12 individual organoids (n = 60 total) within one independent experiment (N).

Data are represented as means ± SEM. See also Figure S4; Tables S2 and S3.

expression across individual organoids at a given time point, and comparable temporal changes supporting an effective onset and progression of retinal histogenesis in the organoid system. However, our results also revealed differential levels of molecular and phenotypic organoid heterogeneity, suggesting that various processes, such as cell maturation, ontogenetic cell death, and contribution of non-retinal organoid tissue, might be origins of variation. Knowing these variability sources will likely facilitate further improvements in organoidogenesis and downstream applications.

Notch Signaling Inhibition Revealed Time-Dependent Progenitor Competence in mESC-Derived Retinal Organoidogenesis and Enabled the Generation of Cone- or Rod-Enriched Organoids

Based on the observed sequence of genes expressed and cells synchronously generated, we hypothesized that the trisection method facilitates reproducible experiments to differentially stimulate the generation of retinal cell types that appear early and late. Thus, we performed timed application of the Notch inhibitor DAPT (Figures 5 and S5), which is widely used to force differentiation and has been applied in late retinal organoidogenesis (Eiraku et al., 2011). We observed that early DAPT treatment (D12–14, Figures 5A and 5B) significantly increased the number of cone photoreceptors indicated by counts of TRBETA2$^+$ (226-fold, $p < 0.0001$) and S-OPSIN$^+$ cells (42-fold, $p < 0.001$) compared with control (N = 3, n = 5). The number of cells expressing OTX2, a homeodomain transcription factor expressed in early and mature photoreceptors and bipolars, was no higher than in the control. However, after early DAPT treatment the majority of OTX2$^+$ cells co-expressed SALL3, a known regulator of cone genesis. After late DAPT treatment (D16–18, Figures 5C, 5D, and S5A–S5C) the total numbers of rod

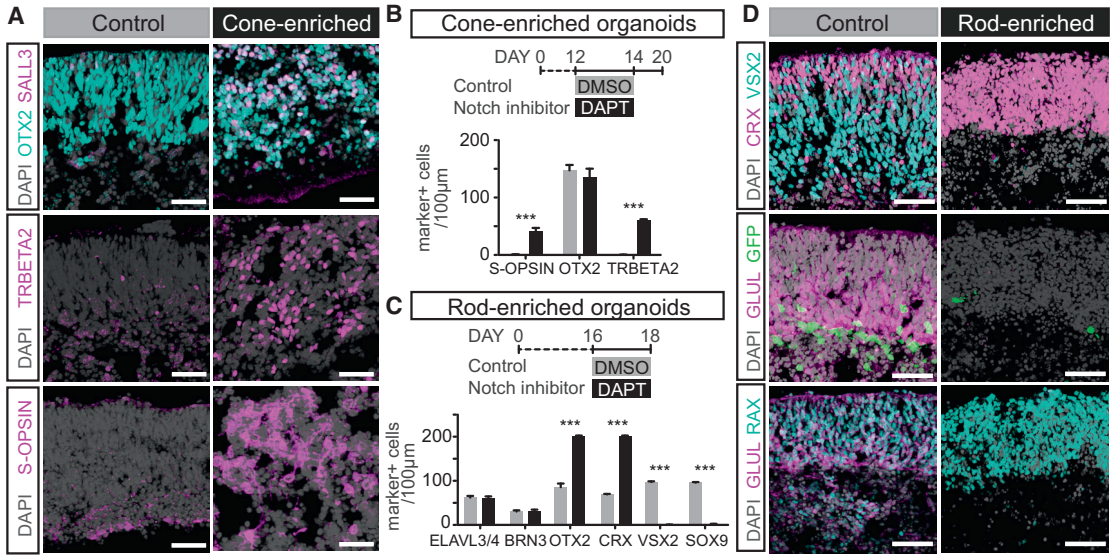

Figure 5. Generation of Rod- or Cone-Photoreceptor-Enriched Organoids by Timed Inhibition of Notch Signaling

(A and B) Notch inhibition by DAPT at early time points (D12–14) increased the number of cone photoreceptors. (A) Images of immunostained organoid sections and (B) graphs with quantification of cone marker expressing cells (TRBETA2$^+$, S-OPSIN$^+$) in DAPT-treated and control (DMSO) organoids (N = 3, n = 5).

(C and D) Notch inhibition at later time points (D16–18) resulted in rod-enriched organoids. (C) Quantification and (D) images of cell-type-specific markers (BRN3$^+$, ganglion cells; CRX$^+$, photoreceptors; ELAVL3/4$^+$, ganglion, amacrine, horizontal cells; GLUL$^+$, Müller glia; VSX2$^+$, progenitors, bipolars) in DAPT-treated and control (DMSO) organoids (N = 3, n = 5). hPAX6GFP-expressing cells were greatly reduced by Notch inhibition. Top panels of (B) and (C) show schemes of the experimental paradigms.

n = individual organoids per independent experiment (N). ***p < 0.001. Scale bars, 50 µm. Data are represented as means ± SD. See also Figure S5.

photoreceptors (CRX$^+$ and RCVRN$^+$) were strongly increased, whereas progenitors (VSX2$^+$, KI67$^+$, PAX6$^+$, hPAX6GFP$^+$), Müller glia (GLUL$^+$, SOX9$^+$), and bipolars (VSX2$^+$, PRKCA$^+$, VSX1$^+$) were almost completely absent after DAPT treatment (not all shown), suggesting that Notch inhibition prevented their fates. The numbers of ganglion and amacrine cells (ELAVL3/4$^+$) were not significantly affected. DAPT applied at D14–16 (Figure S5D) led to a less pronounced increase in photoreceptors at D18, compared with when it was applied at D16–18. Our results suggest that progenitors change their neurogenic competence throughout organoidogenesis, so that by tuning Notch signaling at defined time points it is possible to alter the proportions of retinal cells, specifically increasing cone or rod photoreceptors in correlation with early and late stages of retinal development, respectively.

hPAX6GFP Labeled Retinal Progenitors and Subtypes of Inner Neurons in mESC- and hESC-Derived Retinal Organoids

To further refine our understanding of the course of retinogenesis in the organoid system, we studied hPAX6GFP reporter expression (Figures 6 and S6). hPAX6GFP was first detected with lower fluorescent signal intensity by D10 in the neuroblast layer of organoids derived from mESC clone 1 (Figure 1B). The GFP cell numbers increased until D18 and decreased from D18 to D21. By D21, GFP$^+$ cells had accumulated in the inner nuclear layer (INL)-like region of the organoid, starting to extend processes to an inner plexiform layer (IPL)-like region (Figure 6A). Clone 1 was analyzed in more detail (Figures 6A and S6A), because GFP expression in clone 2 was rather sparse and appeared much later (Figure S6B). GFP$^+$ cells at D15–18 showed co-expression of PAX6 and RAX, SOX9, and VSX2, as well as the proliferation markers PHH3 and MCM6, suggesting retinal progenitor identity (Figures 6A and S6A). Not all PAX6$^+$ cells expressed GFP, which could be due to the species difference (mouse/human) or the lack of enhancer elements in the BAC. With ongoing progenitor depletion, more GFP$^+$ cells accumulated in the INL-like region, suggesting genesis of a subset of retinal interneurons. Indeed, the majority of GFP$^+$ cells at D21 expressed the pan-amacrine marker TFAP2A (Figure 6A). Subsets of GFP$^+$ cells immunostained for bHLHB5 (GABAergic amacrines) and co-expressed EBF3 (glycinergic amacrines) and CALB2, indicating that a broad range of amacrine subtypes can be formed in retinal organoids (Figures 6A and S6A;

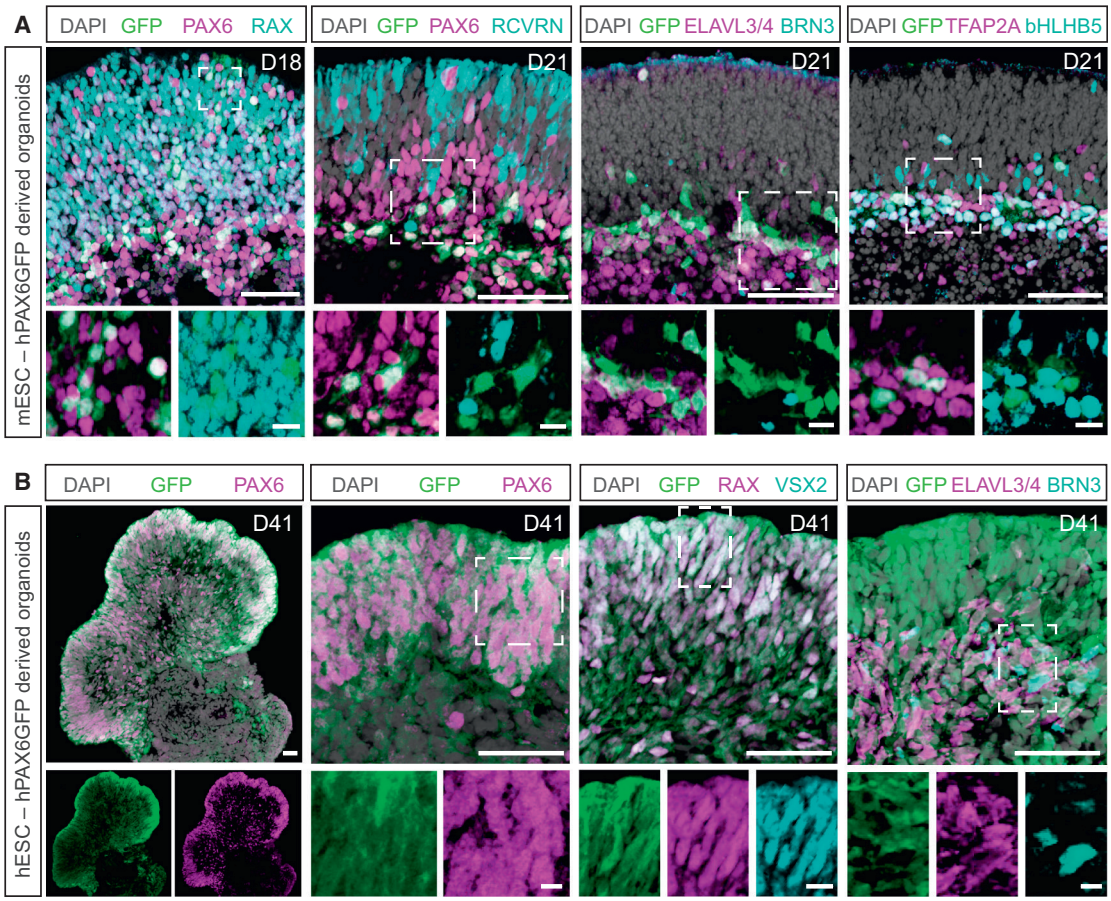

Figure 6. hPAX6GFP in mESC- and hESC-Derived Retinal Organoids

(A and B) Analysis of transgenic hPAX6GFP expression in (A) mESC-derived and (B) hESC-derived retinal organoids. (A) At day (D) 18, weakly GFP$^+$ cells in the neuroblastic layer co-expressed the retinal progenitor markers RAX and PAX6. At D21, GFP$^+$ cells had accumulated in the inner nuclear layer (INL)-like region and co-localized with ELAVL3/4 and PAX6, indicating amacrine and horizontal cells. GFP$^+$ cells are not co-labeled with photoreceptor, bipolar (OTX2, RCVRN), or ganglion cell (BRN3$^+$) markers. GFP$^+$ cells co-expressed the pan-amacrine marker TFAP2a and bHLHB5, expressed by GABAergic amacrines. (B) Overview and ROI images of immunostained human organoid sections at D41: GFP was detected in PAX6$^+$, RAX$^+$, VSX2$^+$, and ELAVL3/4$^+$ cells. Just as in mouse organoids (A), ganglion cells (BRN3) were mostly GFP negative.

Scale bars represent 50 μm, and 10 μm for high magnifications shown in (A) and (B). See also Figure S6.

Table S1). At D21, GFP$^+$ cells expressed PAX6, and did not co-localize with photoreceptor or bipolar markers (CRX, RCVRN, OTX2). The GFP$^+$ progeny contained amacrine and horizontal cells (ELAVL3/4), but no retinal ganglion cells (BRN3) or Müller glia (GLUL). We also positively probed hPAX6GFP reporter expression in CNS regions outside the retina in mESC-derived cerebral organoids (Figure S6C; Eiraku and Sasai, 2011). We sought to provide initial evidence for hPAX6GFP expression in human retinal organoids derived from two previously reported hESC lines (Rostovskaya et al., 2012) by adapting a previously published protocol (Nakano et al., 2012). Comparable with our trisection approach in the mESC system, we manually dissected each individual human organoid into three to five evenly sized tissue parts on D18 after aggregation. In D41 organoids, GFP was detected in regions with neuroepithelial structure in two different hESC reporter lines, which co-labeled with PAX6, RAX, and VSX2: these indicated the identity of the retinal progenitors (Figure 6B; N = 4; line 2 not shown). Comparable with previous reports, we observed the first ELAVL3/4$^+$ (amacrine and horizontal cells) and BRN3$^+$ (ganglion cells) cells in D41 hESC-derived retinal organoids in line 1, but not line 2 (not shown). Thus, just as in mouse retinal organoids (Figure 6A), human ganglion cells (BRN3$^+$) were mostly GFP$^-$ (Figure 6B), while GFP labeled mouse and human progenitor (RAX$^+$, PAX6$^+$) and amacrine cells (ELAVL3/4$^+$).

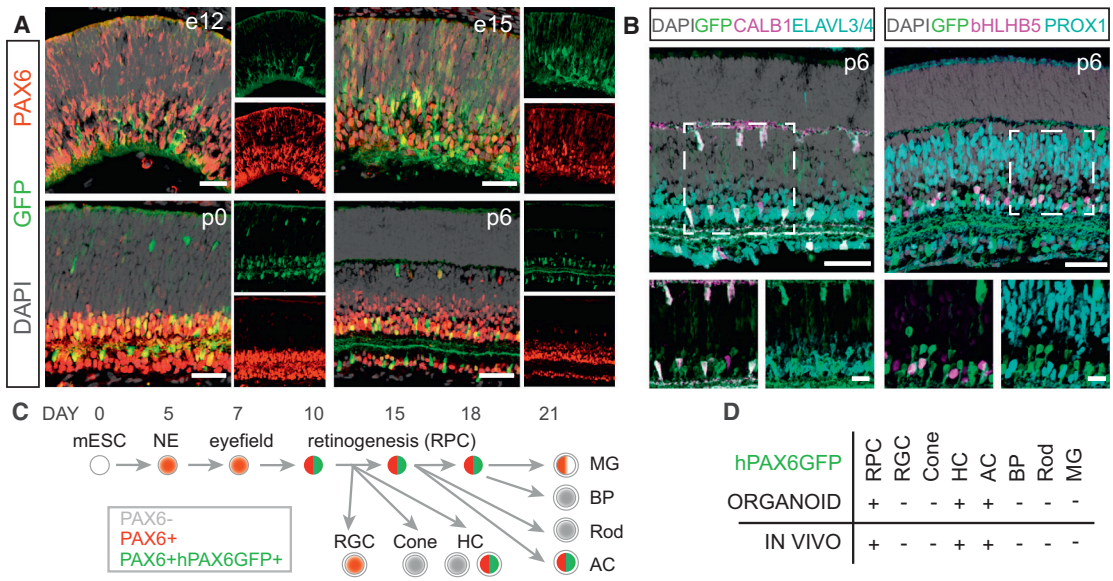

Figure 7. Characterization of Transgenic hPAX6GFP Expression in the Developing and Mature Mouse Retina

(A) Images of GFP and PAX6 immunostained hPAX6GFP reporter mice retina sections at embryonic days (e) 12 and 15, and postnatal days (p) 0 and 6 show GFP in progenitors and subsets of PAX6$^+$ postmitotic horizontal and amacrine neurons.

(B) Similar to the retinal organoids, GFP$^+$ cells in the mouse retina also co-expressed the markers CALB1 (amacrine, horizontal cells) and ELAVL3/4 (amacrine, horizontal, ganglion cells), but not the ganglion cell marker BRN3. Subsets of GFP$^+$ cells also co-expressed PROX1 and bHLHB5 (amacrines).

(C and D) Summary scheme (C) and comparison table (D) show that transgenic hPAX6GFP expression showed similar retinal cell types in the retinal organoid system and mouse retina in vivo. GFP expressed (+)/not expressed (−); RPC, retinal progenitor cell; RGC, retinal ganglion cell; HC, horizontal cell; AC, amacrine cell; BP, bipolar cell; MG, Müller glia; NE, neuroepithelium.

Scale bars represent 50 μm, and 10 μm for high magnifications shown in (B). See also Figures 6, S6, and S7.

Comparative hPAX6GFP Expression Analysis in Retinal Organoids and Mouse Retina In Vivo Revealed Similar Expression Patterns and Timing

We sought to gain further insights into organoidogenesis by comparative analysis of retinal organoids derived from the hPAX6GFP transgenic reporter mESC line (Figures 6 and S6) and the respective transgenic mouse strains (Figures 7 and S7). We generated transgenic mice carrying the same hPAX6GFP reporter as the mESC. GFP was first detected by embryonic day 12 (e12) in the retina in vivo (Figure 7A), when neurogenesis starts. Most GFP$^+$ cells co-expressed PAX6 and various progenitor markers matching our organoid data. By postnatal day 0 (p0), GFP$^+$ progenitors had become more restricted to the central retina (Figures 7A and S7A). By p0–6, GFP was detected in the developing INL and ganglion cell layer (GCL), and by p11 (the end of retinogenesis) and in adults it was also detected in the horizontal cell layer (Figures 7A, 7B, and S7A–S7C). GFP$^+$ cells were evenly distributed in the central and peripheral developing and postmitotic retina (see retina section and flat-mount data, Figures S7A and S7B), but not in the RPE or lens, both of which expressed PAX6 (data not shown). By p6–11, GFP$^+$ cells co-expressed the amacrine and horizontal cell markers CALB1, ELAVL3/4, and PROX1, and the amacrine markers bHLHB5 and SOX2 (Figures 7B and S7D). In line with our results in mouse and human retinal organoids, hPAX6GFP did not co-localize with retinal ganglion cells in vivo (Figure S7D). GFP was not expressed in Müller glia in vivo but was expressed in mouse retinal explant culture, suggesting upregulation of hPAX6GFP in reactive glia (Figure S7E). These comparative analyses reveal that hPAX6GFP is similarly expressed in transgenic mice in vivo and in the mESC- and hESC-derived retinal organoids in a subset of developing retinal progenitors, in amacrine and horizontal cells (Figures 7C and 7D).

DISCUSSION

We developed an efficient approach for retinal organoidogenesis stemming from the pioneering protocol (Eiraku et al., 2011) which makes use of the power of PSC to generate self-organized, complex, stratified 3D retinal tissue. The original protocol utilizes the generation of OC-like structures, but requires the OV-like evagination of the neuroepithelium and its manual dissection. We observed

that about 80% of organoid neuroepithelia developed into eyefields, comparable with previous publications (Table S1). However, using E14TG2a mESC, or the original reported RAX-GFP mESC line (kindly provided by Y. Sasai, Japan [Eiraku et al., 2011]), others (Hiler et al., 2015) and our group (RAX-GFP data not shown) observed that OV-like structures form irregularly and OC-like structures infrequently. The fact that evagination of the eyefield neuroepithelium occurs rather inefficiently in about 20% of aggregates, and varies between PSC lines (Hiler et al., 2015; see also Figure 2G and Table S1), which might depend on the intrinsic capacity of the PSC line or on culture conditions, currently limits retinal organoidogenesis. Notably, eyefield domains achieved with E14TG2a mESCs are rather large (covering up to 50% of the organoid at D10). OV size has been reported to be a critical factor influencing OC formation (Decembrini et al., 2014; Eiraku et al., 2011), suggesting that this may be a major factor preventing OC formation. Thus, factors affecting eyefield restriction and expansion, such as sonic hedgehog, may be differentially regulated in different mESC lines. By merely isolating the aggregate evaginations, the majority of eyefield tissues were discarded. Furthermore, our data show that evaginations frequently lack eyefields, and are thus not reliable predictors of prospective retinas. By trisecting an unbiased simple organoid neuroepithelia, we overcame these limitations. The trisection protocol utilizes all starting aggregates to improve the retinal organoid yield and enables robust generation of large, stratified 3D retinal organoids derived from wild-type mESC.

Our data show that the trisection approach results in the generation of retinal organoids with a cell birth order and developmental timing comparable with mice in vivo. Expression of bHLHB5 (GABAergic amacrines) and EBF3 (largely glycinergic amacrines) in different subsets of amacrine cells at D21 also show not only that the major retinal cell types differentiate in mouse retinal organoids but also that subtype specification is induced. To gain further understanding of the reproducibility of retinal organoidogenesis, we performed cell birthdating experiments and analyzed interindividual organoid variation in gene-expression levels. The molecular data were consistent with the immunostaining-based phenotypic results, showing significant differences in the types of cells born earlier (ganglion cells) and later (photoreceptors), as well as in related gene-expression changes. Overall, the data indicate a robust onset, temporal order, and progression of retinal histogenesis; this suggests that regulated developmental programs are repeated. However, comparing individual organoids also revealed differential gene-expression variability. Although some genes are expressed quite robustly, others are more variable at the onset, end, or even throughout retinal organoidogenesis. Many of the genes investigated have functions not only in the developing but also in the maturing and adult retina. Whether the observed gene-expression variability is the cause of the phenotypic heterogeneity of the organoids at the protein level, or whether they are consequences of other processes (e.g., ontogenetic cell death and cell maturation) remains unknown. Future studies of the origins and consequences of gene-expression variation in retinal development are needed to refine our understanding of the relationships between phenotypic and molecular heterogeneity in retinal organoidogenesis and animals in vivo.

Comparative analysis of transgenic hPAX6GFP expression revealed similarities between the retinal organoid system and the mouse retina in vivo. Our analyses indicated a similar sequence of hPAX6GFP$^+$ retinal cell types in mice in vivo, and in mESC- and hESC-derived retinal organoids: progenitors and retinal interneurons (horizontal and amacrine cells). This was despite differences in the number of hPAX6GFP$^+$ cells. In early postmitotic mouse retinal organoids hPAX6GFP$^+$ cells participated in the formation of an IPL-like region, indicating that important features of the ultimately highly complex inner architecture of the mature retina are generated. The two mESC lines analyzed expressed GFP differentially, possibly due to different insertion sites. The hPAX6GFP transgene does not contain all its enhancers, and carries the GFP-containing cassette in exon 4 (Figure S1), disrupting gene function, so that the observed GFP pattern may also indicate cell heterogeneity. This might be of significance, since the functional importance of spatiotemporal levels of PAX6 expression during development is well established (Shaham et al., 2012). Our results suggest that the hPAX6GFP transgenic reporter in the human and mouse ESC organoid system might be a useful tool for studying progenitor lineages, neuronal differentiation, maturation, survival, stratification, and neural wiring in retinal and brain organoids. Moreover, the organoid system might offer a faster way to identify robust and reliable reporter expression in the tissue of interest, prior to the generation of transgenic mice.

For current and future applications of the 3D retinal organoid system, the neuroepithelium trisection approach provides significant advantages in comparison with the mESC protocols currently available (Table S1 and Figures S1C–S1E) and, as indicated by our experiments with the hPAX6GFP hESC, potentially also for human PSCs. First, this approach does not require any transgenic reporter and does not involve the formation of complex evaginations or eyecups, processes reported to be inefficient in all of the published protocols. Therefore, it provides full flexibility for the application of any, and multiple, fluorescent reporters for retinal-organoid-based research. Second, our protocol yields about twice as many retinal organoids as starting aggregates, and retina sizes are comparable with, or even bigger than, those reported previously. Hiler et al.

(2015) recently reported that, following the evagination isolation protocol, the frequency of retinal organoids derived per starting aggregate is about 46% for the RAX-GFP mESC line: our protocol yields 183%. Third, organoids grown with this protocol develop stratified neural retinal tissue, with defined outer nuclear layer, inner nuclear layer, and GCLs, although at the final time point (D21) the inner and outer plexiform layers had not completely formed. Fourth, previous adaptions (Decembrini et al., 2014; Gonzalez-Cordero et al., 2013) of the original 3D retinal organoid protocol have made reporter and OC formation independent by omitting the manual dissection/selection step and, instead, maintaining and maturing the retinal domain inside the mother aggregate. This approach even allows the protocol to be automated. Although photoreceptors develop well inside the mother aggregate, inner retinal cell types and layers either differentiate less well or degenerate more. This may be an advantage for studies focusing on photoreceptors and requiring high numbers of them. However, it might be inconvenient for studies that require the complete retinal structure. Additional modifications, such as maintaining the organoid in Matrigel for two additional days (Decembrini et al., 2014; Gonzalez-Cordero et al., 2013), which restricts its expansion, might be necessary to develop a 3D retina. Our trisection protocol also reduced the size of the organoid at this temporal stage, and likely facilitates further development by, e.g., increasing access for nutrients and oxygen and allowing for better expansion by removing restrictive neighboring tissue. This might also increase the survival of organoids in long-term culture—specifically in the human retinal organoid system—and potentially also for organoidogenesis of other types of tissue. Fifth, timed drug-based Notch inhibition enables forced differentiation of early and late retinal cell types in the organoid system, indicating that neurogenic competence is regulated in a similar way to retina in vivo (Cepko, 2014). Thus, our data suggest a reliable approach for generating large numbers of cone photoreceptors, which are of interest for various applications such as cell replacement therapy.

Therefore, one of our future endeavors will be to apply and optimize the trisection protocol to the human retinal organoid system, and to perform research on human neuronal development, disease modeling, tissue repair, regeneration, and therapies in translational medicine.

EXPERIMENTAL PROCEDURES

Generation of hPAX6GFP mESCs and Reporter Mouse

The eGFP-IRES-puro-pA-FRT-PGK-neo-pA-FRT cassette was inserted directly after the initiating methionine (ATG) in exon 4 of the *hPAX6* gene in the BAC RP11-26B16, followed by the insertion of piggyBac inverted repeats by recombineering, as previously described (Rostovskaya et al., 2012; Figure S1A). The BAC was co-transfected with hyPBase expression vector to mESC; blasticidin-resistant clones were screened by PCR for transposition signature, and phenotyped using pluripotency markers (Figure S1B). Generation of transgenic mice was performed as previously described (Rostovskaya et al., 2013). Animal licenses were obtained according to the TU Dresden and German Federal regulations. See Supplemental Experimental Procedures.

mESC Culture

E14TG2a (MMRRC, UC Davis) wild-type and hPAX6GFP transgenic mESCs were cultured in mESC medium supplemented with 10^3 U/ml leukemia inhibitory factor and 1 μM PD0325901. Cells were passaged every 2–3 days using TrypLE Express (Invitrogen).

mESC Retinal Organoidogenesis

Retinal differentiation was adapted from a previously reported protocol (Eiraku et al., 2011). In brief, mESC aggregation in 96-well plates was defined as day 0 (D0), and 2% Matrigel was added on D1. After being cultured (20% O_2) until D7, the organoids were transferred to bacterial-grade petri dishes for further culture in retinal maturation medium 1 (40% O_2). On D10, the organoids were manually trisected using surgical tweezers (Fine Science Tools, Dumont No. 5) and further cultured in retinal maturation medium 2. EC23 (0.3 μM) was added from D10 to D14. See Supplemental Experimental Procedures.

hESC Retinal Organoidogenesis

Retinal differentiation of H7.S6 PAX6GFP BAC transgenic hESC was performed by adapting a previously reported protocol (Nakano et al., 2012). Permission to work with hESCs was granted by the Robert Koch Institute, Berlin, Germany. See Supplemental Experimental Procedures.

Tissue Preparation and Immunohistochemistry

Samples were fixed in 4% paraformaldehyde, and cryoprotected (30% sucrose, overnight) and embedded in tissue-freezing medium (Jung). Frozen sections were cut at 12–20 μm. Immunostaining was performed using standard protocols. See Supplemental Experimental Procedures.

Single-Organoid qPCR

RNA from single retinal organoids (n = 12 randomly selected individual organoids per time point) were isolated and reverse transcribed using a Power SYBR Green Cells-to-Ct kit (Ambion). Gene-specific primers were designed using Primer3 (Simgene.com) software, spanning an exon-exon junction where applicable. Real-time qPCR reactions were performed with SsoFast EvaGreen Supermix (Bio-Rad) according to the manufacturer's instructions (C1000, CFX96, Bio-Rad). See Supplemental Experimental Procedures.

Data Analysis

Samples were imaged on a Zeiss ApoTome2, LSM Confocal, or Spinning Disc Confocal microscope. For aggregate scoring, analysis of each aggregate was performed by assessing marker expression on

multiple consecutive sections (>8) on at least two slides (N ≥ 4 independent experiments, n > 10 aggregates/N). For cell counting and co-localization analysis, random ROIs 100 μm wide were used. The x axis of each ROI was positioned radially to the organoid center, with the y axis aligned perpendicular to the organoid surface. ROI images are z axis projections of 5 × 1 μm acquired in Apotome mode using a 20× Plan-Apochromate objective. Cells were counted on 3D reconstructed images using ZEN blue (Zeiss). Organoid circumference and retinal length were measured using the length tool in ZEN blue (Zeiss). Statistical analysis was performed with GraphPad Prism using one-way ANOVA (Tukey's post hoc test) or Student's unpaired t test. Results were considered significant for $p < 0.05$ and data were plotted as mean ± SD if not noted otherwise. See Supplemental Experimental Procedures.

SUPPLEMENTAL INFORMATION

Supplemental Information includes Supplemental Experimental Procedures, seven figures, and three tables and can be found with this article online at http://dx.doi.org/10.1016/j.stemcr.2016.03.001.

AUTHOR CONTRIBUTIONS

M.V., V.B., and M.K. designed the experiments. M.V. and M.K. wrote the paper. M.R. and K.A. generated hPAX6GFP transgenic mESC and mice. M.V. and M.Z. performed the experiments. M.V., M.Z., R.O., and M.K. analyzed the data.

ACKNOWLEDGMENTS

We thank Y. Sasai (RIKEN, Japan) for the RAX-GFP mESC line, M. Wegner (University of Erlangen, Germany) for SOX9, E. Tanaka (CRTD, Germany) for RAX and CRX, and D. Forrest (NIDDK, USA) for TRβ2 antibodies. We thank J. Brzezinski (University of Colorado Denver), S. Oakeley (Basel, Switzerland), G. Kempermann (DZNE), M. Ader, F. Calegari, N. Ninov, and E. Tanaka (all CRTD) for helpful comments on the manuscript. We thank M. Obst, the light microscopy facility, and the animal facility for excellent support. This work was kindly supported by the Funding Programs for DZNE Helmholtz (M.K.), TU Dresden CRTD (M.K.), DFG (KA2794/3-1; SPP1738) (M.K.), MedDrive TU Dresden UKD-Medical Faculty (M.K.), research award Novartis Pharma GmbH (M.K.), Volkswagen Foundation Freigeist fellowship (V.B.), and the European Union's sixth Framework Program ESTOOLS (K.A.).

Received: May 22, 2015
Revised: March 2, 2016
Accepted: March 3, 2016
Published: March 31, 2016

REFERENCES

Boucherie, C., Mukherjee, S., Henckaerts, E., Thrasher, A.J., Sowden, J.C., and Ali, R.R. (2013). Brief report: self-organizing neuroepithelium from human pluripotent stem cells facilitates derivation of photoreceptors. Stem Cells *31*, 408–414.

Busskamp, V., Krol, J., Nelidova, D., Daum, J., Szikra, T., Tsuda, B., Jüttner, J., Farrow, K., Scherf, B.G., Alvarez, C.P., et al. (2014). miRNAs 182 and 183 are necessary to maintain adult cone photoreceptor outer segments and visual function. Neuron *83*, 586–600.

Cepko, C. (2014). Intrinsically different retinal progenitor cells produce specific types of progeny. Nat. Rev. Neurosci. *15*, 615–627.

Decembrini, S., Koch, U., Radtke, F., Moulin, A., and Arsenijevic, Y. (2014). Derivation of traceable and transplantable photoreceptors from mouse embryonic stem cells. Stem Cell Rep. *2*, 853–865.

Eiraku, M., and Sasai, Y. (2011). Mouse embryonic stem cell culture for generation of three-dimensional retinal and cortical tissues. Nat. Protoc. *7*, 69–79.

Eiraku, M., Takata, N., Ishibashi, H., Kawada, M., Sakakura, E., Okuda, S., Sekiguchi, K., Adachi, T., and Sasai, Y. (2011). Self-organizing optic-cup morphogenesis in three-dimensional culture. Nature *472*, 51–56.

Gonzalez-Cordero, A., West, E.L., Pearson, R.A., Duran, Y., Carvalho, L.S., Chu, C.J., Naeem, A., Blackford, S.J., Georgiadis, A., Lakowski, J., et al. (2013). Photoreceptor precursors derived from three-dimensional embryonic stem cell cultures integrate and mature within adult degenerate retina. Nat. Biotechnol. *31*, 741–747.

Hiler, D., Chen, X., Hazen, J., Kupriyanov, S., Carroll, P.A., Qu, C., Xu, B., Johnson, D., Griffiths, L., Frase, S., et al. (2015). Quantification of retinogenesis in 3D cultures reveals epigenetic memory and higher efficiency in iPSCs derived from rod photoreceptors. Cell Stem Cell *17*, 101–115.

Jeon, C.J., Strettoi, E., and Masland, R.H. (1998). The major cell populations of the mouse retina. J. Neurosci. *18*, 8936–8946.

Lamba, D.A., Karl, M.O., Ware, C.B., and Reh, T.A. (2006). Efficient generation of retinal progenitor cells from human embryonic stem cells. Proc. Natl. Acad. Sci. USA *103*, 12769–12774.

La Torre, A., Hoshino, A., Cavanaugh, C., Ware, C.B., and Reh, T.A. (2015). The GIPC1-Akt1 pathway is required for the specification of the eye field in mouse embryonic stem cells. Stem Cells *33*, 2674–2685.

Löffler, K., Schäfer, P., Völkner, M., Holdt, T., and Karl, M.O. (2015). Age-dependent Müller glia neurogenic competence in the mouse retina. Glia *63*, 1809–1824.

Mason, E.A., Mar, J.C., Laslett, A.L., Pera, M.F., Quackenbush, J., Wolvetang, E., and Wells, C.A. (2014). Gene expression variability as a unifying element of the pluripotency network. Stem Cell Rep. *3*, 365–377.

Nakano, T., Ando, S., Takata, N., Kawada, M., Muguruma, K., Sekiguchi, K., Saito, K., Yonemura, S., Eiraku, M., and Sasai, Y. (2012). Self-formation of optic cups and storable stratified neural retina from human ESCs. Cell Stem Cell *10*, 771–785.

Osakada, F., Ikeda, H., Mandai, M., Wataya, T., Watanabe, K., Yoshimura, N., Akaike, A., Akaike, A., Sasai, Y., and Takahashi, M. (2008). Toward the generation of rod and cone photoreceptors from mouse, monkey and human embryonic stem cells. Nat. Biotechnol. *26*, 215–224.

Phillips, M.J., Perez, E.T., Martin, J.M., Reshel, S.T., Wallace, K.A., Capowski, E.E., Singh, R., Wright, L.S., Clark, E.M., Barney, P.M., et al. (2014). Modeling human retinal development with patient-specific induced pluripotent stem cells reveals multiple roles for visual system homeobox 2. Stem Cells *32*, 1480–1492.

Rostovskaya, M., Fu, J., Obst, M., Baer, I., Weidlich, S., Wang, H., Smith, A.J., Anastassiadis, K., and Stewart, A.F. (2012). Transposon-mediated BAC transgenesis in human ES cells. Nucleic Acids Res. *40*, e150.

Rostovskaya, M., Naumann, R., Fu, J., Obst, M., Mueller, D., Stewart, A.F., and Anastassiadis, K. (2013). Transposon mediated BAC transgenesis via pronuclear injection of mouse zygotes. Genesis *51*, 135–141.

Shaham, O., Menuchin, Y., Farhy, C., and Ashery-Padan, R. (2012). Pax6: a multi-level regulator of ocular development. Prog. Retin. Eye Res. *31*, 351–376.

Zhong, X., Gutierrez, C., Xue, T., Hampton, C., Vergara, M.N., Cao, L.-H.H., Peters, A., Park, T.S., Zambidis, E.T., Meyer, J.S., et al. (2014). Generation of three-dimensional retinal tissue with functional photoreceptors from human iPSCs. Nat. Commun. *5*, 4047.

Stem Cell Reports
Article

OPEN ACCESS

Treating Diet-Induced Diabetes and Obesity with Human Embryonic Stem Cell-Derived Pancreatic Progenitor Cells and Antidiabetic Drugs

Jennifer E. Bruin,[1] Nelly Saber,[1] Natalie Braun,[1] Jessica K. Fox,[1] Majid Mojibian,[1] Ali Asadi,[1] Campbell Drohan,[1] Shannon O'Dwyer,[1] Diana S. Rosman-Balzer,[2] Victoria A. Swiss,[2] Alireza Rezania,[2] and Timothy J. Kieffer[1,3,*]

[1]Laboratory of Molecular and Cellular Medicine, Department of Cellular & Physiological Sciences, Life Sciences Institute, University of British Columbia, Vancouver, BC V6T 1Z3, Canada
[2]BetaLogics Venture, Janssen R & D LLC, Raritan, NJ 08869, USA
[3]Department of Surgery, University of British Columbia, Vancouver, BC V6T 1Z3, Canada
*Correspondence: tim.kieffer@ubc.ca
http://dx.doi.org/10.1016/j.stemcr.2015.02.011

SUMMARY

Human embryonic stem cell (hESC)-derived pancreatic progenitor cells effectively reverse hyperglycemia in rodent models of type 1 diabetes, but their capacity to treat type 2 diabetes has not been reported. An immunodeficient model of type 2 diabetes was generated by high-fat diet (HFD) feeding in SCID-beige mice. Exposure to HFDs did not impact the maturation of macroencapsulated pancreatic progenitor cells into glucose-responsive insulin-secreting cells following transplantation, and the cell therapy improved glucose tolerance in HFD-fed transplant recipients after 24 weeks. However, since diet-induced hyperglycemia and obesity were not fully ameliorated by transplantation alone, a second cohort of HFD-fed mice was treated with pancreatic progenitor cells combined with one of three antidiabetic drugs. All combination therapies rapidly improved body weight and co-treatment with either sitagliptin or metformin improved hyperglycemia after only 12 weeks. Therefore, a stem cell-based therapy may be effective for treating type 2 diabetes, particularly in combination with antidiabetic drugs.

INTRODUCTION

The International Diabetes Federation estimates that up to 95% of the ~380 million people worldwide who are affected by diabetes suffer from type 2 diabetes (International Diabetes Federation, 2014). Thus, the potential impact of a novel treatment for type 2 diabetes is enormous. Despite obvious differences in the pathogenesis of type 1 and 2 diabetes, both diseases are characterized by impaired glucose homeostasis resulting from insufficient insulin production by pancreatic beta cells. In type 1 diabetes, beta cell destruction by the immune system is rapid and extensive, causing severe insulin deficiency. In contrast, beta cell failure in type 2 diabetes occurs gradually over time and is associated with peripheral insulin resistance. Clinical studies have shown that patients with type 2 diabetes also have reduced beta cell mass (Butler et al., 2003; Yoon et al., 2003) and declining beta cell function during the progression from pre-diabetes to overt diabetes (Weyer et al., 1999; Ferrannini et al., 2005). Therefore, treatment strategies for type 2 diabetes should be aimed at restoring beta cell mass and/or function, in addition to improving insulin sensitivity (Halban, 2008; Kahn et al., 2014).

Transplantation of cadaveric human islets can restore insulin-independence in patients with type 1 diabetes (Shapiro et al., 2000; Ryan et al., 2001), but this approach has not been actively pursued for type 2 diabetes, likely due to the inadequate supply of donor islets, risk of immunosuppression, and perceived hurdle of insulin resistance. The obstacle of an insufficient cell supply may be overcome with the use of human embryonic stem cells (hESCs). We previously demonstrated that hESC-derived pancreatic progenitor cells reversed hyperglycemia in a mouse model of type 1 diabetes characterized by severe beta cell destruction and insulin deficiency (Rezania et al., 2012, 2013; Bruin et al., 2013). However, the efficacy of this stem cell-based therapy for treating hyperglycemia in an obesogenic and insulin-resistant environment, such as in type 2 diabetes, has not been reported. Based on evidence that intensive insulin therapy improves insulin sensitivity, glycemic control, and beta cell function in patients with type 2 diabetes (Weng et al., 2008; Kramer et al., 2013), we hypothesized that hESC-derived insulin-secreting cells may also be effective for this patient population.

Our first aim was to establish a model of type 2 diabetes in immunodeficient mice that would be compatible with xenotransplantation. Different strains of rodents have widely variable susceptibility to high-fat diet (HFD)-induced obesity and/or hyperglycemia (Srinivasan and Ramarao, 2007; Svenson et al., 2007; Hariri and Thibault, 2010). Moreover, insulin resistance, a hallmark feature of type 2 diabetes (Kahn et al., 2006), is thought to be driven primarily by obesity-associated inflammation (reviewed in Kalupahana et al., 2012; Osborn and Olefsky, 2012), and

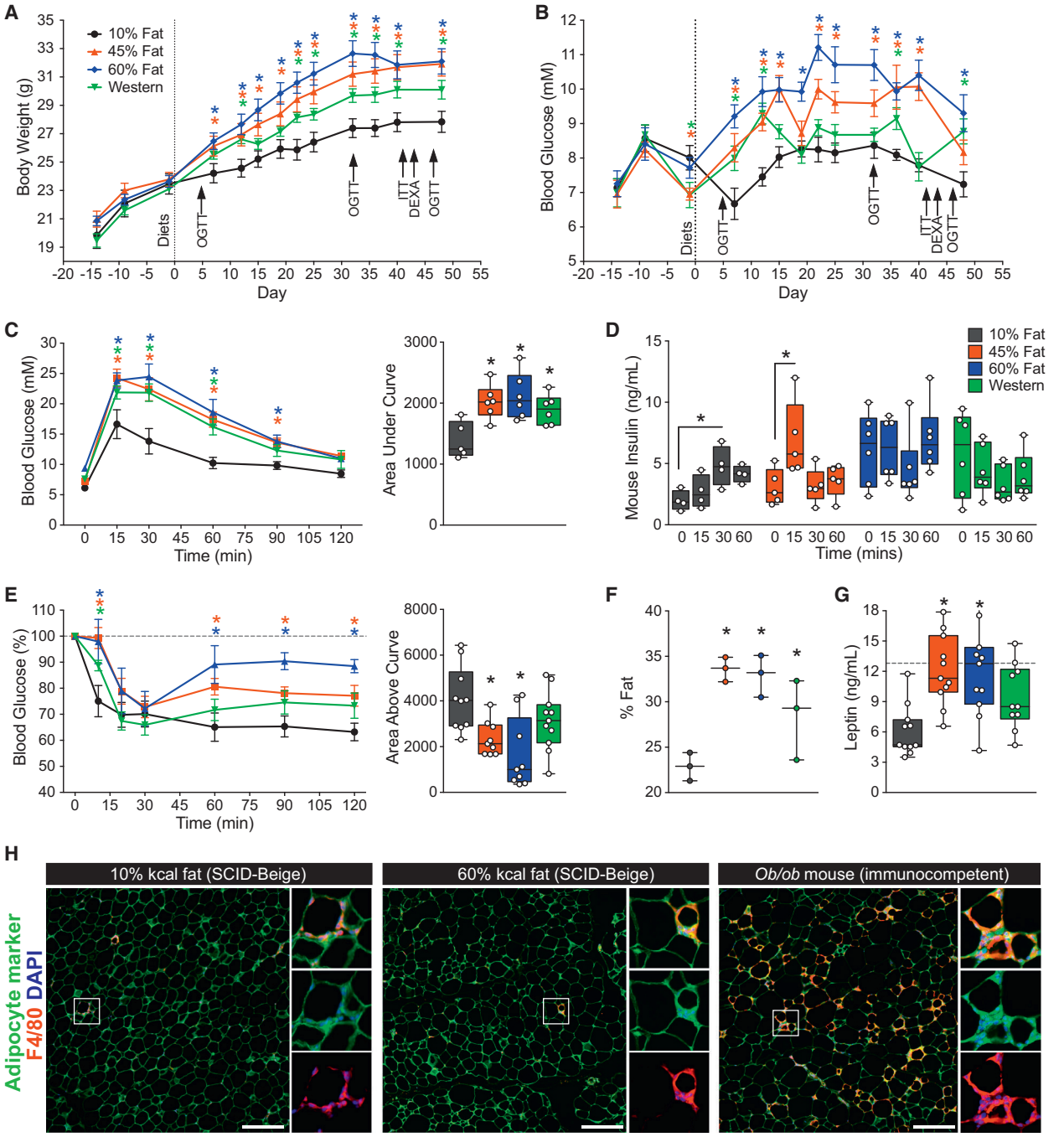

Figure 1. SCID-Beige Mice Rapidly Develop Obesity, Fasting Hyperglycemia, Glucose Intolerance, and Insulin Resistance Following Exposure to HFDs

(A and B) Body weight (A) and fasting blood glucose levels (B) were measured during a 14-day acclimation period on normal chow and for 51 days following administration of one of the following diets: 10% fat (black; n = 11 mice), 45% fat (red; n = 11 mice), 60% fat (blue; n = 11 mice), or Western diet (green; n = 11 mice).

(C and D) Blood glucose (C, raw values and area under the curve) and plasma mouse insulin levels (D) were assessed during an oral glucose tolerance test (OGTT; n = 4–6 mice per group) on day 47. See Figure S1 for OGTTs at days 5 and 32.

(E) An insulin tolerance test (ITT) was performed on day 42 (n = 9–11 mice per group). Glucose levels are presented as a percentage of basal glucose levels (at time 0) and the area above the curve was calculated using 100% as the baseline.

(F) Adiposity (% fat) was assessed by DEXA at day 43 in a subset of mice (n = 3 mice per group).

(legend continued on next page)

recruitment of T cells (Feuerer et al., 2009; Nishimura et al., 2009; Winer et al., 2009) and B cells (Winer et al., 2011) to insulin-sensitive tissues. SCID-beige mice are a spontaneous double-mutant model in which the scid mutation results in a lack of both T and B lymphocytes, and the beige mutation causes defects in cytotoxic T cells, macrophages, and NK cells (http://www.taconic.com). To our knowledge, the susceptibility of double-mutant SCID-beige mice to HFDs has not previously been examined as a potential model of type 2 diabetes.

An important consideration in translating a stem cell-derived pancreatic progenitor therapy to clinical practice is the variability that will be encountered within the patient environment during the period of cell engraftment and maturation in vivo. This is particularly relevant given that macroencapsulated hESC-derived pancreatic progenitor cells are now being tested for safety, tolerability, and efficacy in a phase 1/2 clinical trial by Viacyte (ClinicalTrials.gov, Identifier: NCT02239354). We hypothesized that exposure to HFDs may impair the development of hESC-derived insulin-secreting cells, since obesity-associated lipotoxicity and inflammation contribute to beta cell dysfunction in patients with type 2 diabetes (reviewed in Potter et al., 2014). Furthermore, both human and rodent islets displayed beta cell dysfunction following transplant into HFD-fed rodents (Hiramatsu and Grill, 2001; Gargani et al., 2013). Here, we examined the impact of HFDs on hESC-derived progenitor cell development in vivo, and assessed whether a stem cell-based insulin therapy could improve glycemic control in mice with diet-induced obesity, insulin resistance, and hyperglycemia. We also investigated the efficacy of combining the cell therapy with one of three antidiabetic drugs: sitagliptin (a dipeptidyl peptidase-4 [DPP4 inhibitor]), metformin (suppresses hepatic gluconeogenesis and enhances insulin sensitivity), and rosiglitazone (a PPARγ agonist from the thiazolidinedione [TZD] class). Our studies demonstrated that a combination therapy was more effective in HFD-fed mice than either antidiabetic drugs or progenitor cell transplants alone. Moreover, neither HFDs nor antidiabetic drugs impacted the ability of hESC-derived cells to mature in vivo and appropriately secrete insulin in response to glucose.

RESULTS

SCID-Beige Mice Rapidly Developed Diet-Induced Obesity, Insulin Resistance, and Hyperglycemia

All three of the HFDs used in this study (45% fat, 60% fat, and Western) induced rapid increases in fasting body weight (BW; Figure 1A) and blood glucose levels (Figure 1B) compared with low-fat diet (LFD) controls (10% fat). Moreover, after only 5 days, mice in all three HFD groups were severely glucose intolerant relative to LFD controls (Figure S1A), even though no differences in BW were observed at that time (Figure S1B). At 32 days, HFD mice were both glucose intolerant (Figure S1C) and significantly heavier (Figure S1D) than LFD controls. Mice fed 45% and 60% fat diets were overtly insulin resistant at day 42 (higher glucose levels at 10 and 60–120 min post-insulin, and reduced area above the curve relative to LFD controls), whereas mice on the Western diet only showed significant insulin resistance at 10 min after insulin administration (Figure 1E).

In the week preceding transplantation (day 51), mice in all HFD groups were glucose intolerant (day 47, Figure 1C) and showed insulin-secretion kinetics that differed from LFD controls (either no glucose-induced insulin secretion or altered timing of peak insulin levels; Figure 1D). All HFD mice were significantly overweight (Figure 1A) and had increased adiposity (Figure 1F) compared with LFD controls, and mice fed 45% or 60% fat diets also had significantly elevated circulating leptin levels (Figure 1G). Exposure to HFDs caused dyslipidemia, including significantly reduced plasma free fatty acid levels in all HFD-fed mice (Figure S1E), reduced triglyceride levels in 45% and 60% fat groups (Figure S1F), and elevated cholesterol levels in the Western-diet group compared with LFD controls (Figure S1G). Interestingly, the HFD-induced metabolic defects in immunodeficient mice were not associated with macrophage infiltration in adipose tissue (marked by F4/80 immunoreactivity; Weisberg et al., 2003), whereas significant accumulation of F4/80-positive crown-like structures was observed in the epididymal fat of *ob/ob* mice, an immunocompetent model of type 2 diabetes (Figure 1H). Fibroblast growth factor 21 (FGF21) was used as an adipocyte marker because it is highly expressed in white adipose tissue (Markan et al., 2014).

(G) Mouse leptin levels were measured on days 47–49 following a 4- to 6-hr morning fast (dashed line indicates the highest standard concentration in the leptin assay). See Figures S1E–S1G for circulating lipid levels.

(H) Immunofluorescent staining of epididymal fat from immunocompromised SCID-beige mice fed either a 10% or 60% fat diet for 36 weeks, and from an immunocompetent adult *ob/ob* mouse. F4/80 and FGF21 are shown as macrophage and adipocyte markers, respectively. Crown-like structures, representing macrophage infiltration, are shown in insets. Scale bars, 200 μm.

(A–C and E–G) *$p < 0.05$ versus 10% controls (two-way ANOVA for comparison of multiple time points in line graphs, and one-way ANOVA for bar graphs); (D) *$p < 0.05$ versus time 0 (one-way ANOVA). Data are represented as mean ± SEM (line graphs) or as box-and-whisker plots with individual mice shown as separate data points.

See also Figure S6 and Table S2.

Taken together, these results indicate that 7 weeks of exposure to HFDs generated a type 2-like diabetes model characterized by hyperglycemia, insulin resistance, obesity, and dyslipidemia in immunodeficient mice. Given the phenotypic similarities between mice on the 45% and 60% fat diets, these groups were combined for all further analysis (hereafter referred to as the 45%–60% fat group).

Exposure to HFDs Did Not Affect the Function of hESC-Derived Endocrine Cells In Vivo

Prior to transplantation, differentiated hESC-derived pancreatic progenitor cells were assessed by fluorescence-activated cell sorting (FACS) and immunofluorescent staining (Figure S2). Following in vitro differentiation, ~95% of cells expressed PDX1 and ~65% expressed NKX6.1 (Figures S2A, S2C, S2D, and S2G), two key markers of pancreatic endoderm. Approximately 20% of PDX1-positive cells were in the cell cycle, as indicated by Ki67 or PCNA expression (Figures S2A and S2D), and the pluripotency marker OCT3/4 was not detected (Figure S2A). Although ~14% of progenitor cells expressed endocrine markers (Figures S2A and S2B), only 2.5% of synaptophysin-positive cells co-expressed NKX6.1 (Figure S2A) and most were polyhormonal (Figure S2F), indicative of an immature endocrine population. Indeed, insulin/C-peptide-positive cells only rarely co-expressed PAX6 (Figure S2E) or NKX6.1 (Figure S2C) at this stage of differentiation. These data are consistent with the characteristics of hESC-derived pancreatic progenitor cells described previously by our group (Rezania et al., 2012, 2013; Bruin et al., 2013).

Progenitor cells were encapsulated in Theracyte devices and transplanted subcutaneously into immunodeficient mice from each of the four diet regimens. We used immunodeficient mice because although macroencapsulation devices are predicted to protect human cells from allogeneic immune rejection (Tibell et al., 2001), they are unlikely to protect them from xenograft rejection (Brauker et al., 1996; Mckenzie et al., 2001). The immunoisolation devices allowed us to mimic studies in patients receiving macroencapsulated pancreatic progenitor cells (ClinicalTrials.gov, Identifier: NCT02239354). Following transplantation, hESC-derived cells from all diet groups secreted similar levels of human C-peptide under basal and fed conditions between 8 and 20 weeks (Figure 2A), and produced robust glucose-stimulated human C-peptide secretion at 18 weeks (Figures 2B and 2C). Similarly, human insulin secretion was induced by an arginine challenge in all diet groups at 24 weeks, although due to high variability, the Western-diet group did not reach statistical significance (Figure 2D). We observed a trend toward increased basal glucagon secretion in the HFD groups, but as four out of five mice in the LFD group had undetectable fasting glucagon levels, it was not possible to perform a statistical analysis (Figure 2E). Arginine-stimulated glucagon levels were similar between diet groups (Figures 2E and 2F), and we estimate that approximately half of the circulating glucagon may have originated from hESC-derived cells, as indicated by the difference between glucagon levels in sham-treated mice and transplant recipients (Tx; Figure 2F).

hESC-Derived Endocrine Cells Were Similar following LFD or HFD Exposure, but Grafts from HFD-Fed Mice Contained More Polyhormonal Cells

At 29 weeks post-transplantation, hESC-derived grafts had similar or significantly higher levels of islet-related genes compared with human islets and there were no significant differences between grafts from mice fed LFDs or HFDs (Figure 3). The majority of cells within the harvested devices were immunoreactive for the endocrine marker synaptophysin, and a small proportion expressed the ductal marker CK19. Trypsin-positive exocrine cells were rarely observed (Figure 4A). The grafts were largely composed of cells expressing insulin, glucagon, or somatostatin (Figures 4B and 4E), and the percentage of mono-hormonal insulin-positive and glucagon-positive cells was similar between diet groups (Figure 4C). However, we did note a minor but significantly higher percentage of cells that were immunoreactive for both insulin and glucagon in the HFD grafts compared with LFD grafts (Figures 4C and 4D). Aside from these rare polyhormonal cells, exposure to HFDs did not appear to generally influence the maturation state of hESC-derived insulin-secreting cells: the majority of insulin-positive cells in all transplant recipients co-expressed PDX1 (Figure 4F), NKX2.2 (Figure 4G), NKX6.1 (Figure 4H), and MAFA (Figure 4I) at 29 weeks post-transplantation.

hESC-Derived Insulin-Secreting Cells Improved Diet-Induced Dysglycemia and Insulin Resistance

Long-term tracking revealed that mice in all HFD groups continued to be overweight (Figure S3A) and hyperglycemic under fasting conditions (Figure S3E) compared with LFD controls throughout the duration of the study. Transplantation of hESC-derived cells did not affect either BW (Figures S3B–S3D) or fasting blood glucose levels (Figures S3F–S3H) compared with sham surgery. However, we did observe significant improvements in long-term glycemic control, as measured by HbA1C, following transplantation (Figures 5A and 5B). HbA1C levels were elevated at 12 and 24 weeks in all HFD sham mice compared with LFD sham controls, and were significantly reduced by transplantation in the 45%–60% fat group at both ages (Figures 5A and 5B). Transplant recipients on 45%–60% fat diets also displayed a significantly lower glucose excursion following a mixed-meal stimulus compared with sham mice at 20 weeks (Figure 5C), and all HFD transplant recipients had

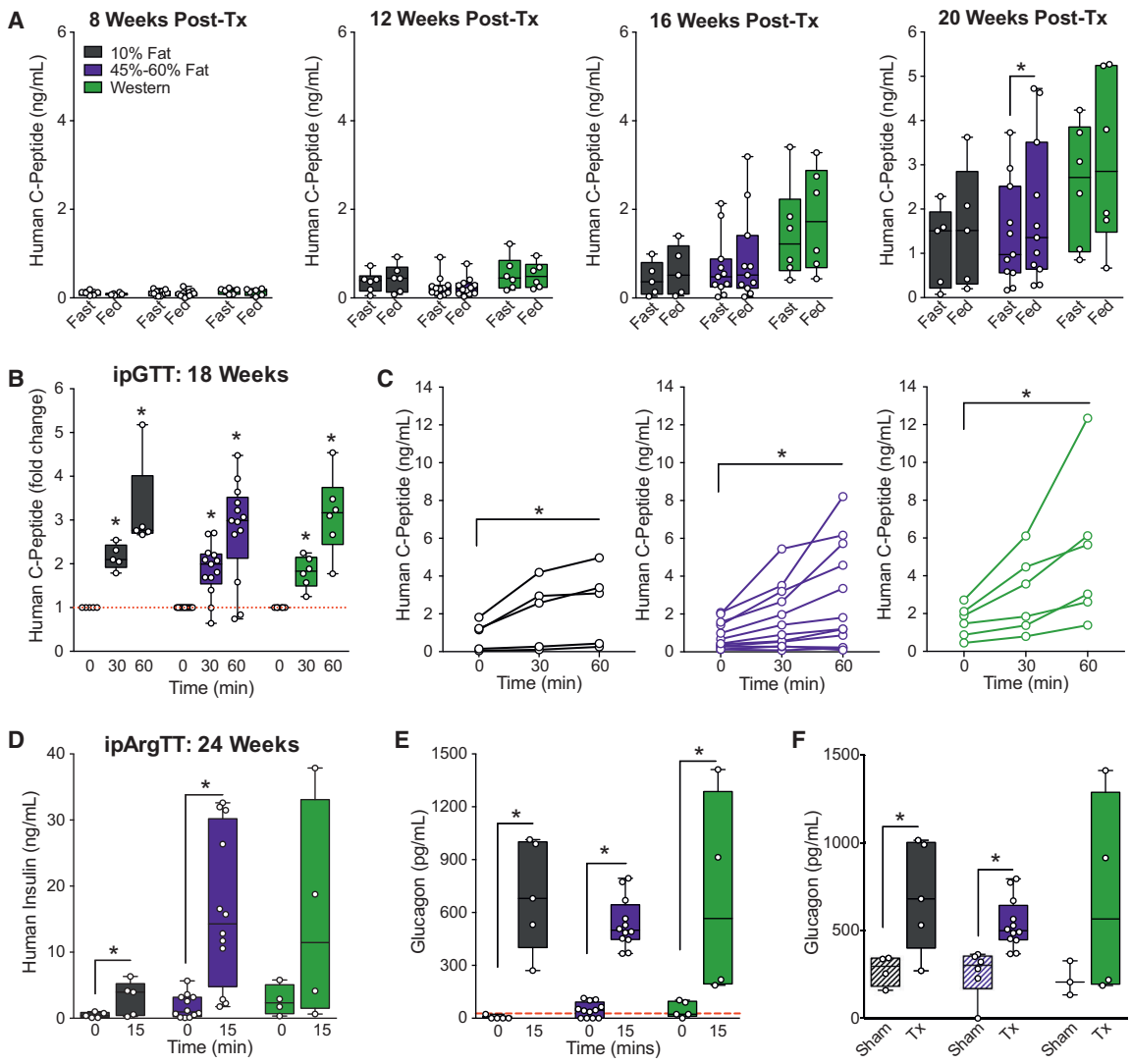

Figure 2. Exposure to HFDs Does Not Affect the Function of hESC-Derived Pancreatic Endocrine Cells In Vivo

The development of hESC-derived progenitor cells into pancreatic endocrine cells was assessed in mice fed a 10% fat (black), 45% or 60% fat (purple), or Western (green) diet. See Figure S2 for characterization of the progenitor cells pre-transplantation.

(A) Human C-peptide levels were measured after an overnight fast and 40 min following an oral mixed-meal challenge ("fed") at 8, 12, 16, and 20 weeks post-transplantation. *$p < 0.05$, paired t test (fast versus fed).

(B and C) At 18 weeks post-transplantation, human C-peptide levels were measured during an i.p. glucose tolerance test (ipGTT). In (B) data are normalized to baseline levels, and in (C) raw levels (ng/ml) are presented for individual animals, with each diet group shown on a separate plot. *$p < 0.05$, one-way repeated-measures ANOVA (versus time 0).

(D–F) At 24 weeks post-transplantation, an i.p. arginine tolerance test (ipArgTT) was performed. Plasma was collected after a 4-hr fast and 15 min following arginine administration to measure human insulin (D) and glucagon (E and F) levels. (E) shows glucagon levels at 0 and 15 minutes in transplant recipients, and (F) shows glucagon levels in sham-treated mice (Sham, striped bars) and transplant recipients (Tx, solid bars) at 15 minutes only. The red line indicates the lower limit of detection for the glucagon assay. (D and E) *$p < 0.05$, one-tailed paired t test (0 versus 15 min); (F) *$p < 0.05$, two-tailed t test (sham versus Tx). Data points from individual mice are shown as box-and-whisker plots. See also Table S2.

significantly improved glucose tolerance at 24 weeks post-transplantation (Figures 5E and S4B). These improvements were not yet evident at 18 weeks (Figures 5D and S4A). Glucose tolerance in the 45%–60% fat group was not completely ameliorated at 24 weeks, but the area under the curve for transplant recipients in the Western group was indistinguishable from that obtained for controls (Figures 5E and S4B). Interestingly, we also observed a modest

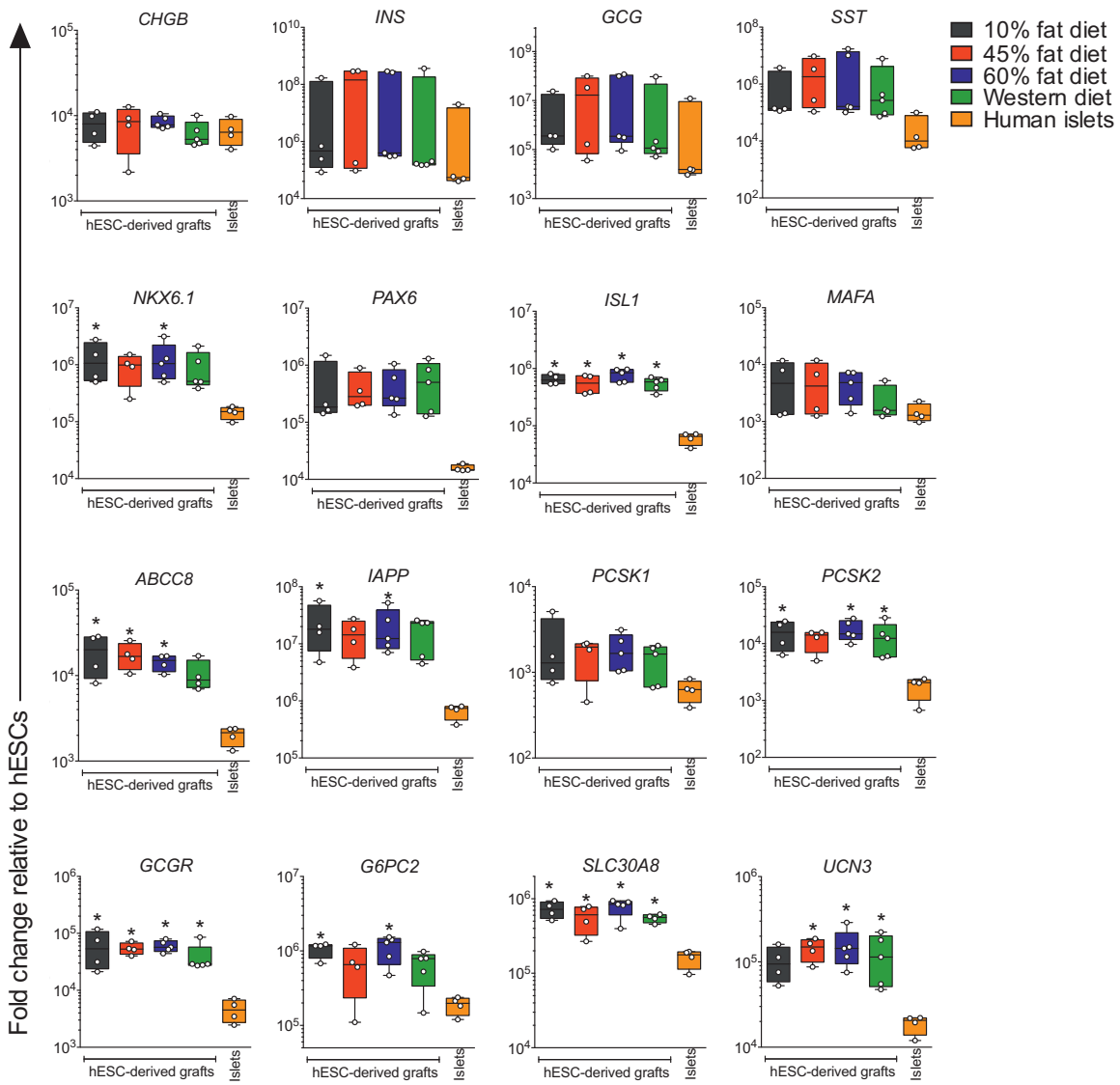

Figure 3. Gene Expression Profiles Are Similar for hESC-Derived Graft Tissues Exposed to Different LFDs or HFDs In Vivo

The gene expression of islet-related genes was assessed in macroencapsulated hESC-derived grafts at 29 weeks post-transplantation from mice fed a LFD (10% fat) or HFD (45% fat, 60% fat, and Western), as well as in adult human islet preparations. All data are presented as the fold change relative to undifferentiated hESCs (H1 cells) using a log scale. Data points from individual mice or different human islet donors are shown as box-and-whisker plots. *$p < 0.05$ for hESC-derived grafts from each diet group versus human islets (one-way ANOVA). See also Tables S2 and S3.

but statistically significant improvement in insulin sensitivity at 22 weeks in transplanted HFD-fed mice compared with shams (Figures 5F, S4C, and S4D), which may have contributed to the improved glucose tolerance in HFD transplant recipients (Figure 5E).

We assessed beta and alpha cell mass in the endogenous pancreas from mice fed 10% or 60% fat diets to determine whether the improved glucose tolerance in HFD-fed transplant recipients could be accounted for by expansion of the endogenous endocrine pancreas. Beta cell mass was significantly higher in all mice on 60% fat diets compared with LFD sham controls, and there was no difference between sham and transplanted mice in either diet group (Figures S5A and S5D). Interestingly, there was no effect of HFDs on alpha cell mass, but a significant reduction in alpha cell mass was observed in LFD transplant recipients compared with LFD shams (Figures S5B and S5D). There were no significant differences in the ratio of insulin-positive to glucagon-positive area in the pancreas of mice on either diet (Figure S5C).

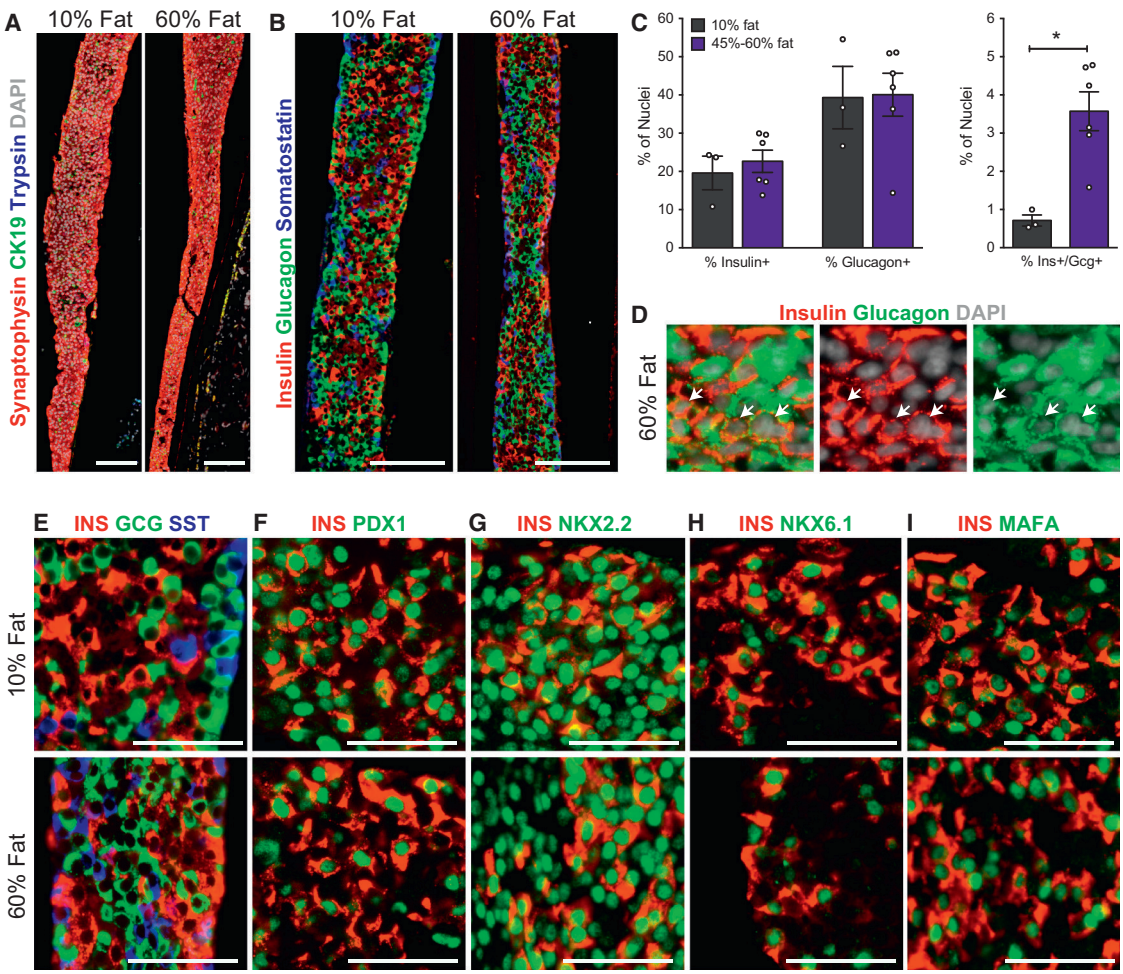

Figure 4. The Morphology of Macroencapsulated hESC-Derived Pancreatic Endocrine Cells Is Similar in Grafts from Mice Fed a LFD or HFD

(A, B, and D–I) Representative immunofluorescent images of Theracyte devices at 29 weeks post-transplantation from mice fed 10% fat or 60% fat diets.

(A) The majority of hESC-derived cells within devices from both diet groups were endocrine cells. The expression of synaptophysin (endocrine marker, red), CK19 (ductal marker, green), trypsin (exocrine marker, blue), and DAPI (nuclear marker, white) is shown. Scale bars, 100 μm.

(B) The endocrine compartment was mainly composed of cells expressing either insulin (red, guinea pig antibody), glucagon (green, rabbit antibody), or somatostatin (blue, Ms antibody); scale bars, 100 μm. Higher-magnification images are shown in (E); scale bars, 50 μm.

(C) The percentage of cells (% of DAPI+ nuclei) within devices that were immunoreactive for insulin (insulin+), glucagon (glucagon+), or both hormones (ins+/gcg+) was quantified in grafts from mice fed 10% fat or 45%–60% fat diets. *$p < 0.05$, two-tailed t test. Data are represented as mean ± SEM and data points from individual mice are also shown.

(D) Example of graft tissue from the 60% fat diet group with a region of endocrine cells that expressed both insulin and glucagon (white arrows); scale bars, 25 μm.

(F–I) The majority of insulin-positive cells (INS, red) show a mature beta cell phenotype, including co-expression of key beta cell transcription factors (green): (F) PDX1, (G) NKX2.2, (H) NKX6.1, and (I) MAFA; scale bars, 50 μm. See also Figure S2 and Tables S2 and S4.

Cell Therapy Had No Effect on the Obesity Phenotype, but Improved Liver Weight in HFD Mice

Although hESC-derived cells improved glucose homeostasis in HFD-fed mice, there was no apparent effect on the obesity phenotype. At the end of our study (29 weeks post-transplantation and 36 weeks post-diet), mice on the 45%–60% fat diets (sham and Tx) had significantly higher BW, adiposity (epididymal fat pad weight as a proportion of BW) and circulating leptin levels than LFD shams (Figures S5E–S5G). The obesity phenotype was more subtle in Western-diet mice during the first 7 weeks (Figure 1A) and by the end of the study there were no significant differences in BW, adiposity, or leptin levels between Western-fed mice (sham and Tx) and LFD sham

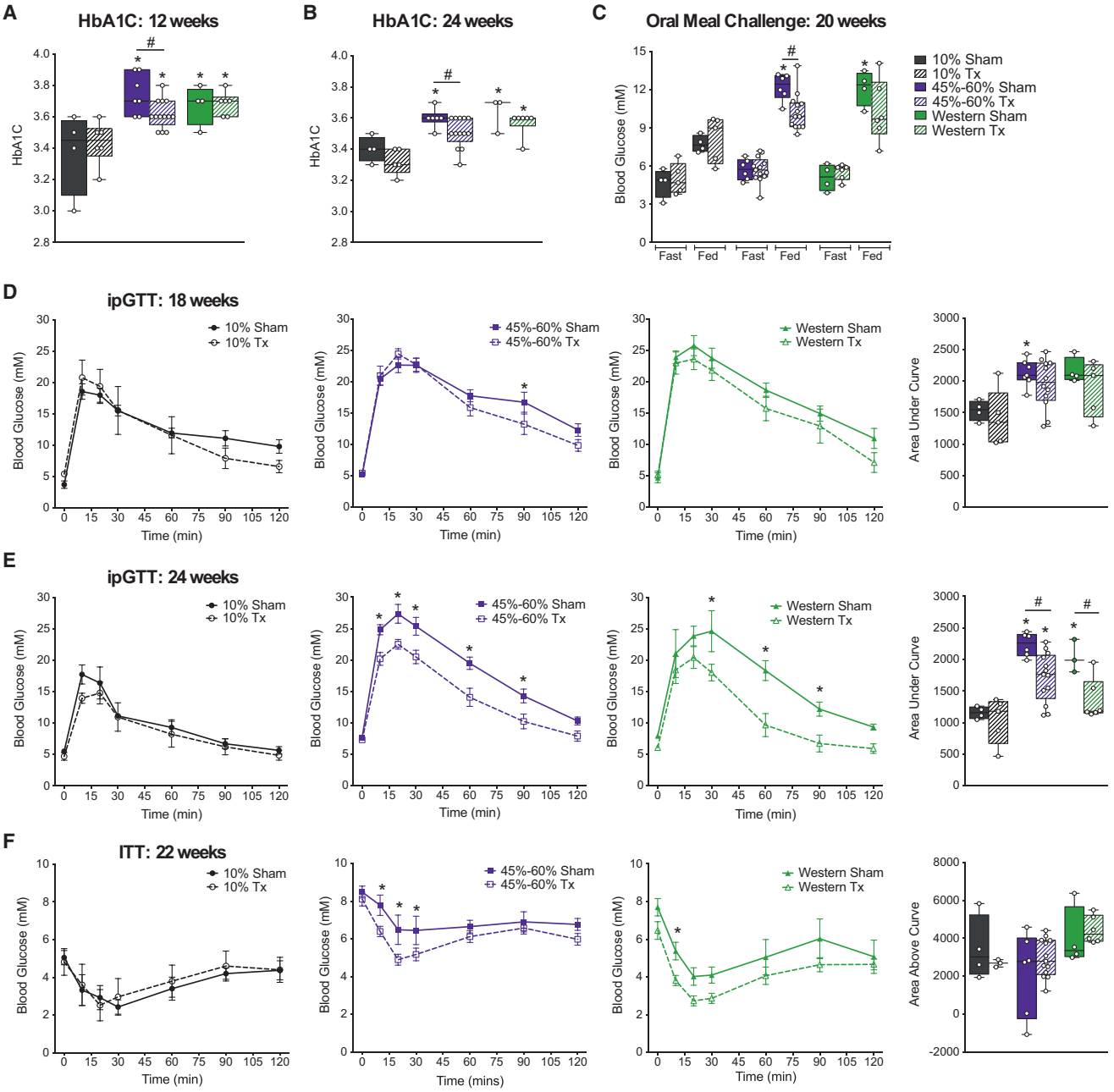

Figure 5. Cell Transplant Recipients on HFDs Show Improved Glucose Homeostasis Compared with Sham-Treated Mice

(A and B) HbA1C levels were measured at 12 (A) and 24 (B) weeks post-transplantation in sham mice (solid bars) and transplant recipients (Tx, striped bars).

(C) At 20 weeks post-transplantation, blood glucose levels were measured after an overnight fast and 40 min following an oral meal challenge ("Fed").

(D and E) ipGTTs were performed at 18 (D) and 24 (E) weeks post-transplantation in sham mice (solid lines with closed symbols; solid bars) and transplant recipients (Tx, dashed lines with open symbols; striped bars) on 10% fat (gray; 18 weeks: Tx/Sham, n = 4 mice; 24 weeks: Tx, n = 5 and Sham, n = 4 mice), 45% or 60% fat (purple; 18 weeks: Tx, n = 12 and Sham, n = 7 mice; 24 weeks: Tx, n = 13 and Sham, n = 6 mice), or Western (green; 18 weeks: Tx, n = 5 and Sham, n = 4 mice; 24 weeks: Tx, n = 6 and Sham, n = 3 mice) diets. The area under the curve is shown to the right for each ipGTT.

(F) An ITT was performed at 22 weeks post-transplantation in sham and transplant recipients from each diet group (10% Tx, n = 5 mice; 10% Sham, n = 4 mice; 45%–60% Tx, n = 12 mice; 45%–60% Sham, n = 6 mice; West Tx, n = 6 mice; West Sham, n = 4 mice). The area above

(legend continued on next page)

controls (Figures S5E–S5G). All HFD groups had significantly higher liver weight (Figure S5H) and evidence of cytoplasmic vacuolation, consistent with dietary lipidosis in the liver (Figure S5I; Western and 45% fat groups not shown) compared with LFD controls. Interestingly, transplant recipients fed 45%–60% fat diets had significantly reduced liver weight relative to shams (Figure S5H), although a pathology assessment did not reveal differences in cytoplasmic vacuolation in H&E-stained liver sections (Figure S5I). Similarly, vacuolation of renal tubular epithelium was observed in kidney sections from all HFD groups (consistent with dietary lipidosis) and there was no effect of cell transplantation on this phenotype (data not shown). Other tissue pathologies (Table S1) were consistent with spontaneous age- and sex-related events and considered to be unrelated to exposure to diets or cell transplants (data not shown).

Combined Treatment of HFD-Fed Mice with Progenitor Cell Transplants and an Antidiabetic Drug Rapidly Improved Diet-Induced Obesity and Glucose Intolerance

Since the progenitor cell therapy resulted in improved glucose tolerance in HFD-fed mice at 24 weeks, but not full reversal of the diabetes phenotype, we next investigated a combination therapy with known antidiabetic drugs. A second cohort of SCID-beige mice was placed on either a LFD (10% fat) or HFD (60% fat) for 6 weeks, followed by long-term administration of either sitagliptin (4 g/kg in 60% fat diet), rosiglitazone (18 mg/kg in 60% fat diet), or metformin (1.25 mg/ml in drinking water) in HFD-fed mice (treatment groups are summarized in Table S2). Similar to our first cohort, SCID-beige mice in this second cohort rapidly developed attributes of type 2 diabetes following HFD administration (Figure S6).

At the time of transplantation (1 week after drug administration), all HFD-fed mice were significantly heavier than LFD controls (Figure 6F). Interestingly, weight loss was observed within the first 2 weeks following transplantation in HFD-fed mice on antidiabetic drugs (Figures 6C–6E). In contrast, no change in BW was observed during this time in either HFD transplant recipients without drug treatment (Figure 6B) or sham mice on any drug (Figures 6A–6E). All transplant recipients that received antidiabetic drugs had significantly lower BW on day 75 (Figure 6F) and reduced epididymal fat pad weight (relative to BW; Figure 6G) compared with sham mice, such that neither parameter was different from LFD-fed sham controls. As in our previous cohort (Figures S3 and S5E), there was no effect of transplantation on BW (Figures 6B and 6F) or circulating leptin levels (Figure 6H) in HFD-fed mice without drug treatment, although we did observe a reduction in relative epididymal fat pad weight in this cohort (Figure 6G). Interestingly, the combination of a cell transplant with either metformin or sitagliptin resulted in significantly reduced circulating leptin levels in the transplant recipients compared with their respective sham controls (Figure 6G). The cell therapy had no effect on restoring leptin levels in the rosiglitazone group (Figure 6G).

Fasting blood glucose levels were not affected by any of the combination therapies throughout the study duration (Figure S7). At 12 weeks post-transplantation, mice in all HFD sham groups were glucose intolerant compared with LFD controls, regardless of the drug treatment used (Figure 7A). As expected based on our previous cohort, we found no effect of the cell therapy on glucose tolerance at 12 weeks post-transplantation in the HFD-fed mice without drug treatment (Figure 7B), and likewise, the combination with rosiglitazone was also ineffective at this time (Figure 7E). Interestingly, the cell therapy significantly improved glucose tolerance at 12 weeks post-transplantation when combined with either metformin (Figure 7C) or sitagliptin (Figure 7D) treatment. In fact, glycemic control during an oral glucose challenge was indistinguishable between the LFD controls and HFD-fed mice receiving sitagliptin with the cell therapy, with the exception of a marginally higher peak glucose level at 15 min post-gavage (Figure 7D). The improved glucose tolerance in cell transplant recipients from the metformin- and sitagliptin-treated groups was associated with significantly reduced fasting mouse C-peptide levels compared with their respective sham controls at 16 weeks post-transplantation (Figure 7G), an effect that was not yet evident at 4 weeks (Figure 7F). Interestingly, the improvements in glucose tolerance were not associated with differences in glucose-stimulated C-peptide secretion by hESC-derived grafts. All transplant recipients showed robust glucose-responsive human C-peptide secretion at 16 weeks, and there were no differences in human C-peptide levels between HFD-fed mice treated with different antidiabetic drugs (Figure 7H).

the curve (right panel) was calculated using the fasting glucose level (100%) for each animal as the baseline. For clarity, all glucose curves (GTTs and ITTs) from sham and transplanted mice are shown separately for each diet group. See Figure S4 for glucose curves combined on the same plots. Data are represented as mean ± SEM (line graphs) or as box-and-whisker plots showing individual mice as separate data points. For all box-and-whisker plots: *$p < 0.05$, one-way ANOVA versus 10% sham; #$p < 0.05$, two-tailed t test (Tx versus sham). For all line graphs: *$p < 0.05$, two-way ANOVA, Tx versus sham. See Figure S3 for long-term body weight and blood glucose tracking, and Figure S5 for the effect of cell transplants on endogenous pancreas, liver, fat, and circulating leptin levels.
See also Table S2.

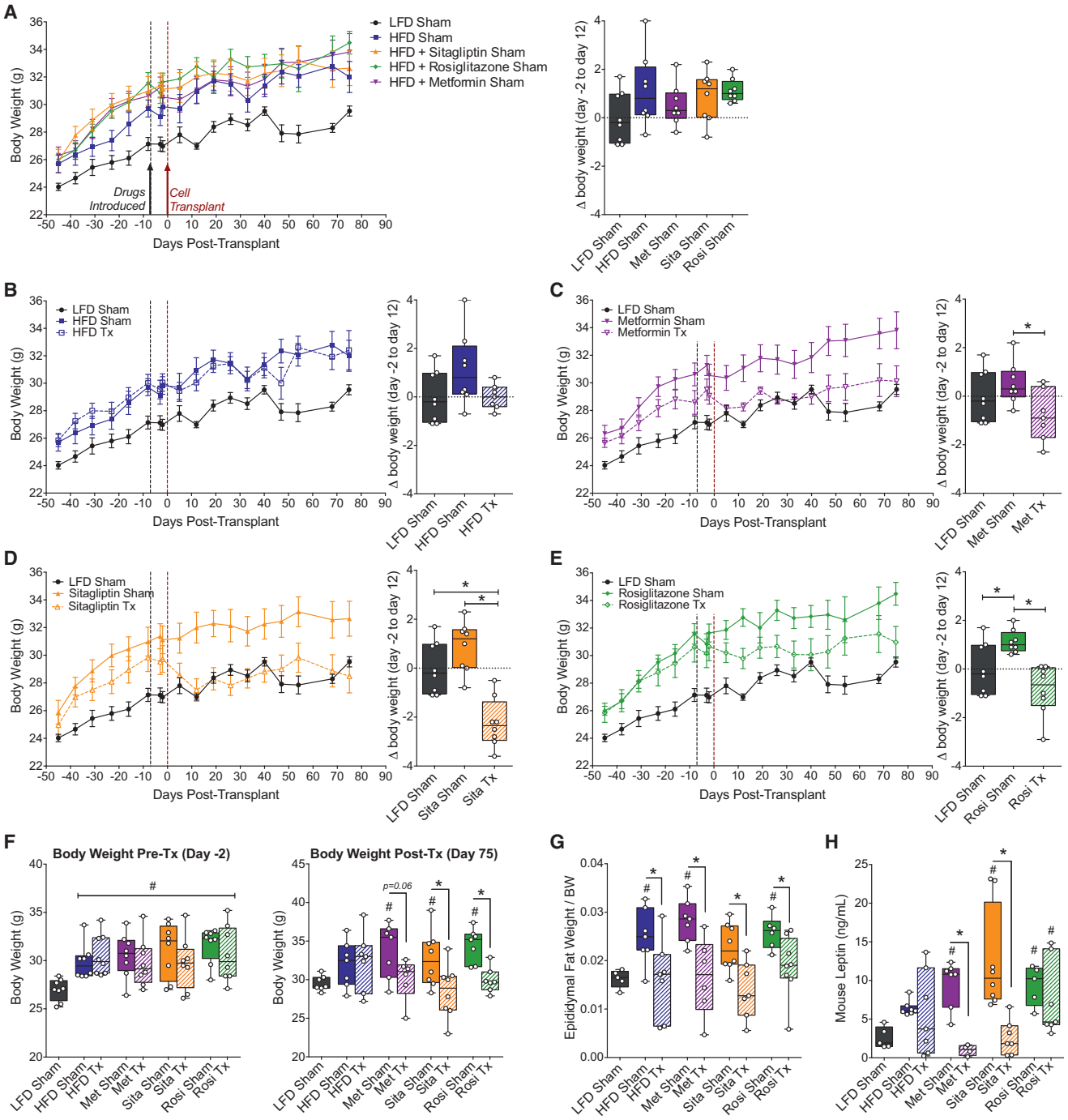

Figure 6. Diet-Induced Obesity Was Reversed Following Progenitor Cell Transplantation Combined with an Antidiabetic Drug

(A–F) Fasting body weight was assessed in mice fed a 10% fat diet without drug (black/gray; all panels; n = 8 mice), 60% fat diet without drug (A and B, blue; n = 7–8 mice per group), 60% fat diet plus metformin (A and C, purple; n = 7–8 mice per group), 60% fat diet plus sitagliptin (A and D, orange; n = 8 mice per group), or 60% fat diet plus rosiglitazone (A and E, green; n = 8 mice per group). Body weight tracking for sham mice from all treatment groups is shown in (A). Sham mice (solid lines, closed symbols) and transplant recipients (Tx; dashed lines, open symbols) from each treatment group are shown together with the LFD control as a reference (B–E). The change in body weight from day −2 to day 12 is shown in box-and-whisker plots to the right of each line graph, with each data point representing an individual mouse. Data on line graphs are represented as mean ± SEM. (F) Body weight pre-transplant (day −2) and post-transplantation (day 75).

(legend continued on next page)

DISCUSSION

Our first goal in these studies was to establish an immunodeficient mouse model of hyperglycemia associated with insulin resistance and obesity that would resemble a type 2 diabetes phenotype. It was not feasible to transplant human progenitor cells into traditional models of type 2 diabetes, such as *db/db* or *ob/ob* mice, because macroencapsulation devices are unlikely to protect human cells from xenograft immune rejection (Brauker et al., 1996; Mckenzie et al., 2001). Although macroencapsulation was not required to protect the cells in immunodeficient mice, we opted to transplant within immunoisolation devices so that our findings would be more clinically relevant (macroencapsulated hESC-derived progenitor cells are currently being evaluated in patients with diabetes by ViaCyte [ClinicalTrials.gov, Identifier: NCT02239354]). We used SCID-beige mice for our studies because the maturation of hESC-derived pancreatic progenitor cells has been well characterized in this strain (Rezania et al., 2012, 2013; Bruin et al., 2013). SCID-beige mice fed 45%–60% fat diets had many characteristics of type 2 diabetes, including increased BW and adiposity, fasting hyperglycemia, and glucose intolerance, insulin resistance, hyperleptinemia, and hepatic lipidosis. However, unlike humans with type 2 diabetes, mice fed 45% or 60% fat diets had reduced circulating free fatty acid and triglyceride levels. We speculate that excess lipids are likely taken up by peripheral tissues, which may explain the severe ectopic lipid deposition observed in the liver and kidneys of these mice. Western-diet-fed mice were similar with respect to glucose intolerance and hepatic/kidney lipidosis, but showed a more mild phenotype in terms of obesity, fasting hyperglycemia, insulin resistance, and leptin levels. We also observed pancreatic beta cell dysfunction in the 60% fat and Western-diet groups, as indicated by the lack of glucose-stimulated insulin secretion. Therefore, although no one diet produced a phenotype that perfectly modeled the human condition, all three HFDs resulted in characteristics that mirrored important features of type 2 diabetes, most notably including hyperglycemia associated with obesity and insulin resistance. The mechanism underlying the rapid HFD-induced metabolic dysregulation in mice lacking T cells, B cells, and fully functioning macrophages remains to be determined and is intriguing given that immune cells reportedly play a central role in the development of obesity-associated inflammation and subsequent insulin resistance (Feuerer et al., 2009; Nishimura et al., 2009; Winer et al., 2009, 2011). Notably, in contrast to *ob/ob* mice, we did not observe infiltration of F4/80-positive macrophages in the epididymal fat tissue of HFD-fed SCID-beige mice, suggesting that other mechanisms may be involved in the development of insulin resistance in this animal model.

Transplantation of human pancreatic progenitor cells into HFD-fed mice resulted in improved glycemic control over time. At 12 weeks post-transplantation, mice on 45%–60% fat diets and with hESC-derived grafts had significantly lower HbA1C levels than sham mice on the same diet, indicative of improved long-term glycemic control, although these mice remained glucose intolerant at 18 weeks. As the progenitor cells matured over time, circulating human C-peptide levels increased, engrafted cells became glucose/arginine responsive, and significant improvements were observed in glucose excursions following mixed-meal and glucose challenges in HFD transplant recipients compared with HFD shams between 20 and 24 weeks post-transplantation. We suspect that the addition of an alternative source of appropriately regulated insulin secretion provided sufficient compensation for peripheral insulin resistance, a feat that the endogenous pancreas was incapable of achieving on its own. Transplantation did not affect the pancreatic beta cell mass, so it is unlikely that expansion of the endogenous pancreas contributed to the observed improvements in glucose homeostasis in HFD-fed mice. Interestingly, transplant recipients from the 45%–60% diet group had enhanced insulin sensitivity compared with shams, which may also have contributed to their improved glucose tolerance. An improvement in insulin sensitivity as a result of higher circulating insulin levels is counterintuitive, but consistent with previous reports in patients with type 1 diabetes following human islet transplantation (Rickels et al., 2013) and patients with type 2 diabetes following short-term intensive insulin therapy (Kramer et al., 2013).

Based on these data, we predicted that co-treating HFD transplant recipients with antidiabetic drugs, particularly insulin sensitizers, would improve the efficacy of the progenitor cell therapy. Although co-treatment with metformin, an insulin sensitizer from the biguanide class, improved BW and glucose intolerance after just 12 weeks, the combination with rosiglitazone, an insulin sensitizer

(G and H) Epididymal fat pad weight relative to body weight (G) and plasma mouse leptin levels (H) were assessed at 20 weeks post-transplantation.

(A–E) *$p < 0.05$, one-way ANOVA for comparisons of all groups (LFD versus HFD Sham, LFD versus HFD Tx, HFD Sham versus HFD Tx); (F–H) #$p < 0.05$, one-way ANOVA for comparison of each group to LFD control; *$p < 0.05$, two-tailed t test, Tx versus Sham. See Figure S6 for the phenotype of mice on HFDs in cohort 2 (pre-transplant) and Figure S7 for long-term blood glucose tracking following administration of drugs with or without cell transplants.

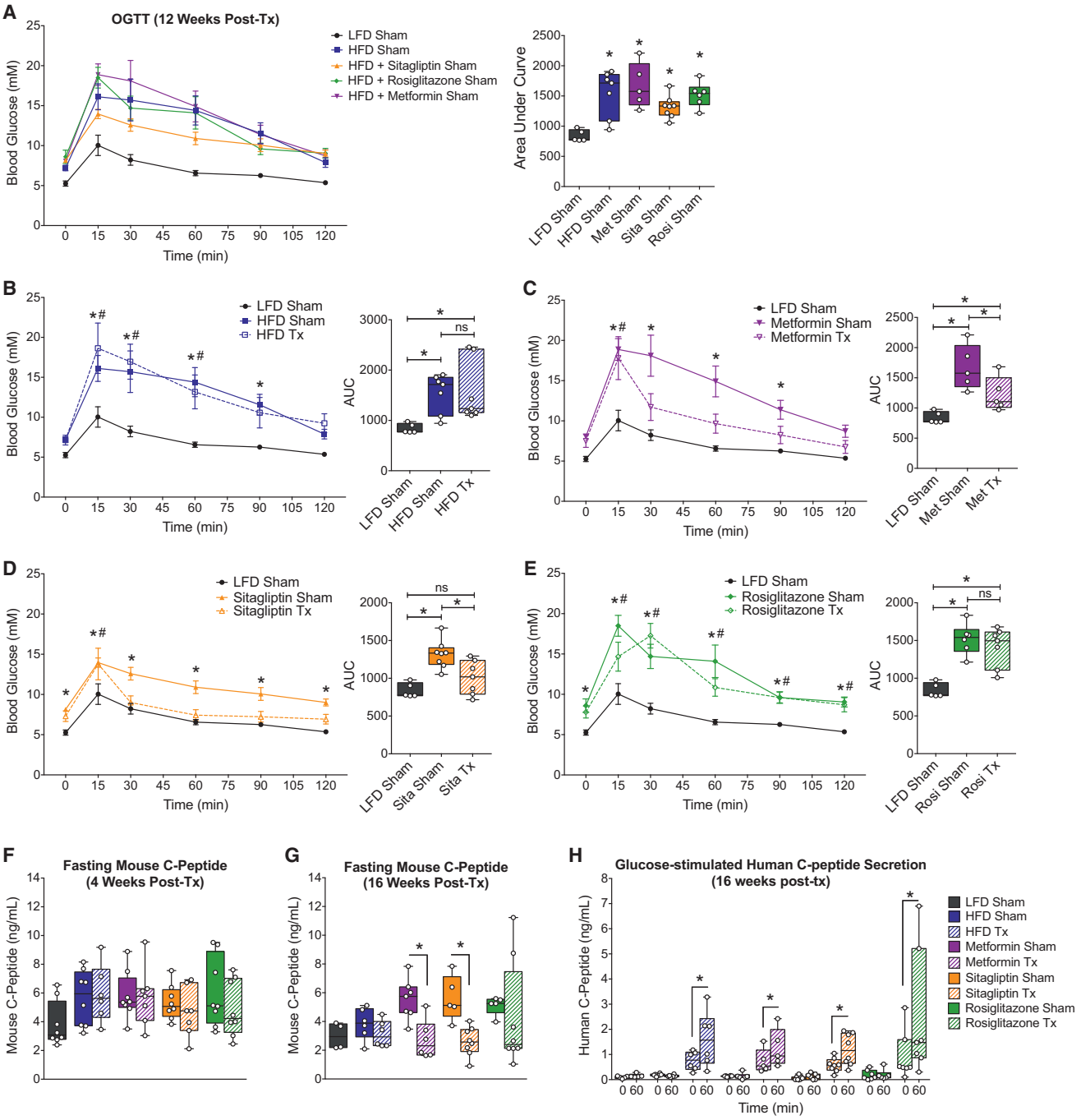

Figure 7. The Combination of Either Sitagliptin or Metformin with a Cell Transplant Resulted in Improved Glucose Tolerance within 12 Weeks

(A–E) OGTTs were performed at 12 weeks post-transplantation in mice fed a 10% fat diet without drug (black/gray; all panels; Sham: n = 5 mice), 60% fat diet without drug (A and B, blue; Tx/Sham: n = 7 mice), 60% fat diet plus metformin (A and C, purple; Tx/Sham: n = 5 mice), 60% fat diet plus sitagliptin (A and D, orange; Tx: n = 7 mice, Sham: n = 8 mice), or 60% fat diet plus rosiglitazone (A and E, green; Tx: n = 7 mice, Sham: n = 6 mice). Blood glucose levels for sham mice from all treatment groups are shown together in (A). Sham mice (solid lines, closed symbols) and transplant recipients (Tx; dashed lines, open symbols) from each treatment group are shown together with LFD controls as a reference (B–E). The area under the curve (AUC) is shown in box-and-whisker plots to the right of each line graph, with separate data points representing individual mice. Data on line graphs are represented as mean ± SEM. (A) *p < 0.05 (one-way ANOVA versus LFD).

(legend continued on next page)

from the TZD class, did not reverse hyperglycemia. Interestingly, the most effective antidiabetic drug tested in our study was the DPP4 inhibitor sitagliptin, which acts to increase circulating incretin levels by preventing inactivation by DPP4. When sitagliptin was combined with the cell therapy, HFD-fed mice had glucose tolerance and BW that was similar to LFD-fed control mice at 12 weeks post-transplantation. Furthermore, transplanted mice on either sitagliptin or metformin had reduced fasting mouse C-peptide levels, which may suggest that the endogenous pancreas has been relieved of the demand to compensate for insulin resistance. The reversal of hyperleptinemia in both sitagliptin- and metformin-treated transplant recipients also suggests a more robust reversal of the obesity phenotype in these groups as compared with the HFD transplant recipients treated with rosiglitazone or without drugs. Taken together, our data suggest that a cell-based insulin replacement therapy could be considered as a future treatment option for type 2 diabetes, particularly if combined with antidiabetic drugs.

Many of the same pathways that trigger obesity-associated beta cell dysfunction in patients with type 2 diabetes may also contribute to graft failure following islet transplantation (Potter et al., 2014). Therefore, a potential caveat in replacing dysfunctional beta cells with healthy insulin-secreting cells is the risk of subsequent graft failure in an obesogenic and hyperglycemic host environment. Indeed, in previous studies, both human and rodent islet grafts displayed beta cell dysfunction following exposure to HFDs (Hiramatsu and Grill, 2001; Gargani et al., 2013) and chronic hyperglycemia (Eizirik et al., 1997; Biarnés et al., 2002). In contrast, the development of hESC-derived pancreatic progenitor cells into insulin-secreting cells was accelerated by exposure to chronic hyperglycemia compared to normoglycemia (Bruin et al., 2013). However, the potential effect of an obesogenic environment on hESC-derived progenitor cells was not previously examined. We also demonstrated previously that short-term exposure to exendin-4, a GLP-1 mimetic, for 4 weeks post-transplantation did not affect the development of progenitor cells (Bruin et al., 2013), but the possible effects of long-term treatment with antidiabetic medications has not been reported. In the current studies there was a tendency for increased basal glucagon levels and arginine-induced human insulin secretion in HFD-fed compared with LFD-fed transplant recipients, but overall the results showed that neither an obesogenic environment nor exposure to antidiabetic drugs had a major impact on the function of hESC-derived insulin-secreting cells in vivo. However, there are several important caveats to our immunocompromised mouse model that should be considered: first, we cannot exclude the possibility that HFDs or antidiabetic drugs may impact the function of hESC-derived endocrine cells in an immunocompetent host environment; second, human progenitor cells may respond differently to mouse versus human diabetogenic/obesogenic stimuli; and third, the potential long-term impact of HFDs or antidiabetic drugs on hESC-derived grafts cannot be examined in mice because of their relatively short lifespan. Regardless, hESC-derived cells secreted similar levels of human C-peptide in response to secretagogue challenges in all diet groups (with or without antidiabetic drugs), and qPCR demonstrated no significant differences in expression of several islet-related genes within grafts from different diet or drug treatment groups. The only sign that an obesogenic environment may have impacted progenitor cell maturation was a small but significant increase in the percentage of insulin/glucagon bihormonal cells in grafts from mice fed 45%–60% fat versus 10% fat diets. These cells may represent a subpopulation of immature, fetal-like endocrine cells (Riedel et al., 2012; Bruin et al., 2014), but without conducting lineage-tracing studies, we cannot know their source or fate. Regardless, the ability of hESC-derived progenitor cells to thrive and mature into functional pancreatic endocrine cells in a chronic obesogenic and hyperglycemic (albeit immunocompromised) environment further supports the feasibility of a stem cell-based therapy for type 2 diabetes.

In our previous studies, a dose of 5 million progenitor cells was sufficient to normalize hyperglycemia in mice with severe insulin deficiency caused by streptozotocin-induced beta cell destruction (Rezania et al., 2012, 2013; Bruin et al., 2013). With diet-induced hyperglycemia, the same dose of progenitor cells generated higher levels of human C-peptide, yet the graft-derived insulin (combined with endogenous mouse insulin) was insufficient to completely normalize glycemia. Therefore, it is likely that a larger mass of insulin-producing cells would be required to ameliorate hyperglycemia in insulin-resistant patients with type 2 diabetes compared with insulin-deficient patients with type 1 diabetes. Alternatively, our studies also suggest that a progenitor-based cell therapy may be more

(B–E) For glucose curves, two-way ANOVA was used to examine differences at each time point during the OGTT (*$p < 0.05$, HFD Sham versus LFD; #$p < 0.05$, HFD Tx versus LFD). For the AUC, one-way ANOVA was used compare all groups (LFD versus HFD Sham, LFD versus HFD Tx, HFD Sham versus HFD Tx; *$p < 0.05$; ns, not significant).
(F and G) Fasting mouse C-peptide levels at 4 weeks (F) or 16 weeks (G) post-transplantation. *$p < 0.05$, two-tailed t test (Tx versus Sham).
(H) Human C-peptide levels were measured after an overnight fast and 60 min following an intraperitoneal glucose challenge. *$p < 0.05$, paired two-tailed t test (0 versus 60 min).

effective in a type 2 diabetic setting if it is combined with an antidiabetic drug. These findings are in line with another report by our lab, in which leptin therapy was shown to enhance the performance of transplanted islets in diabetic mice (Denroche et al., 2013), likely due to the insulin-sensitizing effects of leptin (Denroche et al., 2011).

Conclusions

In conclusion, we have demonstrated that hESC-derived pancreatic progenitor cells may be a feasible option for treating patients with type 2 diabetes, in addition to those with type 1 diabetes. Our data suggest that transplanted hESC-derived insulin-producing cells thrive following chronic exposure to HFDs, at least in immunodeficient mice. Thus, stem cells are a candidate for restoring functional beta cells in an insulin-resistant, obese setting.

EXPERIMENTAL PROCEDURES

In Vitro Differentiation of hESCs and Assessment of Pancreatic Progenitor Cells

The H1 hESC line was obtained from the WiCell Research Institute. All experiments at the University of British Columbia (UBC) with H1 cells were approved by the Canadian Stem Cell Oversight Committee and the UBC Clinical Research Ethics Board. Pluripotent H1 cells were differentiated into pancreatic progenitor cells according to our 14-day, four-stage protocol as previously described (Bruin et al., 2013). Expression of key pancreatic progenitor cell markers was assessed prior to transplantation using custom Taqman qPCR Arrays (Applied Biosystems) and flow cytometry as described in Supplemental Experimental Procedures.

Animals

Male SCID-beige mice (C.B-*Igh*-1b/GbmsTac-*Prkdc*^{scid}-*Lyst*^{bg}N7, 8–10 weeks old; Taconic) were maintained on a 12 hr light/dark cycle throughout the study. All experiments were approved by the UBC Animal Care Committee and carried out in accordance with the Canadian Council on Animal Care guidelines.

Diets and Drug Administration

All mice were given ad libitum access to a standard irradiated diet (Harlan Laboratories, Teklad Diet #2918) for 2 weeks to allow for acclimatization following their arrival at UBC. In the first cohort, mice were placed on one of four different diet regimens (Research Diets) for the 36-week study (n = 11 per diet): (1) "10% fat" control diet (D12450K, 10 kcal% fat, 70 kcal% carbohydrate [no sucrose]), (2) "45% fat" diet (D12451, 45 kcal% fat [primarily lard], 35 kcal% carbohydrate), (3) "60% fat" diet (D12492, 60 kcal% fat [primarily lard], 20 kcal% carbohydrate), or (4) "Western" diet (D12079B, 41 kcal% fat [primarily milk fat], 43 kcal% carbohydrate [primarily sucrose]).

In the second cohort, mice were placed on either the 10% fat control diet (D12450K; n = 8) for the duration of the study or 60% fat diet (D12492; n = 64) for 6 weeks, followed by one of the following treatment regimens for the remainder of the study (n = 16 per group): (1) 60% fat diet with no drug (D12492), (2) 60% fat diet containing rosiglitazone (18 mg/kg diet or ~3 mg/kg BW per day; Cayman Chemical; Research Diets custom diet formulation D08121002), (3) 60% fat diet containing sitagliptin (4 g/kg diet or ~750 mg/kg BW per day; sitagliptin phosphate monohydrate, BioVision; Research Diets custom diet formulation D08062502R), or (4) 60% fat diet (D12492) and metformin (1,1-dimethylbiguanide hydrochloride) in drinking water (1.25 mg/ml or ~250 mg/kg BW per day).

Transplantation of hESC-Derived Pancreatic Progenitor Cells

The procedure used for transplantation of macro-encapsulated pancreatic progenitor cells is described in Supplemental Experimental Procedures. In the first cohort, mice were randomly assigned to receive either a cell transplant (Tx, n = 7 per diet) or sham surgery (sham, n = 4 per diet) after 7 weeks of LFD or HFD feeding. In the second cohort, HFD-fed mice (+/− drug treatment) received either a transplant (n = 8 per group) or sham surgery (n = 8 per group) 1 week after administration of the antidiabetic drugs. LFD controls all received sham surgery. The treatment groups are summarized in Table S2.

Metabolic Assessments

All metabolic analyses were performed in conscious, restrained mice and blood samples were collected via the saphenous vein. BW and blood glucose levels were assessed regularly throughout each study following a 4-hr morning fast. For all other metabolic tests, blood was collected after fasting (time 0) and at the indicated time points following administration of various secretagogues. Details about the fasting time, route of administration, and dose used for each metabolic test are provided in Supplemental Experimental Procedures along with information about the assays used to measure circulating hormones, lipids, and HbA1C levels.

Dual-Energy X-Ray Absorptiometry

Body composition was determined using dual-energy X-ray absorptiometry (DEXA) with a PIXImus Mouse Densitometer (Inside Outside Sales). Data are expressed as % fat.

qRT-PCR

Theracyte devices were harvested at 29 weeks post-transplantation from cohort 1 and stored for qPCR analysis. Details regarding the qPCR analysis, human islet donors, and the procedure used to isolate RNA from engrafted tissue are described in Supplemental Experimental Procedures. Primers are listed in Table S3.

Immunofluorescent Staining and Image Quantification

Prior to transplantation, a portion of differentiated pancreatic progenitor cells were fixed overnight in 4% paraformaldehyde (PFA) and then embedded in 1% agarose prior to paraffin embedding. In cohort 1, the Theractye devices and a variety of tissues (listed in Table S1) were harvested at 29 weeks post-transplantation, fixed in 4% PFA, and stored in 70% EtOH prior to paraffin embedding. All paraffin sections (5 μm thick) were prepared by Wax-it Histology Services. Immunofluorescent staining was performed

as previously described (Rezania et al., 2011) and details about the primary antibodies are provided in Table S4. The procedures used for image analysis and quantification are described in Supplemental Experimental Procedures. H&E staining was performed according to standard procedures and tissue analysis was performed in a blinded fashion by an independent pathologist (Nova Pathology PC).

Statistical Analysis

All statistical analyses were performed using GraphPad Prism software (GraphPad Software). Details about specific statistical tests are described in Supplemental Experimental Procedures. For all analyses, $p < 0.05$ was considered statistically significant. Data are presented as the mean ± SEM (line graphs) or as box-and-whisker plots showing individual data points.

SUPPLEMENTAL INFORMATION

Supplemental Information includes Supplemental Experimental Procedures, seven figures, and five tables and can be found with this article online at http://dx.doi.org/10.1016/j.stemcr.2015.02.011.

AUTHOR CONTRIBUTIONS

J.E.B. wrote the manuscript. J.E.B., A.R., and T.J.K. contributed to the conception and design of experiments. J.E.B., N.S., N.B., M.M., J.K.F., A.A., S.O., C.D., D.S.R., V.A.S., and A.R. were responsible for acquisition, analysis, and interpretation of data. All authors contributed to manuscript revisions and approved the final version of the manuscript.

ACKNOWLEDGMENTS

We thank Subashini Karunakaran and Dr. Susanne Clee for their technical assistance with DEXA. This work was funded by the Canadian Institutes of Health Research (CIHR) Regenerative Medicine and Nanomedicine Initiative, Stem Cell Network (SCN), Juvenile Diabetes Research Foundation (JDRF), and Stem Cell Technologies. J.E.B. and M.M. were funded by JDRF postdoctoral fellowships and the CIHR Transplantation Training Program. J.E.B. was also the recipient of a CIHR postdoctoral fellowship and L'Oréal Canada for Women in Science Research Excellence Fellowship. N.S. and C.D. received funding from the Stem Cell Network, and N.B. was the recipient of a DAAD RISE worldwide international research internship. A.R. is an employee and shareholder of Janssen R&D, LLC. D.S.R. and V.A.S. are employees of Janssen R&D, LLC. T.J.K. received financial support from Janssen R&D, LLC for the research described in this article.

Received: June 5, 2014
Revised: February 12, 2015
Accepted: February 13, 2015
Published: March 19, 2015

REFERENCES

Biarnés, M., Montolio, M., Nacher, V., Raurell, M., Soler, J., and Montanya, E. (2002). Beta-cell death and mass in syngeneically transplanted islets exposed to short- and long-term hyperglycemia. Diabetes *51*, 66–72.

Brauker, J., Martinson, L.A., Young, S.K., and Johnson, R.C. (1996). Local inflammatory response around diffusion chambers containing xenografts. Nonspecific destruction of tissues and decreased local vascularization. Transplantation *61*, 1671–1677.

Bruin, J.E., Rezania, A., Xu, J., Narayan, K., Fox, J.K., O'Neil, J.J., and Kieffer, T.J. (2013). Maturation and function of human embryonic stem cell-derived pancreatic progenitors in macroencapsulation devices following transplant into mice. Diabetologia *56*, 1987–1998.

Bruin, J.E., Erener, S., Vela, J., Hu, X., Johnson, J.D., Kurata, H.T., Lynn, F.C., Piret, J.M., Asadi, A., Rezania, A., and Kieffer, T.J. (2014). Characterization of polyhormonal insulin-producing cells derived in vitro from human embryonic stem cells. Stem Cell Res. (Amst.) *12*, 194–208.

Butler, A.E., Janson, J., Bonner-Weir, S., Ritzel, R., Rizza, R.A., and Butler, P.C. (2003). Beta-cell deficit and increased beta-cell apoptosis in humans with type 2 diabetes. Diabetes *52*, 102–110.

Denroche, H.C., Levi, J., Wideman, R.D., Sequeira, R.M., Huynh, F.K., Covey, S.D., and Kieffer, T.J. (2011). Leptin therapy reverses hyperglycemia in mice with streptozotocin-induced diabetes, independent of hepatic leptin signaling. Diabetes *60*, 1414–1423.

Denroche, H.C., Quong, W.L., Bruin, J.E., Tudurí, E., Asadi, A., Glavas, M.M., Fox, J.K., and Kieffer, T.J. (2013). Leptin administration enhances islet transplant performance in diabetic mice. Diabetes *62*, 2738–2746.

Eizirik, D.L., Jansson, L., Flodström, M., Hellerström, C., and Andersson, A. (1997). Mechanisms of defective glucose-induced insulin release in human pancreatic islets transplanted to diabetic nude mice. J. Clin. Endocrinol. Metab. *82*, 2660–2663.

Ferrannini, E., Gastaldelli, A., Miyazaki, Y., Matsuda, M., Mari, A., and DeFronzo, R.A. (2005). beta-Cell function in subjects spanning the range from normal glucose tolerance to overt diabetes: a new analysis. J. Clin. Endocrinol. Metab. *90*, 493–500.

Feuerer, M., Herrero, L., Cipolletta, D., Naaz, A., Wong, J., Nayer, A., Lee, J., Goldfine, A.B., Benoist, C., Shoelson, S., and Mathis, D. (2009). Lean, but not obese, fat is enriched for a unique population of regulatory T cells that affect metabolic parameters. Nat. Med. *15*, 930–939.

Gargani, S., Thévenet, J., Yuan, J.E., Lefebvre, B., Delalleau, N., Gmyr, V., Hubert, T., Duhamel, A., Pattou, F., and Kerr-Conte, J. (2013). Adaptive changes of human islets to an obesogenic environment in the mouse. Diabetologia *56*, 350–358.

Halban, P.A. (2008). Cell therapy for type 2 diabetes: is it desirable and can we get it? Diabetes Obes. Metab. *10* (*Suppl 4*), 205–211.

Hariri, N., and Thibault, L. (2010). High-fat diet-induced obesity in animal models. Nutr. Res. Rev. *23*, 270–299.

Hiramatsu, S., and Grill, V. (2001). Influence of a high-fat diet during chronic hyperglycemia on beta-cell function in pancreatic islet transplants to streptozotocin-diabetic rats. Eur. J. Endocrinol. *144*, 521–527.

International Diabetes Federation (2014). IDF Diabetes Atlas update poster, 6th ed. (Brussels, Belgium: International Diabetes Federation).

Kahn, S.E., Hull, R.L., and Utzschneider, K.M. (2006). Mechanisms linking obesity to insulin resistance and type 2 diabetes. Nature *444*, 840–846.

Kahn, S.E., Cooper, M.E., and Del Prato, S. (2014). Pathophysiology and treatment of type 2 diabetes: perspectives on the past, present, and future. Lancet *383*, 1068–1083.

Kalupahana, N.S., Moustaid-Moussa, N., and Claycombe, K.J. (2012). Immunity as a link between obesity and insulin resistance. Mol. Aspects Med. *33*, 26–34.

Kramer, C.K., Zinman, B., and Retnakaran, R. (2013). Short-term intensive insulin therapy in type 2 diabetes mellitus: a systematic review and meta-analysis. Lancet Diabetes Endocrinol *1*, 28–34.

Markan, K.R., Naber, M.C., Ameka, M.K., Anderegg, M.D., Mangelsdorf, D.J., Kliewer, S.A., Mohammadi, M., and Potthoff, M.J. (2014). Circulating FGF21 is liver derived and enhances glucose uptake during refeeding and overfeeding. Diabetes *63*, 4057–4063.

Mckenzie, A.W., Georgiou, H.M., Zhan, Y., Brady, J.L., and Lew, A.M. (2001). Protection of xenografts by a combination of immunoisolation and a single dose of anti-CD4 antibody. Cell Transplant. *10*, 183–193.

Nishimura, S., Manabe, I., Nagasaki, M., Eto, K., Yamashita, H., Ohsugi, M., Otsu, M., Hara, K., Ueki, K., Sugiura, S., et al. (2009). CD8+ effector T cells contribute to macrophage recruitment and adipose tissue inflammation in obesity. Nat. Med. *15*, 914–920.

Osborn, O., and Olefsky, J.M. (2012). The cellular and signaling networks linking the immune system and metabolism in disease. Nat. Med. *18*, 363–374.

Potter, K.J., Westwell-Roper, C.Y., Klimek-Abercrombie, A.M., Warnock, G.L., and Verchere, C.B. (2014). Death and dysfunction of transplanted β-cells: lessons learned from type 2 diabetes? Diabetes *63*, 12–19.

Rezania, A., Riedel, M.J., Wideman, R.D., Karanu, F., Ao, Z., Warnock, G.L., and Kieffer, T.J. (2011). Production of functional glucagon-secreting α-cells from human embryonic stem cells. Diabetes *60*, 239–247.

Rezania, A., Bruin, J.E., Riedel, M.J., Mojibian, M., Asadi, A., Xu, J., Gauvin, R., Narayan, K., Karanu, F., O'Neil, J.J., et al. (2012). Maturation of human embryonic stem cell-derived pancreatic progenitors into functional islets capable of treating pre-existing diabetes in mice. Diabetes *61*, 2016–2029.

Rezania, A., Bruin, J.E., Xu, J., Narayan, K., Fox, J.K., O'Neil, J.J., and Kieffer, T.J. (2013). Enrichment of human embryonic stem cell-derived NKX6.1-expressing pancreatic progenitor cells accelerates the maturation of insulin-secreting cells in vivo. Stem Cells *31*, 2432–2442.

Rickels, M.R., Kong, S.M., Fuller, C., Dalton-Bakes, C., Ferguson, J.F., Reilly, M.P., Teff, K.L., and Naji, A. (2013). Improvement in insulin sensitivity after human islet transplantation for type 1 diabetes. J. Clin. Endocrinol. Metab. *98*, E1780–E1785.

Riedel, M.J., Asadi, A., Wang, R., Ao, Z., Warnock, G.L., and Kieffer, T.J. (2012). Immunohistochemical characterisation of cells co-producing insulin and glucagon in the developing human pancreas. Diabetologia *55*, 372–381.

Ryan, E.A., Lakey, J.R., Rajotte, R.V., Korbutt, G.S., Kin, T., Imes, S., Rabinovitch, A., Elliott, J.F., Bigam, D., Kneteman, N.M., et al. (2001). Clinical outcomes and insulin secretion after islet transplantation with the Edmonton protocol. Diabetes *50*, 710–719.

Shapiro, A.M., Lakey, J.R., Ryan, E.A., Korbutt, G.S., Toth, E., Warnock, G.L., Kneteman, N.M., and Rajotte, R.V. (2000). Islet transplantation in seven patients with type 1 diabetes mellitus using a glucocorticoid-free immunosuppressive regimen. N. Engl. J. Med. *343*, 230–238.

Srinivasan, K., and Ramarao, P. (2007). Animal models in type 2 diabetes research: an overview. Indian J. Med. Res. *125*, 451–472.

Svenson, K.L., Von Smith, R., Magnani, P.A., Suetin, H.R., Paigen, B., Naggert, J.K., Li, R., Churchill, G.A., and Peters, L.L. (2007). Multiple trait measurements in 43 inbred mouse strains capture the phenotypic diversity characteristic of human populations. J. Appl. Physiol. *102*, 2369–2378.

Tibell, A., Rafael, E., Wennberg, L., Nordenström, J., Bergström, M., Geller, R.L., Loudovaris, T., Johnson, R.C., Brauker, J.H., Neuenfeldt, S., and Wernerson, A. (2001). Survival of macroencapsulated allogeneic parathyroid tissue one year after transplantation in nonimmunosuppressed humans. Cell Transplant. *10*, 591–599.

Weisberg, S.P., McCann, D., Desai, M., Rosenbaum, M., Leibel, R.L., and Ferrante, A.W., Jr. (2003). Obesity is associated with macrophage accumulation in adipose tissue. J. Clin. Invest. *112*, 1796–1808.

Weng, J., Li, Y., Xu, W., Shi, L., Zhang, Q., Zhu, D., Hu, Y., Zhou, Z., Yan, X., Tian, H., et al. (2008). Effect of intensive insulin therapy on beta-cell function and glycaemic control in patients with newly diagnosed type 2 diabetes: a multicentre randomised parallel-group trial. Lancet *371*, 1753–1760.

Weyer, C., Bogardus, C., Mott, D.M., and Pratley, R.E. (1999). The natural history of insulin secretory dysfunction and insulin resistance in the pathogenesis of type 2 diabetes mellitus. J. Clin. Invest. *104*, 787–794.

Winer, S., Chan, Y., Paltser, G., Truong, D., Tsui, H., Bahrami, J., Dorfman, R., Wang, Y., Zielenski, J., Mastronardi, F., et al. (2009). Normalization of obesity-associated insulin resistance through immunotherapy. Nat. Med. *15*, 921–929.

Winer, D.A., Winer, S., Shen, L., Wadia, P.P., Yantha, J., Paltser, G., Tsui, H., Wu, P., Davidson, M.G., Alonso, M.N., et al. (2011). B cells promote insulin resistance through modulation of T cells and production of pathogenic IgG antibodies. Nat. Med. *17*, 610–617.

Yoon, K.H., Ko, S.H., Cho, J.H., Lee, J.M., Ahn, Y.B., Song, K.H., Yoo, S.J., Kang, M.I., Cha, B.Y., Lee, K.W., et al. (2003). Selective beta-cell loss and alpha-cell expansion in patients with type 2 diabetes mellitus in Korea. J. Clin. Endocrinol. Metab. *88*, 2300–2308.

We don't compromise on quality.

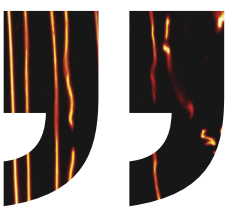

We understand that respect is not a given, it's earned. Our standards are high, but you wouldn't have it any other way. That's why you choose to publish with us.

When you choose Cell Press you get the attention you deserve.

For more information visit: www.cell.com/values

Your **work** is our **life**

Cell PRESS

Stem Cell Reports
Article

OPEN ACCESS

Human iPSC-Derived Hepatocyte-like Cells Support *Plasmodium* Liver-Stage Infection In Vitro

Shengyong Ng,[1] Robert E. Schwartz,[2,3] Sandra March,[2,6] Ani Galstian,[2,6] Nil Gural,[2] Jing Shan,[2] Mythili Prabhu,[2] Maria M. Mota,[4,5] and Sangeeta N. Bhatia[2,3,5,6,*]

[1]Department of Biological Engineering, Massachusetts Institute of Technology, Cambridge, MA 02139, USA
[2]Health Sciences and Technology/Institute for Medical Engineering and Science, Massachusetts Institute of Technology, Cambridge, MA 02139, USA
[3]Department of Medicine, Brigham and Women's Hospital, Boston, MA 02115, USA
[4]Unidade de Malária, Instituto de Medicina Molecular, Universidade de Lisboa, 1649-028 Lisboa, Portugal
[5]Howard Hughes Medical Institute, Koch Institute, and Electrical Engineering and Computer Science, Massachusetts Institute of Technology, Cambridge, MA 02139, USA
[6]Broad Institute, Cambridge, MA 02139, USA
*Correspondence: sbhatia@mit.edu
http://dx.doi.org/10.1016/j.stemcr.2015.01.002

SUMMARY

Malaria eradication is a major goal in public health but is challenged by relapsing malaria species, expanding drug resistance, and the influence of host genetics on antimalarial drug efficacy. To overcome these hurdles, it is imperative to establish in vitro assays of liver-stage malaria for drug testing. Induced pluripotent stem cells (iPSC) potentially allow the assessment of donor-specific drug responses, and iPSC-derived hepatocyte-like cells (iHLCs) can facilitate the study of host genetics on host-pathogen interactions and the discovery of novel targets for antimalarial drug development. We establish in vitro liver-stage malaria infections in iHLCs using *P. berghei*, *P. yoelii*, *P. falciparum*, and *P. vivax* and show that differentiating cells acquire permissiveness to malaria infection at the hepatoblast stage. We also characterize antimalarial drug metabolism capabilities of iHLCs using prototypical antimalarial drugs and demonstrate that chemical maturation of iHLCs can improve their potential for antimalarial drug testing applications.

INTRODUCTION

Malaria affects 250 million people and causes approximately one million deaths each year (World Health Organization, 2013). As an obligatory stage of the *Plasmodium* life cycle that occurs soon after infection of the human host, the liver stage is an attractive target for the development of antimalarial drugs and vaccines (Mazier et al., 2009; Prudêncio et al., 2006), especially with the goal of malaria eradication. Current in vitro models of liver-stage malaria commonly utilize hepatic cell lines such as HepG2 or HC04 in conjunction with *Plasmodium* sporozoites from either rodent malaria species (*P. berghei*, *P. yoelii)* or human malaria species (*P. falciparum, P. vivax*), which have liver stages that range in length from 2 days for *P. berghei* and *P. yoelii* to 6–8 days for *P. falciparum* and *P. vivax*. Due to their better maintenance of hepatic drug metabolism enzymes compared to hepatic cell lines and the fact that they are the natural host for malarial sporozoites, primary human hepatocytes are a preferable cell type to model liver-stage malaria in vitro for the purposes of antimalarial drug development. These traits of primary human hepatocytes mean they may offer better predictive value in in vitro liver-stage malaria phenotypic drug screens and may more accurately recapitulate host-pathogen interactions in vitro than the cell lines that are typically used for modeling liver-stage malaria (March et al., 2013). However, primary human hepatocytes are sourced from a small pool of donors and thus may not represent the genetic diversity of the human population.

Pluripotent stem cell-derived hepatocytes overcome some of the drawbacks of cell lines, fetal tissue, and adult human sources and may be considered an alternative source of primary human hepatocytes. Compared to primary human hepatocytes, stem cell-derived hepatocytes can represent more diverse genotypes, can be personalized to exhibit rare genotypes, and are renewable in culture. Human pluripotent embryonic stem cells were first isolated from human blastocysts (Thomson, 1998), but embryonic stem cells face considerable ethical issues with regards to their availability and use. More recently, the enforced expression of various factors in a variety of differentiated cell types led to the generation of induced pluripotent stem cells (iPSCs) (Takahashi et al., 2007). In particular, iPSCs can, in a reliable and stepwise manner, differentiate through the developmentally appropriate stages (i.e., endoderm, hepatic specified endoderm, hepatoblasts) to produce hepatocyte-like cells (iHLCs) in vitro (Schwartz et al., 2014). The ability to generate iHLCs from different donors provides an opportunity to assess donor-specific drug responses in vitro, akin to conducting an in vitro clinical trial. Our prior work has shown that iHLCs are susceptible to hepatotropic pathogens such as hepatitis C and hepatitis B virus infection (Schwartz et al., 2012; Shlomai et al., 2014). It remains to be seen whether iHLCs can serve as a host population for liver-stage malaria assays,

especially considering that iHLCs generated using current state of the art protocols are developmentally immature and more closely resemble fetal hepatocytes in their cytochrome P450 expression and activity profiles as well as in their antigen expression (Si-Tayeb et al., 2010). However, recent promising attempts to mature iHLCs to a more adult phenotype, including the identification of small molecules (Shan et al., 2013), genetic manipulation with transduction of a gene for a hepatic transcription factor (Takayama et al., 2012), a combination of 3D culture and cAMP signaling (Ogawa et al., 2013), or in vivo transplantation (Takebe et al., 2013), may ultimately contribute to the generation of appropriately mature iHLCs for antimalarial drug screens, which, to date, have largely been carried out in human hepatoma cells (da Cruz et al., 2012; Derbyshire et al., 2012; Meister et al., 2011). Isogenic iHLCs that are more developmentally mature may also facilitate the discovery of host factors for the *Plasmodium* liver stages.

In this study, we show the feasibility of infecting iHLCs with *Plasmodium* sporozoites in vitro and demonstrate *Plasmodium* parasite development over time in culture. We identify the stage at which cells acquire permissiveness to liver-stage malaria infection during the differentiation process. It is also necessary to characterize the responses of malaria-infected iHLCs to known antimalarial drugs in order to establish the utility of this cell type for use in in vitro liver-stage malaria phenotypic drug screens. We observe that iHLCs are not responsive to the antimalarial drug primaquine and hypothesize this deficiency is due to a lack of bioactivation of the drug by hepatic cytochrome P450 drug metabolism enzymes. Consistent with this model, we further demonstrate that chemically matured iHLCs acquire primaquine sensitivity, highlighting the potential to use iHLCs for antimalarial drug testing.

RESULTS

iPSC-Derived Hepatocyte-like Cells Support Liver-Stage Malaria Infection In Vitro

iPSC-derived hepatocyte-like cells (iHLCs) were generated using a 20 day in vitro differentiation protocol that recapitulates the different stages of hepatic development (Si-Tayeb et al., 2010). During this differentiation process, iPSCs adopt an endoderm fate at 5 days and become hepatic-specified endoderm cells at 10 days, hepatoblasts at 15 days, and iHLCs at 20 days after the initiation of differentiation, respectively (Figure 1A). iHLCs demonstrate typical polygonal hepatocyte morphology (Figure 1B) and express prototypical hepatic markers like human albumin, α1-antitrypsin, and α-fetoprotein (Figure 1C). The two known host entry factors for liver-stage malaria, CD81 and SRB1, are both transcribed and translated in iHLCs (Figures 1D and 1E), and the proteins are appropriately localized on the cell surface, as observed via immunofluorescence assays (Figures 1F and 1G). Based on these observations, we hypothesized that day 20 iHLCs may support *Plasmodium* infection.

Cultures of iHLCs were overlaid with media containing *P. berghei* sporozoites for 3 hr and fixed at 1, 2, or 3 days postexposure. Immunofluorescence assays using antibodies specific for *P. berghei* HSP70 were conducted in order to quantitate iHLC infection by *P. berghei* (Figure 2A). HSP70-expressing exoerythrocytic forms (EEFs) were detected as early as 1 day postinfection, and larger EEFs were observed at later time points (Figures 2A and 2B). Furthermore, at 3 days postinfection the *P. berghei* (*P.b.*) EEFs expressed the mature EEF marker, MSP-1 (Figure 2C), suggesting that *P.b.* EEF maturation occurred along with *P.b.* EEF growth. In addition, separate cultures of iHLCs were infected with an alternate rodent *Plasmodium* species, *P. yoelii* (*P.y.*), and were shown to support *P.y.* EEFs that also increased in size over a 48 hr period postinfection (Figures 2D and 2E). iHLCs were next tested for their capacity to be infected by the human malaria parasite, *P. falciparum* (*P.f.*), and were found to harbor HSP70-expressing *P.f.* EEFs at 3 days postexposure (Figure 2F). Moreover, at 6 days postexposure, *P.f.* EEFs also expressed the liver-stage maturation marker, *P.f.* MSP-1 (Figure 2G; 10%–35% *P.f.* EEFs, as compared to 45% for *P.b.* EEFs), and increased in size compared to those observed at 3 days postexposure to *P.f.* sporozoites (Figures 2F and 2H). In addition to *P.f.*, iHLCs were also infected with sporozoites of a different human malaria species, *P. vivax* (*P.v.*), and were found to support HSP70-expressing *P.v.* EEFs that also increased in size from an average of 5 μm at 3 days postinfection to a wide range of sizes up to 77 μm by 8 days postinfection (Figures 2I and 2J). These results indicate that iHLC infectibility with *Plasmodium* sporozoites is not restricted to the rodent malaria species, and that the in-vitro-derived host cells can also support EEF maturation. Last, differentiated iHLCs were phenotypically stable and could be infected with *P.f.* sporozoites up to day 55 after initiation of differentiation (Figure S1 available online), which was the latest time point tested for *Plasmodium* infectibility in this study.

Kinetics of Acquisition of Permissiveness to *Plasmodium* Infectibility

To determine at what point in the 20 day in vitro differentiation process that iPSC-derived hepatic lineage cells become susceptible to malaria infection, cells at different stages of differentiation (iPS cells, endoderm, hepatic-specified endoderm, hepatoblast, iHLCs) were exposed to sporozoites obtained from a single batch of *P.f.*-infected *A. gambiae* mosquitoes. At 4 days postinfection, no *P.f.* EEFs were observed in iPSCs, whereas a small

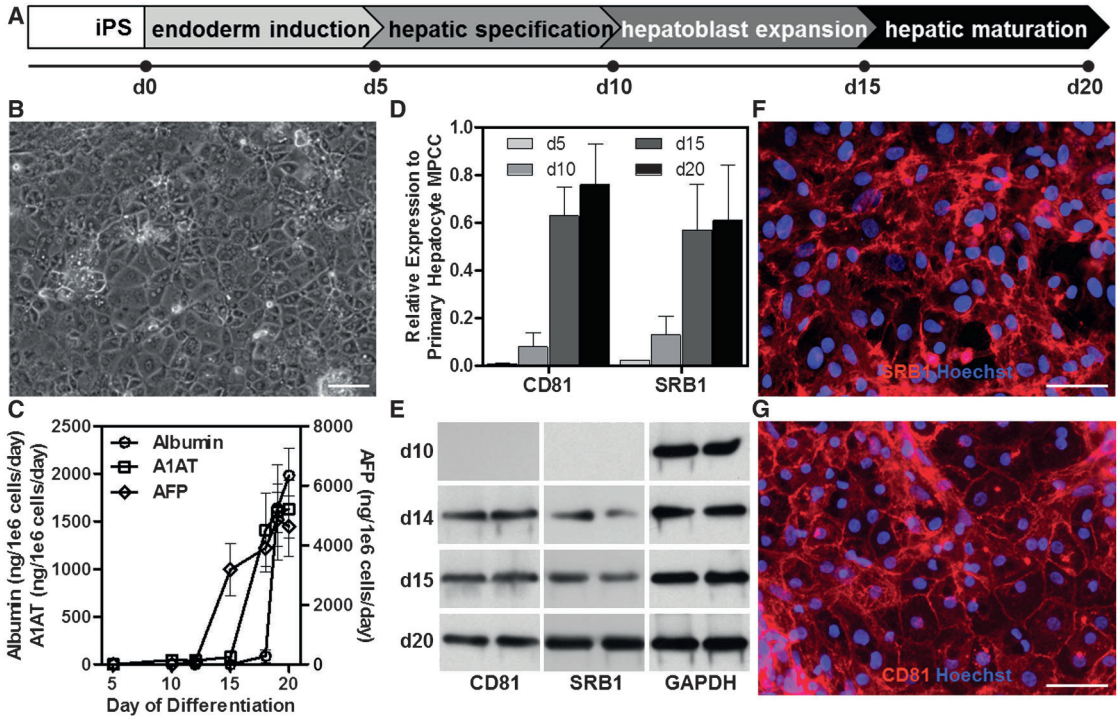

Figure 1. Characterization of iHLCs Derived by In Vitro Differentiation of iPSCs

(A) Schematic of protocol for the in vitro differentiation of iPS cells to iHLCs.

(B) Representative bright-field image showing typical hepatic morphology of iHLCs at d20 postdifferentiation.

(C) Kinetics of human albumin, α1-anti-trypsin (A1AT), and α-fetoprotein (AFP) secretion over the course of differentiation from iPS cells to iHLCs. n = 3 biological replicates per condition. Data are represented as mean ± SEM.

(D) Representative RT-PCR analysis of *CD81* and *SRB1* gene expression over the course of differentiation from iPS cells to iHLCs. n = 3 biological replicates per condition. Data are represented as mean ± SEM.

(E) Representative western blot analysis of CD81 and SRB1 protein expression over the course of differentiation from hepatic-specified endoderm cells to iHLCs. n = 2 biological replicates are shown.

(F and G) Representative immunofluorescence images of d20 iHLCs expressing (F) CD81 and (G) SRB1.

Scale bars, 50 μm.

number were observed in endoderm cells (d5 cells) and hepatic-specified endoderm cells (d10 cells) (Figures 3A and 3B). However, the number of *P.f.* EEFs was significantly higher in hepatoblasts (d15 cells) than in hepatic-specified endoderm cells and the frequency of infection remained elevated in differentiated iHLCs (d20 cells) (Figures 3A and 3B). Although some variability is observed between experiments regarding the relative number of *P.f.* EEFs observed between d15 and d20 cells (Figure 3B, left versus right), likely a product of the established stochastic nature of the iHLC differentiation process and also a function of heterogeneity of iPSC-derived progeny in each well, we consistently observed acquisition of more robust *P.f.* susceptibility between days 10 and 15 of the directed differentiation protocol. Notably, the size distributions of observed *P.f.* EEFs at 4 days postinfection were not significantly different at any time point (d5, d10, d15, d20 postdifferentiation) (Figure 3C), suggesting that the rare cells that exhibit permissiveness to *Plasmodium* sporozoite infection at earlier time points were already capable of supporting parasite survival and growth for at least 4 days postinfection. This pattern is emphasized by the observations at 6 days postinfection that d15 hepatoblasts maintained similar levels of *P.f.* infection as d20 iHLCs (Figure S2A), exhibited increased *P.f.* EEF sizes than at 4 days postinfection (Figure S2B), and supported the maturation of *P.f.* EEFs as demonstrated by the expression of the liver-stage maturation marker, *P.f.* MSP-1 (Figures S2A and S2C), and the appearance of merosome-like structures (Figure S2D). However, a higher proportion of *P.f.* EEFs in d20 iHLCs express *P.f.* MSP1 (~40%) than those in d15 hepatoblasts (~20%) (Figure S2A), and the *P.f.* EEF size distribution is larger in iHLCs than in hepatoblasts (Figure S2B) at 6 days postinfection. These data suggest that, whereas hepatoblasts are also capable of supporting *P.f.* EEF

survival, growth, and maturation, *P.f.* EEFs in hepatoblasts may develop to either a slower or smaller degree than those in iHLCs. In addition to their capacity to be infected by *P.f.* sporozoites, d16 hepatoblasts and completely differentiated iHLCs both support similar numbers of *P.y.* EEFs at 2 days postinfection (Figure S2E), suggesting that incompletely differentiated hepatoblasts have also acquired sufficient host factors to allow the invasion and growth of rodent *Plasmodium* sporozoites.

Plasmodium-Infected iHLCs Are Sensitive to Atovaquone but Not Primaquine

Because iHLCs obtained via the current iPSC in vitro differentiation protocol express a relatively low level of 83 human hepatic drug metabolism enzymes (DMEs) compared to primary human hepatocytes (Shan et al., 2013), we hypothesized that *Plasmodium*-infected iHLCs may only respond to antimalarial drugs that are active in their parent form, such as atovaquone (Biagini et al., 2012), and not to drugs that require bioactivation by hepatic DMEs in order to demonstrate inhibitory activity against the *Plasmodium* liver stages, such as primaquine (Bennett et al., 2013; Pybus et al., 2013). Indeed, when iHLCs infected with *P. yoelii* sporozoites were treated with 10 nM atovaquone or 10 μM primaquine starting at 3 hr postinfection, only the atovaquone-treated cultures were blocked in their ability to support *P.y.* EEFs (Figure 4A). In contrast, no differences in the number or size distribution of *P.y.* EEFs were observed in primaquine-treated iHLCs infected at either 23 or 28 days postdifferentiation (Figures 4B and 4C), suggesting that primaquine exposure had no impact on the infection or growth of *P.y.* EEFs. This finding supports the hypothesis that, whereas iHLCs support *P.y.* invasion and *P.y.* EEF growth, they do not express the appropriate hepatic DMEs, and/or other host factors, necessary for the bioactivation of primaquine into a form that can inhibit liver-stage *P.y.* EEFs. To confirm that the absence of primaquine sensitivity of *Plasmodium*-infected iHLCs extends to the human *Plasmodium* species, iHLCs were infected with *P. falciparum* sporozoites, and primaquine treatment was started 3 hr postexposure to sporozoites. As observed following infection with *P.y.*, primaquine treatment of *P.f.*-infected iHLCs did not reduce the number of *P.f.* EEFs (Figure 4D), nor did it alter the *P.f.* EEF size distribution (Figure 4E).

Small Molecule-Mediated Maturation of iHLCs Confers Primaquine Sensitivity

In order to utilize iHLCs in antimalarial phenotypic drug screens, it would be highly advantageous to obtain iHLCs with a developmentally mature hepatic DME profile. A previous high-throughput small molecule screen identified two small molecules capable of promoting transcriptional upregulation of many adult human hepatic DMEs (Shan et al., 2013), including the four DMEs CYP2D6, CYP3A4, CYP2C19, and MAO-A, that are responsible for the majority of primaquine metabolism and bioactivation in hepatocytes (Jin et al., 2014; Pybus et al., 2012, 2013). To test whether maturation of iHLCs induced by of these small molecules, FPH1, confers primaquine sensitivity, iHLCs were treated with either FPH1 or the DMSO carrier for a total of 6 days (treatment phase, D21–26). The iHLCs were cultured for an additional 1–2 days without the small molecule (washout phase, D27–28) before being exposed to *Plasmodium* sporozoites, in order to avoid any direct effects of the small molecule or DMSO on sporozoite infectivity, or on eventual drug sensitivity during the liver-stage infection (Figure 5A).

For the purposes of a moving toward an eventual high-throughput screening protocol, we used a bioluminescent strain of *P. yoelii* that expresses firefly luciferase (*P.y.-luc*) to readout parasite infection and growth in the presence of primaquine following FPH1-induced maturation of iHLCs. The bioluminescence of *P.y.-luc* liver-stage EEFs is directly proportional to the total liver-stage load, as measured by RT-PCR (Miller et al., 2013; Mwakingwe et al., 2009), and is also a function of the total number of EEFs per well and the mean EEF diameter in that well (Figure S3). Although *P.y.-luc* infection (as measured by BLI) in DMSO-treated iHLCs did not decrease upon primaquine treatment, iHLCs pretreated with FPH1 exhibited significantly lower levels of *P.y.-luc* infection (Figure 5B).

To determine whether primaquine sensitivity was also achieved in *P. falciparum*-infected iHLCs, iHLCs were pretreated with FPH1 or DMSO and exposed to *P.f.* sporozoites. At 4 days postinfection, the infected cultures were fixed, and *P.f.* infection was quantified by manual counts of *P.f.* EEFs immunostained for PfHSP70. As predicted, iHLCs pretreated with DMSO supported an equivalent number and size distribution of *P.f.* EEFs in the presence or absence of primaquine during infection. However, iHLCs pretreated with FPH1 exhibited a significant decrease in the number of *P.f.* EEFs present when infected in the presence of primaquine (Figure 5C). Furthermore, the fewer *P.f.* EEFs observed in FPH1 pretreated iHLCs showed a significant decrease in their size distribution (Figure 5D). Collectively, the data clearly show that primaquine becomes more effective against both *P. yoelii* and *P. falciparum* EEFs in cells exposed to FPH1.

DISCUSSION

In this study, we show the feasibility of infecting iHLCs with *P. berghei*, *P. yoelii*, *P. falciparum*, and *P. vivax*.

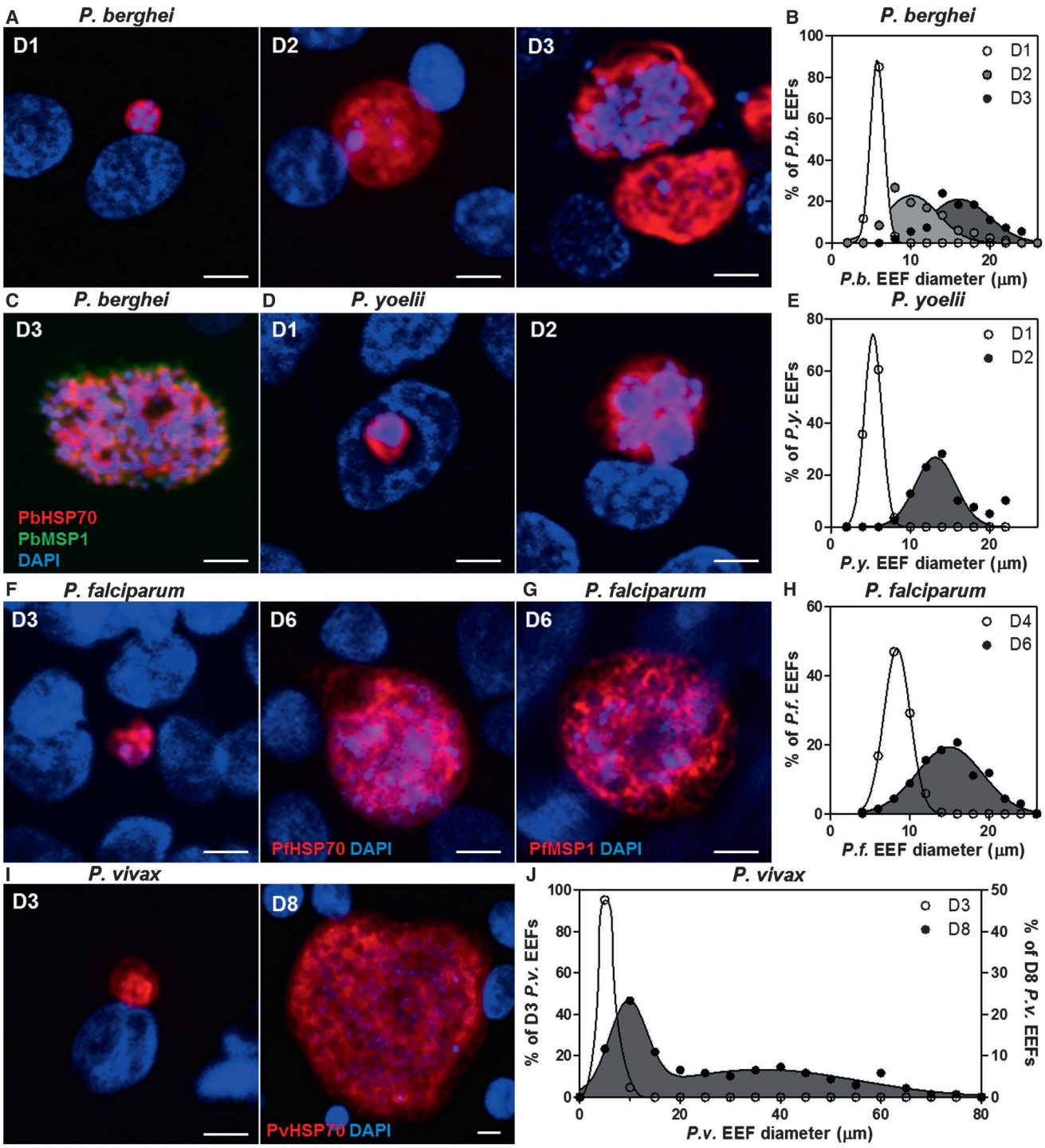

Figure 2. iHLCs Are Susceptible to Liver-Stage *Plasmodium* Infection

(A and B) (A) Representative immunofluorescence images of *P. berghei* (*P.b.*) EEFs and (B) *P.b.* EEF size distributions at D1, D2, or D3 postinfection in iHLCs.

(C) Representative immunofluorescence image of MSP1-positive *P.b.* EEF at D3 postinfection.

(D and E) (D) Representative immunofluorescence images of *P. yoelii* (*P.y.*) EEFs and (E) *P.y.* EEF size distributions at D1 or D2 postinfection in iHLCs.

(legend continued on next page)

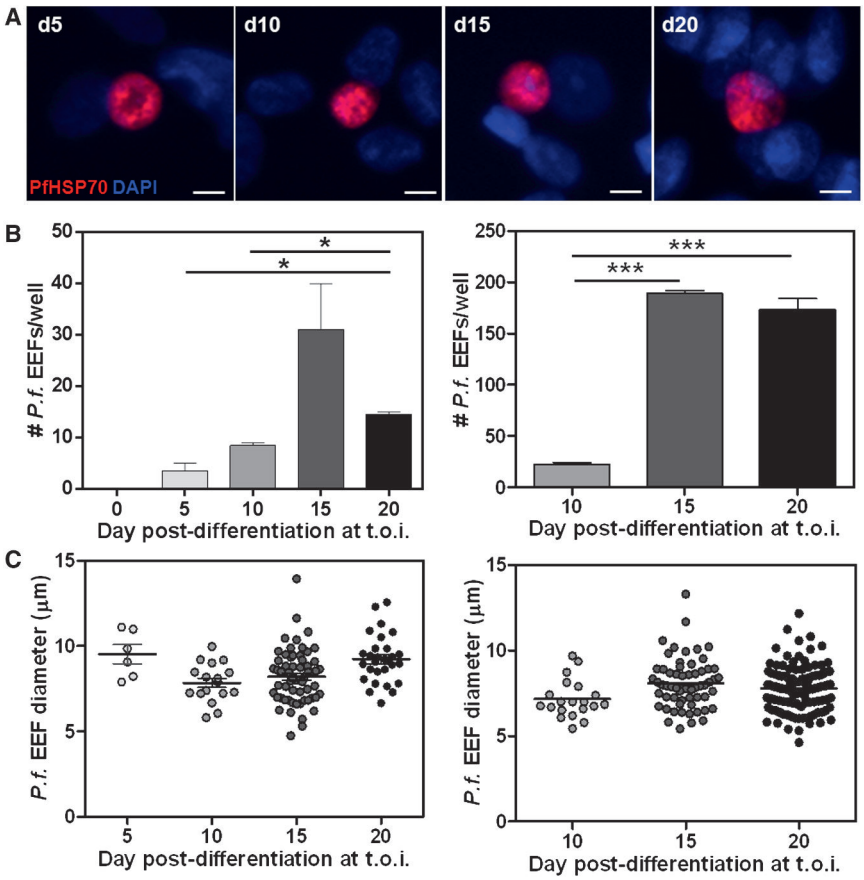

Figure 3. Kinetics of Acquisition of Permissiveness to *Plasmodium* Infectibility

(A) Representative IF images of *P. falciparum* (*P.f.*) EEFs from cells infected at various stages after the initiation of iPSC differentiation at D4 postinfection. Scale bars, 5 μm.

(B) Peak susceptibility to *P.f.* infection is attained at d15 after the initiation of differentiation, at the hepatoblast stage. The left and right panels represent two separate experiments using iHLCs from the same line but two separate differentiations, which were infected with two separate batches of *P.f.* sporozoites. n = 3 biological replicates per condition. Data are represented as mean ± SEM.

(C) Size distributions of *P.f.* EEFs obtained from an infection of cells at the endoderm (d5), hepatic-specified endoderm (d10), hepatoblast (d15), or iHLC (d20) stage.

*p < 0.05, ***p < 0.001; one-way ANOVA with Tukey's multiple comparison test. See also Figure S2.

Liver-stage *Plasmodium* EEFs grow in size over time and express MSP-1, which is typically expressed in more mature EEFs. Although iPS cells and definitive endoderm cells are generally not infectible with *P. falciparum*, some degree of *P. falciparum* infectibility is acquired by the time the cells are further differentiated to a hepatic-specified endoderm lineage. Notably, populations of hepatoblasts are equally or more infectible than the resulting iHLCs at the end of the in vitro differentiation protocol. iHLCs generated by the existing differentiation protocol do not respond to primaquine, a malaria drug that requires bioactivation by mature hepatic cytochrome P450 (CYP450) enzymes. However, further maturation of iHLCs using a previously described small molecule results in the acquisition of primaquine sensitivity, such that the drug treatment diminished infection by *P. yoelii* and *P. falciparum*.

In the context of drug development, there has been a shift from the traditional paradigm of testing drugs in immortalized cell lines to the use of primary cells, which have been increasingly recognized to offer better physiological relevance to drug screening and disease modeling in vitro (Engle and Puppala, 2013). A key goal of early-stage drug discovery platforms is the elimination of drug candidates that generate toxic metabolites that can cause drug-induced liver injury (DILI), a key cause of drug removal from the market (McDonnell and Braverman, 2006). To this end, a hepatic cell type that accurately recapitulates the native cellular physiology of an adult human hepatocyte is advantageous, but most hepatic cell lines lack the expression of a wide array of such key adult hepatic metabolism activity (March et al., 2013) because they are largely tumor derived (i.e., HepG2) or tumor associated

(F and H) (F) Representative immunofluorescence images of *P. falciparum* (*P.f.*) EEFs and (H) *P.f.* EEF size distributions at D3 or D6 postinfection in iHLCs.

(G) Representative immunofluorescence image of MSP1-positive *P.f.* EEF at D6 postinfection.

(I and J) (I) Representative immunofluorescence images of *P. vivax* (*P.v.*) EEFs and (J) *P.v.* EEF size distributions at D3 or D8 postinfection in iHLCs.

Scale bars, 5 μm. See also Figure S1.

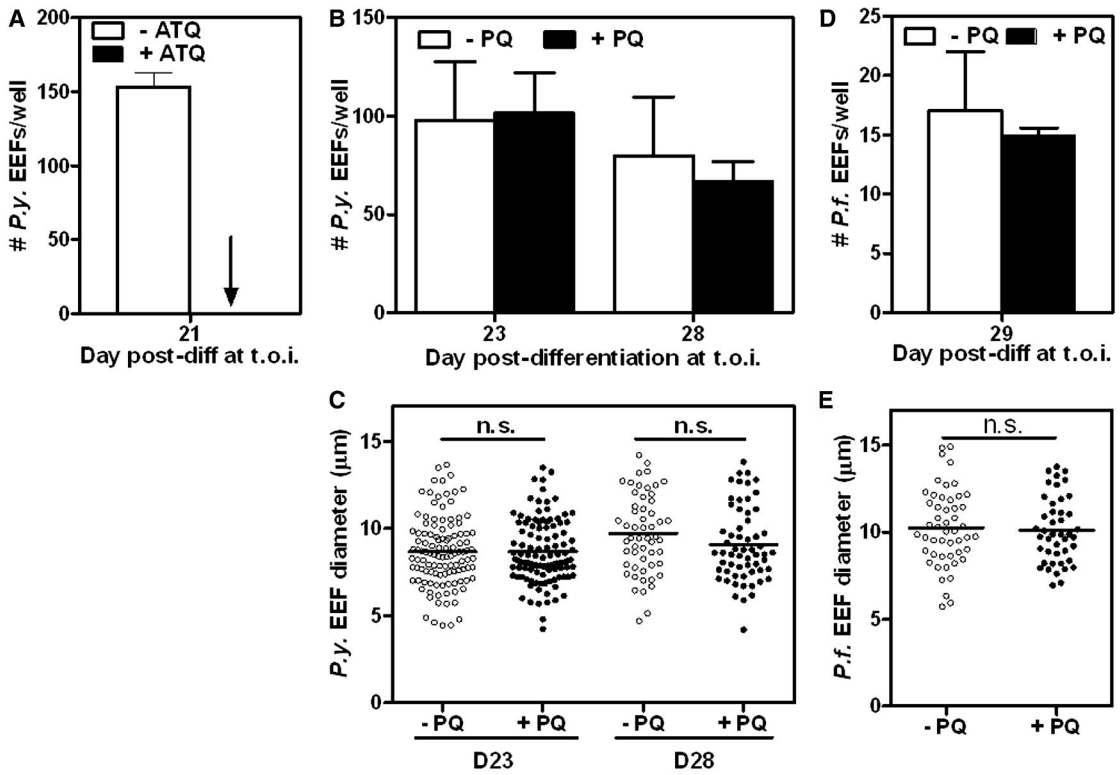

Figure 4. *Plasmodium*-Infected iHLCs Are Sensitive to Atovaquone but Not Primaquine

(A) Number of *P. yoelii* (*P.y.*) EEFs per well in iHLCs that were infected at 21 days postdifferentiation in the presence or absence of 10 nM atovaquone (ATQ). n = 3 biological replicates per condition.

(B and C) (B) Number of *P.y.* EEFs per well and (C) size distributions of *P.y.* EEFs in iHLCs that were infected at 23 or 28 days postdifferentiation in the presence or absence of 10 μM primaquine (PQ). n = 3 biological replicates per condition.

(D and E) (D) Number of *P. falciparum* (*P.f.*) EEFs per well and (E) size distributions of *P.f.* EEFs in iHLCs that were infected at 29 days postdifferentiation in the presence or absence of 10 μM primaquine.

n = 3 biological replicates per condition. Two-tailed t test run for panels (B)–(E). Data are represented as mean ± SEM.

(i.e., HC04). A second major goal of drug discovery platforms is the ability to identify nontoxic compounds that demonstrate differential efficacy in a phenotypic screen relevant to a disease. In the case of drug discovery against the malarial liver stages, it is therefore highly advantageous to utilize a cell type that best represents the primary adult hepatocyte. At the same time, it is also ideal to represent highly polymorphic genetic variants in drug metabolism and different ethnic groups in such drug screens, as these factors may influence the efficacy of potential antimalarial drug candidates. For example, genetic polymorphisms in CYP2D6 metabolism that stratified *P. vivax* patients into poor, intermediate, or extensive CYP2D6 metabolizers were recently reported to correlate with the risk of a failure of primaquine to prevent malaria relapse due to *P. vivax* (Bennett et al., 2013). Several cell sources have been proposed to augment the genetic variation and supply of adult primary human hepatocytes, including xenogenic or fetal human tissue, or embryonic stem cell-derived hepatocytes, but these sources are hampered by safety, ethical, or sourcing issues.

iPSC-derived iHLCs offer a unique advantage in that they can be generated from any donor, which allows a broad spectrum of the human population to be represented in in vitro drug screens and provides an opportunity to assess donor-specific drug responses in vitro. Recent collaborations between drug discovery companies and academic laboratories (Engle and Puppala, 2013) mark the development of an infrastructure that will benefit future personalized models of human diseases, including hepatotropic diseases like the relapsing forms of malaria.

iPSCs can also be engineered using DNA editing techniques to incorporate any genetic abnormality or modification to enable the exploration of the role that host genetics plays in liver-stage malaria infection. Although clinically relevant host factors that influence hepatic susceptibility to liver-stage malaria infection have not been documented, the study of potential host factors may benefit from the

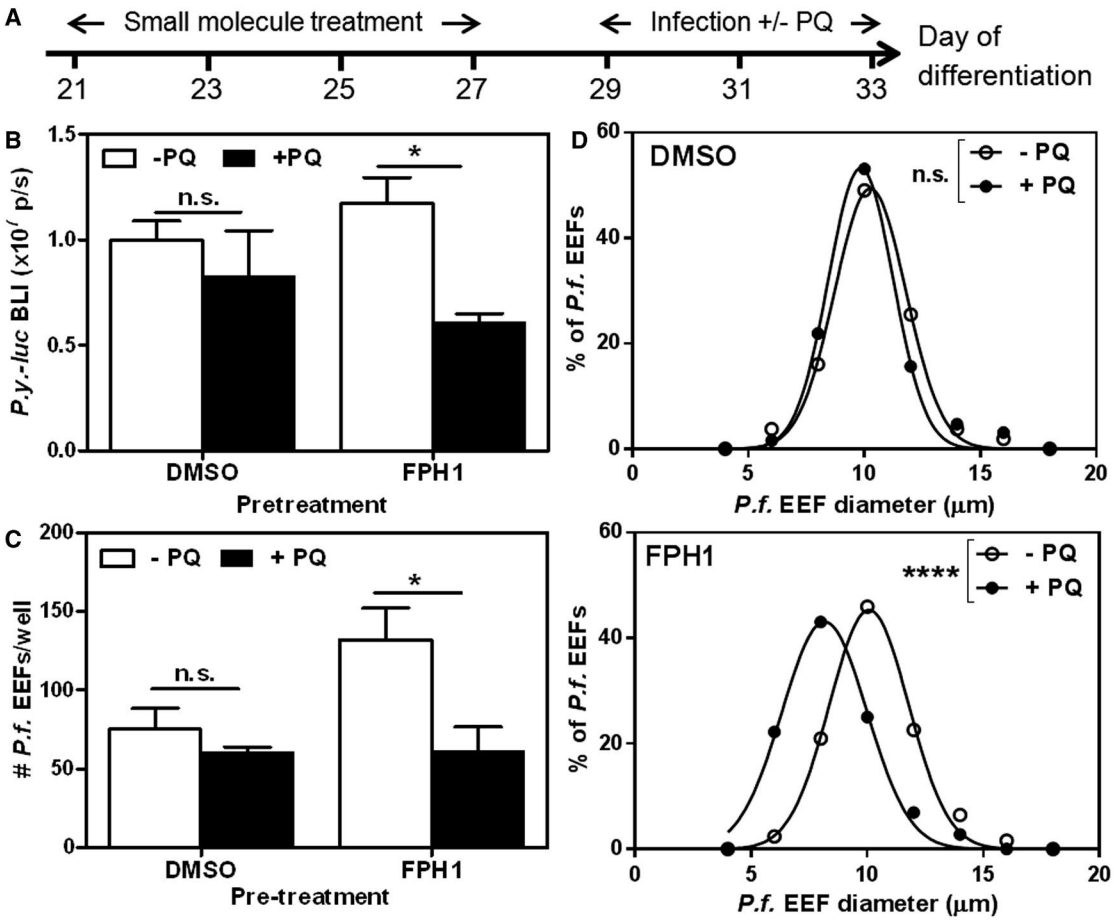

Figure 5. Small Molecule-Mediated Maturation of iHLCs Confers Primaquine Sensitivity

(A) Schematic of small molecule dosing of iHLCs before infection with *P. yoelii-luciferase* (*P.y.-luc*) or *P. falciparum* (*P.f.*).

(B) Effect of FPH1 pretreatment on primaquine (PQ) sensitivity (closed bars, 10 μM primaquine) of iHLCs infected with *P.y.-luc*. Infection was measured by bioluminescence imaging of *P.y.-luc*-infected iHLCs. n = 4 biological replicates per condition. *p < 0.05, two-tailed t test. See also Figure S3.

(C) Effect of FPH1 pretreatment on primaquine sensitivity of iHLCs infected with *P.f.* Infection was measured by counting the number of *P.f.* EEFs per well. n = 4 biological replicates per condition. *p < 0.05, two-tailed t test.

(D) Size distributions of *P.f.* EEFs in *P.f.*-infected iHLCs that were pretreated with the DMSO carrier or FPH1 and treated with or without 10 μM primaquine after infection. ****p < 0.0001, two-tailed t test. Data are represented as mean ± SEM.

larger pool of genetic variation that is accessible with the use of iPSCs. This effort may have implications in drug discovery against the liver stages of malaria species that present with large genetic heterogeneities in different parts of the world, especially the relapsing malaria species like *P. vivax* (e.g., temperate versus tropical strains), which may have coevolved to infect geographically distinct human populations (Cui et al., 2003; Dondorp et al., 2009; Gunawardena et al., 2010; Li et al., 2001).

From a developmental standpoint, the infectibility of iHLCs with liver-stage malaria and other hepatotropic pathogens such as the hepatitis viruses could also be a potential biomarker of hepatic lineage commitment, with iPSCs becoming permissive only when they become sufficiently hepatocyte-like. The ability to study liver-stage malaria infection at different developmental stages during the in vitro directed differentiation of iPSCs into iHLCs within a single donor may also facilitate the identification of host factors required for permissiveness to *Plasmodium* sporozoite infection and the elucidation of the roles that these host factors play in malaria pathogenesis.

One potential measure of how developmentally close iHLCs are to primary human hepatocytes is the efficiency of liver-stage malaria infection of iHLCs compared to primary human hepatocytes. With the multiplicity of infection (MOI) of approximately 0.5 used in the above

P. falciparum experiments (with respect to the estimated number of iHLCs per well based on an estimate of differentiation efficiency), an infection rate of approximately 0.3–1.8 *P.f.* EEFs per 10,000 iHLCs is obtained. In comparison, a microscale human liver platform that was recently reported to support *P. falciparum* infection in primary human hepatocytes reported an infection rate of approximately 100 *P.f.* EEFs per 10,000 hepatocytes at 3.5 days after infection with an MOI of 15 (March et al., 2013). Assuming that the infection rate scales linearly with MOI for the purposes of this analysis, an MOI of 0.5 in primary human hepatocytes would be estimated to give rise to an infection rate of approximately 3 *P.f.* EEFs per 10,000 hepatocytes. This suggests that iHLCs exhibit anywhere from 10%–60% of the infectibility of primary human hepatocytes and indicates that iHLCs have acquired sufficient hepatocyte-like characteristics that confer infectibility with liver-stage malaria.

The observation that iHLCs are infectible with malaria before their in vitro differentiation is complete could reflect the acquisition of some liver-stage malaria host entry factors during the iPSC differentiation process, or heterogeneity in iPSC differentiation that results in faster hepatic maturation of a subpopulation of cells. This observation could also suggest the possibility of some promiscuity in the host entry factors that are required for *Plasmodium* sporozoite entry. Further studies are required to determine whether the EEFs observed in incompletely differentiated iPSCs reflect fully replication-competent EEFs, or whether such EEFs are prone to developmental arrest due to the absence (or presence) of some host factor that promotes (or inhibits) parasite development. It is intriguing that hepatoblasts appear to support similar *P. falciparum* infection rates and similar degrees of parasite growth as iHLCs, with some experiments even exhibiting a trend of increased numbers of *P.f.* EEFs or *P.y.* EEFs in hepatoblasts compared to iHLCs (Figures 3B, left, and S2E). This slight difference in infectibility could suggest the acquisition of sufficient host entry factors that support *Plasmodium* infection and development by d15 postinitiation of differentiation from iPSCs, but that further maturation beyond the hepatoblast stage results in the acquisition of other host factors that henceforth limit EEF development and survival. Because the cells in different stages of in vitro differentiation arise from the same donor, these observations also offer a clean comparative system in which to systematically probe and identify host factors that are essential for liver-stage malaria parasite infections, using proteomics or gene expression technologies, in a donor-independent manner.

A common shortcoming of iHLCs and other iPSC-derived cells lies in the fact that they often resemble a developmentally immature state compared to the fully differentiated adult counterpart (Engle and Puppala, 2013). In the field of iHLCs, current in vitro differentiation protocols result in the production of a hepatic cell type that is biologically closer to fetal hepatocytes than adult hepatocytes, due to the incomplete abrogation of the expression of fetal markers such as alpha-fetal protein (AFP) (Si-Tayeb et al., 2010; Song et al., 2009), and the incomplete acquisition of an adult-like levels of key secretory, detoxification, and metabolic activity (Shan et al., 2013). Our data show that further chemical maturation of iHLCs allows the acquisition of primaquine sensitivity, presumably via the acquisition of a drug metabolism enzyme (DME) expression profile that better resembles the adult human hepatocyte. This advance decreases the biological gap between iHLCs and primary adult hepatocytes and increases the potential utility of iHLCs in drug development efforts for malaria and other diseases. The expression of a developmentally mature repertoire of hepatic DMEs is particularly important considering that current drug development efforts toward malaria eradication revolves around the 8-aminoquinoline family, which is currently the only class of drugs that is efficacious against the cryptic hypnozoite stage of *P. vivax* liver-stage infections (Wells et al., 2009), and the fact that many existing antimalarial drugs such as proguanil, artemether, lumefantrine, and halofantrine are known to undergo metabolism in the liver by hepatic DMEs (Khoo et al., 2005) and whose in vitro efficacy will therefore likely be predictive of in vivo efficacy only if the in vitro hepatocyte model exhibits a primary human hepatocyte DME expression profile. Although the primaquine response in iHLCs pretreated with FPH1 was incomplete, other primary human hepatocyte models of *P. falciparum* treated with the same primaquine concentration (10 μM) also exhibit an incomplete response, with about 10%–20% of the number of *P.f.* EEFs remaining (Dembele et al., 2011; March et al., 2013). An unexpected finding was that FPH1 pretreatment also increased the baseline number of *P.f.* EEFs in iHLCs in the absence of primaquine treatment compared to DMSO pretreatment (Figure 5C). The chemical maturation of iHLCs by FPH1 is likely to involve a complex mechanism, which could theoretically result either in an increase in the adult hepatic phenotype of the existing population of iHLCs and hence their infectibility by *Plasmodium* sporozoites, or an expansion in the population of iHLCs or of other hepatic progenitors. Chemically matured iHLCs with increased baseline infectibility with *Plasmodium* could therefore provide an opportunity to elucidate hepatic host factors that promote liver-stage malaria infection in hepatocytes.

In conclusion, the establishment of *Plasmodium* liver-stage infections in induced pluripotent stem cell-derived hepatocyte-like cells lays the foundation for their use in antimalarial drug discovery as well as paves the way to study the genetic basis of host-*Plasmodium* interactions.

EXPERIMENTAL PROCEDURES

iPSC Culture and Hepatocyte-like Cell Generation

Undifferentiated iPSC were maintained and differentiated into iHLCs as described (Si-Tayeb et al., 2010). In brief, iPSCs were cultured in monolayer on Matrigel (Becton Dickinson), and directed differentiation was achieved by sequential exposure to activin A, bone morphogenic protein 4, basic FGF, HGF, and oncostatin M (OSM). For *P. berghei* and *P. yoelii* experiments, iHLCs differentiated from the iPSC lines, RC2 (reprogrammed from fibroblasts by the laboratory of Darrell Kotton at Boston University) (Somers et al., 2010), iPS.C2a (reprogrammed from foreskin fibroblasts by the laboratory of Stephen Duncan at Medical College of Wisconsin) (Si-Tayeb et al., 2010), or LN4 (a subclone of iPS.C2a with higher uniformity in growth and differentiation) were used. For *P. falciparum* experiments, iHLCs differentiated from the iPSC line, LN4, or cryopreserved iHLCs from Cellular Dynamics International (white female donor, iPSCs reprogrammed from fibroblasts, iCell Hepatocytes 2.0, CDI) were used. For *P. vivax* experiments, cryopreserved iHLCs (white female donor, iPSCs reprogrammed from fibroblasts, or white male donor, iPSCs reprogrammed from peripheral blood mononuclear cells, iCell Hepatocytes 2.0, CDI) were used. Cryopreserved iHLCs from CDI were thawed, plated on collagen I, and maintained according to the manufacturer's instructions until used.

Sporozoites

P. berghei ANKA and *P. yoelii* sporozoites were obtained by dissection of the salivary glands of infected *Anopheles stephensi* mosquitoes obtained from the insectaries at New York University or Harvard School of Public Health. *P. falciparum* sporozoites were obtained by dissection of the salivary glands of infected *Anopheles gambiae* mosquitoes obtained from the insectary at Johns Hopkins School of Public Health. *P. vivax* sporozoites were kindly provided by the insectary at Mahidol Vivax Research Center (Bangkok, Thailand) and were prepared by dissection of the salivary glands of infected *Anopheles dirus* mosquitoes.

Infection of iHLCs

P. berghei, *P. yoelii*, *P. falciparum*, or *P. vivax* sporozoites from dissected mosquito glands were centrifuged at 600 × *g* for 5 min on to iHLCs at a multiplicity of infection of 0.1–1 in the presence of 2% fetal bovine serum. After incubation at 37°C and 5% CO_2 for 2–3 hr, the wells were washed twice before serum-free culture medium was added. Media was replaced daily. Samples were fixed 24, 48, or 65 hr postinfection with *P. berghei* and *P. yoelii*, 3, 4, or 6 days postinfection with *P. falciparum*, and 3 or 8 days postinfection with *P. vivax*. For *P. vivax* experiments, iHLCs from CDI were exposed to *P. vivax* sporozoites at 4 days postplating.

Immunofluorescence Assay

iHLCs were fixed with −20°C methanol for 10 min at 4°C, washed thrice with PBS, blocked with 2% BSA in PBS overnight at 4°C, and then incubated overnight at 4°C with a primary antibody: mouse anti-human CD81 (clone JS-81, BD Pharmingen; 1:200), rabbit anti-SRB1 (Novus Biologicals; 1:100), mouse anti-PbHSP70 (clone 2E6; 1:200 for *P. berghei* and *P. yoelii*), rabbit anti-PbMSP1 (1:500 for *P. berghei*), mouse anti-PfHSP70 (clone 4C9, Sanaria; 1:200 for *P. falciparum*), or mouse anti-PfMSP1 (1:200 for *P. falciparum*). Samples were washed thrice with PBS before incubation for 1–3 hr at room temperature with secondary antibody: goat anti-mouse Alexa Fluor 594 or Alexa Fluor 488 or donkey anti-rabbit-Alexa Fluor 488 (Invitrogen; 1:400). Nuclei were then counterstained with Hoechst 33258 (Invitrogen; 1:1000), samples were washed thrice with PBS, and 1 ml of Aquamount (Thermo-Scientific) was added per well. Images were captured on a Nikon Eclipse Ti fluorescence microscope or an Olympus FV1000 multiphoton laser scanning confocal microscope.

Biochemical Assays

Cell culture supernatants were collected and stored at –20°C. Human albumin, α1-anti-trypsin (A1AT), and α-fetoprotein (AFP) secretion were measured by enzyme-linked immunosorbent assays with horseradish peroxidase detection (Bethyl Labs) and 3,3′,5,5′-tetramethylbenzidine (TMB, Pierce) development.

Statistics

Experiments were repeated with three or more independent batches of differentiated iHLCs with triplicate or quadruplicate biological samples for each condition. Data from representative batches of iHLCs are presented. Two-tailed t tests were performed for all comparisons between two conditions (e.g., with or without primaquine). One-way ANOVAs were performed for comparisons involving three or more conditions (e.g., number of EEFs in cells infected at various time points after differentiation) with Tukey's post hoc test for multiple comparisons. All error bars represent SEM.

SUPPLEMENTAL INFORMATION

Supplemental Information includes three figures and can be found with this article online at http://dx.doi.org/10.1016/j.stemcr.2015.01.002.

AUTHOR CONTRIBUTIONS

S.N., R.E.S., S.M., and S.N.B. designed experiments. S.N., S.M., A.G., and N.G. performed malaria experiments. R.E.S. and M.P. generated and characterized iHLCs. S.N. and S.N.B. analyzed data. S.N. and S.N.B. wrote the manuscript.

ACKNOWLEDGMENTS

We thank Ana Rodriguez and Sandra Gonzalez (New York University) for providing mosquitoes infected with *P. yoelii* and *P. berghei*, Dyann Wirth and Emily Lund (Harvard School of Public Health) for providing mosquitoes infected with *P. berghei*, Photini Sinnis and Abhai Tripathi (Johns Hopkins Bloomberg School of Public Health) for providing mosquitoes infected with *P. falciparum*, Jetsumon Sattabongkot Prachumsri and Rapatbhorn Patrapuvich (Mahidol University) for providing fresh *P. vivax* sporozoites, Cellular Dynamics International (CDI) for providing iCell Hepatocytes 2.0 for *P. vivax* experiments, Jeffrey B. Wyckoff (Koch Institute, MIT) for technical help in confocal microscopy, Stephen Duncan (Medical College of Wisconsin) for iPS cell lines and counsel on iHep generation, and Heather Fleming for critical reading and

help with manuscript preparation. This work was supported by the Bill and Melinda Gates Foundation (award number 51066). S.N. is supported by an A*STAR (Agency for Science, Technology and Research, Singapore) National Science Scholarship, US National Institutes of Health (NIH) grant UH3-EB017103, and in part by the Koch Institute Support (core) Grant P30-CA14051 from the National Cancer Institute. S.N.B. is a Howard Hughes Medical Institute Investigator.

Received: August 11, 2014
Revised: January 4, 2015
Accepted: January 5, 2015
Published: February 5, 2015

REFERENCES

Bennett, J.W., Pybus, B.S., Yadava, A., Tosh, D., Sousa, J.C., McCarthy, W.F., Deye, G., Melendez, V., and Ockenhouse, C.F. (2013). Primaquine failure and cytochrome P-450 2D6 in Plasmodium vivax malaria. N. Engl. J. Med. *369*, 1381–1382.

Biagini, G.A., Fisher, N., Shone, A.E., Mubaraki, M.A., Srivastava, A., Hill, A., Antoine, T., Warman, A.J., Davies, J., Pidathala, C., et al. (2012). Generation of quinolone antimalarials targeting the Plasmodium falciparum mitochondrial respiratory chain for the treatment and prophylaxis of malaria. Proc. Natl. Acad. Sci. USA *109*, 8298–8303.

Cui, L., Escalante, A.A., Imwong, M., and Snounou, G. (2003). The genetic diversity of Plasmodium vivax populations. Trends Parasitol. *19*, 220–226.

da Cruz, F.P., Martin, C., Buchholz, K., Lafuente-Monasterio, M.J., Rodrigues, T., Sönnichsen, B., Moreira, R., Gamo, F.-J., Marti, M., Mota, M.M., et al. (2012). Drug screen targeted at Plasmodium liver stages identifies a potent multistage antimalarial drug. J. Infect. Dis. *205*, 1278–1286.

Dembele, L., Gego, A., Zeeman, A.-M., Franetich, J.-F., Silvie, O., Rametti, A., Le Grand, R., Dereuddre-Bosquet, N., Sauerwein, R., van Gemert, G.-J., et al. (2011). Towards an in vitro model of Plasmodium hypnozoites suitable for drug discovery. PLoS ONE *6*, e18162.

Derbyshire, E.R., Prudêncio, M., Mota, M.M., and Clardy, J. (2012). Liver-stage malaria parasites vulnerable to diverse chemical scaffolds. Proc. Natl. Acad. Sci. USA *109*, 8511–8516.

Dondorp, A.M., Nosten, F., Yi, P., Das, D., Phyo, A.P., Tarning, J., Lwin, K.M., Ariey, F., Hanpithakpong, W., Lee, S.J., et al. (2009). Artemisinin resistance in Plasmodium falciparum malaria. N. Engl. J. Med. *361*, 455–467.

Engle, S.J., and Puppala, D. (2013). Integrating human pluripotent stem cells into drug development. Cell Stem Cell *12*, 669–677.

Gunawardena, S., Karunaweera, N.D., Ferreira, M.U., Phone-Kyaw, M., Pollack, R.J., Alifrangis, M., Rajakaruna, R.S., Konradsen, F., Amerasinghe, P.H., Schousboe, M.L., et al. (2010). Geographic structure of Plasmodium vivax: microsatellite analysis of parasite populations from Sri Lanka, Myanmar, and Ethiopia. Am. J. Trop. Med. Hyg. *82*, 235–242.

Jin, X., Pybus, B.S., Marcsisin, R., Logan, T., Luong, T.L., Sousa, J., Matlock, N., Collazo, V., Asher, C., Carroll, D., et al. (2014). An LC-MS based study of the metabolic profile of primaquine, an 8-aminoquinoline antiparasitic drug, with an in vitro primary human hepatocyte culture model. Eur. J. Drug Metab. Pharmacokinet. *39*, 139–146.

Khoo, S., Back, D., and Winstanley, P. (2005). The potential for interactions between antimalarial and antiretroviral drugs. AIDS *19*, 995–1005.

Li, J., Collins, W.E., Wirtz, R.A., Rathore, D., Lal, A., and McCutchan, T.F. (2001). Geographic subdivision of the range of the malaria parasite Plasmodium vivax. Emerg. Infect. Dis. *7*, 35–42.

March, S., Ng, S., Velmurugan, S., Galstian, A., Shan, J., Logan, D.J., Carpenter, A.E., Thomas, D., Sim, B.K.L., Mota, M.M., et al. (2013). A microscale human liver platform that supports the hepatic stages of Plasmodium falciparum and vivax. Cell Host Microbe *14*, 104–115.

Mazier, D., Rénia, L., and Snounou, G. (2009). A pre-emptive strike against malaria's stealthy hepatic forms. Nat. Rev. Drug Discov. *8*, 854–864.

McDonnell, M.E., and Braverman, L.E. (2006). Drug-related hepatotoxicity. N. Engl. J. Med. *354*, 2191–2193, author reply 2191–2193.

Meister, S., Plouffe, D.M., Kuhen, K.L., Bonamy, G.M., Wu, T., Barnes, S.W., Bopp, S.E., Borboa, R., Bright, A.T., Che, J., et al. (2011). Imaging of Plasmodium liver stages to drive next-generation antimalarial drug discovery. Science (80-.). *334*, 1372–1377.

Miller, J.L., Murray, S., Vaughan, A.M., Harupa, A., Sack, B., Baldwin, M., Crispe, I.N., and Kappe, S.H.I. (2013). Quantitative bioluminescent imaging of pre-erythrocytic malaria parasite infection using luciferase-expressing Plasmodium yoelii. PLoS ONE *8*, e60820.

Mwakingwe, A., Ting, L.-M., Hochman, S., Chen, J., Sinnis, P., and Kim, K. (2009). Noninvasive real-time monitoring of liver-stage development of bioluminescent Plasmodium parasites. J. Infect. Dis. *200*, 1470–1478.

Ogawa, S., Surapisitchat, J., Virtanen, C., Ogawa, M., Niapour, M., Sugamori, K.S., Wang, S., Tamblyn, L., Guillemette, C., Hoffmann, E., et al. (2013). Three-dimensional culture and cAMP signaling promote the maturation of human pluripotent stem cell-derived hepatocytes. Development *140*, 3285–3296.

Prudêncio, M., Rodriguez, A., and Mota, M.M. (2006). The silent path to thousands of merozoites: the Plasmodium liver stage. Nat. Rev. Microbiol. *4*, 849–856.

Pybus, B.S., Sousa, J.C., Jin, X., Ferguson, J.A., Christian, R.E., Barnhart, R., Vuong, C., Sciotti, R.J., Reichard, G.A., Kozar, M.P., et al. (2012). CYP450 phenotyping and accurate mass identification of metabolites of the 8-aminoquinoline, anti-malarial drug primaquine. Malar. J. *11*, 259.

Pybus, B.S., Marcsisin, S.R., Jin, X., Deye, G., Sousa, J.C., Li, Q., Caridha, D., Zeng, Q., Reichard, G.A., Ockenhouse, C., et al. (2013). The metabolism of primaquine to its active metabolite is dependent on CYP 2D6. Malar. J. *12*, 212.

Schwartz, R., Trehan, K., Andrus, L., Sheahan, T.P., Ploss, A., Duncan, S.A., Rice, C.M., and Bhatia, S.N. (2012). Modeling hepatitis C

virus infection using human induced pluripotent stem cells. Proc. Natl. Acad. Sci. USA *109*, 2544–2548.

Schwartz, R.E., Fleming, H.E., Khetani, S.R., and Bhatia, S.N. (2014). Pluripotent stem cell-derived hepatocyte-like cells. Biotechnol. Adv. *32*, 504–513.

Shan, J., Schwartz, R.E., Ross, N.T., Logan, D.J., Thomas, D., Duncan, S.A., North, T.E., Goessling, W., Carpenter, A.E., and Bhatia, S.N. (2013). Identification of small molecules for human hepatocyte expansion and iPS differentiation. Nat. Chem. Biol. *9*, 514–520.

Shlomai, A., Schwartz, R.E., Ramanan, V., Bhatta, A., de Jong, Y.P., Bhatia, S.N., and Rice, C.M. (2014). Modeling host interactions with hepatitis B virus using primary and iPSC-derived hepatocellular systems. Proc. Natl. Acad. Sci. USA *111*, 12193–12198.

Si-Tayeb, K., Noto, F.K., Nagaoka, M., Li, J., Battle, M.A., Duris, C., North, P.E., Dalton, S., and Duncan, S.A. (2010). Highly efficient generation of human hepatocyte-like cells from induced pluripotent stem cells. Hepatology *51*, 297–305.

Somers, A., Jean, J.-C., Sommer, C.A., Omari, A., Ford, C.C., Mills, J.A., Ying, L., Sommer, A.G., Jean, J.M., Smith, B.W., et al. (2010). Generation of transgene-free lung disease-specific human induced pluripotent stem cells using a single excisable lentiviral stem cell cassette. Stem Cells *28*, 1728–1740.

Song, Z., Cai, J., Liu, Y., Zhao, D., Yong, J., Duo, S., Song, X., Guo, Y., Zhao, Y., Qin, H., et al. (2009). Efficient generation of hepatocyte-like cells from human induced pluripotent stem cells. Cell Res. *19*, 1233–1242.

Takahashi, K., Tanabe, K., Ohnuki, M., Narita, M., Ichisaka, T., Tomoda, K., and Yamanaka, S. (2007). Induction of pluripotent stem cells from adult human fibroblasts by defined factors. Cell *131*, 861–872.

Takayama, K., Inamura, M., Kawabata, K., Katayama, K., Higuchi, M., Tashiro, K., Nonaka, A., Sakurai, F., Hayakawa, T., Furue, M.K., and Mizuguchi, H. (2012). Efficient generation of functional hepatocytes from human embryonic stem cells and induced pluripotent stem cells by HNF4α transduction. Mol. Ther. *20*, 127–137.

Takebe, T., Sekine, K., Enomura, M., Koike, H., Kimura, M., Ogaeri, T., Zhang, R.-R., Ueno, Y., Zheng, Y.-W., Koike, N., et al. (2013). Vascularized and functional human liver from an iPSC-derived organ bud transplant. Nature *499*, 481–484.

Thomson, J. a. (1998). Embryonic Stem Cell Lines Derived from Human Blastocysts. Science (80-.). *282*, 1145–1147.

Wells, T.N.C., Alonso, P.L., and Gutteridge, W.E. (2009). New medicines to improve control and contribute to the eradication of malaria. Nat. Rev. Drug Discov. *8*, 879–891.

World Health Organization (2013). World malaria report 2013.

Find your way with Cell Press Reviews

Whether you're looking for answers to fundamental questions, brushing up on a new subject or looking for a synthesis on a hot topic, turn to Cell Press Reviews. We publish reviews in a vast array of disciplines spanning the life sciences.

Propel your research forward, faster with Cell Press Reviews. Our insightful, authoritative reviews—published in our primary research and Trends journals—go beyond synthesis and offer a point of view.

www.cell.com/reviews

CellPress
Your work is our life

Stem Cell Reports
Article

OPEN ACCESS

In Vivo Repopulating Activity Emerges at the Onset of Hematopoietic Specification during Embryonic Stem Cell Differentiation

Stella Pearson,[1] Sara Cuvertino,[1] Maud Fleury,[1] Georges Lacaud,[2,*] and Valerie Kouskoff[1,*]
[1]Stem Cell Hematopoiesis Group
[2]Stem Cell Biology Group
Cancer Research UK Manchester Institute, University of Manchester, Wilmslow Road, Manchester M20 4BX, UK
*Correspondence: georges.lacaud@cruk.manchester.ac.uk (G.L.), valerie.kouskoff@cruk.manchester.ac.uk (V.K.)
http://dx.doi.org/10.1016/j.stemcr.2015.01.003

SUMMARY

The generation of in vivo repopulating hematopoietic cells from in vitro differentiating embryonic stem cells has remained a long-standing challenge. To date, hematopoietic engraftment has mostly been achieved through the enforced expression of ectopic transcription factors. Here, we describe serum-free culture conditions that allow the generation of in vivo repopulating hematopoietic cells in the absence of ectopically expressed factors. We show that repopulating activity arises immediately upon the commitment of mesodermal precursors to the blood program, within the first wave of hematopoietic specification. We establish that the formation of these progenitors is extremely transient and exquisitely sensitive to the cytokine milieu. Our findings define the precise differentiating stage at which hematopoietic repopulating activity first appears in vitro, and suggest that during embryonic stem cell differentiation, all hematopoietic programs are unraveled simultaneously from the mesoderm in the absence of cues that restrict the coordinated emergence of each lineage as is normally observed during embryogenesis.

INTRODUCTION

Recent advances in the generation, propagation, and differentiation of pluripotent stem cells (PSCs) offer great promise in the field of regenerative medicine. Both embryonic stem cells (ESCs) and induced PSCs (iPSCs) provide limitless sources of self-renewing cells endowed with the potential to generate tissue-specific cell populations that can be used in transplantation therapy (Grabel, 2012; Keller, 2005). However, one major hurdle in realizing this potential is the lack of specific and efficient protocols for differentiating these PSCs to specific populations that can be used for therapeutic applications. Although stem-cell-based regenerative medicine is still a distant goal, outstanding progress has been made in generating and engrafting ESC-derived lineages such as dopamine neurones (Kriks et al., 2011) and cardiomyocytes (Shiba et al., 2012; Yang et al., 2008). In contrast, since the first report of blood cell generation from ESCs 30 years ago (Doetschman et al., 1985), progress in deriving hematopoietic cells that are able to engraft in vivo has been rather modest. To date, the most successful in vitro derivation of hematopoietic cells capable of repopulating mouse models has relied on the ectopic expression of transcription factors such as HOXB4 (Kyba et al., 2002), CDX4 (Wang et al., 2005b), LHX2 (Kitajima et al., 2011), and RUNX1a (Ran et al., 2013). However, although HOXB4 overexpression has been shown to confer reproducible engraftment capability in differentiating mouse ESCs (Bonde et al., 2008; Kyba et al., 2002; Lesinski et al., 2012; Matsumoto et al., 2009), this approach has not been successfully translated to human ESCs (Wang et al., 2005a). An alternative approach to the use of HOXB4 in differentiated human ESCs was recently reported by Doulatov et al. (2013), who showed that the ectopic expression of transcription factors (HOXA9, ERG, RORA, SOX4, and MYB) in differentiating ESCs promotes short-term erythroid and myeloid engraftment. Few reports have documented the in vitro generation of hematopoietic repopulating potential from unmanipulated ESCs (Burt et al., 2004; Hole et al., 1996; Müller and Dzierzak, 1993; Potocnik et al., 1997). However, these approaches have not been reproduced or pursued, suggesting that they involve serum-dependent conditions that cannot be easily replicated. The use of high serum concentrations (Wang et al., 2005a) and/or stroma cell lines (Ledran et al., 2008) to support the formation of repopulating hematopoietic cells derived from human ESCs has also shown promising results, but to date, no follow-up studies have further validated or extended these differentiation protocols. It is likely that the reported successes in deriving repopulating hematopoietic cells relied on specific factors present in rare batches of serum—parameters that are impossible to control for and thus are extremely difficult to reproduce.

It is thought that a better understanding of the molecular and cellular mechanisms that regulate the emergence and maintenance of long-term repopulating hematopoietic stem cells (HSCs) during embryonic development would aid in the development of optimal protocols to generate such cells in vitro from PSCs. HSCs have been shown to emerge first from the aorta-gonad-mesonephros (AGM) region around embryonic day 10.5 (E10.5) in murine

embryos (Medvinsky and Dzierzak, 1996). This occurs several days after the actual onset of hematopoietic activity, which is observed first in the yolk sac from E7.5 and next in the embryo proper from E9.0 (Palis et al., 1999). These early waves of hematopoiesis successively give rise to primitive erythroid, myeloid, definitive erythroid, and lymphoid progenitors (Costa et al., 2012; Lin et al., 2014). Several studies, including lineage tracing (Zovein et al., 2008) and in vivo imaging (Boisset et al., 2010) studies, have revealed the endothelial origin of HSCs emerging from a hemogenic endothelium (HE) population within the AGM region. Similarly, earlier waves of hematopoietic progenitors were also shown to derive from the HE (Ema et al., 2006; Lancrin et al., 2010; Nishikawa et al., 1998).

The in vitro differentiation of ESCs has been widely used as a model system to dissect and understand the early events of hematopoietic specification in terms of both molecular mechanisms and cellular steps. The careful dissection of this in vitro program has demonstrated that, similarly to in vivo development, blood cells are generated from mesodermal hemangioblast precursors through an HE intermediate (Choi et al., 1998, 2012; Eilken et al., 2009; Fehling et al., 2003; Huber et al., 2004; Kennedy et al., 2007; Lancrin et al., 2009; Wang et al., 2004) and that the same network of transcription factors orchestrates both in vivo and in vitro processes (Moignard et al., 2013). Detailed studies of the generation of primitive erythroid, myeloid, and lymphoid progenitors have suggested a temporal emergence of these blood lineages in vitro, reflecting their sequential emergence in vivo during embryonic development (Irion et al., 2010). This led to the concept that repopulating activity might emerge at late stages of the hematopoietic program during ESC differentiation (Kardel and Eaves, 2012; Lis et al., 2013; Sturgeon et al., 2013) and that the emergence of lymphoid potential marks the establishment of the definitive program (Kennedy et al., 2012; Slukvin, 2013). To date, however, attempts to derive in vivo repopulating hematopoietic cells from late stages of ESC differentiation have been largely unsuccessful. To revisit this long-standing challenge, we took an alternative approach and explored the very first step of hematopoietic specification from the mesoderm. We hypothesized that multilineage progenitors with in vivo repopulating ability might be specified very early upon commitment of mesoderm to the blood program, and might be difficult to maintain as such in the presence of serum or hematopoietic cytokines. We first evaluated the growth factor requirement for optimal specification of hemangioblast to HE. Next, defining the full hematopoietic potential of this emerging population, we observed the concomitant emergence of erythroid, myeloid, and lymphoid progenitors. Interestingly, this early population was also endowed with the capability to engraft immunocompromised mice and to confer multilineage, long-term engraftment. Further studies allowed us to define the temporal emergence of this repopulating ability and to determine the growth factor requirement and immunophenotypic characteristic of this population. Collectively, our findings demonstrate that in vitro repopulating cells emerge very rapidly from mesoderm precursors, are extremely transient, and are exquisitely sensitive to the growth factors present in the differentiating conditions.

RESULTS

BMP4, Activin A, and VEGF Are Critically Required for the Generation of HE and CD41$^+$ Progenitor Cells

We previously showed that a combination of BMP4, Activin A, FGF, and VEGF was sufficient to efficiently drive the formation of blood precursors from differentiating ESCs in serum-free culture conditions (Pearson et al., 2008). However, optimal specification to each differentiation stage is likely to require precise temporal exposure to cytokine stimuli. Therefore, we set out to define which cytokines were specifically required for the transition from hemangioblast to HE, and then from HE to hematopoietic progenitors, with a particular emphasis on HE, from which repopulating cells are known to emerge in vivo (Bertrand et al., 2010; Boisset et al., 2010; Kissa and Herbomel, 2010). As depicted in Figure 1A, ESCs were differentiated via embryoid body (EB) for 3 days in serum-free culture with the successive addition of BMP4 at day 0, and then Activin A and FGF at day 2.5. This sequential exposure to growth factors was previously shown to promote hemangioblast specification efficiently in developing mesoderm (Pearson et al., 2008). At day 3 of the EB culture, FLK1$^+$ cells enriched for hemangioblast were isolated and then further cultured with no added factors, a combination of four factors (BMP4 [B], Activin A [A], FGF [F], and VEGF [V]), or various combinations of these factors. The successful differentiation of FLK1$^+$ cells into HE was measured at day 2 of the culture by the coexpression of TIE2 and cKIT, as previously described (Lancrin et al., 2009). The efficient generation of hematopoietic progenitors was assessed at day 3 by CD41 expression, which is known to mark emerging progenitors (Ferkowicz et al., 2003; Mikkola et al., 2003). In the absence of added factors, few cells coexpressed TIE2 and cKIT (Figure 1B), and the generation of CD41$^+$ cells was limited (Figure 1C). In contrast, the addition of all factors (BAFV) led to the detection of a substantial TIE2$^+$cKIT$^+$ population and the enhanced generation of CD41$^+$ cells. Dissecting the role of each factor individually or in combination revealed that individual factors on their own and most combinations were not able to generate or maintain an HE population (Figure 1B) and/or to produce a

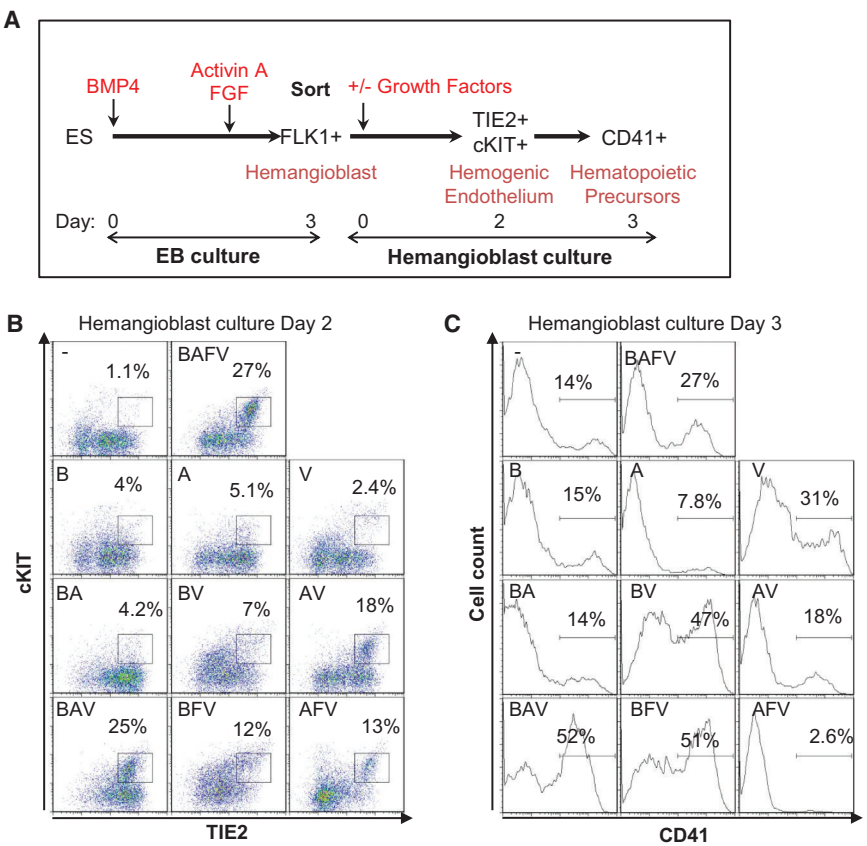

Figure 1. Optimal Cytokine Combinations for HE and Blood Cell Generation from FLK1$^+$ Mesoderm Cells

(A) Schematic representation of the experimental strategy. ESCs were differentiated via embryoid body (EB) formation in serum-free culture supplemented with BMP4 at day 0 and with Activin A and FGF2 at day 2.5. FLK1$^+$ cells sorted from day 3 EBs were seeded on gelatinized plates in serum-free media supplemented or not with cytokines (—, no cytokines; B, BMP4; A, ActivinA; V, VEGF; F, FGF2).

(B) Representative flow cytometry of cells analyzed at day 2 of the culture for the coexpression of TIE2 and cKIT marking HE.

(C) Representative flow cytometry of cells analyzed at day 3 of the culture for CD41 expression marking the emergence of blood cells. Data are representative of four independent experiments.

See also Figure S1.

substantial frequency of CD41$^+$ cells (Figure 1C). Both Activin A and VEGF appeared to be critically required for the generation and maintenance of HE cells, since only culture conditions containing both factors led to the formation of a clear TIE2$^+$cKIT$^+$ population (AV, AFV, and BAV). As observed in V, BV, and BFV culture conditions, the absence of Activin A in the culture led to CD41 cell production associated with a decrease in TIE2$^+$cKIT$^+$ frequency that was already observed at day 2 (Figures 1B and 1C). In contrast, the absence of BMP4 in the culture led to a dramatic decrease in CD41$^+$ cell production, as observed in A, AV, and AFV culture conditions, suggesting that while this factor is dispensable for the generation or maintenance of a TIE2$^+$cKIT$^+$ population, BMP4 is required for the emergence of CD41$^+$ cells. To address this issue, we supplemented AV culture with BMP4 at day 2 and assayed for CD41 expression at day 3 (Figures S1A and S1B). However, the delayed addition of BMP4 did not enhance the generation of CD41$^+$ cells, suggesting that although it does not impact the generation of a TIE2$^+$cKIT$^+$ immunophenotypic population from FLK1$^+$ cells, BMP4 exposure is nonetheless critical for shaping the hematopoietic potential of this population at the onset of FLK1 differentiation. The expression of a panel of endothelial markers, such as ICAM2, FLK1, and CD144 (VE-cadherin), further revealed that the presence of both BMP4 and Activin A was critical to maintain the endothelial identity of the cKIT$^+$ population at day 2 of the culture (Figure S1C). Only a fraction of cKIT$^+$ cells maintained the expression of these endothelial markers when cultured in the presence of AFV or BFV. Altogether, these data revealed that the combination of BMP4, Activin A, and VEGF is critical for the generation of both HE and CD41$^+$ cells. Interestingly, early exposure to BMP4 appears to confer hematopoietic potential to the TIE2$^+$cKIT$^+$ population.

Inhibitory Effect of FGF and Activin A on Further Hematopoietic Commitment

We next compared the emergence and frequency of HE when FLK1$^+$ cells were cultured with BAV and BAFV, as these two conditions were the most effective for generating HE (Figure 1B). In both cases, a low frequency of TIE2$^+$cKIT$^+$ cells was observed at day 1 of the culture; the frequency of this population peaked at day 2 and decreased thereafter (Figure 2A). No noticeable differences were observed in the temporal emergence and frequency of this population regardless of whether FGF was added to the culture or not (Figures 2A and 3D). In contrast, the formation of CD41$^+$ cells was negatively affected by the presence of FGF in the culture, with on average a 2-fold increase in the frequency

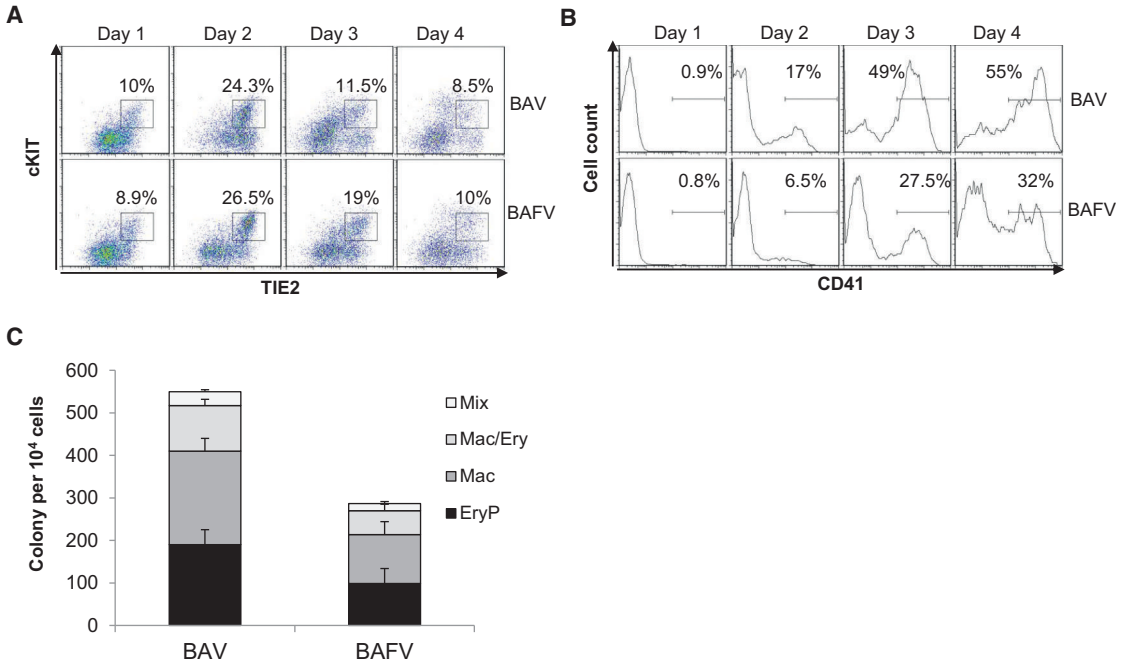

Figure 2. FGF2 Impairs the Generation of CD41$^+$ Cells from HE

FLK1$^+$ cells sorted from day 3 EBs were seeded on gelatinized plates in serum-free media supplemented with a BAV or BAFV cytokine combination (B, BMP4; A, Activin A; V, VEGF; F, FGF2).

(A and B) Cells were analyzed daily by flow cytometry for (A) coexpression of TIE2 and cKIT marking HE and (B) CD41 expression marking blood cells.

(C) At day 2 of the culture, cells were plated in clonogenic assay for hematopoietic precursors, and colonies were counted at day 5 for primitive erythroid (EryP) and day 8 for all other colonies (Mac, macrophages; Mac/Ery, macrophages and erythroid; Mix, multilineage myeloid and erythroid). Data shown are representative of at least three experiments. In (C), data are presented as the mean number of colonies from three dishes from one representative experiment; bars represent SEM.

of CD41$^+$ cells produced in the absence of FGF from day 2 onward (Figures 2B and 3E). Both cultures gave rise to primitive erythroid and definitive colonies upon replating in clonogenic assays; however, FLK1$^+$ cells cultured in the BAV condition resulted in the production of higher frequencies of hematopoietic precursors (Figure 2C), in agreement with the CD41 flow cytometry data. Altogether, these data suggest that although FGF does not affect the temporal emergence and frequency of HE, this growth factor negatively impacts the formation of hematopoietic progenitors.

We next assessed the influence of Activin A on the emergence of CD41$^+$ progenitor cells because this factor was previously shown to negatively affect the generation of definitive hematopoiesis (Kennedy et al., 2012). For this purpose, sorted FLK1$^+$ cells were cultured for 1 day in the presence of BMP4, Activin A, and VEGF (BAV), and then switched to media containing only BMP4 and VEGF (BV) as depicted in Figure 3A. Flow cytometric analysis revealed that removing Activin A after 1 day of culture significantly enhanced the frequency of TIE2$^+$cKIT$^+$ cells (Figures 3B and 3D), as well as the generation of CD41$^+$ cells (Figures 3C and 3E). Time-lapse imaging of these cultures over a 3-day period illustrated the formation of adherent colonies of endothelial cells followed by the emergence of individual floating blood cells (Figures 3F and 3G), as previously shown in serum-supplemented cultures (Lancrin et al., 2009). The BAV-BV culture condition led to the emergence of large and healthy clusters of round floating cells (Figures 3F and S2A). In contrast, maintenance of Activin A in the culture (BAV) appeared to reduce the viability and size of the clusters of round floating cells (Figures 3G and S2B). This was further highlighted by the overall growth of the cultures in which a change of media from BAV to BV led to a marked increase in cell confluency (Figure S2C). Altogether, these data reveal that restricting the temporal exposure to Activin A is critically important for optimal specification of HE and hematopoietic precursors.

Multilineage Hematopoietic Potential of cKIT$^+$ Cells

Having defined the optimal serum-free culture condition for the early steps of hematopoietic specification, we next

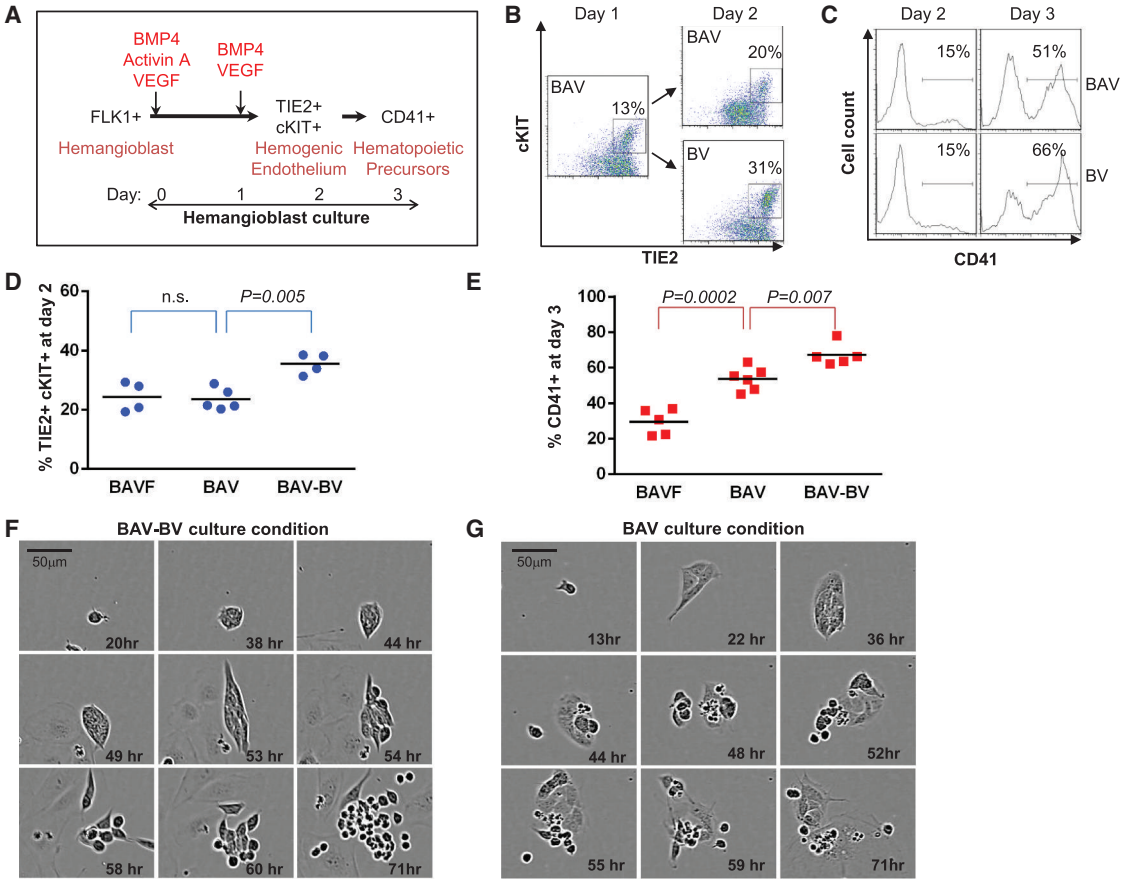

Figure 3. Activin A Impairs the Maintenance of HE

(A) Schematic representation of the experimental strategy. FLK1$^+$ cells sorted from day 3 EBs were seeded on gelatinized plates in serum-free media supplemented with BAV for the first day and then with BV from day 1 onward (B, BMP4; A, Activin A; V, VEGF).

(B) Flow cytometry analysis of TIE2 and cKIT coexpression at day 1 and 2 of FLK1$^+$ cell culture grown in a BAV or BAV-BV cytokine combination.

(C) Flow cytometry analysis of CD41 expression at days 2 and 3 of the same cultures.

(D and E) Graph of data obtained from BAFV, BAV, and BAV-BV cultures, showing the frequencies of TIE2$^+$cKIT$^+$ cells at day 2 (D) and CD41$^+$ cells at day 3 (E). Each point represents an independent experiment.

(F and G) Representative time-lapse imaging of FLK1$^+$ sorted cells cultured in serum-free media supplemented with a BAV-BV (F) or BAV (G) cytokine combination. Data shown are representative of at least three independent experiments (n.s., nonsignificant).

See also Figure S2.

evaluated the biological characteristics of cKIT-expressing cells generated in this condition. As shown by multiparameter flow cytometry analysis, cKIT$^+$ cells coexpressed all endothelial markers tested (Figure 4A), including ICAM2 and CD40, which were previously shown to mark HE (Pearson et al., 2010). At this stage of the culture, a small fraction of cKIT$^+$ cells also coexpressed low levels of CD41, but none expressed CD45 (Figure 4A; both of these markers are indicative of a further commitment to hematopoiesis). We next evaluated the biological potential of this cKIT$^+$ population sorted at day 2 of BAV-BV culture. When cKIT$^+$ cells were plated in clonogenic assays for hematopoietic progenitors, we observed the formation of both primitive erythroid colonies and definitive colonies (Figures 4B, S3A, and S3B). After 1 week, the culture of cKIT$^+$ cells on OP9 or OP9-DL1 stroma in lymphoid-promoting conditions led to the formation of clusters of free-floating cells in the culture media and cobblestone-like areas underneath the stromal layer (Figure 4C). Analysis of cells derived from the OP9-DL1 cocultures after 3–4 weeks revealed the generation of T lymphocytes as defined by the expression of T cell-specific genes (Figure S3C); CD4, CD8, and CD3 expression; an immature CD4$^+$CD8$^+$ population; and low frequencies of more mature CD4$^+$ and CD8$^+$ cells (Figure 4D). Similarly, analysis of cells derived from OP9 cocultures demonstrated the generation of B lymphocytes as marked by the

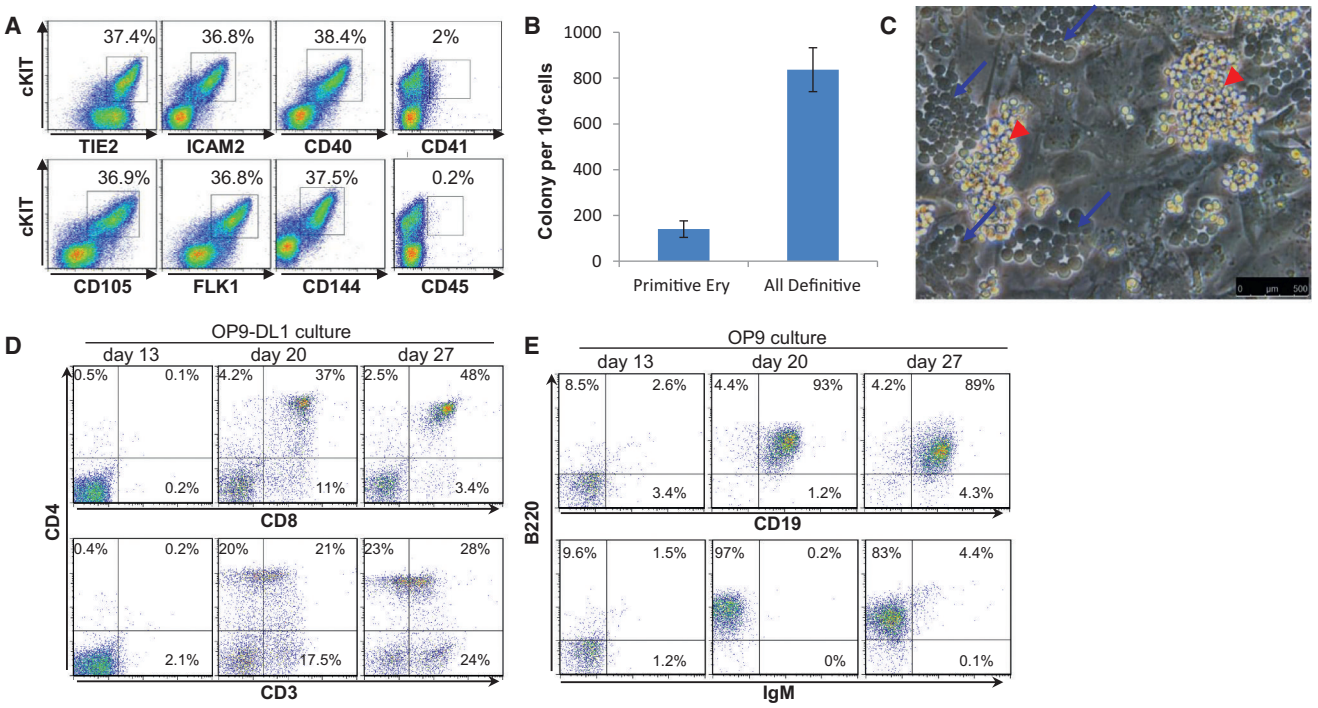

Figure 4. The cKIT$^+$ Cell Population Derived from FLK1$^+$ Hemangioblast Contains Erythroid, Myeloid, and Lymphoid Potential

(A and B) FLK1$^+$ cells sorted from day 3 EBs were seeded on gelatinized plates in serum-free media supplemented with BAV for the first day and then with BV from day 1 onward (B, BMP4; A, Activin A; V, VEGF). At day 2 of culture, cells were analyzed for the coexpression of cKIT with a panel of endothelium and hematopoietic cell-surface markers.

(B) Day 2 sorted cKIT cells were plated in clonogenic assay for hematopoietic precursors. Primitive Ery: primitive erythrocytes; all definitive colonies: macrophages, macrophages/erythrocytes, GM, and GEMM colonies. Data are presented as the mean number of colonies from three dishes; bars represent SEM.

(C) Bright-field picture taken at 1 week of culture. Blue arrows mark cobblestone areas; red arrowheads mark free-floating hematopoietic clusters.

(D) Cells derived from OP9-DL1 culture were stained at the indicated time for the coexpression of CD4, CD8, and CD3 marking T lymphocytes.

(E) Cells derived from OP9 culture were stained at the indicated time for the coexpression of B220, CD19, and IgM marking B lymphocytes. Data shown are representative of at least three experiments.

See also Figure S3.

expression of B cell-specific genes (Figure S3D) and the coexpression of B220 and CD19, with a small fraction of these cells expressing immunoglobulin M (IgM; Figure 4E). Altogether, these data reveal that FLK1$^+$ mesodermal progenitors that have grown for 2 days in the sequential presence of BMP4, Activin A, and VEGF (BAV) followed by BMP4 and VEGF (BV) give rise to a population of cKIT$^+$ cells endowed with the capacity to generate erythroid, myeloid, and lymphoid cells.

Long-Term and Multilineage Engraftment Potential of the cKIT$^+$ Population

Given the in vitro multilineage capacity of the cKIT$^+$ population isolated from FLK1$^+$ cells that had differentiated for 2 days, we next investigated whether this population contained cells that were able to engraft in vivo. For this purpose, cKIT$^+$ cells were isolated from BAV-BV culture at day 2 and injected into sublethally irradiated recipient mice as depicted in Figure 5A. Blood samples were taken every 4 weeks over a 16-week period and analyzed by flow cytometry for the expression of CD45.1 (marking recipient cells) and CD45.2 (marking in vitro-derived donor cells). In the initial experiments, the persistence of a small CD45.2$^+$ population was observed in four out of ten mice over the 16-week period (Figures 5B and 5C). The in vitro origin of the CD45.2$^+$ cells was further confirmed by detection of the *Brachyury-GFP* knockin allele, which was present in the starting ESC line but absent from the recipient mice (Figure 5D). Similar in vivo engraftment results were also obtained with cKIT$^+$ cells derived from the in vitro

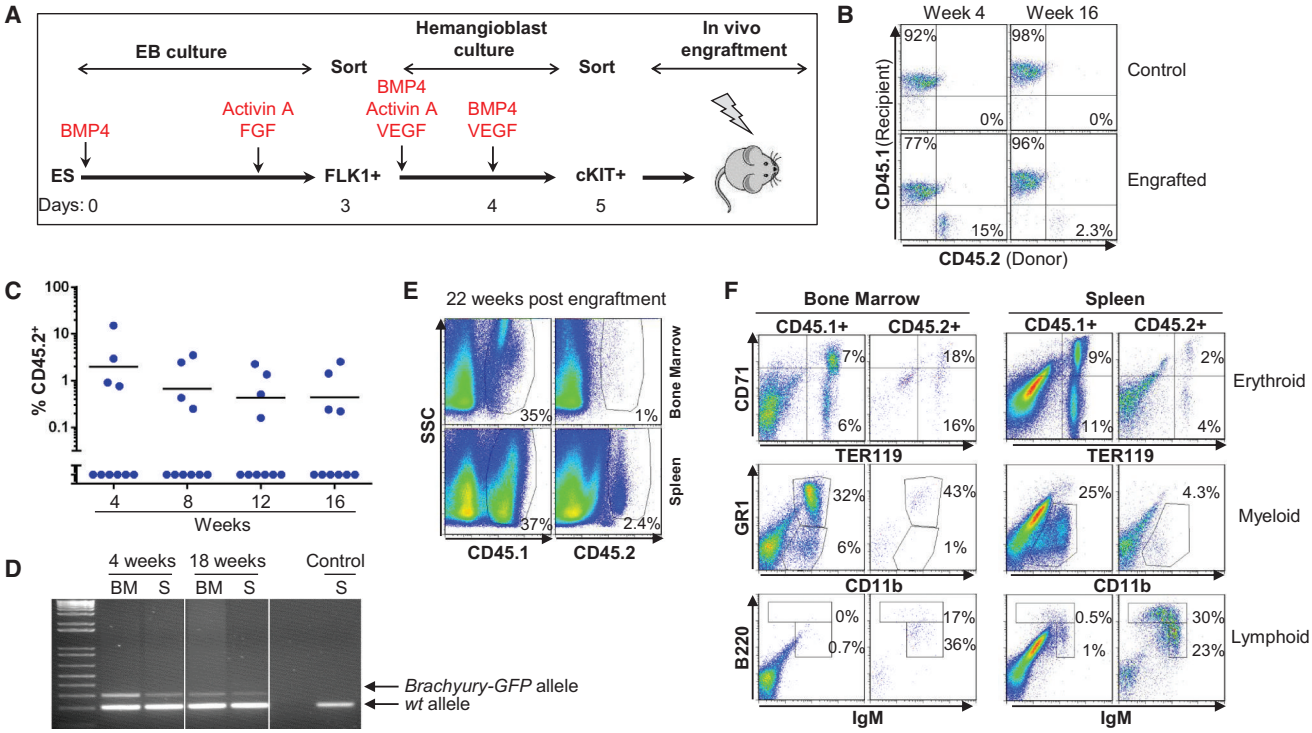

Figure 5. The cKIT$^+$ Population Contains In Vivo Repopulating Activity

(A) Schematic representation of the experimental strategy.

(B) Blood cells from control and engrafted mice were stained for CD45.1 expression (marking recipient cells) and CD45.2 expression (marking ESC-derived cells).

(C) Frequency of CD45.2$^+$ cells (blue circles) in the blood at the indicated week. Each point represents a mouse (n = 2, with 5 mice per experiment).

(D) PCR detection of the *Brachyury* endogenous and *Brachyury-GFP* knockin alleles carried by ESC-derived blood cells (BM, bone marrow; S, spleen).

(E) Bone marrow and spleen cells harvested 22 weeks after engraftment were stained for CD45.1 and CD45.2.

(F) Staining for lineage analysis is shown for CD45.1$^+$ recipient and CD45.2$^+$ ESC-derived cells from bone marrow and spleen at 22 weeks after engraftment. CD71 and TER119 mark erythroid cells, CD11b and GR1 mark myeloid cells, and IgM and B220 mark B lymphocytes. See also Figure S4.

differentiation of two other ESC lines (Figures S5D and S5G–S5J). Analysis of the lineage contribution in bone marrow and spleen at 22 weeks after engraftment revealed the presence of CD45.2$^+$ cells expressing cell-surface markers characteristic of erythroid (TER119 and CD71), myeloid (Gr1 and CD11b), and B lymphoid (IgM and B220) lineages (Figures 5E and 5F). The B lymphocytes generated upon engraftment coexpressed IgM, CD19, and B220 (Figure S4A), and were able to secrete immunoglobulins (Figure S4B). It has been shown that embryonic hematopoietic precursors preferentially give rise to B-1 B lymphoid cells involved in innate immunity (Montecino-Rodriguez and Dorshkind, 2012). In addition to IgM expression, these B lymphocytes are characterized by the expression of CD11b and CD5 for the B-1a subset and CD11b for the B-1b subset. Given the embryonic origin of the cKIT$^+$ donor cells, we further assessed the immunophenotype of the B lymphoid population generated upon engraftment. None of the IgM$^+$ cells expressed CD11b or CD5, suggesting that these cells are B-2 type B lymphocytes (Figure S4C). Altogether, these data demonstrate that cKIT$^+$ cells isolated from ESCs that have differentiated in serum-free culture with restricted temporal exposure to specific growth factors are able to confer long-term and multilineage engraftment in vivo.

Temporal Emergence of Hematopoietic Repopulating Activity

The repopulating activity observed upon engraftment of cKIT$^+$ cells isolated from day 2 culture was reproducible but remained low in terms of both the chimerism level and frequency of mouse repopulation (Table 1). Therefore,

Table 1. Summary of the In Vivo Engraftment Experiments

Population Tested	Cytokines in FLK1 Culture	n	Engrafted Mice	Chimerism Frequency at 4 Weeks (Percentage CD45.2$^+$)
FLK1$^+$	no further culture	2	0/8	0
cKIT$^+$ day 1	BAFV	6	14/26	4, 5.9, 6.5, 0.37, 4.5, 2.32, 0.77, 21, 3.36, 2.17, 10.04, 15.66, 5.04, 16.36
	BAV	2	3/8	0.4, 19.9, 15.65
	AV	1	1/4	0.43
	BNVF	1	0/4	0
	BNV	1	1/4	0.09
	BFV	1	0/4	0
cKIT$^+$ day 2	BAV(day 1)-BV(day 2)	7	9/28	2.96, 15.09, 0.76, 0.91, 1.44, 0.18, 0.58, 0.44, 0.26
	BAV(day 1)-A(day 2)	1	2/4	0.12, 2.9
	BAV(day 1)-SB(day 2)	1	2/4	0.19, 2.5
	BAV(day 1)-B(day 2)	1	1/4	1.5
	BAV(day 1)-none(day 2)	1	1/3	0.24
	BAFV	2	5/12	0.78, 1.04, 1.3, 2.9, 6.1
	BAV	1	1/8	1.42
	BNVF	1	0/4	0
	BNV	1	0/4	0
cKIT$^+$ day 3	BAV(day 1)-BV(day 2)	2	0/12	0

B, BMP4; A, Activin A; V, VEGF; F, FGF2; N, Nodal; SB, SB-431542. See also Figure S5.

we explored whether we could achieve a higher repopulation activity by changing the timing of cKIT$^+$ cell isolation during the course of FLK1 differentiation to hematopoiesis. The cKIT$^+$ population isolated from day 3 culture was unable to engraft in vivo, whereas day 1 cKIT$^+$ cells gave rise to reproducible engraftment capability (Figure 6A). The overall level of chimerism observed with cKIT$^+$ cells derived from day 1 culture was higher than that observed with cells derived from day 2 culture. Given this very rapid onset of repopulating activity upon culture of FLK1$^+$ mesodermal precursors, we also evaluated the potential of FLK1$^+$ cells to engraft directly without further culture. However, FLK1$^+$ cells isolated from EBs and directly injected in vivo did not give rise to any repopulation activity (Figure 6A). Altogether, these findings suggest that the repopulating ability of ESC-derived hematopoietic precursors emerges rapidly upon mesoderm specification and is very transient.

Growth Factor Requirement for the Emergence of Hematopoietic Repopulating Activity

We next evaluated how altering the cytokine combination during the differentiation of FLK1$^+$ mesoderm might impact the generation of in vivo repopulating cells. In a first set of experiments, we assessed the growth factor requirement for the generation of this repopulating activity. We tested combinations of cytokines in which FLK1$^+$ cells were cultured for the first day with BAV cytokines and then either maintained with BAV or changed to Activin A, BMP4, TGFβ inhibitor (SB-431542), or no cytokines for the second day of culture. In addition, cKIT$^+$ cells isolated after 2 days of culture with BAFV were also tested in engraftment experiments. In all conditions tested, no improvement was observed in either the chimerism level or frequency of engrafted mice when compared with the BAV-BV cytokine combination (Table 1). Altogether, these data suggest that a variation in cytokine exposure during the second day of FLK1 culture does not affect the repopulating activity of the cKIT$^+$ population isolated at day 2. Additionally, cKIT$^+$ cells isolated from day 1 culture gave higher engraftment levels, suggesting that the first day of FLK1 culture is critical for determining in vivo repopulating competency. We therefore focused on the cytokine requirement for the first day of culture. Data presented in Figure 1A show that the cytokine combinations BAV, BAFV, and AV were the best conditions for generating a TIE2$^+$cKIT$^+$ HE population at day 2. When analyzed at day 1 of culture,

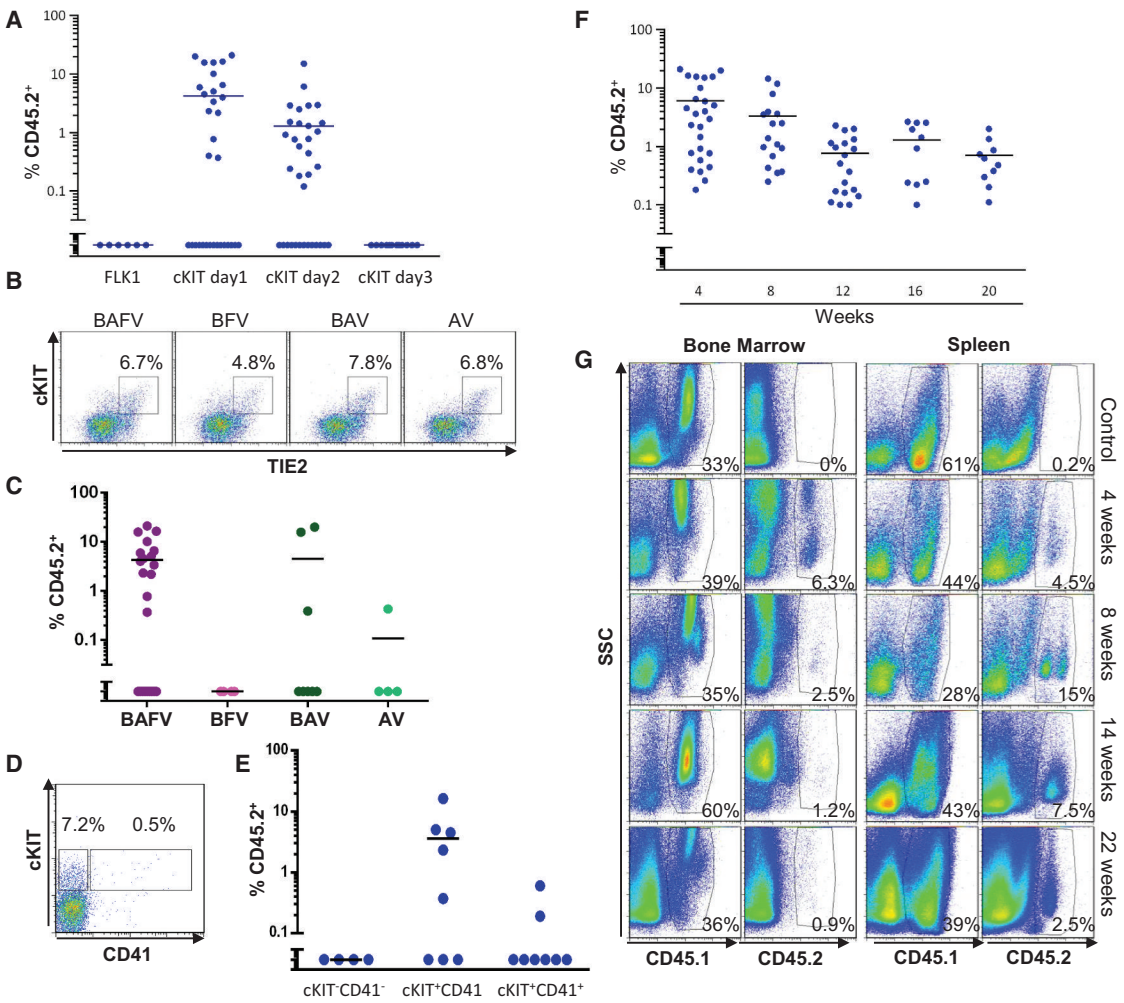

Figure 6. Successful Engraftment Is Highly Dependent on Cytokine Exposure

(A) Frequency of CD45.2$^+$ cells (blue circles) in the blood of recipient mice 4 weeks after engraftment with the indicated population. The data presented in this graph for cKIT$^+$ cells at days 1 and 2 were obtained under BAFV, BAV, and BAV-BV culture conditions. Each point represents one mouse; the number of experiments conducted for each population is shown in Table 1 (B, BMP4; A, ActivinA; V, VEGF; F, FGF2).

(B) Representative flow cytometric analysis of cKIT and TIE2 expression for cells obtained from day 1 FLK1 culture grown in the indicated cytokines.

(C) Frequency of CD45.2$^+$ cells in the blood of recipient mice 4 weeks after engraftment with cKIT$^+$ cells isolated from day 1 FLK1 culture grown in the indicated cytokine mix (BAFV, purple circles; BFV, pink circles; BAV, dark green circles; AV, light green circles). Each point represents one mouse; the numbers of mice and experiments are detailed in Table 1.

(D) Representative flow cytometric analysis of cKIT and CD41 expression for cells obtained from day 1 FLK1 culture grown in the presence of BAFV cytokines.

(E) Frequency of CD45.2$^+$ cells (blue circles) in the blood of recipient mice 4 weeks after engraftment with the indicated cells isolated from day 1 FLK1 culture grown in the presence of the BAFV cytokine mix. Each point represents one mouse (n = 2, with 4 mice per experiment, except for group CD41$^-$cKIT$^-$ with 2 mice per experiment).

(F) Frequency of CD45.2$^+$ cells (blue circles) in the blood of recipient mice at the indicated number of weeks after engraftment. Data in this graph represent a summary of all recipients that successfully engrafted. Each point represents one mouse, n = 18 with 4 mice per experiment as detailed in Table 1.

(G) Flow cytometric analysis of CD45.1 and CD45.2 expression relative to side scatter (SSC) for bone marrow and spleen cells at the indicated weeks after engraftment.

See also Figure S6.

the TIE2$^+$cKIT$^+$ population was detected at equivalent frequencies in those three cytokine mixes (Figure 6B). However, when tested in an in vivo repopulation assay, the absence of BMP4 was detrimental to engraftment, as shown by a comparison of engraftment for cKIT$^+$ cells derived from AV and BAV (Figure 6C). Interestingly, cKIT$^+$ cells derived from BFV culture did not give rise to any repopulating activity, even though this cytokine combination gave rise to a high frequency of blood progenitors (Figure S5A). Furthermore, although the chimerism levels observed in mice repopulated with cKIT$^+$ cells derived from BAV and BAFV were similar, the number of mice engrafted was substantially higher in the presence of FGF (14/26; 53.8%) than in its absence (3/8; 37.5%; Figure 6C). It was recently shown that in vitro differentiated, Nodal-derived endoderm contributed in vivo to embryonic endoderm much more efficiently than Activin A-derived endoderm (Chen et al., 2013). Therefore, we assessed the in vivo repopulating ability of cKIT$^+$ cells obtained from cultures in which Activin A was replaced by Nodal. Although Nodal was able to induce the formation of a TIE2$^+$cKIT$^+$ population at days 1 and 2 of FLK1$^+$ cell culture (Figure S5B), we only observed a very low level of engraftment (0.09%) in one mouse out of 12 for all conditions tested (Figure S5C). Finally, to ensure the reproducibility and specificity of the differentiation process that is promoted by the BAFV cytokines, we performed the differentiation and engraftment protocol using BAFV cytokines from another commercial supplier. We observed similar levels of engraftment and contributions to erythroid, myeloid, and lymphoid lineages with these cytokines (Figures S5D–S5F). Altogether, these data demonstrate that very specific growth factor exposure during FLK1$^+$ differentiation to cKIT$^+$ is critically important to generate in vivo repopulating cells. Changes in a single cytokine can dramatically alter the potential of these in vitro-generated cells to engraft in vivo.

Immunophenotype of In Vitro-Derived Cells Endowed with Repopulation Activity

In order to refine our analysis of the cell population that harbored in vivo engraftment potential, we aimed to further define the immunophenotypic characteristics of this population. All endothelial cell-surface markers tested were coexpressed by cKIT$^+$ cells and therefore could not be used to subfractionate the cKIT$^+$ population. In contrast, CD41, which is known to be expressed on early embryonic HSCs (McKinney-Freeman et al., 2009; Robin et al., 2011), showed a distinct expression in a small subset of cKIT$^+$ cells (Figure 6D). Surprisingly, however, when tested in in vivo engraftment, the cKIT$^+$CD41$^-$ fraction was more enriched in repopulating activity than the cKIT$^+$CD41$^+$ fraction, whereas, as expected, the cKIT$^-$CD41$^-$ subset was devoid of this activity (Figure 6E). These results establish that as soon as TIE2$^+$cKIT$^+$ HE cells acquire CD41 expression, their in vivo engrafting ability is dramatically decreased, further reinforcing the hypothesis that the potential for in vitro-derived hematopoietic cells to repopulate recipient mice is extremely transient.

Long-Term and Multilineage Engraftment

The two most fundamental characteristics of HSCs are their abilities to self-renew and to give rise to all lineages of the blood system. As shown above in Figure 5F, blood progenitor contribution to the myeloid, erythroid, and lymphoid lineages was observed at 22 weeks after engraftment, but also at all stages analyzed (Figure S6). To address the self-renewing property of these in vitro-derived repopulating cells, we followed the frequency of CD45.2$^+$ cells in the peripheral blood of recipients for up to 20 weeks (Figure 6F), considering that engraftment past 16 weeks is a readout of long-term repopulation. From 4 to 12 weeks after engraftment, we observed a progressive decline in the contribution of donor cells, with the frequency of these cells plateauing from 12 weeks onward. Analysis of donor cell contributions in the bone marrow and spleen revealed that initially the frequency of CD45.2$^+$ cells was high in the bone marrow and low in the spleen (Figure 6G), a ratio that was reversed over time. By 22 weeks, the contribution to the bone marrow was low but still clearly detectable. Altogether, these data suggest that in vitro-derived repopulating cells are able to provide long-term multilineage engraftment, but their self-renewing ability is not as robust as that of in vivo-derived repopulating cells. In the future, it will be important to determine whether this is an intrinsic property of in vitro-derived repopulating cells or whether self-renewal can be modulated by the culture conditions.

DISCUSSION

The present study defines the temporal emergence of repopulating activity in vitro, identifying the precise step at which this population is generated. Altogether, our data establish that the presence of this repopulating activity is remarkably transient and the emergence/maintenance of this cell population is critically dependent on a precise set of growth factors.

To investigate the presence of long-term in vivo repopulating hematopoietic progenitor cells during ESC differentiation, we made the assumption that this activity might emerge rapidly upon specification of the hematopoietic program in mesoderm precursors, and we implemented several experimental strategies to test this hypothesis. First, the differentiating conditions were designed to avoid exposure to serum and cytokines such as SCF, IL6, and IL3 to prevent further differentiation of newly emerging

hematopoietic progenitors as much as possible. Second, we only considered cKIT expression as a potential marker of repopulating activity, since to date it is the only cell-surface marker that has been shown to be expressed on all HSCs throughout embryonic development and adulthood (all other markers are either expressed transiently during embryonic development or are only expressed on adult HSCs). Finally, to test for engraftment potential, we used sublethally conditioned recipients, reasoning that, in contrast to lethal irradiation, the remaining endogenous hematopoietic system would allow recipient mice to survive even with very low levels of contribution from the donor cells. A possible drawback to this approach is that the full engraftment potential might be underestimated due to competition between recipient and donor cells. However, the combination of these various experimental settings allowed us to reproducibly monitor the serum- and stroma-free generation of ESC-derived repopulating hematopoietic cells.

Our data demonstrate that both the emergence and maintenance of in vivo repopulating cells are extremely sensitive to the cytokine milieu: a change in a single factor will completely abolish the detection of engrafting cells. When we compared the outcome of FLK1 cells cultured in the presence of BAFV versus BFV, the absence of Activin A dramatically affected the detection of in vivo engrafting cells, as they were most likely rapidly pushed toward differentiation when exposed only to BFV. Taken together, our results strongly suggest that the signaling pathway activated by Activin A, but not Nodal, is critical, but not sufficient, for maintaining the repopulating ability of the $TIE2^{+}cKIT^{+}$ population. The addition of FGF seems to reinforce the role of Activin A; however, on its own, FGF is not able to maintain the population of engrafting hematopoietic progenitors. Finally, BMP4 signaling appears to be critical for conferring hematopoietic competency to the HE, an observation that is consistent with the known role of BMP4 in the regulation of *Runx1* (Burns et al., 2005; Pimanda et al., 2007). Although our study identifies differentiating conditions that allow the detection of engrafting hematopoietic cells, further work will be required to improve and optimize the culture conditions for the maintenance and expansion of these repopulating cells.

An important conceptual aspect of our findings relates to the relationship between ESC-derived repopulating cells and their in vivo counterparts. Based on their immunophenotypic characteristics, the ESC-derived cells more closely resemble the $VE\text{-}cad^{+}CD45^{-}CD41^{low}$ pre-HSC type I population identified in the AGM region at E11.5 (Rybtsov et al., 2011). However, these type I pre-HSCs express a low level of CD41 and do not engraft recipients unless they are cocultured for 4 days with OP9, in contrast to ESC-derived repopulating cells, which do not express CD41 and are able to engraft directly, albeit when injected intrafemorally. Based on their limited self-renewal characteristics, the ESC-derived engrafting cells might correspond to lineage-committed progenitors with a repopulating ability in which the multilineage potential is dissociated from the self-renewal capacity, as recently described for adult mouse bone marrow progenitors (Yamamoto et al., 2013). An interesting finding in our study is the concomitant emergence of primitive erythroid, myeloid, definitive erythroid, and lymphoid potential very early upon mesoderm specification. This is in contrast to previous studies that reported the sequential generation of these progenitors during in vitro differentiation of ESCs (Keller et al., 1993; Kennedy et al., 2012; Rafii et al., 2013). In those studies, serum-supplemented factors may have conditioned or altered the timing of differentiation and delayed the emergence of specific progenitor subsets. During embryonic development, the emergence of hematopoietic progenitors occurs in successive waves, with primitive erythroid progenitors emerging first around E7.25, followed by erythro-myeloid progenitors from E8.25 and lymphoid progenitors from E9, whereas definitive HSCs are only detected from E10.5 onward (Costa et al., 2012; Lin et al., 2014). One possible explanation to account for our findings is that during serum-free ESC differentiation, all hematopoietic programs unravel simultaneously because there are no extrinsic factors restricting or altering the developmental timing for the emergence of each lineage. During embryonic development, these cues are provided by the microenvironment in which these precursors reside.

The present study establishes a first critical step toward the generation of in vitro-derived, repopulating hematopoietic cells that might be suitable for therapeutic applications. Further work will need to be carried out to translate this protocol to the differentiation of human ESCs and iPSCs.

EXPERIMENTAL PROCEDURES

ESC Growth and Differentiation

Unless specified otherwise, the ESC line used in this study is an E14.1 (129/ola) carrying a GFP reporter cassette knocked in the Brachyury locus (Fehling et al., 2003). The F1 (129/B6) and RI (129/sv) ESC lines were also tested for engraftment potential. ESCs were maintained on irradiated mouse embryonic fibroblasts in Dulbecco's modified Eagle's medium (DMEM) supplemented with 50 μg/ml penicillin-streptomycin (GIBCO), 15% fetal calf serum (FCS; PAA Laboratories), 1% leukemia inhibitory factor (conditioned medium from Chinese hamster ovary cells), and 1.5×10^{-4} M monothioglycerol (Sigma). Prior to differentiation, ESCs were passaged twice on gelatinized tissue-culture-grade plates to remove the mouse embryonic fibroblasts. For the first passage, ESCs were grown in DMEM supplemented as above, and the second passage was performed in Iscove's modified Dulbecco's medium

supplemented as above. For gelatin treatment, dishes were coated for 20 min with 0.1% w/v gelatin in ddH_20. For EB generation, ESCs were trypsinized and plated at 50,000 cells/ml in petri-grade dishes in StemPro-34 SFM (GIBCO) supplemented with 2 mM L-glutamine (GIBCO), transferrin (Roche), 0.5 mM ascorbic acid (Sigma), and 4.5×10^{-4} M monothioglycerol (Sigma). BMP4, bFGF, Activin A, Nodal, and VEGFa (R&D Systems or PeproTech) were used at 5 ng/ml unless otherwise stated. For hemangioblast culture, $FLK1^+$ sorted cells were seeded on gelatinized plates in StemPro-34 SFM supplemented as above with the addition of cytokines as stated for each experiment.

Mice Engraftments

NOD.Cg-*Prkdc*^{scid} *Il2rg*^{tm1Wjl}/SzJ mice were purchased from The Jackson Laboratory and bred in-house or at Harlan. Male mice were irradiated with a 125 cGy sublethal dose and injected intrafemorally with sorted cells. Depending on the experiment, between 10^5 and 5×10^5 sorted cells were injected per mouse. All animal work was performed in accordance with regulations established by Home Office Legislation under the 1986 Animal Scientific Procedures Act.

SUPPLEMENTAL INFORMATION

Supplemental Information includes Supplemental Experimental Procedures and six figures and can be found with this article online at http://dx.doi.org/10.1016/j.stemcr.2015.01.003.

AUTHOR CONTRIBUTIONS

S.P., S.C., and M.F. performed the research and analyzed the data. V.K. and G.L. designed and supervised the research, analyzed the data, and wrote the manuscript.

ACKNOWLEDGMENTS

The authors thank members of V.K. and G.L.'s laboratories for critical readings of the manuscript, and the Cancer Research UK Manchester Institute facilities for technical support. Our work is funded by Cancer Research UK and the BBSRC.

Received: May 3, 2014
Revised: January 7, 2015
Accepted: January 7, 2015
Published: February 5, 2015

REFERENCES

Bertrand, J.Y., Chi, N.C., Santoso, B., Teng, S., Stainier, D.Y., and Traver, D. (2010). Haematopoietic stem cells derive directly from aortic endothelium during development. Nature *464*, 108–111.

Boisset, J.C., van Cappellen, W., Andrieu-Soler, C., Galjart, N., Dzierzak, E., and Robin, C. (2010). In vivo imaging of haematopoietic cells emerging from the mouse aortic endothelium. Nature *464*, 116–120.

Bonde, S., Dowden, A.M., Chan, K.M., Tabayoyong, W.B., and Zavazava, N. (2008). HOXB4 but not BMP4 confers self-renewal properties to ES-derived hematopoietic progenitor cells. Transplantation *86*, 1803–1809.

Burns, C.E., Traver, D., Mayhall, E., Shepard, J.L., and Zon, L.I. (2005). Hematopoietic stem cell fate is established by the Notch-Runx pathway. Genes Dev. *19*, 2331–2342.

Burt, R.K., Verda, L., Kim, D.A., Oyama, Y., Luo, K., and Link, C. (2004). Embryonic stem cells as an alternate marrow donor source: engraftment without graft-versus-host disease. J. Exp. Med. *199*, 895–904.

Chen, A.E., Borowiak, M., Sherwood, R.I., Kweudjeu, A., and Melton, D.A. (2013). Functional evaluation of ES cell-derived endodermal populations reveals differences between Nodal and Activin A-guided differentiation. Development *140*, 675–686.

Choi, K., Kennedy, M., Kazarov, A., Papadimitriou, J.C., and Keller, G. (1998). A common precursor for hematopoietic and endothelial cells. Development *125*, 725–732.

Choi, K.D., Vodyanik, M.A., Togarrati, P.P., Suknuntha, K., Kumar, A., Samarjeet, F., Probasco, M.D., Tian, S., Stewart, R., Thomson, J.A., and Slukvin, I.I. (2012). Identification of the hemogenic endothelial progenitor and its direct precursor in human pluripotent stem cell differentiation cultures. Cell Rep. *2*, 553–567.

Costa, G., Kouskoff, V., and Lacaud, G. (2012). Origin of blood cells and HSC production in the embryo. Trends Immunol. *33*, 215–223.

Doetschman, T.C., Eistetter, H., Katz, M., Schmidt, W., and Kemler, R. (1985). The in vitro development of blastocyst-derived embryonic stem cell lines: formation of visceral yolk sac, blood islands and myocardium. J. Embryol. Exp. Morphol. *87*, 27–45.

Doulatov, S., Vo, L.T., Chou, S.S., Kim, P.G., Arora, N., Li, H., Hadland, B.K., Bernstein, I.D., Collins, J.J., Zon, L.I., and Daley, G.Q. (2013). Induction of multipotential hematopoietic progenitors from human pluripotent stem cells via respecification of lineage-restricted precursors. Cell Stem Cell *13*, 459–470.

Eilken, H.M., Nishikawa, S., and Schroeder, T. (2009). Continuous single-cell imaging of blood generation from haemogenic endothelium. Nature *457*, 896–900.

Ema, M., Yokomizo, T., Wakamatsu, A., Terunuma, T., Yamamoto, M., and Takahashi, S. (2006). Primitive erythropoiesis from mesodermal precursors expressing VE-cadherin, PECAM-1, Tie2, endoglin, and CD34 in the mouse embryo. Blood *108*, 4018–4024.

Fehling, H.J., Lacaud, G., Kubo, A., Kennedy, M., Robertson, S., Keller, G., and Kouskoff, V. (2003). Tracking mesoderm induction and its specification to the hemangioblast during embryonic stem cell differentiation. Development *130*, 4217–4227.

Ferkowicz, M.J., Starr, M., Xie, X., Li, W., Johnson, S.A., Shelley, W.C., Morrison, P.R., and Yoder, M.C. (2003). CD41 expression defines the onset of primitive and definitive hematopoiesis in the murine embryo. Development *130*, 4393–4403.

Grabel, L. (2012). Prospects for pluripotent stem cell therapies: into the clinic and back to the bench. J. Cell. Biochem. *113*, 381–387.

Hole, N., Graham, G.J., Menzel, U., and Ansell, J.D. (1996). A limited temporal window for the derivation of multilineage repopulating hematopoietic progenitors during embryonal stem cell differentiation in vitro. Blood *88*, 1266–1276.

Huber, T.L., Kouskoff, V., Fehling, H.J., Palis, J., and Keller, G. (2004). Haemangioblast commitment is initiated in the primitive streak of the mouse embryo. Nature *432*, 625–630.

Irion, S., Clarke, R.L., Luche, H., Kim, I., Morrison, S.J., Fehling, H.J., and Keller, G.M. (2010). Temporal specification of blood progenitors from mouse embryonic stem cells and induced pluripotent stem cells. Development *137*, 2829–2839.

Kardel, M.D., and Eaves, C.J. (2012). Modeling human hematopoietic cell development from pluripotent stem cells. Exp. Hematol. *40*, 601–611.

Keller, G. (2005). Embryonic stem cell differentiation: emergence of a new era in biology and medicine. Genes Dev. *19*, 1129–1155.

Keller, G., Kennedy, M., Papayannopoulou, T., and Wiles, M.V. (1993). Hematopoietic commitment during embryonic stem cell differentiation in culture. Mol. Cell. Biol. *13*, 473–486.

Kennedy, M., D'Souza, S.L., Lynch-Kattman, M., Schwantz, S., and Keller, G. (2007). Development of the hemangioblast defines the onset of hematopoiesis in human ES cell differentiation cultures. Blood *109*, 2679–2687.

Kennedy, M., Awong, G., Sturgeon, C.M., Ditadi, A., LaMotte-Mohs, R., Zúñiga-Pflücker, J.C., and Keller, G. (2012). T lymphocyte potential marks the emergence of definitive hematopoietic progenitors in human pluripotent stem cell differentiation cultures. Cell Rep. *2*, 1722–1735.

Kissa, K., and Herbomel, P. (2010). Blood stem cells emerge from aortic endothelium by a novel type of cell transition. Nature *464*, 112–115.

Kitajima, K., Minehata, K., Sakimura, K., Nakano, T., and Hara, T. (2011). In vitro generation of HSC-like cells from murine ESCs/iPSCs by enforced expression of LIM-homeobox transcription factor Lhx2. Blood *117*, 3748–3758.

Kriks, S., Shim, J.W., Piao, J., Ganat, Y.M., Wakeman, D.R., Xie, Z., Carrillo-Reid, L., Auyeung, G., Antonacci, C., Buch, A., et al. (2011). Dopamine neurons derived from human ES cells efficiently engraft in animal models of Parkinson's disease. Nature *480*, 547–551.

Kyba, M., Perlingeiro, R.C., and Daley, G.Q. (2002). HoxB4 confers definitive lymphoid-myeloid engraftment potential on embryonic stem cell and yolk sac hematopoietic progenitors. Cell *109*, 29–37.

Lancrin, C., Sroczynska, P., Stephenson, C., Allen, T., Kouskoff, V., and Lacaud, G. (2009). The haemangioblast generates haematopoietic cells through a haemogenic endothelium stage. Nature *457*, 892–895.

Lancrin, C., Sroczynska, P., Serrano, A.G., Gandillet, A., Ferreras, C., Kouskoff, V., and Lacaud, G. (2010). Blood cell generation from the hemangioblast. J. Mol. Med. *88*, 167–172.

Ledran, M.H., Krassowska, A., Armstrong, L., Dimmick, I., Renström, J., Lang, R., Yung, S., Santibanez-Coref, M., Dzierzak, E., Stojkovic, M., et al. (2008). Efficient hematopoietic differentiation of human embryonic stem cells on stromal cells derived from hematopoietic niches. Cell Stem Cell *3*, 85–98.

Lesinski, D.A., Heinz, N., Pilat-Carotta, S., Rudolph, C., Jacobs, R., Schlegelberger, B., Klump, H., and Schiedlmeier, B. (2012). Serum- and stromal cell-free hypoxic generation of embryonic stem cell-derived hematopoietic cells in vitro, capable of multilineage repopulation of immunocompetent mice. Stem Cells Transl. Med. *1*, 581–591.

Lin, Y., Yoder, M.C., and Yoshimoto, M. (2014). Lymphoid progenitor emergence in the murine embryo and yolk sac precedes stem cell detection. Stem Cells Dev. *23*, 1168–1177.

Lis, R., Rafii, S., and James, D. (2013). Wading through the waves of human embryonic hemogenesis. Cell Cycle *12*, 859–860.

Matsumoto, K., Isagawa, T., Nishimura, T., Ogaeri, T., Eto, K., Miyazaki, S., Miyazaki, J., Aburatani, H., Nakauchi, H., and Ema, H. (2009). Stepwise development of hematopoietic stem cells from embryonic stem cells. PLoS ONE *4*, e4820.

McKinney-Freeman, S.L., Naveiras, O., Yates, F., Loewer, S., Philitas, M., Curran, M., Park, P.J., and Daley, G.Q. (2009). Surface antigen phenotypes of hematopoietic stem cells from embryos and murine embryonic stem cells. Blood *114*, 268–278.

Medvinsky, A., and Dzierzak, E. (1996). Definitive hematopoiesis is autonomously initiated by the AGM region. Cell *86*, 897–906.

Mikkola, H.K., Fujiwara, Y., Schlaeger, T.M., Traver, D., and Orkin, S.H. (2003). Expression of CD41 marks the initiation of definitive hematopoiesis in the mouse embryo. Blood *101*, 508–516.

Moignard, V., Woodhouse, S., Fisher, J., and Göttgens, B. (2013). Transcriptional hierarchies regulating early blood cell development. Blood Cells Mol. Dis. *51*, 239–247.

Montecino-Rodriguez, E., and Dorshkind, K. (2012). B-1 B cell development in the fetus and adult. Immunity *36*, 13–21.

Müller, A.M., and Dzierzak, E.A. (1993). ES cells have only a limited lymphopoietic potential after adoptive transfer into mouse recipients. Development *118*, 1343–1351.

Nishikawa, S.I., Nishikawa, S., Hirashima, M., Matsuyoshi, N., and Kodama, H. (1998). Progressive lineage analysis by cell sorting and culture identifies FLK1+VE-cadherin+ cells at a diverging point of endothelial and hemopoietic lineages. Development *125*, 1747–1757.

Palis, J., Robertson, S., Kennedy, M., Wall, C., and Keller, G. (1999). Development of erythroid and myeloid progenitors in the yolk sac and embryo proper of the mouse. Development *126*, 5073–5084.

Pearson, S., Sroczynska, P., Lacaud, G., and Kouskoff, V. (2008). The stepwise specification of embryonic stem cells to hematopoietic fate is driven by sequential exposure to Bmp4, activin A, bFGF and VEGF. Development *135*, 1525–1535.

Pearson, S., Lancrin, C., Lacaud, G., and Kouskoff, V. (2010). The sequential expression of CD40 and Icam2 defines progressive steps in the formation of blood precursors from the mesoderm germ layer. Stem Cells *28*, 1089–1098.

Pimanda, J.E., Donaldson, I.J., de Bruijn, M.F., Kinston, S., Knezevic, K., Huckle, L., Piltz, S., Landry, J.R., Green, A.R., Tannahill, D., and Göttgens, B. (2007). The SCL transcriptional network and BMP signaling pathway interact to regulate RUNX1 activity. Proc. Natl. Acad. Sci. USA *104*, 840–845.

Potocnik, A.J., Kohler, H., and Eichmann, K. (1997). Hematolymphoid in vivo reconstitution potential of subpopulations derived from in vitro differentiated embryonic stem cells. Proc. Natl. Acad. Sci. USA *94*, 10295–10300.

Rafii, S., Kloss, C.C., Butler, J.M., Ginsberg, M., Gars, E., Lis, R., Zhan, Q., Josipovic, P., Ding, B.S., Xiang, J., et al. (2013). Human ESC-derived hemogenic endothelial cells undergo distinct waves of endothelial to hematopoietic transition. Blood *121*, 770–780.

Ran, D., Shia, W.J., Lo, M.C., Fan, J.B., Knorr, D.A., Ferrell, P.I., Ye, Z., Yan, M., Cheng, L., Kaufman, D.S., and Zhang, D.E. (2013). RUNX1a enhances hematopoietic lineage commitment from human embryonic stem cells and inducible pluripotent stem cells. Blood *121*, 2882–2890.

Robin, C., Ottersbach, K., Boisset, J.C., Oziemlak, A., and Dzierzak, E. (2011). CD41 is developmentally regulated and differentially expressed on mouse hematopoietic stem cells. Blood *117*, 5088–5091.

Rybtsov, S., Sobiesiak, M., Taoudi, S., Souilhol, C., Senserrich, J., Liakhovitskaia, A., Ivanovs, A., Frampton, J., Zhao, S., and Medvinsky, A. (2011). Hierarchical organization and early hematopoietic specification of the developing HSC lineage in the AGM region. J. Exp. Med. *208*, 1305–1315.

Shiba, Y., Fernandes, S., Zhu, W.Z., Filice, D., Muskheli, V., Kim, J., Palpant, N.J., Gantz, J., Moyes, K.W., Reinecke, H., et al. (2012). Human ES-cell-derived cardiomyocytes electrically couple and suppress arrhythmias in injured hearts. Nature *489*, 322–325.

Slukvin, I.I. (2013). Hematopoietic specification from human pluripotent stem cells: current advances and challenges toward de novo generation of hematopoietic stem cells. Blood *122*, 4035–4046.

Sturgeon, C.M., Ditadi, A., Clarke, R.L., and Keller, G. (2013). Defining the path to hematopoietic stem cells. Nat. Biotechnol. *31*, 416–418.

Wang, L., Li, L., Shojaei, F., Levac, K., Cerdan, C., Menendez, P., Martin, T., Rouleau, A., and Bhatia, M. (2004). Endothelial and hematopoietic cell fate of human embryonic stem cells originates from primitive endothelium with hemangioblastic properties. Immunity *21*, 31–41.

Wang, L., Menendez, P., Shojaei, F., Li, L., Mazurier, F., Dick, J.E., Cerdan, C., Levac, K., and Bhatia, M. (2005a). Generation of hematopoietic repopulating cells from human embryonic stem cells independent of ectopic HOXB4 expression. J. Exp. Med. *201*, 1603–1614.

Wang, Y., Yates, F., Naveiras, O., Ernst, P., and Daley, G.Q. (2005b). Embryonic stem cell-derived hematopoietic stem cells. Proc. Natl. Acad. Sci. USA *102*, 19081–19086.

Yamamoto, R., Morita, Y., Ooehara, J., Hamanaka, S., Onodera, M., Rudolph, K.L., Ema, H., and Nakauchi, H. (2013). Clonal analysis unveils self-renewing lineage-restricted progenitors generated directly from hematopoietic stem cells. Cell *154*, 1112–1126.

Yang, L., Soonpaa, M.H., Adler, E.D., Roepke, T.K., Kattman, S.J., Kennedy, M., Henckaerts, E., Bonham, K., Abbott, G.W., Linden, R.M., et al. (2008). Human cardiovascular progenitor cells develop from a KDR+ embryonic-stem-cell-derived population. Nature *453*, 524–528.

Zovein, A.C., Hofmann, J.J., Lynch, M., French, W.J., Turlo, K.A., Yang, Y., Becker, M.S., Zanetta, L., Dejana, E., Gasson, J.C., et al. (2008). Fate tracing reveals the endothelial origin of hematopoietic stem cells. Cell Stem Cell *3*, 625–636.

Give your research a boost with alerts from Cell Press. You'll be glad you did.

Get first access with immediate, regular electronic table of contents (eToCs) alerts delivered directly to your desktop, free of charge, that keep you informed of breakthroughs in your field.

Exciting extra features like video abstracts, podcasts, and blog posts give you additional depth and context and you can access news and commentary, normally not accessible online, in advance of publication.

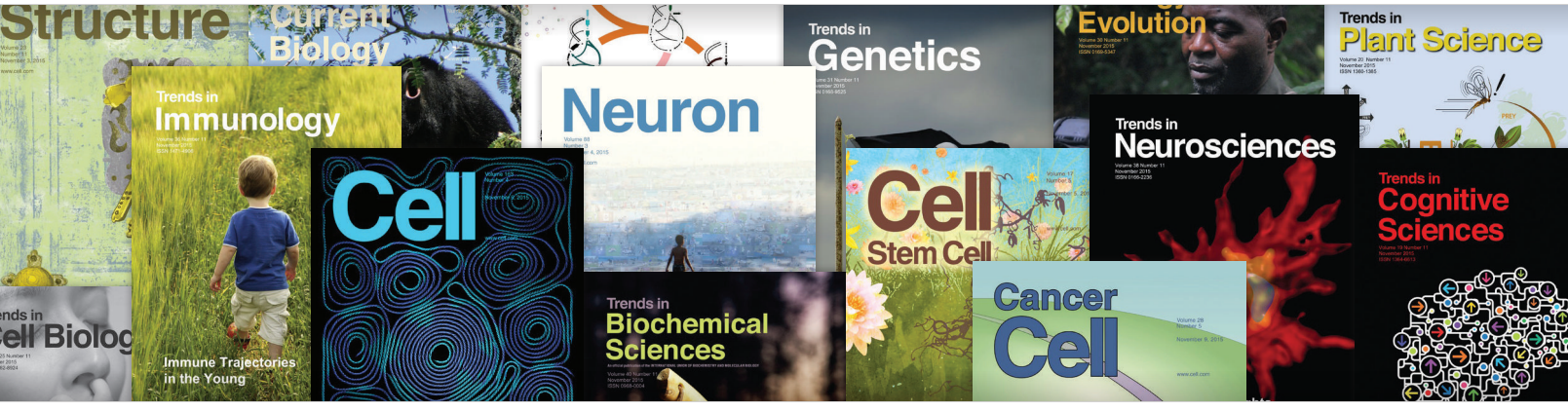

Register today
Visit cell.com/alerts

CellPress

Stem Cell Reports
Resource
OPEN ACCESS

Cloning-free CRISPR

Mandana Arbab,[1,2] Sharanya Srinivasan,[3,4] Tatsunori Hashimoto,[4] Niels Geijsen,[1,2] and Richard I. Sherwood[1,3,*]

[1]Hubrecht Institute and UMC Utrecht, Uppsalalaan 8, 3584 CT Utrecht, the Netherlands
[2]Department of Clinical Sciences of Companion Animals, Faculty of Veterinary Medicine at Utrecht University, Yalelaan 108, 3583 CM Utrecht, the Netherlands
[3]Division of Genetics, Department of Medicine, Brigham and Women's Hospital and Harvard Medical School, Boston, MA 02115, USA
[4]Computer Science and Artificial Intelligence Laboratory, Massachusetts Institute of Technology, Cambridge, MA 02142, USA
*Correspondence: rsherwood@partners.org
http://dx.doi.org/10.1016/j.stemcr.2015.09.022

SUMMARY

We present self-cloning CRISPR/Cas9 (scCRISPR), a technology that allows for CRISPR/Cas9-mediated genomic mutation and site-specific knockin transgene creation within several hours by circumventing the need to clone a site-specific single-guide RNA (sgRNA) or knockin homology construct for each target locus. We introduce a self-cleaving palindromic sgRNA plasmid and a short double-stranded DNA sequence encoding the desired locus-specific sgRNA into target cells, allowing them to produce a locus-specific sgRNA plasmid through homologous recombination. scCRISPR enables efficient generation of gene knockouts (~88% mutation rate) at approximately one-sixth the cost of plasmid-based sgRNA construction with only 2 hr of preparation for each targeted site. Additionally, we demonstrate efficient site-specific knockin of GFP transgenes without any plasmid cloning or genome-integrated selection cassette in mouse and human embryonic stem cells (2%–4% knockin rate) through PCR-based addition of short homology arms. scCRISPR substantially lowers the bar on mouse and human transgenesis.

INTRODUCTION

The clustered regularly interspaced short palindromic repeats (CRISPR)/CRISPR-associated protein 9 (Cas9) system has emerged as an efficient tool to mutate, delete, and insert genomic DNA sequences in a site-specific manner (Cong et al., 2013; Jinek et al., 2013; Mali et al., 2013). In CRISPR-mediated genome editing, Cas9 protein is directed to cleave DNA by an associated single-guide RNA (sgRNA) hairpin structure that can be designed to target almost any genomic site of interest (Jinek et al., 2012). Site-specific mutagenesis and targeted transgenesis are key applications for studying development and disease, and the ability to easily edit any genomic locus is revolutionizing genetics and stem cell research.

Currently, CRISPR/Cas9 targeting requires molecular cloning of a site-specific sgRNA plasmid for every new locus, which involves the time-consuming and costly steps of plasmid ligation, transformation, purification, and sequence verification over the course of about 1 week. This investment hinders large-scale sgRNA screening necessary for multiplexed and high-throughput genome editing applications. Additionally, knockin transgenesis of genes such as GFP using CRISPR/Cas9 still requires the time-consuming construction of homology constructs typically with 600 to 6,000 bp homology arms, a laborious process that impedes routine knockin line generation. These barriers are holding back the revolutionary potential of large-scale targeted genome manipulation. In this work, we provide alternative methods of sgRNA and homology construct generation that eliminate the need for plasmid cloning and, thus, substantially reduce the time, workload, and cost of CRISPR/Cas9-mediated genome editing, while maintaining high efficiency of site-specific mutation and transgene insertion (Table S1).

In the standard CRISPR/Cas9 method, once a site-specific sgRNA sequence is found, it is cloned into a plasmid containing a hairpin structure enabling Cas9 binding and a U6 promoter capable of transcribing the sgRNA hairpin in target cells (Ran et al., 2013; Yang et al., 2014). As each locus to be targeted requires a unique sgRNA sequence, this plasmid-cloning step must be performed for every new sgRNA to be used, providing a bottleneck to the throughput of CRISPR/Cas9-mediated genome editing and, thus, limiting mutation-based functional genomic screening applications. We have designed methods that circumvent any cloning steps in the gene editing process and demonstrate their efficacy at genome editing in both mouse and human embryonic stem cells (ESCs) as well as HEK293T cells. This method vastly simplifies the generation of targeted transgenic or knockout cell lines without compromising efficiency, creating an ideal platform for large-scale genome editing and screening applications.

RESULTS

Self-cloning CRISPR/Cas9 (scCRISPR) relies on the target cells to clone the desired sgRNA sequence. Mammalian cells are known to repair introduced plasmid DNA through

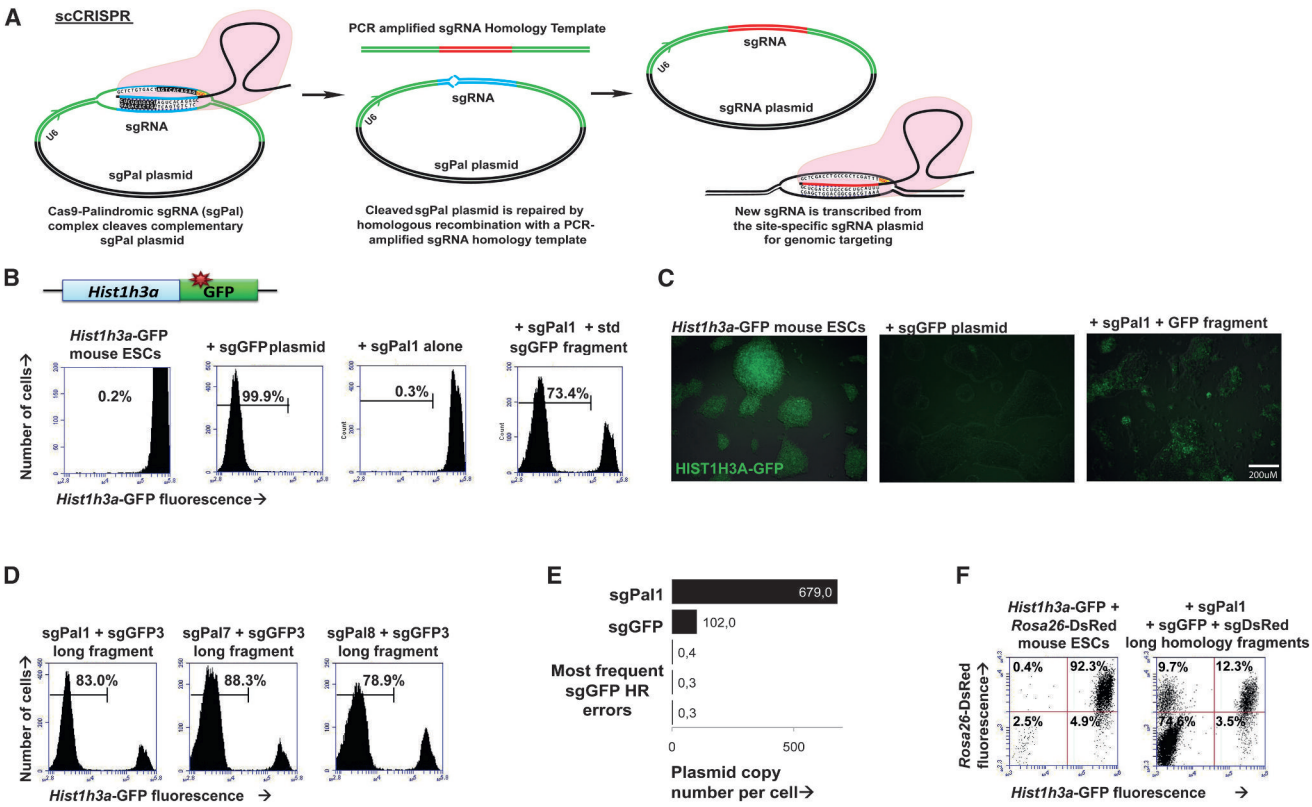

Figure 1. Simplified, Efficient Genome Editing Using scCRISPR

(A) Schematic shows the scCRISPR/Cas9 process that occurs inside target cells.

(B) Histograms show flow cytometric GFP fluorescence (x axis) in *Hist1h3a* mouse ESCs (left) after electroporation with Cas9 and plasmid sgRNA (second from left), sgPal1 plasmid alone (third from left), and sgPal1 plasmid and sgGFP homology fragment with standard-length arms (fourth from left).

(C) Fluorescence microscopy shows GFP fluorescence in *Hist1h3a*-GFP mouse ESCs (left) after targeting with Cas9 and plasmid sgRNA (second from left) and sgPal1 plasmid and sgGFP homology fragment (third from left).

(D) Histograms show flow cytometric GFP fluorescence (x axis) in *Hist1h3a*-GFP knockin mouse ESCs after electroporation with Cas9 and (from left to right) sgPal1, sgPal7, and sgPal8 plasmids together with a long sgGFP homology fragment.

(E) MiSeq plasmid copy numbers per cell of sgPal1, sgGFP, and the three most frequently mismatched sgGFP species 96 hr after co-electroporation of mouse ESCs are shown.

(F) Multiplexed mutation of GFP (x axis) and dsRed (y axis) in *Hist1h3a*-GFP *Rosa26*-dsRed mouse ESCs (left) after co-introduction of Cas9, sgPal1 plasmid, and sgGFP and sgDsRed long-armed homology fragments (right) is shown.

See also Figure S1.

homologous recombination (HR) (Folger et al., 1982; Small and Scangos, 1983; Wake and Wilson, 1979). We asked whether we could take advantage of plasmid HR by introducing a template sgRNA plasmid into cells that could be recombined with a small DNA fragment containing the desired site-specific sgRNA sequence to form a functional site-specific sgRNA plasmid. The HR pathway is stimulated by double-stranded DNA breaks (Rouet et al., 1994), so we designed a self-cleaving palindromic template sgRNA plasmid that, upon transcription in cells, should induce a DNA break in its own sequence, which subsequently could be repaired into a functional site-specific sgRNA (Figure 1A).

To implement scCRISPR, we designed self-complementary palindromic sgRNA plasmids (sgPals) that should induce their own cleavage after complexing with Cas9 in cells. We used the improved "FE" sgRNA design that has been shown to increase Cas9 cleavage efficiency (Chen et al., 2013). To minimize off-target genomic DNA cleavage by sgPal, we designed an sgPal sequence with minimal predicted off-target cleavage potential (see the Supplemental Experimental Procedures). We also designed an oligonucleotide that, upon PCR amplification, contains an sgRNA sequence-targeting GFP flanked by arms of homology to the sgPal plasmid on either side (Figure 1A). We co-electroporated a Cas9 expression plasmid, our

sgPal1 plasmid, and the GFP-targeting sgRNA homology fragment into Histone H3.1 (*Hist1h3a*)-GFP knockin mouse ESCs. The Cas9 plasmid encodes Blasticidin resistance and the sgPal1 plasmid encodes Hygromycin resistance, allowing transient antibiotic selection to enrich for cells that received both plasmids. All introduced components are transient and should not integrate into target cells such that the introduced mutation is the only lasting consequence of scCRISPR.

Electroporation of sgPal1, Cas9, and a GFP-targeting sgRNA homology fragment induced loss of GFP in 73% of cells 1 week after electroporation, while Cas9 and sgPal1 alone with no GFP-targeting sgRNA homology fragment produced minimal (0.3%) detectable GFP loss (Figures 1B and 1C). Comparatively, conventional CRISPR/Cas9 targeting with an sgRNA plasmid induced 99.9% loss of GFP. Sequence analysis confirmed loss of GFP was a result of genomic mutations at and around the target site of the sgGFP fragment (Figure S1A). scCRISPR-based treatment of Histone H2BJ (*HIST1H2BJ*)-GFP HEK293T cells also induced efficient (66%) GFP loss (Figure S1B). Thus, scCRISPR is an efficient method of inducing site-specific genomic mutation in mouse and human cell types, producing GFP loss in a majority of cells within the targeted population.

To determine whether scCRISPR indeed functions through plasmid HR, we varied the sgRNA plasmid and HR donor fragments. We found that substituting the sgPal plasmid with a non-self-cleaving sgRNA plasmid produced 9% GFP loss (Figure S1C), likely due to plasmid HR occurring in the absence of a double-strand break. When we varied the length of homology in the sgRNA homology fragment, we found that decreasing our standard homology arm length to short 60 bp arms of homology decreased the GFP loss after recombination with sgPal1 to 27% (Figure S1C), providing evidence that plasmid HR is required for scCRISPR. We designed nine additional sgPal plasmids and evaluated their efficiency in scCRISPR. All ten sgPals induced substantial GFP loss, although efficiencies ranged from 22% to 84% with sgPal7 yielding significantly more efficient GFP loss than sgPal1 (Figure S1D). The differences in efficiency between the distinct sgPals may be due to sequence characteristics affecting Cas9 cleavage, which are not yet well understood (Ren et al., 2014). Additional amplification of sgRNA fragments creating long homology arms further enhanced sgRNA targeting efficiency to 83% for sgPal1 and 88% for sgPal7 (Figure 1D). Thus, scCRISPR can achieve up to 88% mutation frequency with a self-cleaving sgRNA donor and an sgRNA acceptor amplified as a short double-stranded DNA homology fragment. Subsequent experiments reported here were carried out with sgPal1, using standard-length sgRNA homology fragments unless stated otherwise.

To assess sgPal plasmid recombination efficiency and accuracy inside target cells, we performed deep sequencing of sgRNA plasmid protospacer region in *Hist1h3a*-GFP mouse ESCs 4 days after electroporation of Cas9, sgPal1, and sgGFP homology fragment. The cells used for this experiment also contained a single-copy genomically integrated sgRNA cassette, which allowed us to calculate the average numbers of copies of each sgRNA species per cell. We found that by far the most abundant sgRNA plasmids inside cells were sgPal1 and sgGFP, with 15% of sgRNA plasmids having recombined from sgPal into sgGFP (Figure 1E). Copy-number analysis indicated that ~100 copies of sgGFP plasmid are present at this time point as compared to 600 copies of sgPal. We estimated that plasmid copy number per cell was 5- to 10-fold higher than this during the peak CRISPR targeting period between 24 and 72 hr after electroporation and was diluted upon cell division. The dataset shows a low frequency of sequences similar to sgPal or sgGFP but with a single nucleotide mismatch (Figure 1E). These erroneous sequences occur at less than 0.5% of the frequency of the correct sequences, a rate that is indistinguishable from technical MiSeq sequencing error (Quail et al., 2012). While we cannot determine conclusively whether these mutant sgRNA reads are present inside cells or are artifacts of sequencing, this error rate represents at most fewer than 0.5% of correctly recombined sgRNA plasmids. Hence, scCRISPR induces efficient and faithful sgRNA recombination within target cells.

We next asked whether the HR of sgPal plasmids in cells occurs at a high enough frequency to target multiple sites in a single experiment. We designed sgRNA homology fragments targeting two additional locations within GFP and two within dsRed. All four additional sgRNAs produced >50% loss of GFP or dsRed (Figure S1E) in *Hist1h3a*-GFP or *Rosa26*-CAGGS-dsRed cells, respectively, suggesting that scCRISPR works with a variety of sgRNAs. We then introduced two sgRNAs simultaneously into mouse ESCs, finding high rates of GFP loss with two GFP-targeting sgRNAs in *Hist1h3a*-GFP cells (70%; Figure S1E), two dsRed-targeting oligos in *Rosa26*-CAGGS-dsRed cells (75%), or one GFP-targeting and one off-target dsRed-targeting sgRNA in single-positive *Hist1h3a*-GFP cells (51% loss of GFP; Figure S1E). Dual targeting with GFP-targeting sgRNAs led to deletion mutations as opposed to indels induced by single-targeted scCRISPR (Figure S1F), indicating that scCRISPR allows efficient site-specific deletion.

To further assess the capability to multiplex sgRNAs in scCRISPR, we targeted both GFP and dsRed simultaneously in *Hist1h3a*-GFP *Rosa26*-dsRed double-positive mouse ESCs by co-electroporation of sgPal1, Cas9, and two separate sgRNA homology fragments targeting GFP and dsRed. Simultaneous dual-site targeting with long-armed

homology fragments induced 84% and 78% loss of GFP and dsRed, respectively, in the double-positive mouse ESCs with 75% double knockout (Figure 1F). Dual targeting with standard homology arms induced 69% and 64% loss of GFP and DsRed fluorescence, respectively, with both genes knocked out in 59% of cells (Figure S1G). These rates of mutation are similar to single-targeting rates, indicating that scCRISPR maintains equivalent efficiency in a multiplexed setting. Thus, scCRISPR is well suited to study the effects of compound mutations by simultaneous genome editing at multiple genomic loci in parallel.

One of the most transformative applications of CRISPR/Cas9 is the generation of gene knockins through site-specific HR to create fluorescent reporters of gene expression. Traditional knockin creation utilizing CRISPR/Cas9 requires the construction of a plasmid homology template with 600 to 6,000 bp homology arms flanking the insert sequence, a laborious undertaking requiring 1–2 weeks of molecular cloning for each targeted site and, thus, severely limiting the throughput of knockin generation. In the traditional approach, a gene-specific sgRNA plasmid (which also must be constructed), Cas9, and the plasmid homology template are co-electroporated into target cells, and screening is performed to purify the small percentage of clones that have undergone successful knockin. Having enabled cloning-free gene mutation, we asked whether we could perform plasmid-free GFP knockin.

To conduct plasmid-free GFP knockin, we designed an sgRNA targeting the C terminus of the *Hist1h3a* gene in wild-type mouse ESCs, and we performed PCR to generate a GFP homology template with a short *Hist1h3a* homology sequence on either side of GFP that should produce an in-frame C-terminal GFP fusion protein when recombined into the genome. We found that adding 80 bp of *Hist1h3a* homology sequence on either side of GFP allowed for quick and robust homology template generation in two PCR steps and under 2 hr total. To test PCR-based GFP knockin, we co-electroporated Cas9, *Hist1h3a*-targeting sgRNA plasmid, and *Hist1h3a*-GFP homology template fragment into mouse ESCs. One week after electroporation, 1.5% of cells expressed strong nuclear GFP and showed site-specific GFP integration by genomic DNA PCR (Figure 2A; Figure S2A). We achieved similar results constructing a *Nanog*-GFP knockin mouse ESC line (1.1%; Figure S2B). To demonstrate the reproducibility of mouse ESC knockin generation with PCR-based homology arms, we constructed nine additional site-specific GFP knockin lines, including C-terminal GFP fusion lines in the *Esrrb*, *Fam25c*, *Gata6*, *Klf4*, *Nfya*, *Rpp25*, and *Sox2* loci and GFP replacements in the *Tdgf1* and *Zfp42* loci (Figure S2C). We successfully derived clonal GFP knockin lines in these 11 loci, demonstrating the dramatically increased throughput in mouse ESC knockin made possible by eliminating plasmid cloning from homology arm generation.

We carried out scCRISPR plasmid-free GFP knockin by co-electroporating Cas9, sgPal1, *Hist1h3a*-targeting sgRNA homology fragment, and *Hist1h3a*-GFP homology template fragment into mouse ESCs. One week after electroporation, 0.6% of cells expressed strong nuclear GFP and showed site-specific GFP integration by genomic DNA PCR (Figures 2A and 2B; Figure S2A). We achieved similar results constructing a *Nanog*-GFP knockin mouse ESC line (0.6%; Figure S2B). To ensure that the linear GFP homology fragment did not integrate promiscuously in the genome, we ascertained the number of GFP integrations in the genome in five scCRISPR-generated GFP knockin lines by Taqman qPCR copy-number assessment. We found that all five lines have one integration of GFP per cell (heterozygous) (Figure S2D), which is supported by PCR spanning the GFP integration site (Figure S2E). Thus, our plasmid-free GFP knockin method facilitates site-specific genomic integration of the transgene. Finally, we verified whether GFP expression faithfully reports on gene function in scCRISPR-generated *Sox2*-GFP mouse ESCs. After 96 hr in serum-deprived differentiation media, we saw a significant loss of *Sox2*-GFP fluorescence (Figure S2F). Additionally, scCRISPR-based mutation of an endogenous *Sox2* promoter region resulted in loss of GFP expression (Figure S2G). Together, these results indicate that GFP expression accurately reflects endogenous gene expression.

We explored whether our approaches for fluorescent reporter generation perform just as efficiently in human ESCs, for which knockin line generation traditionally has been prohibitively difficult. We co-electroporated HUES2 human ESCs with Cas9 and sgPal1, this time in conjunction with an *HIST1H2BJ*-targeting homology fragment and *HIST1H2BJ*-GFP homology template fragment to target the C terminus of the human *HIST1H2BJ* locus in human ESCs. Fourteen days after electroporation, 1.1% of cells expressed GFP fluorescence, equivalent to targeting with conventional plasmid CRISPR/Cas9 (1.4%; Figures 2C and 2D). Thus, we present an approach that allows efficient construction of human ESC knockin lines with a total of 2 hr preparation time, a finding that will allow for a substantial increase in the throughput of human ESC knockin line generation.

It remains, however, that plasmid sgRNAs enable slightly more efficient GFP knockin than scCRISPR. Therefore, we devised a strategy to achieve high-efficiency gene insertion with a wholly plasmid-free technique. We reasoned that introducing only the sgRNA expression cassette without the entirety of the sgRNA plasmid should allow efficient sgRNA production from a minimally sized DNA sequence. We thus PCR amplified 500 bp gBlock fragments composed of a U6 promoter, GFP-targeting sgRNA sequence, and

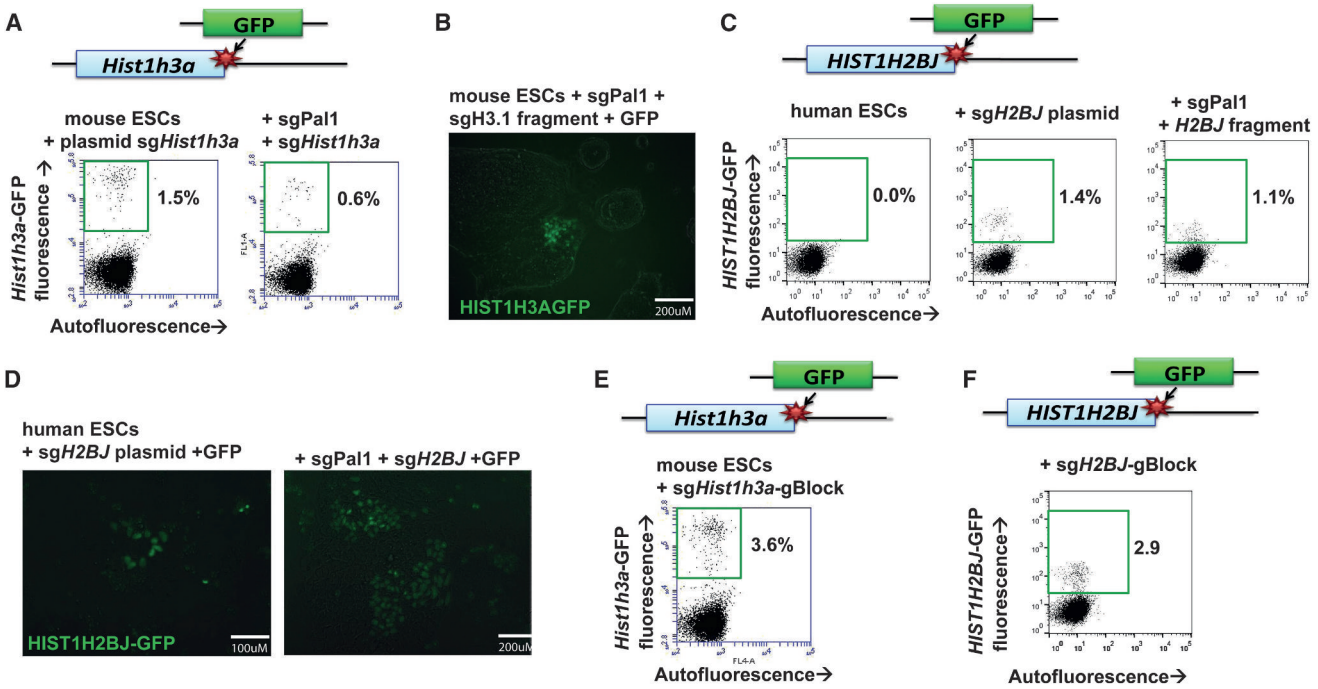

Figure 2. Efficient, Cloning-Free Knockin Transgenesis Using PCR-Amplified Homology Arms

(A) Flow cytometric analysis shows efficient generation of *Hist1h3a*-GFP knockin mouse ESCs (y axis) using a PCR-amplified GFP fragment with 80 bp *Hist1h3a* homology arms and plasmid-based sgRNA (left) or scCRISPR sgRNA (right).

(B) Fluorescence microscopy shows *Hist1h3a*-GFP mouse ESCs generated through scCRISPR-based knockin.

(C) Flow cytometric analysis shows efficient generation of *HIST1H2BJ*-GFP knockin HUES2 human ESCs (y axis) with PCR-amplified homology arms and plasmid-based sgRNA (second from left) or scCRISPR-based sgRNA (right). Untargeted human ESC fluorescence is shown for comparison (left).

(D) Fluorescence microscopy shows *HIST1H2BJ*-GFP human ESCs generated through plasmid-based (left) or scCRISPR-based (right) knockin.

(E and F) Flow cytometric analysis shows that a cloning-free approach introducing a gBlock sgRNA and a PCR-amplified homology fragment leads to even more efficient generation of *Hist1h3a*-GFP knockin mouse ESCs (E) and *HIST1H2BJ*-GFP human ESCs (F).

See also Figure S2.

sgRNA hairpin sequence, which can be commercially synthesized cost-effectively (Table S1). We co-electroporated this GFP-targeting gBlock sgRNA into *Hist1h3a*-GFP knockin mouse ESCs along with a Cas9 expression plasmid. The GFP-targeting gBlock sgRNA knocked out GFP fluorescence in 93.5% of targeted cells (Figures S2H and S2I), equivalent to the standard plasmid sgRNA CRISPR/Cas9 method.

We then performed a wholly plasmid-free GFP knockin using a gBlock sgRNA and a PCR-based GFP homology fragment. We achieved 3.6% GFP knockin at the *Hist1h3a* locus and 2.5% *Nanog*-GFP knockin (Figure 2E; Figures S2A, S2B, S2I, and S2J) in mouse ESCs. gBlock sgRNA also yielded efficient (2.9%) *HIST1H2BJ*-GFP fusion in human ESCs (Figure 2F; Figure S2J), over double the efficiency of conventional plasmid-targeted cells. GFP insertion by gBlock sgRNA also yielded highly efficient (12%) *HIST1H2BJ*-GFP gene insertion in HEK293T cells (Figure S2K). Thus, we show that genomic knockin can be performed without any molecular cloning at enhanced efficiency to the traditional plasmid-based method. Our approaches of sgRNA generation and construction of short homology sequences for gene integration dramatically decrease the time, cost, and labor involved in transgenesis.

As a proof of principle of the transformative capacity of scCRISPR in enabling functional genomic screens that are otherwise costly and time consuming, we asked whether mutation of genes involved in non-homologous end joining (NHEJ) could improve mouse ESC HR efficiency. Transient inhibition of NHEJ is known to improve HR (Chu et al., 2015; Maruyama et al., 2015), but a comprehensive screen to determine which genes are most important in the NHEJ/HR decision in mouse ESCs has not been carried out. We designed scCRISPR sgRNAs targeting 13 genes reported to regulate NHEJ in mouse ESCs and generated bulk mutant lines for each gene. We then tested

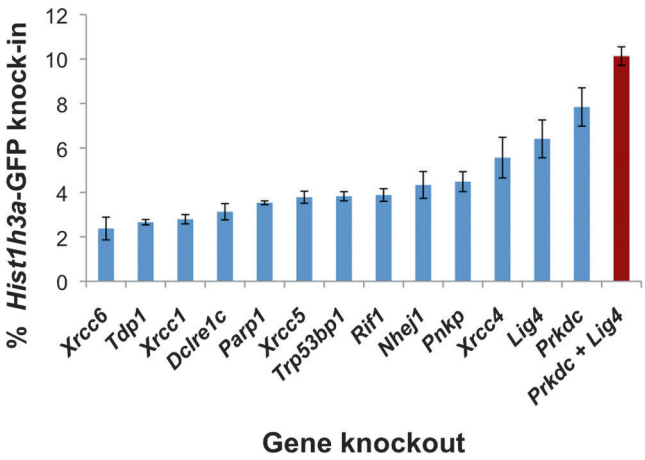

Figure 3. An scCRISPR-Based NHEJ Gene Knockout Screen Improves HR Efficiency 3-Fold

Hist1h3a-GFP knockin efficiency (y axis) is shown for 13 scCRISPR-generated bulk knockout lines of genes reported to play a role in NHEJ (x axis). Values and SDs are averaged from three independent biological experiments. A clonal double knockout line for *Prkdc* and *Lig4* (red) exhibits 3-fold more efficient HR than wild-type mouse ESCs (dotted line).

Hist1h3a-GFP knockin efficiency in all 13 lines as compared to controls (Figure 3). Mutants in *Prkdc*, *Lig4*, and *Xrcc4* led to the most significant increases in GFP knockin efficiency, a finding that meshes with the enhanced HR efficiency after small molecule and shRNA-based *Lig4* knockdown (Böttcher et al., 2014; Chu et al., 2015; Maruyama et al., 2015). We then generated dual knockouts for all combinations of *Prkdc*, *Lig4*, and *Xrcc4* using scCRISPR targeting, finding that dual mutation of *Prkdc* and *Lig4* elevated the level of GFP integration by more than 3-fold as compared to wild-type cells to over 10% of cells (Figure 3). This NHEJ-impaired mouse ESC line capable of 3-fold more efficient HR should facilitate high-throughput knockin screens. More importantly, this experiment proves that the ease of scCRISPR combined with its high-efficiency mutation rate enables quick and cheap functional genomic screening. Considering cost and effort of sgRNA cloning compound for every targeted gene in an arrayed screen such as this, scCRISPR represents a transformative tool for functional genomic screening of large gene sets.

DISCUSSION

We present scCRISPR as a unique tool for rapid (3 hr from oligonucleotide arrival versus 6 days for conventional CRISPR/Cas9), cost-effective (approximately one-sixth the cost), and efficient (up to 88% mutation rate) application of CRISPR/Cas9, optimally suited for high-throughput comparison and multiplexing of sgRNA sequences. We demonstrate that scCRISPR works efficiently in mouse and human ESCs as well as in HEK293 cells, and we expect it will show efficacy in any cell line or in vivo cell type capable of efficient homologous recombination. We show that 80 bp of homology is sufficient for efficient insertion of DNA up to 1 kb with the help of CRISPR/Cas9-mediated genome editing without the risk of off-target genome integration. These methodologies advance CRISPR/Cas9 technology by substantially reducing the effort and increasing the throughput of CRISPR/Cas9-mediated genomic mutation and gene knockin in mouse and human cell lines. By eliminating molecular cloning, these methods lower the bar for targeted genome editing, opening up opportunities for novel high-throughput genome editing and knockin screening applications.

EXPERIMENTAL PROCEDURES

Cell Culture

Mouse embryonic stem cell culture was performed according to previously published protocols (Sherwood et al., 2014). All experiments were performed with 129P2/OlaHsd mouse ESCs except for the DsRed targeting, which was performed using the IB10 mouse ESC line. Mouse ESCs were maintained on gelatin-coated plates feeder-free in mouse ESC media composed of Knockout DMEM (Life Technologies) supplemented with 15% defined fetal bovine serum (FBS, HyClone), 0.1 mM nonessential amino acids (NEAA, Life Technologies), Glutamax (GM, Life Technologies), 0.55 mM 2-mercaptoethanol (b-ME, Sigma), 1X ESGRO LIF (Millipore), 5 nM GSK-3 inhibitor XV, and 500 nM UO126. Cells were regularly tested for mycoplasma. Mouse ESC differentiation was performed by switching to serum-deprived differentiation media consisting of Advanced DMEM (Life Technologies) supplemented with 2% FBS and GM for 96 hr.

Hist1h3a-GFP fusion mouse ESCs were created using the gBlock-CRISPR method described in this work and cloned such that >99.5% of cells expressed strong nuclear GFP. *Rosa26*-CAGGS-DsRed IB10 mouse ESCs were created using plasmid-based knockin and also cloned to enrich for DsRed-expressing cells.

HEK293FT cells were cultured using DMEM (Life Technologies) supplemented with 10% FBS (HyClone).

Human ESC culture was performed according to previously published protocols. All experiments were performed with HUES2 human ESCs. Human ESCs were maintained on gelatin-coated plates on a feeder layer of irradiated murine embryonic fibroblasts (MEFs) in complete human ESC media composed of 1:1 DMEM:F12 (Life Technologies) supplemented with 15% KOSR, 0.1 mM NEAA (Life Technologies), GM (Life Technologies), 3.2 mM b-ME (Sigma), 20 ng/ml bFGF (R&D Systems), 5 nM GSK-3 inhibitor XV, and 500 nM UO126. Cells were regularly tested for mycoplasma.

Prior to electroporation, human ESCs were enzymatically passaged using 0.05% trypsin and quenched with complete human ESC media supplemented with 1% FBS (HyClone) and

10 μM Y-27632 (Tocris). For depletion of the cell suspension of feeders, the cells were plated onto a 15-cm dish in 7 ml quenching media and incubated at 37°C for 30 min. The media were then carefully transferred to a 15-ml tube and pelleted to remove excess serum.

scCRISPR Off-Target Effect Analysis

For the CRISPR in genome editing, a site-specific sgRNA sequence must be designed by a set of rules that determines both the efficiency and specificity of CRISPR targeting. sgRNAs are typically 20 bp long although 17- to 21 bp sgRNAs have been reported to be functional (Cong et al., 2013; Mali et al., 2013; Fu et al., 2014; Ran et al., 2013). Cas9 will recognize and cleave DNA only when there is a PAM sequence (-NGG) in the genome that is directly 3′ of the sgRNA sequence (Cho et al., 2014; Gilbert et al., 2013; Fu et al., 2013). Lastly, Cas9 can generate off-target DNA cleavage at sites bearing close similarity to the sgRNA sequence, especially in the 10 bp PAM-adjacent sequence (Fu et al., 2013; Wu et al., 2014; Kuscu et al., 2014), so sgRNAs with high similarity to other genomic sequences should be avoided.

To avoid unwanted off-target effects of sgPal in human and mouse applications, we searched for 10 bp sequences largely unique to the mouse and human genomes. CRISPR is highly specific but can tolerate up to five nucleotide mismatches between the sgRNA and template DNA (Cho et al., 2014). Cas9 will cleave at non-specific sites with a low efficiency so long as no more than two nucleotide differences occur within the final 11 nt, and crucially a PAM sequence must be present at the 3 bp directly downstream of the complementary region (Kuscu et al., 2014; Lin et al., 2014). sgPal sequence similarity to off-target genomic loci was determined by BLAST comparison of the 10 bp mirrored sequences to the mouse and human genomes. BLAST hits in coding regions for all palindromic sgRNAs used in this work are listed in the Supplemental Experimental Procedures.

scCRISPR

We ordered sets of oligonucleotides to clone palindromic sgRNA sequences for use in scCRISPR (all sequences are listed in the Supplemental Experimental Procedures). scCRISPR palindromic sgRNAs have an initial G nucleotide followed by an 18 or 20 bp palindromic sequence. We used a published cloning protocol (Ran et al., 2013) to clone these sequences into a BbsI-digested plasmid subcloned from the pX330 sgRNA expression cassette into a plasmid with a pT2AL200R175 backbone (Urasaki et al., 2006), Hygromycin resistance, and a modified hairpin structure to incorporate the FE alterations shown to improve sgRNA hairpin stability (Chen et al., 2013). Because the 2 nt at the end of the U6 promoter immediately upstream of the sgRNA sequence are CC, the cloned palindromic sgRNA is of the form CCG(18 to 20 bp palindromic sgRNA sequence). The reverse complement of this sequence is (18 to 20 bp palindromic sgRNA sequence)CGG, so palindromic sgRNAs of this form are capable of self-cleaving once they are transcribed in target cells and complex with Cas9.

We also subcloned the CBh Cas9 expression cassette from pX330 (Ran et al., 2013) into a plasmid with a pT2AL200R175 backbone (Urasaki et al., 2006) and Blasticidin resistance.

To prepare site-specific sgRNA homology fragments, we designed a two-step PCR amplification protocol. First, we ordered an oligonucleotide from Integrated DNA Technologies (IDT) that contains the sgRNA sequence and ~20 bp of homology to the upstream and downstream regions of the sgRNA expression cassette. Homology arm lengths used in this paper varied from short (60 bp of homology on either side), to standard (150 and 122 bp of homology on the left and right, respectively), to long (210 and 148 bp of homology on the left and right, respectively). All specific oligonucleotides are listed in the Supplemental Experimental Procedures and are of the following form: for 20 bp sgRNA, TGGAAAGGACGAAACACCGN19GTTTAAGAGCTATGCTGGAAAC; for 21 bp sgRNA, GGAAAGGACGAAACACCGN20GTTTAAGAGCTATGCTGGAAAC; and for 19 bp sgRNA, TGGAAAGGACGAAACACCGN18GTTTAAGAGCTATGCTGGAAACA.

To create standard-length homology fragments, we performed 35 cycles of Onetaq PCR using a three-step protocol (94°C for 15 s followed by 60°C for 30 s followed by 68°C for 30 s) using the following reaction mix that contains two primer sets that combine to add standard homology arms to the sgRNA oligonucleotide: 2X Onetaq master mix with standard buffer (New England Biolabs), 50% of reaction volume; 20 μM sg[LocusX], 2.5% of reaction volume; 20 μM scCRISPR_homology_fw, 2.5% of reaction volume; 20 μM scCRISPR_homology_rv, 2.5% of reaction volume; 20 μM scCRISPR_homology_extension_fw, 2.5% of reaction volume; 20 μM scCRISPR_homology_extension_rv, 2.5% of reaction volume; and dH2O, 37.5% of reaction volume.

We used a reaction volume of 100 μl per electroporation to be performed. A 2 μl aliquot of this second PCR product was run on 2% agarose to test for the expected ~292 bp product.

To create long homology fragments, we performed the first PCR but for only ten cycles, using at least 15 μl reaction volume for this first PCR.

We then performed a second PCR using the first PCR reaction as the template without purification. For this PCR, we performed 35 cycles of Onetaq PCR using a three-step protocol (94°C for 15 s followed by 60°C for 30 s followed by 68°C for 30 s) using the following reaction mix: 2X Onetaq master mix with standard buffer, 50% of reaction volume; unpurified first PCR product, 5% of reaction volume; 20 μM scCRISPR_homology_double extension_fw, 2.5% of reaction volume; 20 μM scCRISPR_homology_double extension_rv, 2.5% of reaction volume; and dH2O, 40% of reaction volume.

We used a reaction volume of 100 μl per electroporation to be performed. A 2 μl aliquot of this second PCR product was run on 2% agarose to test for the expected ~378 bp product. The products of standard and long homology fragment PCRs with different formatting to denote the initial oligonucleotide (bold), standard homology primers (underline), and long homology primers (italic) are as follows: *CGATACAAGGCTGTTAGAGAGATAATTGGAATTAATTTGACTGTAAACACAAAGATATTA*GTACAAAATACGTGACGTAGAAAGTAATAATTTCTTGGGTAGTTTGCAGTTTTAAAATTATGTTTTAAAATGGACTATCATATGCTTACCGTAACTTGAAAGTATTTCGATTTCTTGGCTTTATATATCTTG**TGGAAAGGACGAAACACC**G[N18-20]**GTTTAAGAGCTATGCTGGAAAC**AGCATAGCAAGTTTAAATAAGGCTAGTCCGTTATCAACTTGAAAAAGTGGCACCGAGTCGGTGCTTTTTTGTTTTAGAGCTAGAAATAGCAAGTTAAAAT*CGAGCAGACATGATAAGATACATTGA*.

Once verified, we performed minElute PCR purification (QIAGEN) on the product, loading a maximum of 200 μl of PCR product into a single minElute column.

For targeting of mouse ESCs, we then electroporated a mixture of 5 μg CBh Cas9-BlastR plasmid, 5 μg sgPal plasmid, and minElute purified product of 100 μl sg(LocusX) homology fragment into ~10^6 mouse ESCs. For control experiments using sgRNA plasmid, a mixture of 5 μg CBh Cas9-BlastR plasmid and 5 μg sgLocusX plasmid was used. We vacuum centrifuged the DNA mixture to a final volume of <20 μl and added 120 μl EmbryoMax Electroporation Buffer (ES-003-D, Millipore) to the mouse ESCs. DNA mixture and mouse ESC suspension were mixed and electroporated in a 0.4-cm electroporation cuvette using a BioRad electroporator at 230 V, 0.500 μF, and maximum resistance.

Electroporated cells were plated onto a single well of a 12-well tissue culture plate (BD Falcon) in >2 ml mouse ESC media supplemented with 7.5 μM Y-27632 (Tocris). From 24 to 72 hr after electroporation, media were refreshed daily with mouse ESC media supplemented with 10 μg/ml Blasticidin (Life Technologies) and 66 μg/ml (1:666) Hygromycin (Cellgro). After selection, media were refreshed every day and cells were trypsinized and replated when confluent. Testing of CRISPR mutation or homologous recombination efficiency was performed 7 days after electroporation.

We found that transfection using Lipofectamine 3000 (Life Technologies) using the standard protocol was slightly less effective (~80%–90% as efficient) than electroporation at scCRISPR and gBlock-CRISPR in mouse ESCs. For 293FT experiments, we used Lipofectamine transfection, as this cell line is known to be particularly amenable to transfection.

For targeting of human ESCs, we electroporated a mixture of 5 μg CBh Cas9-BlastR plasmid, 5 μg sgPal plasmid, and minElute purified product of 100 μl sg(LocusX) homology fragment into ~10^6 human ESCs depleted of feeder cells. For control experiments using sgRNA plasmid, a mixture of 5 μg CBh Cas9-BlastR plasmid and 5 μg sgLocusX plasmid was used. We vacuum centrifuged the DNA mixture to a final volume of <20 μl and added 100 μl electroporation buffer from the Amaxa Human Stem Cell Nucleofector kit 1 to the human ESCs. DNA mixture and human ESC suspension were mixed and electroporated in an Amaxa Nucleofector II with program B-16.

Electroporated cells were plated onto a single well of a six-well tissue culture plate (BD Falcon) previously coated with gelatin and irradiated MEFs in >2 ml complete human ESC media supplemented with 10 μM Y-27632 (Tocris). From 24 to 72 hr after electroporation, media were refreshed daily with complete human ESC media supplemented with 2 μg/ml Blasticidin (Life Technologies) and 66 μg/ml (1:666) Hygromycin (Cellgro). After selection, media were refreshed every day and cells were trypsinized and replated when confluent. Testing of CRISPR mutation or homologous recombination efficiency was performed at the first and second passages, circa 10 and 14 days after electroporation.

gBlock-Mediated CRISPR

The gBlock sequences containing the full U6 promoter, locus-specific sgRNA, and FE-modified sgRNA hairpin were ordered from IDT as gBlocks using the following template: AGTATTACGGCATGT GAGGGCCTATTTCCCATGATTCCTTCATATTTGCATATACGATAC AAGGCTGTTAGAGAGATAATTGGAATTAATTTGACTGTAAACAC AAAGATATTAGTACAAAATACGTGACGTAGAAAGTAATAATTTCT TGGGTAGTTTGCAGTTTTAAAATTATGTTTTAAAATGGACTATCA TATGCTTACCGTAACTTGAAAGTATTTCGATTTCTTGGCTTTATAT ATCTTGTGGAAAGGACGAAACACC G[N18–20] GTTTAAGAGCT ATGCTGGAAACAGCATAGCAAGTTTAAATAAGGCTAGTCCGTTA TCAACTTGAAAAAGTGGCACCGAGTCGGTGCTTTTTTGTTTTAG AGCTAGAAATAGCAAGTTAAAATAAGGCTAGTCCGTTTTTAGCG CGTGCGCCAATTCTGCAGACAAATGGCTCTAGAGGTACGGCC GCTTCGAGCAGACATGATAAGATACATTGA.

For 21 bp sgRNAs, the final A was omitted, and for 19 bp sgRNAs, a T was added at the beginning. We then performed 35 cycles of Onetaq PCR amplification on the gBlock using a three-step protocol (94°C for 15 s followed by 60°C for 30 s followed by 68°C for 30 s) using the following reaction mix: 2X Onetaq master mix with standard buffer, 50% of reaction volume; gBlock resuspended at 1 ng/μl, 0.25% of reaction volume; 20 μM gBlock-CRISPR_fw, 2.5% of reaction volume; 20 μM gBlock-CRISPR_rv, 2.5% of reaction volume; and dH2O, 44.75% of reaction volume.

We used a reaction volume of 100 μl per electroporation to be performed. A 2 μl aliquot of this PCR product was run on 2% agarose to test for the expected 500 bp product. Once verified, we performed minElute PCR purification (QIAGEN) on the product, loading a maximum of 200 μl PCR product into a single minElute column. Alternatively, we achieved equivalent results when we PCR amplified existing sgRNA plasmids with the same gBlock-CRISPR fw and rv primers, which also occur in our sgRNA plasmid.

For targeting of mouse ESCs, we electroporated a mixture of 5 μg CBh Cas9-BlastR plasmid and minElute purified product of 100 μl sg(LocusX) gBlock fragment into ~10^6 mouse ESCs using the same protocol as above. Electroporated cells were plated onto a single well of a 12-well tissue culture plate (BD Falcon) in >2 ml mouse ESC media supplemented with 7.5 μM Y-27632 (Tocris). From 24 to 72 hr after electroporation, media were refreshed daily with mouse ESC media supplemented with 10 μg/ml Blasticidin (Life Technologies) only since no Hygromycin plasmid was added. After selection, media were refreshed every day and cells were trypsinized and replated when confluent. Testing of CRISPR mutation or homologous recombination efficiency was performed 7 days after electroporation.

For targeting of human ESCs, we electroporated a mixture of 5 μg CBh Cas9-BlastR plasmid and minElute purified product of 100 μl sg(LocusX) gBlock fragment into ~10^6 human ESCs depleted of feeder cells using the same protocol as above. Electroporated cells were plated onto a single well of a six-well tissue culture plate (BD Falcon) previously coated with gelatin and irradiated MEFs in >2 ml complete human ESC media supplemented with 10 μM Y-27632 (Tocris). From 24 to 72 hr after electroporation, media were refreshed daily with complete human ESC media supplemented with 2 μg/ml Blasticidin (Life Technologies). After selection, media were refreshed every day and cells were trypsinized and replated when confluent. Testing of CRISPR mutation or homologous recombination efficiency was performed

at the first and second passages, circa 10 and 14 days after electroporation.

Homologous Recombination

GFP was amplified using two successive PCR reactions to add ~70 to 80 bp homology arms to each side. Homology arms were designed to encode GFP in frame immediately upstream of the stop codon of the *Hist1h3a* and *Nanog* genes and to include a stop codon after the GFP open reading frame (ORF). The sgRNA sequences were designed to cleave DNA as close as possible to the endogenous stop codon of the gene to be targeted. Homology arms were designed so as not to overlap with the sgRNA sequence by more than the 10 bp on the side opposite the PAM sequence, and no overlap was ever allowed on the PAM side to avoid CRISPR cleavage of the GFP homology template. The first homology primer pair is of the following format: LocusX_GFPhomologyarm_fw (LocusX pre-stop40bp)GTGAGC AAGGGCGAGGAGCT, and LocusX_GFPhomologyarm_rv (LocusX post-stop reverse complement40bp)TGAGGAGTGAATTG CGGCCG.

The common 20 bp sequences allow amplification of the entire GFP ORF and include the stop codon. These primers produce an 819 bp product. We PCR amplified GFP using 25 cycles of Phusion (NEB) PCR amplification using a two-step protocol (98°C for 10 s followed by 72°C for 45 s) using the following reaction mix: 2X Phusion master mix with standard buffer, 50% of reaction volume; GFP plasmid at 100 ng/μl, 0.5% of reaction volume; 20 μM LocusX_GFPhomologyarm_fw, 2.5% of reaction volume; 20 μM LocusX_GFPhomologyarm_rv, 2.5% of reaction volume; DMSO, 3% of reaction volume; and dH2O, 41.5% of reaction volume. For each electroporation to be performed, we used at least 10 μl reaction volume for this first PCR.

We then performed a second PCR using the first PCR reaction as the template without purification. For this PCR, we ordered 60 bp primers that extend the locus-specific homology by 30–40 bp on each end. To do so, we designed a set of PCR primers that overlapped with the first homology arm by 20–30 bp. We chose the minimal overlap such that the overlapping region was estimated to have a Tm >65°C using the NEB Tm calculator (http://tmcalculator.neb.com/#!/). We then PCR amplified the unpurified product of the previous reaction using 35 cycles of Phusion PCR amplification using a two-step protocol (98° for 10 s followed by 72° for 45 s) using the following reaction mix: 2X Phusion master mix with standard buffer, 50% of reaction volume; unpurified product of PCR1, 5% of reaction volume; 20 μM LocusX_homologyarmextension_fw, 2.5% of reaction volume; 20 μM LocusX_homologyarmextension_rv, 2.5% of reaction volume; DMSO, 3% of reaction volume; and dH2O, 37% of reaction volume.

For each electroporation to be performed, we used at least 100 μl reaction volume for this second PCR. A 2 μl aliquot of this PCR product was run on 2% agarose to test for the expected ~900 bp product. Once verified, we performed minElute PCR purification (QIAGEN) on the product, loading a maximum of 200 μl PCR product into a single minElute column.

For targeting mouse ESCs, we then electroporated a mixture of 5 μg CBh Cas9-BlastR plasmid, minElute purified product of 100 μl GFP LocusX homology arm fragment, and either gBlock or sgPal and homology fragment at the same amounts as mentioned above into ~10^6 mouse ESCs using the same protocol as above. Electroporated cells were plated onto a single well of a 12-well tissue culture plate (BD Falcon) in >2 ml mouse ESC media supplemented with 7.5 μM Y-27632 (Tocris). From 24 to 72 hr after electroporation, media were refreshed daily with mouse ESC media supplemented with 10 μg/ml Blasticidin and 66 μg/ml (1:666) Hygromycin (only with sgPal, not with gBlock). After selection, media were refreshed every day and cells were trypsinized and replated when confluent. Testing of homologous recombination efficiency was performed 7 days after electroporation.

For human ESCs, we electroporated a mixture of 5 μg CBh Cas9-BlastR plasmid, minElute purified product of 100 μl GFP LocusX homology arm fragment, and either gBlock or sgPal and homology fragment at the same amounts as mentioned above into ~10^6 human ESCs depleted of feeder cells using the same protocol as above. Electroporated cells were plated onto a single well of a six-well tissue culture plate (BD Falcon) previously coated with gelatin and irradiated MEFs in >2 ml complete human ESC media supplemented with 10 μM Y-27632 (Tocris). From 24 to 72 hr after electroporation, media were refreshed daily with complete human ESC media supplemented with 2 μg/ml Blasticidin and 66 μg/ml (1:666) Hygromycin (only with sgPal, not with gBlock). After selection, media were refreshed every day and cells were trypsinized and replated when confluent. Testing of CRISPR mutation or homologous recombination efficiency was performed at the first and second passages, circa 10 and 14 days after electroporation.

Flow Cytometry

Cells to be analyzed by flow cytometry were trypsinized, quenched, and fluorescence of 2 × 10^4 cells was measured using a BD Accuri C6 flow cytometer and accompanying software (BD Biosciences).

Fluorescence Imaging

Live-cell imaging was performed using a DMI 6000b inverted fluorescence microscope (Leica), and image analysis was performed with the Leica AF6000 software package.

SUPPLEMENTAL INFORMATION

Supplemental Information includes Supplemental Experimental Procedures, two figures, and one table and can be found with this article online at http://dx.doi.org/10.1016/j.stemcr.2015.09.022.

AUTHOR CONTRIBUTIONS

Experiments were designed by M.A. and R.I.S. Experiments were carried out and analyzed by M.A., S.S., and R.I.S. Computational analysis was performed by T.H. The manuscript was prepared by M.A., N.G., and R.I.S.

ACKNOWLEDGMENTS

The authors thank Koichi Kawakami and Feng Zhang for reagents, Lendy Chu and Nisha Rajagopal for technical assistance, and

Yiling Qiu for flow cytometric assistance. The authors acknowledge funding from NIH 5UL1DE019581, RL1DE019021, 1K01DK101684-01, 1U01HG007037, and 5P01NS055923; the Harvard Stem Cell Institute's Sternlicht Director's Fund award; and Human Frontier Science Program grant to R.I.S.

Received: May 31, 2015
Revised: September 28, 2015
Accepted: September 29, 2015
Published: October 29, 2015

REFERENCES

Böttcher, R., Hollmann, M., Merk, K., Nitschko, V., Obermaier, C., Philippou-Massier, J., Wieland, I., Gaul, U., and Förstemann, K. (2014). Efficient chromosomal gene modification with CRISPR/cas9 and PCR-based homologous recombination donors in cultured Drosophila cells. Nucleic Acids Res. *42*, e89.

Chen, B., Gilbert, L.A., Cimini, B.A., Schnitzbauer, J., Zhang, W., Li, G.W., Park, J., Blackburn, E.H., Weissman, J.S., Qi, L.S., and Huang, B. (2013). Dynamic imaging of genomic loci in living human cells by an optimized CRISPR/Cas system. Cell *155*, 1479–1491.

Cho, S.W., Kim, S., Kim, Y., Kweon, J., Kim, H.S., Bae, S., and Kim, J.S. (2014). Analysis of off-target effects of CRISPR/Cas-derived RNA-guided endonucleases and nickases. Genome Res. *24*, 132–141.

Chu, V.T., Weber, T., Wefers, B., Wurst, W., Sander, S., Rajewsky, K., and Kühn, R. (2015). Increasing the efficiency of homology-directed repair for CRISPR-Cas9-induced precise gene editing in mammalian cells. Nat. Biotechnol. *33*, 543–548.

Cong, L., Ran, F.A., Cox, D., Lin, S., Barretto, R., Habib, N., Hsu, P.D., Wu, X., Jiang, W., Marraffini, L.A., and Zhang, F. (2013). Multiplex genome engineering using CRISPR/Cas systems. Science *339*, 819–823.

Folger, K.R., Wong, E.A., Wahl, G., and Capecchi, M.R. (1982). Patterns of integration of DNA microinjected into cultured mammalian cells: evidence for homologous recombination between injected plasmid DNA molecules. Mol. Cell. Biol. *2*, 1372–1387.

Fu, Y., Foden, J.A., Khayter, C., Maeder, M.L., Reyon, D., Joung, J.K., and Sander, J.D. (2013). High-frequency off-target mutagenesis induced by CRISPR-Cas nucleases in human cells. Nat. Biotechnol. *31*, 822–826.

Fu, Y., Sander, J.D., Reyon, D., Cascio, V.M., and Joung, J.K. (2014). Improving CRISPR-Cas nuclease specificity using truncated guide RNAs. Nat. Biotechnol. *32*, 279–284.

Gilbert, L.A., Larson, M.H., Morsut, L., Liu, Z., Brar, G.A., Torres, S.E., Stern-Ginossar, N., Brandman, O., Whitehead, E.H., Doudna, J.A., et al. (2013). CRISPR-mediated modular RNA-guided regulation of transcription in eukaryotes. Cell *154*, 442–451.

Jinek, M., Chylinski, K., Fonfara, I., Hauer, M., Doudna, J.A., and Charpentier, E. (2012). A programmable dual-RNA-guided DNA endonuclease in adaptive bacterial immunity. Science *337*, 816–821.

Jinek, M., East, A., Cheng, A., Lin, S., Ma, E., and Doudna, J. (2013). RNA-programmed genome editing in human cells. eLife *2*, e00471.

Kuscu, C., Arslan, S., Singh, R., Thorpe, J., and Adli, M. (2014). Genome-wide analysis reveals characteristics of off-target sites bound by the Cas9 endonuclease. Nat. Biotechnol. *32*, 677–683.

Lin, Y., Cradick, T.J., Brown, M.T., Deshmukh, H., Ranjan, P., Sarode, N., Wile, B.M., Vertino, P.M., Stewart, F.J., and Bao, G. (2014). CRISPR/Cas9 systems have off-target activity with insertions or deletions between target DNA and guide RNA sequences. Nucleic Acids Res. *42*, 7473–7485.

Mali, P., Yang, L., Esvelt, K.M., Aach, J., Guell, M., DiCarlo, J.E., Norville, J.E., and Church, G.M. (2013). RNA-guided human genome engineering via Cas9. Science *339*, 823–826.

Maruyama, T., Dougan, S.K., Truttmann, M.C., Bilate, A.M., Ingram, J.R., and Ploegh, H.L. (2015). Increasing the efficiency of precise genome editing with CRISPR-Cas9 by inhibition of nonhomologous end joining. Nat. Biotechnol. *33*, 538–542.

Quail, M.A., Smith, M., Coupland, P., Otto, T.D., Harris, S.R., Connor, T.R., Bertoni, A., Swerdlow, H.P., and Gu, Y. (2012). A tale of three next generation sequencing platforms: comparison of Ion Torrent, Pacific Biosciences and Illumina MiSeq sequencers. BMC Genomics *13*, 341.

Ran, F.A., Hsu, P.D., Wright, J., Agarwala, V., Scott, D.A., and Zhang, F. (2013). Genome engineering using the CRISPR-Cas9 system. Nat. Protoc. *8*, 2281–2308.

Ren, X., Yang, Z., Xu, J., Sun, J., Mao, D., Hu, Y., Yang, S.J., Qiao, H.H., Wang, X., Hu, Q., et al. (2014). Enhanced specificity and efficiency of the CRISPR/Cas9 system with optimized sgRNA parameters in Drosophila. Cell Rep. *9*, 1151–1162.

Rouet, P., Smih, F., and Jasin, M. (1994). Expression of a site-specific endonuclease stimulates homologous recombination in mammalian cells. Proc. Natl. Acad. Sci. USA *91*, 6064–6068.

Sherwood, R.I., Hashimoto, T., O'Donnell, C.W., Lewis, S., Barkal, A.A., van Hoff, J.P., Karun, V., Jaakkola, T., and Gifford, D.K. (2014). Discovery of directional and nondirectional pioneer transcription factors by modeling DNase profile magnitude and shape. Nat. Biotechnol. *32*, 171–178.

Small, J., and Scangos, G. (1983). Recombination during gene transfer into mouse cells can restore the function of deleted genes. Science *219*, 174–176.

Urasaki, A., Morvan, G., and Kawakami, K. (2006). Functional dissection of the Tol2 transposable element identified the minimal cis-sequence and a highly repetitive sequence in the subterminal region essential for transposition. Genetics *174*, 639–649.

Wake, C.T., and Wilson, J.H. (1979). Simian virus 40 recombinants are produced at high frequency during infection with genetically mixed oligomeric DNA. Proc. Natl. Acad. Sci. USA *76*, 2876–2880.

Wu, X., Scott, D.A., Kriz, A.J., Chiu, A.C., Hsu, P.D., Dadon, D.B., Cheng, A.W., Trevino, A.E., Konermann, S., Chen, S., et al. (2014). Genome-wide binding of the CRISPR endonuclease Cas9 in mammalian cells. Nat. Biotechnol. *32*, 670–676.

Yang, L., Yang, J.L., Byrne, S., Pan, J., and Church, G.M. (2014). CRISPR/Cas9-directed genome editing of cultured cells. Curr. Protoc. Mol. Biol. *107*, 31.1.1–31.1.17.

ISSCR INTERNATIONAL SOCIETY FOR STEM CELL RESEARCH

INTERNATIONAL 2016 SYMPOSIA

EUROPEAN SOCIETY OF GENE & CELL THERAPY

XXIV[TH] ANNUAL CONGRESS

IN COLLABORATION WITH

abcd Associazione di Biologia Cellulare e del Differenziamento

CHANGING THE FACE OF MODERN MEDICINE:
STEM CELLS & GENE THERAPY

FLORENCE ITALY

18-21 OCTOBER 2016

REGISTRATION AND ABSTRACT SUBMISSION NOW OPEN

WWW.ISSCR.ORG • WWW.ESGCT.EU • WWW.ABCD-IT.ORG

Culture of Excellence

ISSCR ANNUAL MEETING GOLD SUPPORTER

Visit BI booth
#1419

Redefining Stem Cell Excellence

and Advancing Clinical Applications

NutriStem® Family of Stem Cell Products

- Defined, serum-free, xeno-free, and feeder-free culture systems for hiPSC, hESC and hMSC
- Specially developed solutions for attachment, dissociation, cryopreservation and differentiation
- Hundreds of publications
- Complete protocols and application data
- FDA Drug Master File (DMF) available

Discover how our innovative, reliable, high performance products facilitate stem cell research and advancing cell-based therapies

Growth curve of hPSC

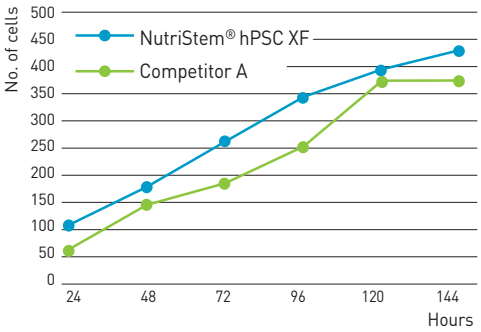

H1 cells (passage 6) were seeded in 96 well plates (Matrigel-coated) in the various media. Media were changed every 24 hours. The number of cells was determined using a CyQuant cell proliferation assay kit.

Growth Curve of hMSC

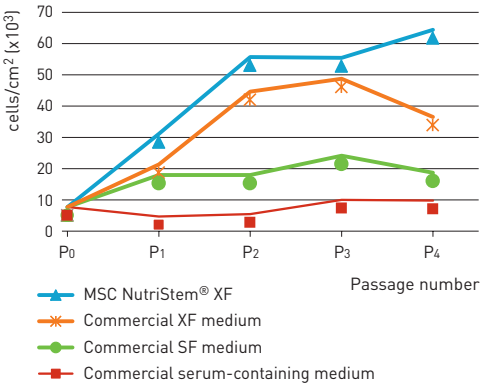

Expansion of hMSC-AT in MSC NutriStem® XF and commercial competitors XF, SF, and serum-containing media. Cells were cultured in plates, pre-coated with MSC Attachment Solution. Initial seeding was 5000 cells/cm² for each of the tested media (Day 0). Cells were counted at day 3 in each passage.

BI Biological Industries
Culture of Excellence

USA - Tel. 860-316-2702 | orders-usa@bioind.com
Global - Tel. 972-4-9960595 | info@bioind.com
www.bioind.com

CERTIFIED QMS ISO 9001 2008
CERTIFIED QMS ISO 13485 2003
CE
cGMP Manufacturing Facility